Synthesis, Structure and Properties of Zintl-Type Thermoelectric Materials

Ruth Amy Downie

Submitted for the degree of Doctor of Philosophy

Heriot-Watt University

Institute of Chemical Sciences

July 2014

ABSTRACT

Zintl-type materials are of great interest in the field of thermoelectrics as their structures lend themselves to independent optimization of properties. For this reason, three distinct series, that can all be described using a Zintl-type model, were prepared using standard solid state reactions.

A detailed investigation of $X_{1-x}X'_xNiSn$ (X = Ti, Zr, Hf) half-Heusler compositions was undertaken, results of which are presented in Chapters 3-5. These materials are well established as promising thermoelectrics but progress in increasing efficiencies has been hindered by a lack of understanding of the structure and irreproducibility of properties. The work presented herein therefore aimed to provide a detailed analysis of the structure of these compositions. This was achieved primarily by neutron powder diffraction which has not previously been used in the study of these materials. Complimentary electron microscopy analysis was also carried out to gain information on the structure over various length-scales and thermoelectric property measurements were performed. Significant multiphase behaviour was discovered in all compositions where $x \neq 0, 1$. Our data indicates that the compositional variations occur over long length-scales and has no significant impact on the thermoelectric properties. In addition, 0-3% excess Ni, located on interstitial sites in the half-Heusler structure was found in all samples, regardless of the synthesis method used. This has not previously been acknowledged in the literature and is difficult to identify without neutron diffraction. Three $TiNiM_ySn$ series (M = Ni, Co, Cu) were subsequently prepared. Up to 8% interstitial metal was successfully introduced to the TiNiSn structure and had a doping effect on the thermoelectric properties. The introduction of interstitial metals was therefore found to be a new route to controlling the electronic properties of these promising thermoelectric materials.

TiNiX (X = Si, Ge) and RMnSbO (R = Nd, La) were considered as new materials to the field of thermoelectrics as described in Chapters 6 and 7, respectively. Both series showed some promise for thermoelectric applications, with a large Seebeck coefficient found in NdMnSbO and low resistivity values displayed by the TiNiX compositions. In addition, detailed X-ray and neutron powder diffraction experiments and measurements of their magnetic properties were undertaken. Large magnetoresistances were found in TiNiX and incommensurate magnetic ordering was uncovered in NdMnSbO.

Acknowledgements

First and foremost, I would like to thank Dr. Jan-Willem Bos for supervising this PhD. I am truly grateful for the opportunity to carry out this research, and all the opportunities you have provided throughout, to further my learning. I have very much enjoyed my three and half years at Heriot-Watt and that is in no small part due to the encouragement and support you have shown.

I would also like to thank the technical and support staff at Heriot-Watt - in particular, Alan and Paul, who have saved the day on more than one occasion! Thanks are also due to Ron Smith and Pascal Manuel, our local contacts at ISIS; and Jim Buckman and Donald MacLaren, who carried out the electron microscopy analysis. I have also been lucky to work alongside many different people as part of the solid state group at Heriot-Watt. Each one of them has helped me along the way and I am truly grateful. Particular thanks go to Sarah, Steven and Alexandra, whose enthusiasm and friendship have been a great support to me.

I would like to thank all my friends and family for their encouragement and feigning interest in the finer points of materials chemistry. I am especially grateful to my parents, who have shown unwavering belief in me and always encouraged me to be the best that I can be. To my brother and sister, Ian and Jenna, you have each shown me your unique brand of support and it is much appreciated. Huge thanks are also due to my best friend, Ruth – your self-proclaimed title as ‘queen of pep-talks’ is certainly justified! Last but not least, I would like to thank Graeme, who has had to suffer stress, strops and general neglect at the hands of this thesis. I am sure I have not been easy to live with these past few months but coming home to you at the end of a long day has made it immeasurably easier.

DECLARATION STATEMENT

TABLE OF CONTENTS

LIST OF PUBLICATIONS BY THE CANDIDATE

1. ‘Enhanced thermoelectric performance in TiNiSn-based half-Heuslers’ – R. A. Downie, D. A. MacLaren, R. I. Smith and J. W. G. Bos; *Chemical Communications*; 49 (2013) 4148-4186.

2. ‘Thermoelectric Performance of Multiphase XNiSn (X = Ti, Zr, Hf) half-Heusler Alloys’ – R. A. Downie, D. A. MacLaren and J. W. G. Bos; *Journal of Materials Chemistry A*; 2 (2014) 6107-6114.

LIST OF ABREVIATIONS

ZT	thermoelectric figure-of-merit
VB	valence band
CB	conduction band
DOS	density of states
PGEC	phonon-glass-electron-crystal
VEC	valence electron count
XRD	X-ray diffraction
NPD	neutron powder diffraction
GSAS	General Structure Analysis System
TEM	transmission electron microscopy
STEM	scanning transmission electron microscopy
SEM	scanning electron microscopy
EDX	energy dispersive X-ray analysis
SPS	spark-plasma-sintering
DFT	density functional theory
SQUID	superconducting quantum interference device
PPMS	physical property measurement system
MPMS	magnetic property measurement system

Chapter 1 - Introduction

Modern society is heavily dependent on fossil fuels that are becoming increasingly depleted and costly.[1] Sustainable and renewable energy development is therefore vital in maintaining living standards. Solar, wind and biomass energy conversion, amongst others, are receiving increasing attention as alternative energy sources, but no single technique is thought to have the capacity to entirely replace fossil fuels. It seems increasing likely that any energy future will be based on multiple technologies, working in unison to harness otherwise ignored energy sources. Amongst these, thermoelectric devices can play an important role.[2]

As much as 60% of the energy produced from fossil fuels worldwide is lost in the form of heat.[3] Thermoelectric devices can convert heat to electricity or vice versa, via the Seebeck or Peltier effect. The production of electricity from heat energy gives them power generation applications and they can be used as primary energy sources, in which they harness heat from the sun or combustion processes.[3] However, the greatest potential of thermoelectric generators is probably in the recovery of waste heat where the excess heat generated by other processes is harnessed. This improves the fuel efficiency of such processes, which is another key concern in any modern technology. In addition, thermoelectric devices are a green technology, emitting no harmful gases in the electricity-production process.[4] They are solid state devices thus are easily scalable and long-lived, due to the absence of moving parts. This means they can be easily adapted to almost any situation, from the domestic, to the industrial scale.[5, 6] Much research, for example, has been directed at using thermoelectric generators in car exhaust systems. Here, they replace the alternator and use the waste heat generated by the engine to produce electricity, thus mileage is improved and electricity is produced that can run the electrical systems in the car. On the larger scale, thermoelectric devices that use radioactive decay as their heat source have been used (and are still in use) in space travel, for example in the Mars Rover and Voyager satellite. The longevity of these devices should, in theory, allow shuttles to continue to travel for 10s of years.[7]

In addition to power generation, thermoelectric devices may be used as refrigerators, where they turn electricity into a temperature gradient. So-called Peltier coolers offer an alternative to conventional refrigerators that do not require a mechanical system and harmful gases, thus they are more reliable and a much greener option.[8] Other uses in

this mode include the cooling of laser diodes and microelectronics.[9] Temperatures as low as 160 K can be reached using these devices, thus their applications could be wide-ranging.[10]

Despite the obvious advantages that thermoelectric devices offer, widespread use is not yet possible. The best performing thermoelectric devices are composed of relatively scarce elements and are expensive to prepare. The efficiencies of the best devices are not yet sufficient to make them viable for large scale applications and only niche markets currently make use of this technology. With the demand for greener, more sustainable technologies growing dramatically in recent years there has been renewed interest in this field and the search for new, more efficient materials has gained momentum. A large number of promising thermoelectrics have since been discovered but attainment of 10-20% efficiency levels at low cost remains elusive. The work presented in this thesis forms part of the far-reaching search for better performing materials. Herein, investigations of the structure and properties of promising TiNiSn-based half-Heuslers are reported, along with similar investigations into TiNiX (X = Si, Ge) and RMnSbO (R = Nd, La) compounds, which are less well studied in this field but contain features which make them possible candidates for thermoelectric applications.

1.1 Thermoelectric Effects

1.1.1 The Seebeck Effect

The Seebeck effect was first observed in 1821 by Thomas Seebeck. He reported that the needle of a compass was deflected when it was placed near a closed loop composed of two dissimilar metals, where the junctions between the metals were held at different temperatures, as illustrated in Figure 1.1.

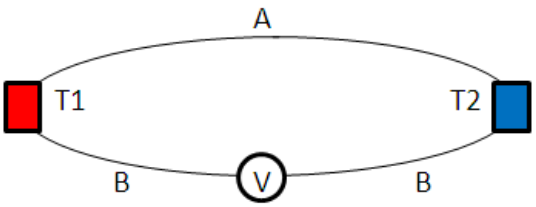

Figure 1.1: Illustration of the Seebeck effect, where the junctions of a closed loop containing metals A and B are held at different temperatures, T1 and T2.

He concluded that the temperature gradient caused the metals to become magnetised but it was later determined that, in fact, the temperature difference gave rise to an electric current in the loop. This is because applying a temperature gradient within a material creates differing chemical potentials for the charge carriers at the hot and cold ends. The charge carriers then flow through the material, from the hot to the cold end, to compensate for these differing potentials. This causes a charge to build up at one end, resulting in electrostatic repulsion which forces some carriers to diffuse back to the hot end. The maximum charge build up is therefore achieved when the chemical and electrostatic potentials are balanced. A build-up of charge means that a voltage is produced and completion of the circuit allows a current to flow. The magnitude of the Seebeck effect is defined by the Seebeck coefficient (S), defined in Equation (1.1). This is the voltage produced in a material (ΔV), for a given temperature difference (ΔT).[11]

$$S = \frac{\Delta V}{\Delta T} \qquad \text{Equation (1.1)}$$

The Seebeck coefficient and the properties of a material that control it are discussed in greater detail in Section 1.4.1.

1.1.2 The Peltier Effect

The Peltier effect, discovered by Jean Peltier in 1834, is the reverse of the Seebeck effect. If a current is passed through a closed loop containing two materials, then heat is liberated at one junction and absorbed at the other, i.e. a temperature gradient is created.

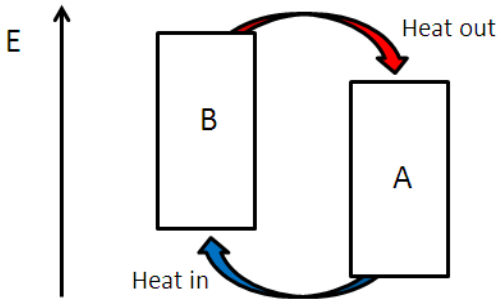

Figure 1.2: Schematic of the Peltier effect, whereby passing a current around a closed loop containing metals A and B results in heat generation at one junction and heat absorption at the other.

This effect is a result of electrons moving from lower energy levels in one material to higher levels in the other at one junction, and from the higher to lower energy levels at the other, as illustrated in Figure 1.2. It is then easy to see that movement from material A to material B (Figure 1.2) requires energy and heat is absorbed, while the opposite is true when moving from B to A, where energy is released in the form of heat. The amount of heat generated (Q) is related to the Peltier coefficients (Π) of the two materials and the applied current (I), as described in Equation (1.2).

$$Q = (\Pi_A - \Pi_B)I \qquad \text{Equation (1.2)}$$

The cooling power of a Peltier device is somewhat reduced, compared to the value that may be expected from the description set out above. This is due to Joule heating and heat conduction. Heat conduction results from a temperature gradient that naturally occurs upon movement of the charge carriers, and causes heat to flow from the hot to the cold end. Joule heating is often referred to as resistive heating and occurs in all materials where a current flows. It is irreversible and independent of the direction of current flow. The amount of heat released (Q) in time (t) is related to the resistance (R) and the current (I) passed through a material in that time, as defined by Joule's first law (Equation (1.3)).

$$Q = I^2Rt \qquad \text{Equation (1.3)}$$

It can therefore be seen that simply increasing the current to very large values will not continuously improve the cooling power of a Peltier device as, at some point, Joule heating becomes dominant. There is therefore an optimum current that can be applied to produce a maximum temperature gradient and maximum cooling power within the device.[5]

1.1.3 The Thomson Effect

In 1854, William Thomson (Lord Kelvin) attempted to relate the Seebeck and Peltier effects to one another, and in doing so discovered a third thermoelectric effect – the Thomson effect. He posited, and later proved experimentally, that a single material subjected to both an applied current and a temperature gradient will either generate or absorb heat, in addition to Joule heating, as expressed in Equation (1.4).

$$Q = -\mu I \frac{dT}{dx} \qquad \text{Equation (1.4)}$$

where Q is the heat produced in the conductor per unit volume per second, I is the current, σ is the conductivity, μ is the Thomson heat and *dT/dx* is the temperature gradient. He was subsequently able to draw relationships between the three effects, as set out in Equation (1.5) and Equation (1.6).

$$\mu = T \frac{dS}{dT} \qquad \text{Equation (1.5)}$$

$$\Pi = TS \qquad \text{Equation (1.6)}$$

Thus the close relationship between the Seebeck and Peltier effects is clearly demonstrated.

1.2 Thermoelectric Devices

Thermoelectric couples are composed of two thermoelectric 'legs', one n- and one p-type, that are linked electrically in series and thermally in parallel, as depicted in Figure 1.3.

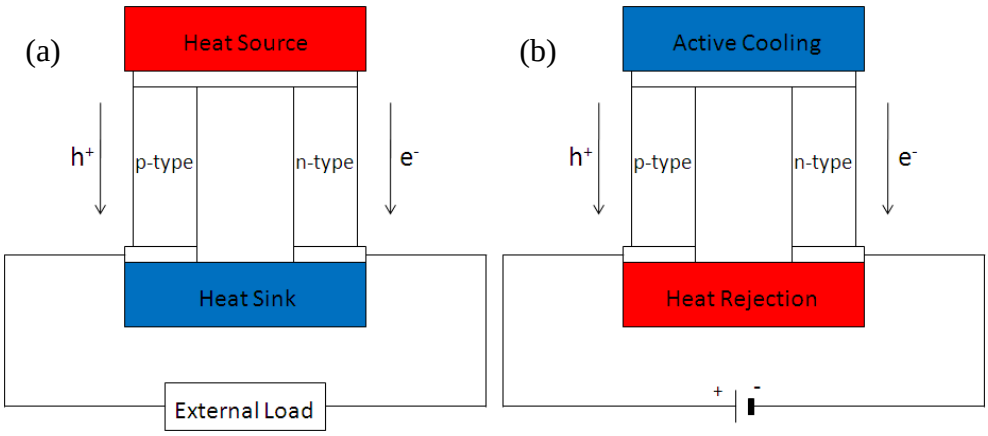

Figure 1.3: Thermoelectric couples in (a) heat generation mode and (b) cooling mode.

In the n-type material the dominant charge carriers are electrons, while the p-type material contains holes. In power generation mode, heat is applied to one end of the couple, producing a temperature gradient. The Seebeck effect is then exploited as the

charge carriers in each leg migrate from the hot to the cold end, producing a voltage. If the circuit is completed, a current will then flow and power any applied external load. This process is represented schematically in Figure 1.3(a). In cooling mode, illustrated in Figure 1.3(b), a current is applied and, via the Peltier effect, one side is cooled whilst the other acts as a heat sink. A thermoelectric device is composed of multiple couples, linked electrically in series and thermally in parallel. This set-up highlights the scalability of thermoelectric devices as the number of couples used is easily varied.

1.3 Thermoelectric Efficiency

The power generation efficiency (η) of a thermoelectric device is determined by the applied temperature gradient (ΔT) and the combined thermoelectric figure-of-merit (ZT) of the materials involved. Both these parameters are combined with the Carnot efficiency ($\Delta T/T_{hot}$) to produce the thermoelectric efficiency of the device, as per Equation (1.7).

$$\eta = \frac{\Delta T}{T_{hot}} \frac{\sqrt{1 + ZT_{avg}} - 1}{\sqrt{1 + ZT_{avg}} + \frac{T_{cold}}{T_{hot}}} \qquad \text{Equation (1.7)}$$

where T_{hot} and T_{cold} are the temperatures of the hot and cold ends, respectively, $\Delta T = T_{hot} - T_{cold}$, T_{avg} is the average temperature and ZT_{avg} is the average ZT of the n- and p-type materials involved. ZT and ΔT must therefore both be large in order to reach efficiency levels high enough to allow widespread use of thermoelectric devices. Current thermoelectric materials in use offer ZT ≈ 1 which equates to 5-6% efficiency. This is not high enough to allow thermoelectric devices to compete with current power generation and refrigeration technology and only allows use in niche applications where factors other than efficiency, such as size and reliability, are deemed most important. ZT values above 3 would give rise to efficiencies of around 30% making thermoelectric devices competitive with power generation from fossil fuels and conventional refrigerator technology.[12]

$$ZT = \frac{S^2 \sigma T}{\kappa_{el} + \kappa_{lat}} \qquad \text{Equation (1.8)}$$

The thermoelectric figure-of-merit of a particular material, ZT, is a measure of its intrinsic efficiency and is dependent on its Seebeck coefficient (S), electrical conductivity (σ), absolute temperature (T) and thermal conductivity (κ), as illustrated by Equation (1.8). In this equation, κ_{el} is the heat carried by the charge carriers and κ_{lat} is the heat carried by phonons through the lattice. Together, S and σ make up the power factor ($S^2\sigma$) of a material.

Attainment of high ZT values is therefore reliant on maximising S and σ, whilst minimising κ. This is not straightforward, however, as these factors are not independent of one another. S, σ and κ_{el} are all dependent on the band structure of the material and the relationships between them are complex. Inspection of their respective dependences on carrier concentration clearly highlights the conflicts that must be overcome to maximise ZT. Figure 1.4 has been taken from Ref. [13] and clearly demonstrates that vastly different concentrations are beneficial for optimisation of different properties. A low carrier concentration, as found in insulators for example, promotes a high Seebeck coefficient and low thermal conductivity, but results in low electronic conductivity. The opposite is true for high carrier concentrations, as found in metals. Analysis of Figure 1.4 makes it clear that compromises must be made. The optimal carrier concentration for attaining the highest ZT values is in the range 10^{19} to 10^{21} carriers cm^{-3}.[13] This means the most suitable materials for thermoelectric applications are heavily doped semiconductors, and this is where the vast majority of thermoelectrics research is focussed.

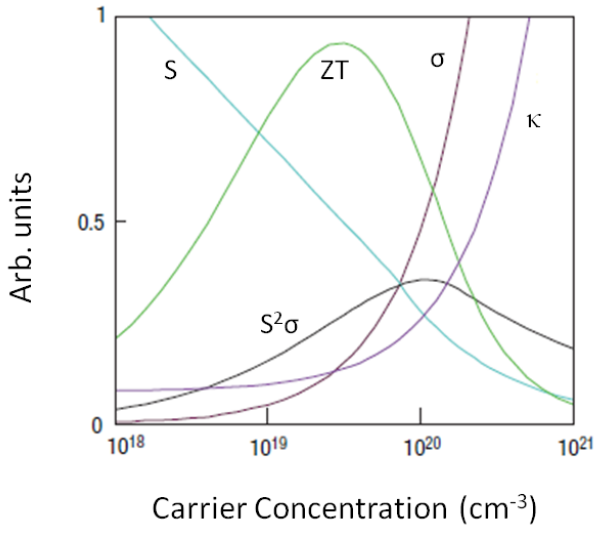

Figure 1.4: Dependence of S, σ, κ, $S^2\sigma$ and ZT on carrier concentration.[13]

1.4 Thermoelectric Properties

1.4.1 Seebeck Coefficient, S

First and foremost, a large Seebeck coefficient (S) relies on there being one dominant charge carrier. A negative Seebeck coefficient is caused by n-type conduction (where the charge carriers are electrons) and a positive S-value is a consequence of p-type conduction (where holes are the charge carriers). If both carrier types are present, then they cancel one another out, resulting in low S-values.

As defined in Equation (1.1), S is a measure of the voltage produced by a material when subjected to a given temperature gradient. A more instructive definition of S, which gives an indication of the properties that are desirable for a large Seebeck effect, comes from the Mott equation, defined in Equation (1.9).[14]

$$S = \frac{\pi^2}{3}\frac{k^2 T}{e}\frac{\mathrm{d}\ln\sigma(E)}{\mathrm{d}E}\bigg|_{E=E_f} \qquad \text{Equation (1.9)}$$

where k is the Boltzmann constant, e is the charge of the carrier and σ(E) is the electrical conductivity. This approximation only holds if the electronic scattering is independent of energy, in which case $\sigma(E) \propto N(E)$, where N(E) is the density of states at the Fermi level (E_f).

The basic conclusion that can be derived from Equation (1.9) is that a rapidly changing density of states (DOS), near the Fermi level (E_f), will give rise to large values of S.[12] Materials with complex band structures containing sharp, narrow bands are therefore desirable for high performance thermoelectrics. This is demonstrated by evaluating the effects of reduced dimensionality, which results in increasingly sharp peaks in the DOS (Figure 1.5) and corresponds to an increase in S.[15] Reductions in dimensionality include layered materials (2D), nano-wires (1D) and nano-particles (0D). A complex band structure with numerous degenerate maxima is also beneficial, as each will contribute to the overall value of S and they are additive. This is a property of high symmetry systems.[9] It is therefore unsurprising that most of the current materials of interest for thermoelectric applications are cubic, hexagonal or tetragonal and the most significant progress in improving ZT has involved nano-effects.

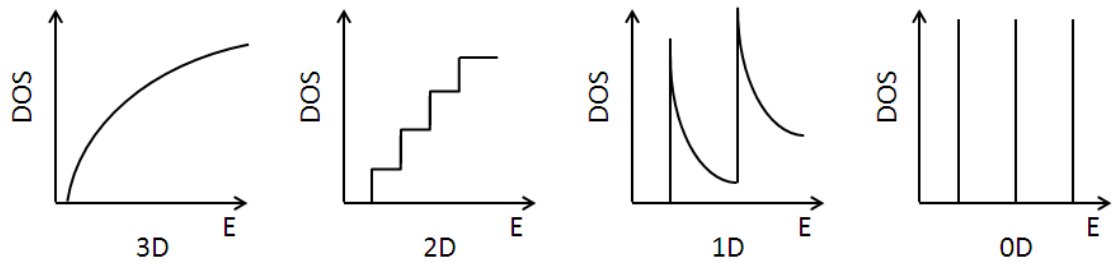

Figure 1.5: Effects of reduced dimensionality on the density of states (DOS).

A further approximation for S, that assumes parabolic bands and that electronic scattering does not depend on energy, is presented in Equation (1.10).[13]

$$S = \frac{8\pi^2 k^2}{3eh^2} m^* T \left(\frac{\pi}{3n}\right)^{2/3} \qquad \text{Equation (1.10)}$$

where h is Planck's constant, m* is the effective mass of the carrier and n is the carrier concentration.

From this it is readily seen that S is inversely proportional to n (and therefore σ, Equation (1.11)), as illustrated by Figure 1.4 in Section 1.3.

1.4.2 Electrical Conductivity, σ

As may be inferred from Figure 1.4 in Section 1.3, the electrical conductivity is directly proportional to the carrier concentration. The simplest relationship, which ignores the energy dependence of σ is set out in Equation (1.11).

$$\sigma = \frac{1}{\rho} = ne\mu \qquad \text{Equation (1.11)}$$

where ρ is the resistivity, n is the carrier concentration, e is the charge of the carrier and μ is the carrier mobility. The resistivity of a material may be related to its resistance by Equation (1.12).

$$\rho = \frac{RA}{l} \qquad \text{Equation (1.12)}$$

where R is resistance, A is the cross-section area of a sample and l is its length.

A large carrier concentration is therefore vital for high electrical conductivity but this is in direct conflict with the requirements of S. Improvements in σ must therefore centre round an improved carrier mobility (μ). The carrier mobility is given by Equation (1.13).[9]

$$\mu = e\left(\frac{\tau}{m^*}\right) \qquad \text{Equation (1.13)}$$

where e is the carrier charge, τ is the relaxation time (time between scattering events) and m* is the effective carrier mass.

Heavier carriers move more slowly, thus a smaller effective mass is preferable for high electrical conductivity. This in direct conflict with the Seebeck coefficient, which requires large m*, as defined in Equation (1.10). It is therefore only possible to improve σ, without sacrificing S, by increasing τ.

1.4.3 Thermal Conductivity, κ

The thermal conductivity of a material has two contributing factors: κ_{el} and κ_{lat}. These are the heat carried by the charge carriers and the phonons, respectively. The total thermal conductivity must be kept low, in order to maintain a large temperature gradient, which is required for efficient power generation.

The Wiedemann-Franz Law, defined in Equation (1.14), shows that the electronic contribution to the thermal conductivity (κ_{el}) is directly proportional to σ. This is evident upon inspection of Figure 1.4.

$$\kappa_{el} = L\sigma T \qquad \text{Equation (1.14)}$$

where L = 2.45 x 10^{-8} W Ω K^{-2} is the Lorentz factor for degenerate semiconductors and metals.

High σ therefore equates to high κ_{el}, which is not desirable. This means that improvement of the electrical conductivity in a material is not an effective route to improving ZT, as any benefit is cancelled out by the increase in thermal conductivity.

The lattice component, κ_{lat} is the only factor in ZT (Equation (1.8)) that is not dependent on the electronic structure. Many of the techniques employed to improve ZT focus on

reducing κ_{lat} as this is less likely to have such a significant impact on the other properties. The value of κ_{lat} in a structure is dependent on the specific heat (C_v), the mean free phonon path (l) and the velocity of sound (v_s), as defined in Equation (1.15).[16]

$$\kappa_{lat} = \frac{1}{3} C_v l v_s \qquad \text{Equation (1.15)}$$

Above the Debye temperature (θ_D), C_v becomes constant. κ_{lat} is therefore determined by the mean free phonon path (l) which, in turn, is dependent on phonon scattering in the lattice. Techniques employed to effectively scatter phonons in materials of interest are discussed in Section 1.6. This is not simple, however, as phonons with widely differing wavelengths (from 1 nm to 10 μm) are generally present in a material. Phonon scattering must therefore occur on several length-scales in order to effectively reduce κ_{lat}.[13]

1.5 Electronic Properties of Solids

There are two basic approaches to explaining the bonding in extended solids. The first is a chemical approach that is based on molecular orbital (MO) theory. This is the tight-bonding approximation and starts by assuming that the electrons are localised. In MO theory, atomic orbitals combine to create bonding (lower energy) and anti-bonding (higher energy) molecular orbital pairs, as illustrated by the schematic in Figure 1.6(a). Inclusion of more atoms creates more MOs that are closer in energy to one another. Eventually, there are so many atoms (and subsequently MOs) that a continuum of levels is generated, called a band, as shown in Figure 1.6(b). The bands have been likened to enormous MOs that extend over the whole solid. The core electrons of each atom stay localised but the valence electrons occupy the lower (valence) band while the upper (conduction) band remains empty (at 0 K). The energy gap between them defines whether a material is a metal, semiconductor or insulator. The width of the energy bands is dependent on the extent of orbital overlap between the atoms, and stronger overlap leads to wider bands.

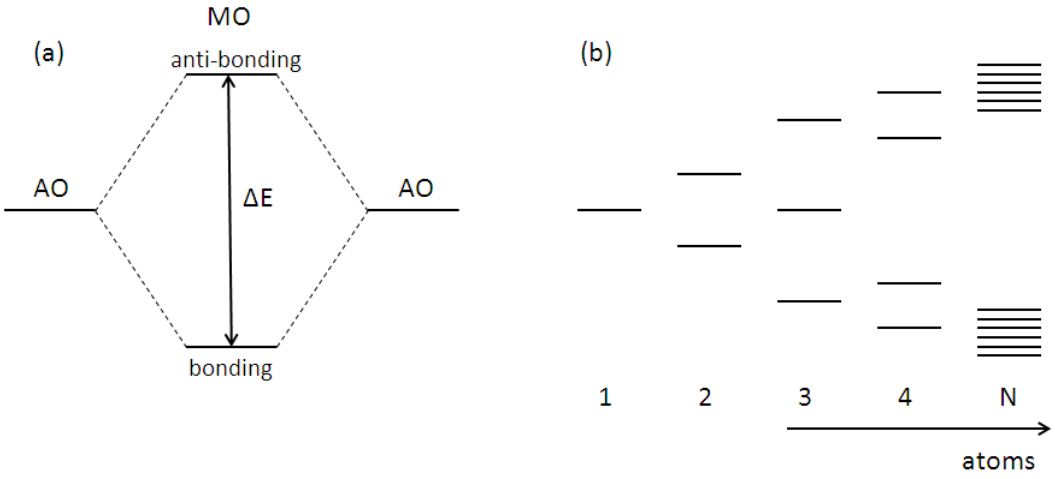

Figure 1.6: (a) Molecular orbital (MO) diagram representing the formation of bonding and anti-bonding MOs upon the combination of 2 atomic orbitals (AO). (b) Formation of energy bands as large numbers of atomic orbitals (N) are combined.

The second approach is the free electron theory which considers the valence electrons to be completely delocalised and trapped in a potential well. Within this well, the electrons are paired up in energy levels that fill from the bottom. The highest filled level defines the Fermi energy (E_f) and the work function (φ) is the energy required to excite an electron out of the potential well. This is otherwise known as the ionisation potential. The number of energy levels (called the density of states – DOS), for a given energy, using this model is represented in Figure 1.7.

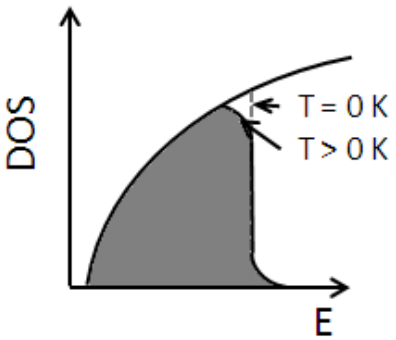

Figure 1.7: DOS for a band formed using the free-electron model. The dashed line indicates the filling of the band at 0 K. The filled region represents filled levels above 0 K, accounting for thermal excitation.

The E_f at T = 0 K is a sharp feature, as indicated by the dashed line. Above 0 K, some electrons can be excited and occupy levels above the Fermi level, as illustrated by the shaded area. In reality, the potential well is periodic, rather than continuous. In a regular array of nuclei, the potential energy of an electron is reduced when it gets close to a nucleus and increases as it moves away, as represented in Figure 1.8.

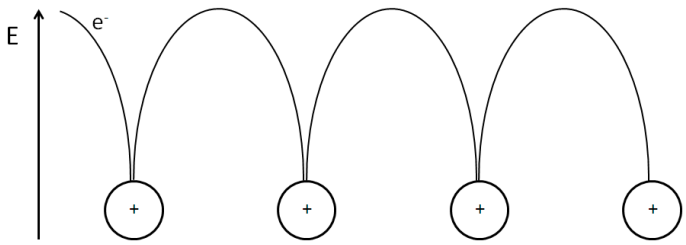

Figure 1.8: Periodic potential experienced by an electron in a regular lattice.

This results in a DOS as represented in Figure 1.9, where certain energies are forbidden. This is the origin of the band gap and the filling of the bands and size of the band gap determines whether a solid is a metal, semiconductor or insulator. The conclusions reached by the two approaches are therefore the same.

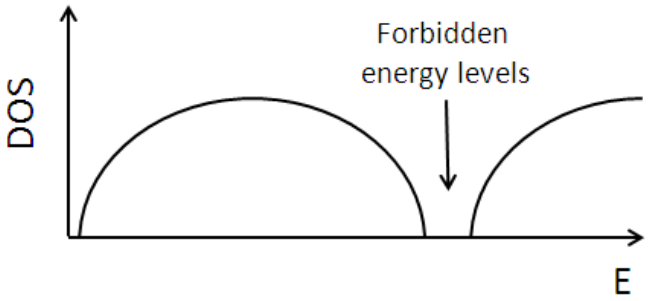

Figure 1.9: DOS as determined by the nearly-free electron model, taking into account lattice periodicity.

In a metal, the highest occupied band is not completely filled and the Fermi level sits within a band. Above T = 0 K, it is therefore easy for electrons to migrate through the band. The difference between a semiconductor and an insulator is the size of the band gap. In both cases bands are completely, rather than partially, filled. The highest-energy filled band is the valence band (VB) and the band above that is the conduction band

(CB). The Fermi level sits in the gap between these, as demonstrated in Figure 1.10(a). To allow conduction, electrons must be promoted from the VB to the CB. If the band gap is sufficiently big, this is not possible unless extremely high temperatures are reached. Such materials are insulating. Where the band gap is smaller, and only a small rise in temperature increases electrical conductivity, the material is semiconducting.[17]

Due to the band gap, the number of mobile electrons in a semiconductor is small. To increase conductivity, this must be increased and this may be achieved by either raising the temperature or doping. The relationship between the number of mobile carriers (n) and temperature (T) is presented in Equation (1.16).

$$n = n_0 exp\left(-\frac{E_g}{2kT}\right) \qquad \text{Equation (1.16)}$$

where n_0 is the total number of carriers, E_g is energy (eV) and k is the Boltzmann constant.

There is therefore an exponential rise in carrier concentration (and therefore conductivity) with temperature and these are called intrinsic semiconductors.

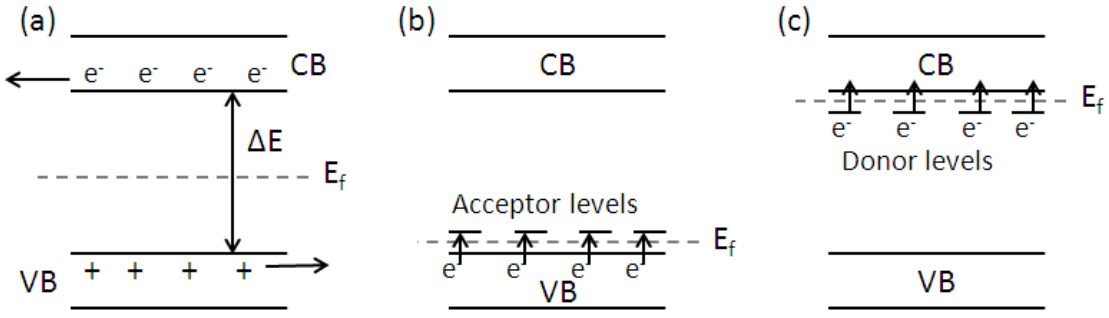

Figure 1.10: Valence (VB) and conduction bands (CB) in (a) intrinsic, (b) p-type and (c) n-type semiconductors.

Extrinsic semiconductors are created when samples are doped. The addition of carriers by a dopant overwhelms the intrinsic behaviour at low temperatures and an elevated conductivity is observed. As the temperature is increased, however, intrinsic carriers begin to dominate and behaviour is the same for intrinsic and extrinsic semiconductors at high temperatures.

Semiconductors can be either n- or p-doped. Taking Si as an example, doping with Ga will result in an electron-deficient Ga-Si bond. The energy level associated with this bond appears as a discrete level just above the VB and E_f is shifted so that it lies between the VB and the impurity levels, as illustrated in Figure 1.10(b). This is called an acceptor level as electrons from the VB can then be easily promoted to it, leaving holes in the VB. These holes are then responsible for the conduction and the semiconductor is termed p-type. Doping Si with As, on the other hand, results in discrete energy levels, containing one excess electron, just below the CB (Figure 1.10(c)). The electrons in these 'donor' levels can be easily promoted to the CB and are responsible for conduction, resulting in an n-type material. It should be noted that this description is only applicable for low levels of doping, as at higher levels, the impurity levels form impurity bands. This causes more metallic behaviour, as E_f lies between the impurity band and either the VB or the CB. A heavily doped semiconductor cannot be considered as a pure metal however, as its carrier concentration is still much lower than that of a metal.[17]

1.6 Maximising ZT

As discussed in Section 1.4, there are multiple conflicting requirements when attempting to increase ZT. This has made progress rather slow since the 1950s. ZT is dependent on two things: the band structure and scattering of phonons/charge carriers, thus the more that is understood about the crystallographic and electronic structures, the easier it becomes to identify, design and improve promising materials. Advances in structure determination (X-ray diffraction) and band structure calculations have therefore aided the search and targeted design of high efficiency materials and much progress has been made in recent years.[9]

1.6.1 Reducing κ_{lat}: The Phonon-Glass-Electron-Crystal Concept

As κ_{lat} is the only factor in the ZT formula that is not defined by the band structure, it is an obvious place to start when trying to improve a thermoelectric material. As it is dependent on the mean-free-phonon-path, reduction of κ_{lat} is achieved by scattering phonons more effectively, and this can be achieved in a number of ways. Strategies employed to reduce κ_{lat} include: the use of heavy elements; introducing point defects;

creating structures with large and complex unit cells; micro-/nano-structuring to enhance boundary scattering. Examples of each of these are available in the literature and have been proved successful in reducing κ_{lat}. However, in order to have a real impact on ZT, these effects must not have any significant negative effect on the power factor. While κ_{lat} itself does not depend on the band structure, any alterations made to a structure can have an impact on it which, in turn, may alter the electronic properties. One central idea in thermoelectrics research is therefore the phonon-glass-electron-crystal (PGEC) concept.[18] A structure that adheres to the PGEC model contains separate regions that are responsible for charge carrier and phonon transport. The part that is responsible for charge carrier transport should act like an electron-crystal and promote good electrical properties, while the phonon-glass regions hinder phonon flow as much as possible. Ideally the two regions can be manipulated independently to optimise each of the properties. Clathrates and skutterudites, for example, have large covalently bound cage-like structures that are responsible for electrical conduction. Large atoms can then be placed in the cages. These do not significantly affect the cage structure but do create disorder and point defects that hinder phonon-flow, thus κ_{lat} can be reduced without impacting the power factor.[19, 20] Where this concept has been applied, advances in ZT values by reducing κ_{lat} have been observed.

1.6.2 Increasing the Power Factor, $S^2\sigma$

High power factor ($S^2\sigma$) values allow the production of large voltages and current in thermoelectric devices. Optimisation of $S^2\sigma$ is complex due to the conflicting requirements for maximisation of S and σ, individually. As discussed, $S^2\sigma$ (and κ_{el}) is dependent on the band structure of a material thus band gap size, the shape and degeneracy of the DOS around E_f, the effective mass of the carriers, and their mobility and concentration must all be considered, as described in section 1.4.1.[9, 10, 12] Adjusting the carrier concentration through doping is extensively used as a means to optimising $S^2\sigma$ but as yet there is no general approach to increasing both S and σ in bulk materials. In order to significantly improve $S^2\sigma$, a method for simultaneously improving these properties must be found and this is vital to the future of thermoelectric materials. It is thought that improvements in κ_{lat} may allow a maximum of ZT = 2 to be achieved, but improvements beyond this will also require significantly higher $S^2\sigma$ values.[12] This

will rely mainly on large improvements in S without reduction of σ, rather than large increases in σ which would cause a similar increase in κ_{el}.

Despite the interdependence of S and σ and the lack of a real strategy to decouple these properties in bulk materials, some reports do exist, where S has been significantly increased and σ has either remained constant or even increased.[21-24] Quantum confinement has been demonstrated for thin films and individual nanowires for example, which maximise S as described in section 1.4.1 and illustrated in Figure 1.5. Such systems are not ideal for application purposes, as their manufacture on the large scale is difficult and not cost effective.[8] In bulk materials, improved properties have been attributed to doping effects in conjunction with altered micro- or nano-structures which cause changes in mobility, different scattering mechanisms and energy filtering effects. Energy filtering is an effect where only the low energy carriers are scattered. This increases S by reducing the carrier concentration but keeps σ relatively constant due to an increase in carrier mobility.[25] This process is very complex, however, and a definitive explanation of carrier filtering is still open to some debate.[26] Nonetheless, evidence therefore suggests that simultaneous enhancement of S and σ is possible and much higher power factor values are achievable with further study and understanding.

1.6.3 Current Thermoelectric Materials

The research of thermoelectric materials has been extensive and spanned several decades already. Many interesting materials have been identified and improved in these years and there are now many promising thermoelectric materials that operate in different temperature ranges, as illustrated by Figure 1.11, taken from Ref. [12]. A wide range of different heat sources, from body heat to waste incineration, can now be catered for by the current best performing materials, leading to a large number of potential applications.[6] A very brief summary of selected materials is presented, below.

Chalcogenide-based materials have been very successful in this field and keep the thermal conductivity low as they contain heavy elements. This group includes $Bi_{2-x}Sb_xTe_3$ and $Bi_2Te_{3-x}Se_x$ which set an industry standard as some of the most widely used commercial thermoelectric materials.[27] $ZT_{max} = 1$ at 300 K is generally observed for these compositions thus they are ideal for refrigeration applications. TAGS (Te–Ag–

Ga–Sb) reach ZT = 1.2 at 400 K but are significantly more expensive.[28] PbTe has been shown to reach ZT = 0.8 at 770 K, so is better for higher temperature applications.[29]

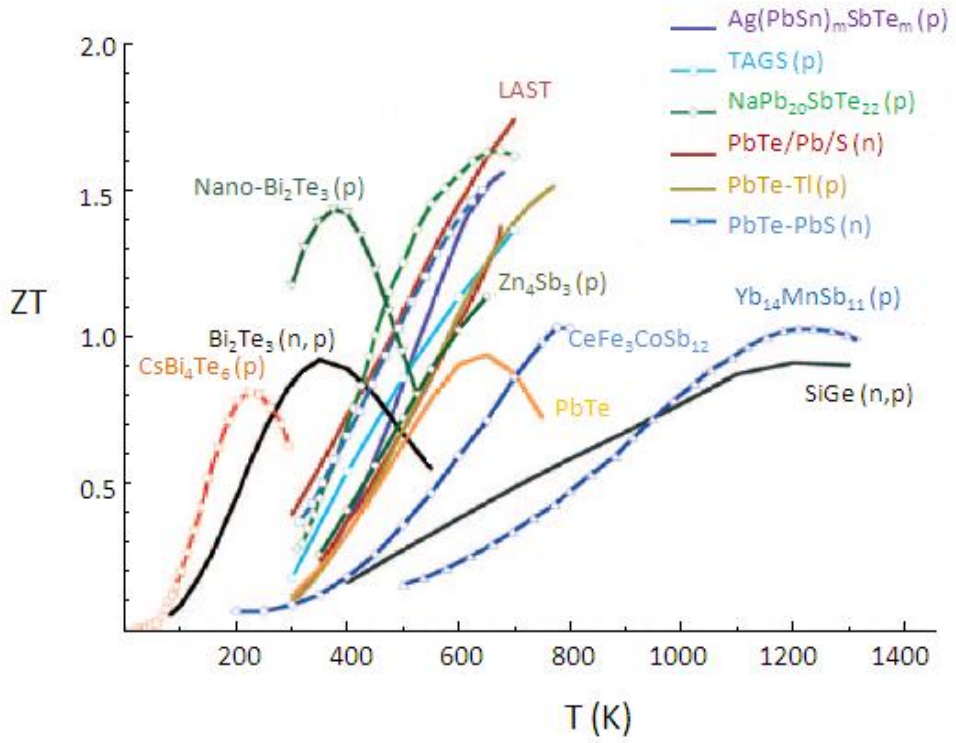

Figure 1.11: High ZT thermoelectric materials.

Clathrates and skutterudites have achieved dramatic reductions in κ_{lat} due to point defects caused by so-called 'rattling' atoms. Both have large cage-like structures in which ions can reside. These ions are then free to rattle, causing point defects and disorder that inhibit phonon flow. This effect is more pronounced for heavier 'rattling' atoms. As previously motioned, these structures adhere to the PGEC model. The electrical properties are relatively unaffected by the rattling and the cage may be separately doped to optimise carrier concentration. For example, the skutterudite cage $CoSb_3$ has κ_{lat} = 10 W m^{-1} K^{-1} at room temperature and ZT_{max} = 0.15 at 500 K but κ_{lat} = 3 W m^{-1} K^{-1} at room temperature and ZT_{max} = 1.25 at 900 K for $Ba_{0.3}Ni_{0.05}Co_{3.95}Sb_{12}$, where Ba is the 'rattling' atom and the cage has been electron doped by Ni-substitution on the Co site.[30] Even higher ZT_{max} = 1.35 at 900 K has been reported for the

clathrate structure $Ba_8Ga_{16}Ge_{30}$, where Ga and Ge make up the cage within which the Ba resides.[31]

Clathrates and skutterudites are examples of Zintl compounds, which can be described as structures where electropositive cations donate their valence electrons to polyatomic anions, which use them to form bonds and satisfy valence.[32, 33] The precise nature of the valence count results in formation of a band gap and semiconducting behaviour.[13] As described for skutterudites and clathrates, Zintl-compounds are excellent examples of the PGEC concept and this is due to the presence of both ionic and covalent bonding, which provide ideal alloying sites to reduce κ_{lat} and high mobility for the charge carriers, respectively. This makes them ideal structures for thermoelectric optimisation. Other examples of Zintl-type thermoelectrics include $Ca_{1-x}Yb_xZn_2Sb_2$ (which will be discussed further in Chapter 7),[34] Zn_4Sn_3 which reaches ZT_{max} = 1.4 at 673 K,[35] and $Yb_{11}MnSb_{14}$ which achieved ZT = 1 at 1200 K, due to an extremely low κ_{lat} = 0.7-0.9 W m^{-1} K^{-1} over the temperature range 200-1275 K.[36] The particularly low κ_{lat} value reported for this composition has been attributed to its large unit cell and complex structure that together provide a longer, more tortuous path for the phonons.[13]

As evidenced above, significant progress has been made in ZT values for bulk thermoelectric materials. However, maximum ZT values are generally in the region of 1.5, which is not sufficient for widespread applications. Much larger values have been reported for thin-film samples, for example ZT = 2.4 at 300K was reported for Bi_2Te_3/Sb_2Te_3 thin films, where the current flow was in the direction perpendicular to the layers.[37] The reduction of dimensionality to 2D has been theorised to increase the Seebeck coefficient, as described in Section 1.4.1, however, it is unclear whether this is actually achieved in this (and related) samples and the improvement has often been ascribed to low κ_{lat} values, caused by boundary scattering far in excess of what is achievable in the bulk material.[38] There are also difficulties in measuring thermoelectric properties of thin films making reproducibility difficult and, in terms of application, thin films are harder to produce on large scales than bulk materials. It is therefore preferable to further improve bulk materials, but lessons have been learned from the thin-film results and 'nano-effects' have been explored in the last few years as a route to higher ZT values. Examples of this include LAST-*m* compositions ($Ag_{1-x}Pb_mSb_{1+z}Te_{2+m}$, m = 18-22) which form as bulk materials with spontaneously-formed

nano-inclusions.[39] This allowed ZT_{max} = 2.2 at 700 K to be achieved.[40] Another example is the PbTe-PbS system in which nano-inclusions of PbS are embedded in PbTe. At an 8% level, ZT_{max} = 1.5 at 650 K was reported.[41] This is due to a marked reduction in κ_{lat}, which has been observed to half on inclusion of nano-particles.[42]

1.7 Half-Heuslers

Half-Heuslers are ternary intermetallic alloys that crystallise in the cubic AlLiSi-type structure (space group *F-43m*). They are composed of three interpenetrating face-centred-cubic lattices, each containing one of the constituent elements (X, Y and Z), and a fourth that is vacant, as illustrated in Figure 1.12. X occupies the 4a (0, 0, 0) site in the structure, while Y and Z occupy *4c* (¼, ¼, ¼) and *4b* (½, ½, ½), respectively.[43] The *4d* site (¾, ¾, ¾) is unoccupied. There are a number of different ways to describe this structure that highlight the different types of bonding present, as well as the opportunities to alter the structure for optimisation of various properties. These will be introduced and utilised where appropriate throughout this thesis.

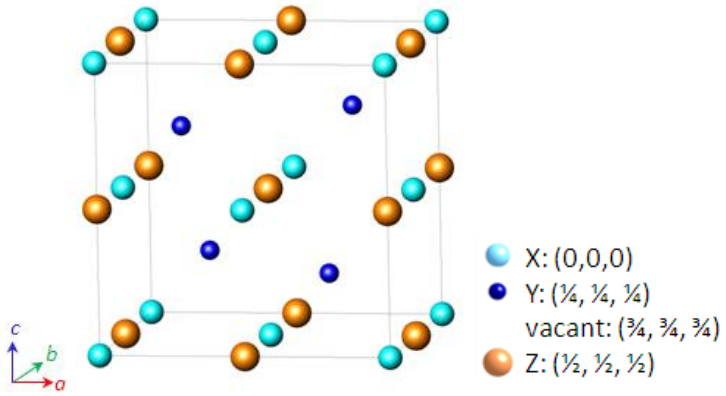

Figure 1.12: Schematic representation of the half-Heusler structure.

A large number of half-Heusler compositions exist as X, Y and Z can be chosen from a large pool of different elements. In general, X is an early transition metal or rare-earth element, Y is a late transition metal and Z is a late main group element, usually Sn or Sb. There are therefore a large number of different possible combinations, which results in structures with varying valence electron counts. The valence electron count (VEC) is the total number of valence electrons per formula unit and has a large impact on the

properties displayed by the material.[44] NiMnSb and PtMnSb, for example, which have VEC = 22, sparked the first interest in half-Heuslers when they were discovered to be half-metallic ferromagnets.[45]

The VEC can range from 16-23 in this class of compounds and, with the exception of VEC = 18, compositions are either ferromagnetic of paramagnetic metals.[46] Half-Heuslers with VEC = 18 are, by far, the most common in this diverse family of materials as these are closed shell configurations and are, therefore, the most stable. These samples are usually narrow bandgap semiconductors, which is remarkable given that they are composed entirely from metallic elements.[43, 47, 48] Giant magnetoresistance has been found in some $18e^-$ RNiSb-based half-Heuslers,[49] but the semiconducting properties have made them of great interest in the field of thermoelectrics. In particular, XNiSn and XCoSb have been widely investigated and show much promise. The following discussion of half-Heuslers therefore focuses on VEC = 18 compositions, and in particular on XNiSn compounds (X = Ti, Zr, Hf) which are the main concern of the work presented in this thesis.

1.7.1 Electronic Structure

As indicated above, the valence electron count is vital in determining the properties of half-Heuslers. An ionic model is generally employed for electron counting in these structures and is based on the electronegativity differences between the three elements. In the composition XYZ, the electronegativity values increase, going from X to Z. X is therefore the least electronegative and is considered to give up its electrons to the other elements in the structure.[50] Taking TiNiSn as an example, Ti donates its d-electrons to Ni and Sn, producing Ti^{4+} (d^0) and allowing Ni and Sn to attain closed shell arrangements of d^{10} (Ni^0) and s^2p^6 (Sn^{4-}), respectively.

While useful, this model fails to represent the true nature of the bonding in the half-Heusler structure. It is better described as a covalently bound zinc-blende lattice $(YZ)^{n-}$, that is stuffed with X^{n+} cations, as illustrated in Figure 1.13. This is still an oversimplification but highlights the presence of both ionic and covalent bonding within the structure, in line with a Zintl-type model. This is of key importance in isolating the structural features responsible for thermal and electronic conduction, as discussed in detail later. As with most intermetallic compounds, the bonding picture is not as well

defined as that outlined above suggests,[51] and covalent bonding between Ti and Ni is more significant than Figure 1.13 indicates.[46, 52]

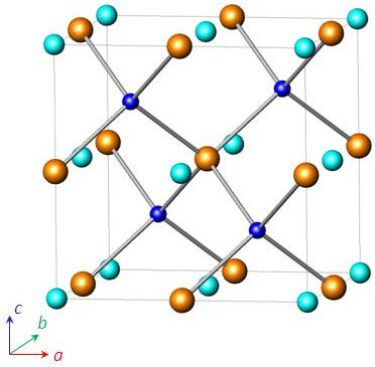

Figure 1.13: Ball and stick representation of the half-Heusler structure, highlighting the zinc-blende $(NiSn)^{4-}$ sublattice.

Several computational studies have been reported for this structure and all indicate covalent bonding to exist between Y and Z, as expected. However, the X interaction with the (YZ) lattice is not solely ionic as suggested by the Zintl model and varying degrees of d-d hybridisation between X and Y has also been indicated.[46, 52, 53] Ionic bonding is still present, primarily between X and Z, which make up a rock-salt sublattice within the half-Heusler structure.[43, 52, 54, 55]

Based on the results of the calculations, it is possible to produce a more detailed bonding picture using a molecular orbital approach.[56] Taking TiNiSn as an example, and first inspecting the $(NiSn)^{4-}$ lattice, there is significant hybridisation between the empty 4s and 4p orbitals of Ni and the full 5s and 5p orbitals of Sn,[53] as illustrated in Figure 1.14(a). The Ni d-orbitals do not appear to undergo any hybridisation in this case, but the resulting non-bonding molecular orbitals interact and hybridise with the Ti^{4+} d-orbitals to create a weak covalent bond, as the schematic in Figure 1.14(b) shows. This is the origin of the band gap in VEC = 18 compounds and the Fermi level can be found in this gap for such compositions. The valence band (VB) has predominantly Ni character while the conduction band (CB) has a strong Ti contribution.

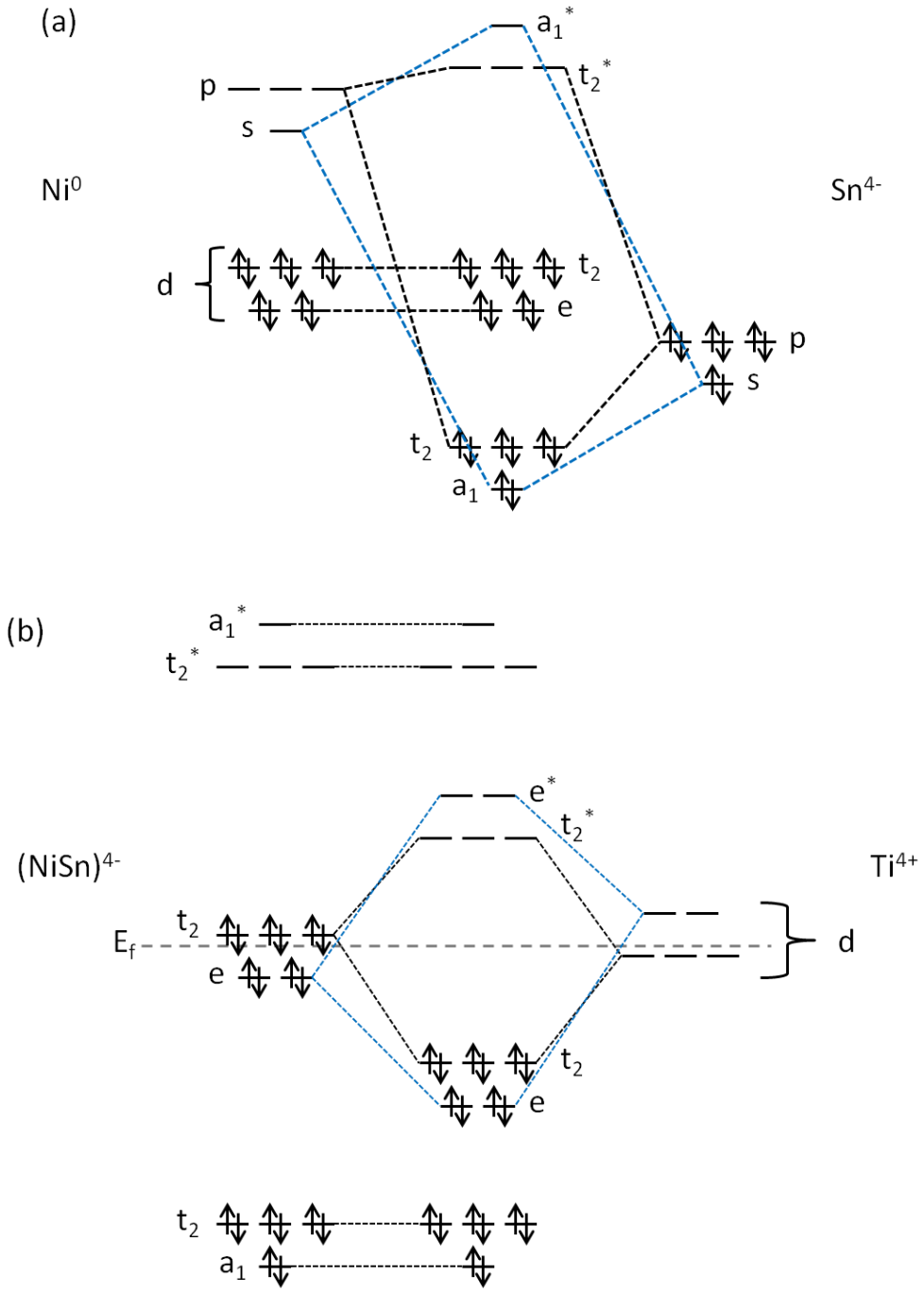

Figure 1.14: Molecular orbital diagrams for the bonding in the half-Heusler structure. (a) Depicts the bonding in the $(NiSn)^{4-}$ sub-lattice and (b) illustrates the bonding between $(NiSn)^{4-}$ and Ti^{4+}.

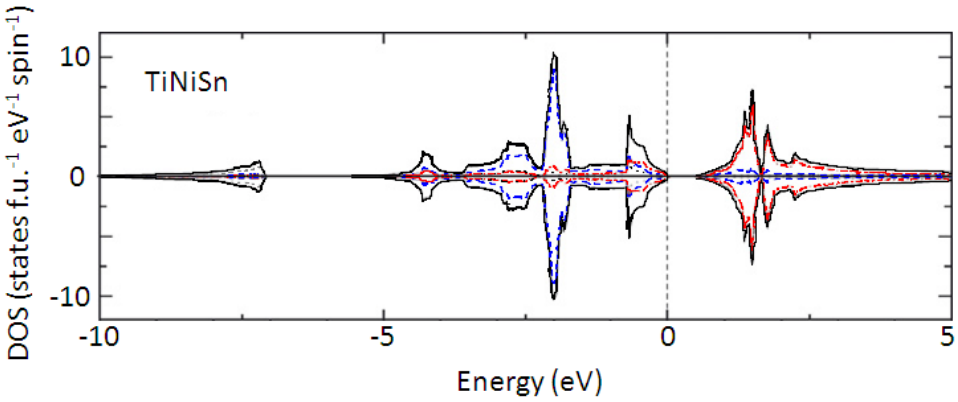

Figure 1.15: Density of states for TiNiSn. The red line indicates Ti, the blue line represents Ni and the grey line corresponds to Sn orbital contributions.

Density-of-states (DOS) calculations show that the band gap is indirect and confirm the existence of hybridisation between Ti and Ni, as well as the nature of the valence and conduction bands.[53] This has also been shown to be the case for other VEC = 18 half-Heulsers.[57] Data, reproduced from Ref. [53], is presented in Figure 1.15 and clearly shows both Ti and Ni contributions in the bands surrounding the Fermi level. The major contribution of X (Ti) to the conduction band, above the Fermi level, confirms the assumption that Ti gives up its valence electrons to the NiSn (YZ) lattice.[52] The size of the band gap depends on the electronegativity difference between X and Y in the generic composition XYZ. TiNiSn, for example has a band gap of 0.42 eV, compared with 0.95 eV for TiCoSb,[46] as Ti and Co are closer in energy and overlap more effectively. This produces a stronger bond and lowers the energy of the bonding orbital.[53] The band gap may also be affected by disorder in the structure. The bonding picture presented in Figure 1.14 helps explain why compositions with VEC $\neq$ 18 are metallic, as removal of an electron (VEC = 17, e.g. TiCoSn) leaves holes in the valence band, while addition of an electron (VEC = 19, e. g. TiCoSb) results in population of the conduction band. Half-Heuslers with VEC = 18 therefore represent a uniquely stabilised composition.

1.7.2 Half-Heuslers vs. Full-Heuslers

The full-Heusler structure has the general composition XY_2Z, where X, Y and Z are as defined for the half-Heusler compositions. Where the half-Heusler may be described as

a face-centred cubic lattice of Z, where all octahedral holes are filled by X and half the tetrahedral holes are occupied by Y, the full-Heusler structure contains Y in all its tetrahedral holes, as illustrated in Figure 1.16. The symmetry is therefore increased with respect to the half-Heusler, and the full-Heusler crystallises in the *Fm-3m* space group. Where VEC = 24 (e.g. VFe_2Al) full-Heuslers are semi-conducting but have much smaller band gaps than those found in the half-Heuslers, with VEC = 18.[56] Of interest in this thesis however, is $TiNi_2Sn$, which has VEC = 27 and is metallic. Half-Heuslers (TiNiSn) have much poorer Ni-Ni orbital overlap, compared to their 'equivalent' full-Heuslers ($TiNi_2Sn$), due to the longer Ni-Ni distances in the structure. This is a result of the vacant sites in the half-Heusler structure and produces narrow bands and gaps in the density-of-states, resulting in the semiconducting behaviour observed for such compositions.[44, 58]

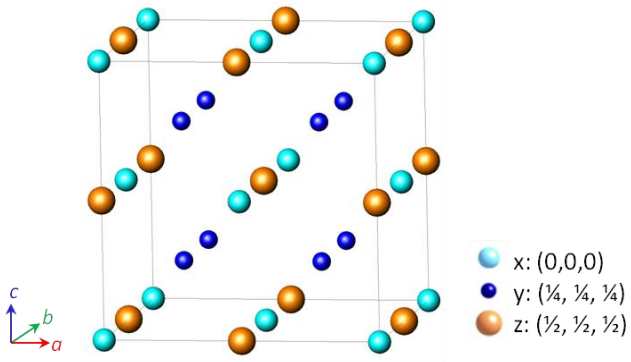

Figure 1.16: Schematic representation of the full-Heusler structure.

1.7.3 Half-Heuslers with Thermoelectric Applications

The narrow bands, heavy charge carriers[59] and small band gaps offered by half-Heuslers make them of great interest in the field of thermoelectrics. These properties lead to naturally high Seebeck coefficients and low resistivity values.[47] Both n- and p-type materials are found within this structure-type and the elements used in the most promising compositions are relatively cheap and abundant, making them very appealing in the renewable energy field. A number of half-Heusler compositions have been investigated or could have some potential in the field of thermoelectrics.[60] However, the most promising half-Heusler thermoelectric materials are p-type XCoSb-based and n-type XNiSn-based compositions, where X = Ti, Zr or Hf. TiCoSb has a much larger

band gap than XNiSn-compositions (0.95 eV, compared with 0.4-0.6 eV),[46] while ZrCoSb and HfCoSb are reported to be semimetallic,[61] but promising efficiencies have been obtained where the structure has been optimised.[62, 63] $Ti_{0.5}Zr_{0.25}Hf_{0.25}Co_{0.95}Ni_{0.05}Sb$, for example, was reported to have ZT = 0.51 at 813 K.[64] However, these compositions are not the focus of the work in this thesis, and will not be discussed further. In terms of electronic properties, XNiSn-based compounds show impressive power factor values but resulting ZT values are not as high as might be hoped, due to high κ_{lat} values. Selected κ and ZT values from the literature are summarised in Table 1.1 for these promising materials. Reduction of these high κ-values has therefore been the focus of a large part of the research into these compositions and several strategies have been employed.

Table 1.1: Selected thermal conductivity (κ) values and ZT for TiNiSn, ZrNiSn and HfNiSn, from the available literature.

	κ (W m^{-1} K^{-1})	ZT	Ref.
TiNiSn	8-10	0.29 at 700 K 0.4 at 650 K	[59] [65]
ZrNiSn	10-20	0.2 at 1000 K 0.5 at 850 K	[59] [66]
HfNiSn	10-20	0.22 at 700 K	[65]

1.7.3.1 Aliovalent Substitution in XNiSn

The effect of aliovalent substitutions on each of the three occupied sites in the structure has been investigated. Such substitutions alter the VEC and can therefore be used to either electron- or hole-dope the system and optimise the electronic properties. As described in Section 1.7.1, the structure, to a first approximation, may be considered as a covalent $(NiSn)^{4-}$ lattice, that is stuffed with X^{4+} cations. The $(NiSn)^{4-}$ sublattice is generally considered to be responsible for the electronic conduction through the sample. Aliovalent substitution on this lattice has been found to be a particularly effective route to optimising the carrier concentration.

Sb-doping on the Sn-site has an electron-doping effect, as Sb contains one more p-electron than Sn. This results in large reductions in the electrical resistivity (ρ), with samples often becoming metallic. For example, ρ_{RT} = 8 mΩ cm for TiNiSn is reduced to

0.1 mΩ cm for $TiNiSn_{0.9}Sb_{0.1}$. This is, of course, offset by a simultaneous reduction in S. $TiNiSn_{0.9}Sb_{0.1}$, for example, produces S = -50 μV K^{-1} at 300 K, compared with S = -250 μV K^{-1} for TiNiSn.[67] Improvements in the power factor are still observed however, for low levels of doping and S^2/ρ = 1 mW m^{-1} K^{-2} at room temperature was reported for $TiNiSn_{0.95}Sb_{0.05}$. This is double the value reported for TiNiSn and rises to 4.5 mW m^{-1} K^{-2} at 650 K, with higher values possible at even higher temperatures.[67]

Aliovalent substitutions have also been investigated for the Ni-site. Co-doping caused an increase in ρ and reduction in S, and at the 4% level causes a transition to p-type behaviour. $ZrNi_{0.98}Co_{0.02}Sn$ has been reported to produce S^2/ρ = 0.8 mW m^{-1} K^{-2}, compared with 3 mW m^{-1} K^{-2} for ZrNiSn at 875 K, resulting in a reduction in ZT_{max} from 0.5 to 0.14 at 875 K.[68] Cr and Mn substitutions cause a general reduction in ρ and eventual onset of metallic-type behaviour at high substitution levels, and this is accompanied by a large reduction in S. N-type behaviour is, however, maintained. Cu substitution causes the immediate onset of metallic behaviour, lowering of ρ and decrease in S.[69]

Despite the NiSn lattice being mainly responsible for the electronic conduction in the half-Heusler structure, the electronic properties can still be altered by aliovalent doping on the X site. It may even be advantageous as the NiSn lattice is not disturbed. Several possibilities have been investigated. For example, Y-doping in ZrNiSn has been found to widen the band gap and cause the onset of p-type behaviour.[70, 71] Nb-doping of TiNiSn and ZrNiSn causes the onset of metallic type behaviour at low doping levels, similar to Sb-doping, and improvements in S^2/ρ were observed. However, thermal conductivity values also increased due to enhanced κ_{el} and ZT gains were limited.[72] Ta- and V-doping have also been explored and have similar effects as those described for Nb-doping, in that metallic behaviour emerged immediately.[73-75] While these substitutions may offer similar improvements in power factor values as Sb-doping, Sb-doping is by far the most commonly used method of optimising carrier concentration, as it leaves the X-site free for other substitutions to reduce thermal conductivity, as discussed below.

1.7.3.2 Isovalent Substitution in XNiSn

The largest barrier to the attainment of high ZT values in XNiSn-based thermoelectrics is the naturally high thermal conductivity exhibited by each of these samples. The most intensively investigated route to lowering the thermal conductivity has been through isovalent substitution on the X-site. By mixing Ti, Zr and/or Hf on the X site, strain and mass fluctuation effects are expected as mass, size and bonding differences occur between the three group 4 elements.[76] These effects result in point defects that scatter the phonons in the lattice and thus reduce κ_{lat} which is the main contributor to the thermal conductivity in these compounds. As the X-site is largely not responsible for the conduction of charge carriers through the lattice, alloying on this site should not negatively impact the electronic properties, thus the Zintl-type structure of the half-Heuslers offers a genuine opportunity to significantly improve ZT values. Early investigations into alloying on the X-site usually involved mixing Zr and Hf. These elements are close in size but have a large mass difference, and so mass fluctuation effects were expected to significantly reduce κ. This approach was proved successful with Culp *et al* reporting ZT = 0.81 at 1025 K for $Zr_{02.5}Hf_{0.75}NiSn_{0.975}Sb_{0.025}$, where κ = 5.75 W m^{-1} K^{-1}.[77] In general, large reductions in κ are achieved through this type of alloying. For example, Shen *et al* reported a drop from 11.5 W m^{-1} K^{-1} at room temperature for ZrNiSn to 7 W m^{-1} K^{-1} for $Zr_{0.5}Hf_{0.5}NiSn$,[78] and Uher et al reported κ_{RT} = 17.2 W m^{-1} K^{-1} for ZrNiSn and κ_{RT} = 5.3 W m^{-1} K^{-1} for $Zr_{0.5}Hf_{0.5}NiSn$.[66]

Introduction of Ti to the X-site adds an extra source of fluctuation as it is much smaller than both Zr and Hf. It is also cheaper and more readily available, than Hf in particular, thus inclusion of this element is of great advantage in possible wider-spread applications. Use of Ti led to a report of ZT = 1.5 at 700 K for $Ti_{0.5}(Zr_{0.5}Hf_{0.5})_{0.5}NiSn_{0.998}Sb_{0.002}$, the highest reported value for the half-Heusler compounds to date.[79] This has not since been reproduced but demonstrates the significant potential of these compositions in the field of thermoelectrics. Use of Ti on the X-site does, however, tend to result in an improvement of the thermoelectric properties of XNiSn-based compositions. TiNiSn generally has the lowest thermal conductivity of the three parent compositions (Table 1.1). Mixing with Zr or Hf drives this lower still. For example, Kim *et al* reported $Ti_{0.8}Hf_{0.2}NiSn$ to reduce κ from 7 W m^{-1} K^{-1} (TiNiSn) to 4 W m^{-1} K^{-1}, at room temperature, with little change to the power factor;[80] Muta *et al*

reported κ_{RT} = 6 W m^{-1} K^{-1} for $Zr_{0.7}Ti_{0.3}NiSn$, compared with κ_{RT} = 13 W m^{-1} K^{-1} for ZrNiSn;[81] and Katayama *et al* reported even more impressive reductions with κ_{RT} = 3 W m^{-1} K^{-1} for $Ti_{0.6}Hf_{0.4}NiSn$ and κ_{RT} = 5 W m^{-1} K^{-1} for $Ti_{0.9}Zr_{0.1}NiSn$.[82]

1.7.3.3 Interstitial Site in XNiSn

In recent years, focus has turned to the pseudo-binary system XNiSn-XNi_2Sn, where the vacant site in the half-Heusler structure is exploited and additional Ni is added to the unit cell.[83] This technique offers an apparently simple route to improvement of ZT as no additional elements are required, as is the case for doping or alloying. Instead, only a small amount of additional Ni is required making it an inexpensive alteration. The crystal structure is not significantly altered as the vacant tetrahedral site is exploited. The half-Heusler structure is presented in Figure 1.17 with these interstitial sites highlighted in red.

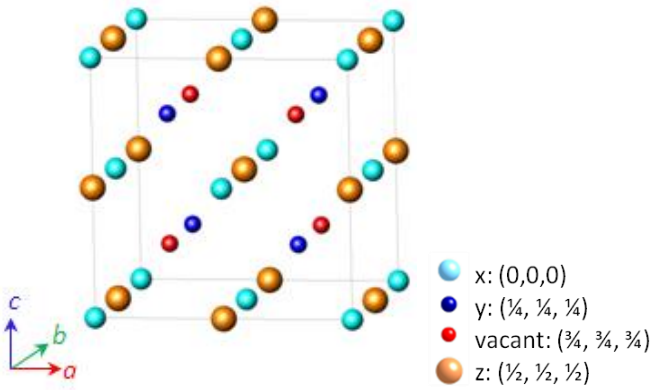

Figure 1.17: Schematic representation of the half-Heusler structure with the interstitial tetrahedral sites highlighted in red.

The open nature of the half-Heusler structure makes it possible to accommodate atoms on this site and indeed this is fully-occupied in the full-Heusler structure. Several groups have now reported on the effects of adding excess Ni to XNiSn structures and conflicting results on the thermoelectric properties and structure have been observed. The first question that arises is how the excess Ni is incorporated into the structure. To date, three options have been reported and each of these will be addressed separately, below.

1.7.3.3.1 Full-Heusler Micro-Inclusions

An early TEM investigation into $TiNi_{1.5}Sn$ reported that its grains contained full-Heusler inclusions on the micron-scale within a half-Heusler matrix. Within the full-Heusler domains there was also evidence for smaller half-Heusler regions.[84] A similar observation has since been made in $TiNi_{1+y}Sn$ samples with lower values of y. The authors of this paper cite small 1 μm half-Heusler regions within 20 μm full-Heusler regions thus deduced that phase segregation on multiple different length scales may be produced in samples containing excess Ni.[85] Images from this paper are replicated in Figure 1.18. These full-Heusler domains have been observed to increase in size as the level of excess Ni is increased and eventually begin to interconnect.[86] Other studies do not report half-Heusler domains in the full-Heusler micro-inclusions but do still observe micron sized full-Heusler domains.[87] The result of the formation of full-Heusler micro-inclusions is an irregular microstructure and possible phase segregation on multiple length-scales, which has been shown to be beneficial to the thermoelectric properties.[88] Such features are very effective at phonon scattering thus a reduction in the thermal conductivity is expected. This has been proven to be the case with reports of κ_{RT} = 8 W m^{-1} K^{-1} for TiNiSn being reduced to κ_{RT} = 5.5 W m^{-1} K^{-1} in $TiNi_{1.15}Sn$.[85] This reduction is not as large at high temperatures due to an increase in κ_{el}. In a separate report, κ_{RT} = 5.2 W m^{-1} K^{-1} for TiNiSn was reduced to κ_{RT} = 3.9 W m^{-1} K^{-1} in $TiNi_{1.06}Sn$.[87] This was maintained to higher temperatures.

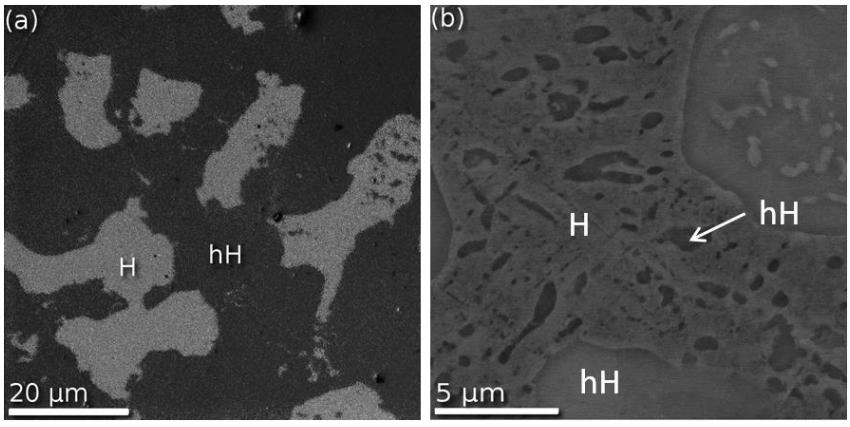

Figure 1.18: (a) Micro-inclusions of a full-Heusler phase (H) within a half-Heusler matrix (hH). (b) half-Heusler inclusions within the full-Heusler inclusion.[85]

There is some discrepancy over the effect of micro-inclusions of full-Heusler on the electronic properties. One report suggests an increase in S and decrease in σ which the authors attribute to a reduction in carrier concentration.[87] Other reports indicate a decrease in S and increase in σ at room temperature. DFT calculations show the Fermi level of the full-Heusler micro-inclusion to lie in the centre of the half-Heusler band gap, as illustrated in Figure 1.19. Carriers in the half-Heusler phase are therefore likely to be excited to the empty bands of the full-Heusler at low temperature, rather than the CB of the half-Heusler, as they are lower in energy. This is consistent with extrapolations to 0 K that predict σ of full-Heusler containing samples to be lower than those without inclusions. At higher temperatures, carriers at the full-Heusler Fermi level are more easily excited to the CB of the half-Heusler resulting in the observed increase in conductivity with increasing amounts of full-Heusler. There is also an observed increase in the temperature at which the maximum S value is achieved. This indicates band-filling effects, whereby holes in the VB are filled by electrons from the Fermi level of the full-Heusler phase.

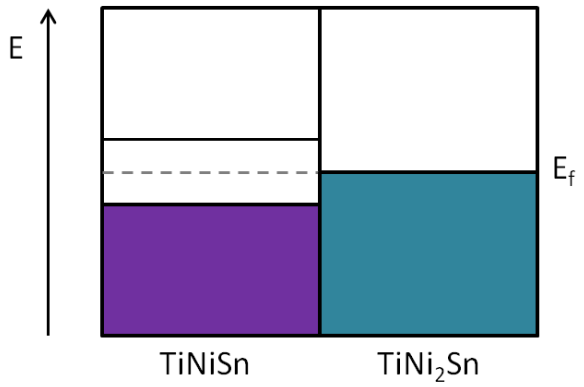

Figure 1.19: Fermi levels of TiNiSn and $TiNi_2Sn$ at the boundary between the half-Heusler bulk and full-Heusler micro-inclusion.[85]

1.7.3.3.2 Full-Heusler Nano-Inclusions

A significant number of reports have been published that observe the formation of full-Heusler nano-inclusions in the half-Heusler matrix, as illustrated in Figure 1.20.[8, 89-95] The effect that nano-inclusions have on thermoelectric materials has previously been explored in PbTe-based systems. For example, in $(PbTe)_x(AgSbTe_2)_{1-x}$ that achieved ZT = 2.2, the outstanding performance has been attributed to nanoscale

clustering of Sb and Ag.[39, 40] A significant improvement in S for PbTe has also been attributed to the formation of Pb nano-inclusions.[96] The effect of full-Heusler nano-inclusions on the thermoelectric properties of half-Heuslers is not yet clear, with various different properties reported.

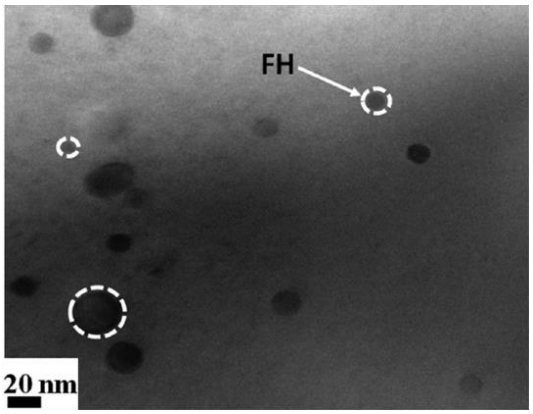

Figure 1.20: Nano-inclusions of a full-Heusler phase (FH) embedded in a half-Heusler sample.[90]

Some groups report that the inclusions act as scattering centres that help reduce the thermal conductivity.[93] Liu *et al*, for example, report a drop in κ_{RT} from 13 to 9 W m^{-1} K^{-1} for $Ti_{0.9}Zr_{0.1}NiSn$, upon addition of excess Ni,[95] while Makongo *et al* attribute a 40% reduction in κ_{lat} for $Zr_{0.25}Hf_{0.75}NiSn$ with 2% full-Heusler inclusions to the coherent phase boundaries, grain boundaries and point defects created by their formation.[90] These features scatter mid-frequency, mid-long-frequency and short-frequency phonons, respectively, thus nano-inclusions can be a very efficient way of reducing κ. However, others do not report any improvement in κ,[92] and some even see increases in κ at high levels of excess.[89] The increase has been attributed to the large size of the nano-inclusions in this particular sample (5-20 nm), and the authors argue that their metallic nature causes a doping effect that increases σ and κ_{el}. Indeed a reduction in S and increase in σ are observed, consistent with this theory. The impact that full-Heusler nano-inclusions have on the thermal conductivity is therefore not straightforward and depends strongly on their physical properties (size and shape). These can be difficult to control and depend heavily on synthesis methods.

Perhaps of greater interest is the effect that nano-inclusions have on the electronic properties of the half-Heuslers. While these are generally very good compared with some other thermoelectric materials, further improvement is required if ZT values in excess of 2-3 are to be achieved. In particular, Seebeck coefficients must be improved as these are not linked to the thermal conductivity. Improvements in the electrical conductivity are easily achievable through doping but result in increased κ_{el}, which cancels out any gain. Enhancement of S, without significant reduction of σ, is therefore the best route to genuinely improved ZT values. This is not facile due to the opposing dependencies on carrier concentration, but full-Heusler nano-inclusions may hold the key to achieving these improvements. Large enhancements in S have been reported by several groups, in conjunction with only minor decreases in σ. For example, S_{RT} increases from 100 to 240 $\mu V\ K^{-1}$ in p-type $Ti_{0.5}Hf_{0.5}CoSb_{0.9}Sn_{0.1}$ upon addition of excess Co, while σ_{RT} decreases from 120 S cm^{-1} to 65 S cm^{-1} and from 135 S cm^{-1} to 115 S cm^{-1} at 750 K.[92] This has resulted in large power factor values being achieved, for example $S^2/\rho =$ 3.5 mW $m^{-1}\ K^{-2}$ at 700 K in $TiNi_{1+x}Sn$,[94] 2 mW $m^{-1}\ K^{-2}$ at 750 K in $Ti_{0.1}Zr_{0.9}Ni_{1+x}Sn$,[95] and 3.4 mW $m^{-1}\ K^{-2}$ at 750 K for 6% full-Heusler in $Zr_{0.25}Hf_{0.75}NiSn_{0.975}Bi_{0.025}$ (compared with 1.5 mW $m^{-1}\ K^{-2}$ for the same composition without nano-inclusions).[90]

The various reports that observe this behaviour all point to calculations made by Faleev *et al* that describe the enhancement in S in terms of an energy filtering effect.[25] They suggest that the nano-inclusions cause a band bending effect at the interfaces between the half-Heusler matrix and full-Heusler inclusions which creates an energy barrier. This then allows only the highest energy charge carriers to cross the boundary to the nano-inclusion, and scatters the lower energy carriers, as illustrated in Figure 1.21. This means that the carrier concentration is reduced which is favourable for S. In theory, the electrical conductivity should drop as it is directly proportional to the carrier concentration, but the energy filtering appears to increase carrier mobility, as there are fewer carrier-carrier collisions which results in an increase in relaxation time. Relaxation time, τ and mobility, μ are directly proportional to one another as shown in Equation (1.13).

The energy filtering model is supported by the fact that, even just above room temperature, the carrier concentrations of $Zr_{0.25}Hf_{0.75}Ni_{1+x}Sn$ and $Ti_{0.5}Hf_{0.5}Co_{1+x}Sb$-

$_{0.9}Sn_{0.1}$ were observed to increase.[90, 92] This implies that carriers are being thermally excited across the barrier. Interestingly, S is not observed to decrease as the carrier concentration begins to increase suggesting that the effective mass (m*) of the carriers is increased by the nano-inclusions. m* was indeed found to change in $Ti_{0.5}$-$Hf_{0.5}Co_{1+x}Sb_{0.9}Sn_{0.1}$ samples but not systematically with x. This suggests that a change in band structure may occur upon formation of nano-inclusions.

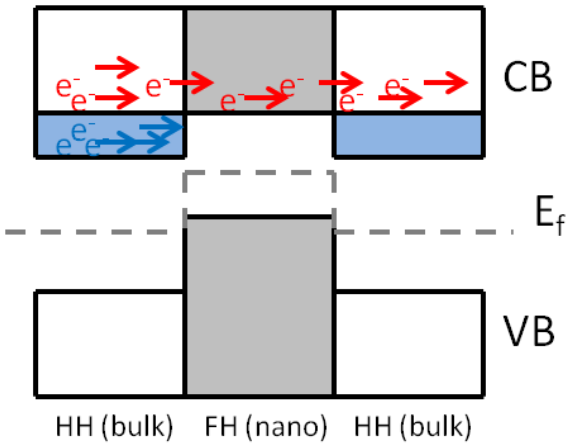

Figure 1.21: Energy filtering of charge carriers by full-Heusler nano-inclusions in the half-Heusler bulk.[90]

The size of the energy barrier is related to the size of the nano-inclusion. The bulk full-Heusler is metallic and its Fermi level sits in the centre of the half-Heusler band gap. However, nano-inclusions of full-Heusler are thought to be narrow-band semiconductors due to quantum confinement effects. As the inclusion is made smaller, the size of the band gap increases, until eventually its valence band is pushed below that of the half-Heusler bulk. The energy filtering effect is therefore highly dependent on the size of the nano-inclusion and, in turn on the synthesis method used to prepare the sample.

It must be noted that the energy filtering model has not been proven thus far and an alternative model has recently been proposed in which charge carriers are selectively filtered.[97, 98] This would account for the increase in S as holes and electrons cease to cancel each other out.

1.7.3.3.3 Random Distribution of Excess Ni on the Interstitial Sites

Solubility of excess Ni into the half-Heusler structure is not predicted on inspection of the phase diagram.[99, 100] At first glance, this is surprising, given the very similar nature of the two structures, but is understandable from the viewpoint of bonding. The bonding in the half-Heusler phase is predominantly covalent in character, while the full-Heusler phase is much more metallic. Computational investigations have shown that placing additional transition metal in the half-Heusler phase, on the vacant site, delocalises the Sn s- and p-orbitals, thus weakens the covalent bonding to Ni, destabilising the structure.[101, 102] Do *et al* have also recently published a computational study of $ZrNi_{1+x}Sn$, in which they investigated the likely distribution of excess Ni in the structure and concluded that consecutively added excess Ni atoms prefer to be close to one another. This supports the formation of nano-inclusions within the half-Heusler bulk.[97]

Despite this, the presence of Ni on the interstitial site has been indicated in several studies. Muta *et al* detected excess Ni in a $ZrNi_{1.05}Sn$ sample but did not observe any indication of full-Heusler in either the electron microscopy images or XRD pattern, suggesting incorporation of the excess Ni into the half-Heusler structure.[103] Hazama *et al* also prepared off-stoichiometric TiNiSn samples and used energy calculations to show that the lowest energy model that could account for the off-stoichiometry involved random distribution of the excess Ni atoms on the vacant sites throughout the lattice.[104, 105] Calculations by Larson *et al* support this somewhat, as they deduced that placing Ni on the interstitial site was the least energetically costly form of disorder (compared with inversion effects etc.).[106] Douglas *et al* have recently reported an increase in lattice parameter of their half-Heusler phases, despite formation of a segregated full-Heusler phase, indicating some solubility of Ni in TiNiSn.[85, 86]

The effect of genuine Ni interstitials on the band structure is the introduction of filled in-gap states. It is worth noting that Miyamoto *et* al reported the presence of in-gap states in nominal TiNiSn which they assigned to Ni occupying the interstitial site. This indicates that some disordering of Ni onto this site naturally occurs anyway and that excess Ni on this site may not be as unlikely as some theoretical investigations suggest.[107] The filled in-gap states are likely to act as charge reservoir and fill any holes in the valence band of the half-Heusler and allow easier promotion of electrons to

the conduction band. This should therefore result in increased electrical conductivity, possibly without too much impact on the Seebeck coefficient, as the increased carrier concentration may be offset by the eradication of holes. Thermal conductivity values for the samples which are considered to contain genuine Ni interstitials have been observed to decrease, for example $\kappa = 2.93$ W m^{-1} K^{-1} was reported for a $TiNi_{1+y}Sn$ sample,[105] suggesting that the randomly distributed Ni atoms could act as point scattering centres.

Compared with the formation of inclusions, the random distribution of Ni in the half-Heusler structure is essentially unexplored, as this behaviour has seldom been seen. Even in the few reports where the authors suggest interstitial Ni does exist, very little further investigation has been undertaken. The effect of interstitial Ni on the thermoelectric properties is therefore unknown.

1.7.3.4 Effect of Synthesis on the Thermoelectric Properties

A brief overview of the available literature for XNiSn reveals many inconsistencies in the reported properties for nominally identical compositions. Even the properties of the parent compounds are not uniform, with reported room temperature thermal conductivity values spanning the range 11-17 W m^{-1} K^{-1} for ZrNiSn, for example. ZT = 1.5 has also not yet been reproduced. This indicates that nominally identical samples are not, in fact, the same and synthesis plays a large role in the overall and local structure that is produced.

Also of utmost importance is the purity of the sample. Katayama *et al* used arc melting, followed by annealing to prepare TiNiSn and showed that after the annealing step, significant Ti_6Sn_5, Sn and $TiNi_2Sn$ impurities were contained in the sample. This was found to result in metallic behaviour. The sample was then annealed at 800 °C for two weeks which significantly reduced, but did not eradicate, the impurities. The more familiar semiconducting behaviour then emerged, with $S_{RT} = -318$ μV K^{-1} and $\rho_{RT} = 12$ mΩ cm.[82] Impurity phases can therefore have a significant impact on the properties and care must be taken to achieve high purity samples, in order to determine their intrinsic properties.[108]

The effect of anneal time was investigated by Uher *et al* who prepared samples by arc-melting, followed by either two day or one week annealing at 800 °C in ZrNiSn, HfNiSn and $Zr_{0.5}Hf_{0.5}NiSn$. Through low temperature thermal conductivity

measurements they found that κ for ZrNiSn and HfNiSn increases with annealing time, while it decreases for $Zr_{0.5}Hf_{0.5}NiSn$. This indicates increased order for each of the samples. In the case of ZrNiSn and HfNiSn, a more ordered structure decreases the number of point defects, resulting in increased κ, while in $Zr_{0.5}Hf_{0.5}NiSn$, annealing promotes a truly random distribution of Zr and Hf, increasing the point defects and reducing κ.[66] The fact that a simple change in annealing time can have such an effect on the ordering of a sample makes it imperative that as much is known about the structure of the particular sample under investigation as possible. It is only possible to determine the true impact of doping a sample, if these details are known. Muta *et al* investigated the effect of spark-plasma-sintering (SPS) on $Zr_{0.7}Ti_{0.3}NiSn$ samples which were arc-melted then annealed at 800 °C, before being ground and subjected to SPS at 1100 °C or 1200 °C. They noted a narrowing of the diffraction peaks upon SPS, particularly at 1200 °C, and a reduction in impurity peaks is also evident. They linked the narrowing of the peaks to increased homogeneity in the samples and found this to coincide with an increase in the power factor.[81] This could be a result of the increased homogeneity, however density effects and differing impurity levels could also have an effect in this case as this data is not provided. Kurosaki *et al* also investigated the effect of different SPS temperatures in nominal $(Zr_{0.6}Hf_{0.4})_{0.7}Ti_{0.3}NiSn$ and reported broad peaks after arc-melting and for the SPS samples, prepared at 700, 900 and 1100 °C. The broad peaks were attributed to the presence of two different half-Heusler phases with differing Ti:Zr:Hf ratios. The SPS samples achieved 70, 90 and 95% density, respectively, and the peak shape in each case was markedly different. This was attributed to variation in the ratio of phases present. Analysis of the electronic properties revealed the 90%, 95% and the 99% arc-melted sample to have almost identical electronic properties, while the 70% sample exhibit values over three times higher. The thermal conductivity of the 70% sample is also half that of the others. This indicates that the density of the samples was the dominant effect on the properties of these samples.[109]

Grain size has also been found to have a large impact on the thermoelectric properties with the some of the lowest κ values found for samples with small grain sizes. Zou *et al*, for example, reported $\kappa = 3.14$ W m^{-1} K^{-1} at 300 K for TiNiSn prepared by mechanical alloying and SPS. The resultant grains in these samples were 200-400 nm in diameter and allowed a high ZT = 0.32 at 785 K for TiNiSn.[110] Bhattacharya *et al* have also

investigated this effect and reported a systematic drop in κ_{lat} as the diameter of the average grain was reduced in $TiNiSn_{1-x}Sb_x$ samples.[111, 112] Joshi *et al* reported ZT = 1 at 600-700 °C for $Zr_{0.75}Hf_{0.25}NiSn_{0.99}Sn_{0.01}$ with grain sizes on the order of 200-300 nm. This is a 25% improvement on the previously reported highest ZT value for similar compositions and is a result of the much reduced thermal conductivity (κ_{RT} drops from 6.5 to 4.5 W m^{-1} K^{-1}).[113] The same group also reported ZT = 1 at 500 °C for $Hf_{0.5}Zr_{0.25}Ti_{0.25}NiSn_{0.99}Sb_{0.01}$ which were prepared in the same manner (ball-milling and hot-pressing of an arc-melted ingot) and had a typical grain size of 200-300 nm. The thermal conductivity in this sample was found to be 3-3.5 W m^{-1} K^{-1} in the temperature range 300-500 °C.[114] This effect has also been observed in p-type materials. For example a $Hf_{0.8}Ti_{0.2}CoSb_{0.8}Sn_{0.2}$ sample, with grain size 50-300 nm was prepared by ball-milling and hot pressing of the pellets and led to κ_{lat} = 2.7 W m^{-1} K^{-1} and ZT = 1 at 800 °C.[115, 116] The reduction in thermal conductivity in these samples has been attributed to additional phonon scattering at the grain boundaries, thus ball-milling should be considered as a useful tool in the processing of these materials.

1.7.4 Concluding Remarks

At a first glance, half-Heuslers appear to be relatively simple structures, but inspection of the available literature on these materials shows this is categorically not the case. The widely varying properties observed for nominally similar compositions shows that these compounds are very sensitive to small structural features. Compositional deviations and inclusion formation are frequent and are highly dependent on the synthesis and processing techniques employed. In order to allow targeted design of a material for a specific application, the cause and effect of structural changes, from the unit cell to microstructure, must be well defined. There is a general dearth of structural information available for half-Heusler thermoelectric materials and given the high dependence on synthesis method it is often difficult, if not impossible, to rationalise the differences in the observed properties. In order to exploit the half-Heusler structure to its fullest, and make compositional changes that truly maximise ZT, the synthesis must be tightly controlled and the resulting structure fully characterised. Until this is done, a meaningful explanation of the resulting properties cannot be attained and the maximum possible ZT values will remain elusive.

1.8 Aims

Zintl materials show a lot of promise in the field of thermoelectrics as they have structures that adhere to the phonon-glass-electron-crystal model, thus κ_{lat} and $S^2\sigma/\kappa_{el}$ can be optimised almost independently. The compounds investigated in this thesis may be described by a Zintl-type model, thus are good candidates for high performance thermoelectric applications.

A large portion of the work presented here concerns the half-Heusler compositions which are well established to show a lot of promise in the field of thermoelectrics. Progress in optimising these materials has, however, been hindered by a lack of understanding of the structural features that lead to a change in properties. The work in this thesis therefore aims to provide new insight into the structure of TiNiSn-based compositions, through tight control of the synthesis and careful structural analysis. The related, but less well-investigated TiNiX (X = Si, Ge) compositions have been similarly investigated to ascertain their physical and structural properties and to determine their potential in this field. Finally, a third set of compositions, RMnSbO (R = La, Nd) has been synthesised and characterised. This series has not previously been considered for thermoelectric applications, but is structurally related to the high performance AZn_2Sb_2 Zintl thermoelectric materials.

Chapter 2 – Experimental Methods and Theory

2.1 Introduction

A complete solid state chemistry experiment involves both the synthesis and analysis of the samples under investigation. There are therefore several steps to a solid state project, each as important as the next. Described in this chapter, are the various synthetic procedures used, structural characterisation techniques and physical property measurements undertaken.

2.2 Synthesis Methods

In general, samples in this thesis were prepared from elemental starting materials of 99.9%+ purity, combined in stoichiometric amounts. All starting materials were obtained from either Alfa Aesar or Sigma-Aldrich. Samples were prepared by either standard solid state reactions or arc-melting, as detailed below.

2.2.1 Solid State Reactions

For all samples, powders of the starting materials were ground together using an agate mortar and pestle and pellets were cold-pressed at 10 tonnes. Samples were sealed in quartz tubes and the samples were annealed. A more detailed overview of the solid state reactions used to prepare each series of samples (e.g. annealing conditions etc) are given in the relevant results chapters.

2.2.2 Arc-Melting

Some samples presented in this thesis were prepared by arc-melting using the Edmund Buehler compact arc-melter, MAM-1. An electric arc is established in this instrument by passing a current between a tungsten electrode and water-cooled copper base plate. The intensity of the arc can be somewhat controlled by altering the current. Laboratory arc-melters are capable of heating materials up to 3500 °C, thus starting materials are rapidly heated and melted. Synthesis can subsequently take a matter of seconds. All sample preparation using this technique was carried out in an argon atmosphere. After an initial melting, the resulting ingot was turned and melted again to encourage homogeneity.

2.2.3 Densification

Densification of samples can be very important in accurately determining physical properties. Thermal conductivity in particular, can be dominated by the porosity of a sample and the contributions from air and sample are difficult to deconvolute. Resistivity can also be adversely affected by poor density. For this reason, two approaches were investigated for the densification of samples presented in this thesis.

2.2.3.1 Spark Plasma Sintering

Spark plasma sintering (SPS) involves applying a pulsed DC current to a sample, under pressure, in a graphite die. This causes internal heating of the sample and high temperatures can be achieved rapidly. Heating rates are rapid and it is not necessary to hold a material at the maximum temperature for more than a few minutes. This is therefore a very quick method for sintering and densification of samples. SPS was attempted for some half-Heusler samples. Conditions and results are set out in Chapter 4. This process was carried out by Prof. Mike Reece at Queen Mary University, London.

2.2.3.2 Hot Pressing

In hot pressing, as with SPS, both temperature and pressure may be applied simultaneously. In this process however, the temperature source is a conventional, external heater. Hot-pressing of some of the presented samples was attempted using a hot press built in-house. The powdered samples were loaded into a graphite die and pressure was applied, up to 60 bar oil pressure. The die was enclosed in a heater, and the temperature was raised to a maximum of 700 ºC (its maximum power output). This process was carried out in a nitrogen atmosphere and samples were held at the maximum temperature for around 30 minutes, with additional time required for heating and cooling.

2.3 Structure Determination

Determination of the structure of materials is of utmost importance in the field of solid state chemistry. Accurate knowledge of the arrangement of atoms within a structure

allows structure-property relationships to be determined. The crystallographic structures of the materials discussed in this thesis were analysed using a combination of X-ray and neutron powder diffraction. The magnetic structures of RMnSbO (R = La and Nd) were also investigated using neutron diffraction. Electron microscopy was performed on selected half-Heusler samples to further probe the micro-structure within these samples.

2.3.1 X-ray Diffraction

2.3.1.1 Theory

X-ray diffraction has been used since the early part of the twentieth century to determine the crystallographic structure of compounds. It is the most widely used technique in structure determination. Monochromated X-rays for diffraction experiments are produced by accelerating electrons through a voltage of ~30 kV and smashing them into a metal target, often copper or molybdenum. The electrons hit the metal with sufficient energy to ionise an electron from the inner 1s electron shell. An electron in an outer orbital then drops down to fill the hole, emitting electromagnetic radiation of a specific wavelength.

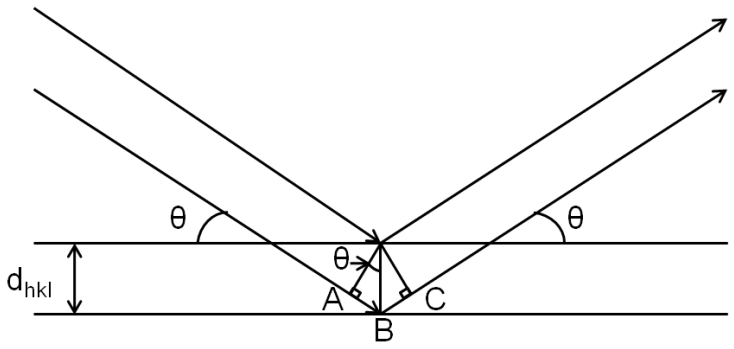

Figure 2.1: Diffraction from adjacent Bragg planes in a structure.

Crystal structures are composed of a regular 3 dimensional array of atoms, where the inter-atomic spacing is comparable with the wavelength of X-rays. This allows the crystal to act as a 3-dimensional diffraction grating. Incident radiation may be considered to be reflected by crystallographic planes in a structure. These planes are not composed of atoms but are imaginary sets of parallel planes defined by the size and shape of the unit cell. Once reflected, the X-ray beams may interfere with each other

either constructively or destructively. A reflection is only observable if constructive interference occurs and this only happens if the path difference between two photons reflected from adjacent planes is equal to an integer number of wavelengths, as may be deduced from Figure 2.1.

This is summarised by Bragg's Law:

$$2d_{hkl}sin\theta = n\lambda \qquad \text{Equation (2.1)}$$

where d_{hkl} is the distance between crystallographic planes in a structure, θ is the angle between the incident beam and the plane, *n* is any integer and λ is the wavelength of the incident radiation.[11, 17, 117, 118]

Each set of planes within a structure therefore produces a reflection at a given angle. The distance between these planes, d, which are defined by Miller indices *h*, *k* and *l*, may then be determined, as both λ and θ are known.

Determination of the d-spacing for a given (*hkl*) reflection allows the unit cell parameters of a structure to be calculated as shown by Equation (2.2).

$$\frac{1}{{d_{hkl}}^2} = \frac{h^2}{a^2} + \frac{k^2}{b^2} + \frac{l^2}{c^2} \qquad \text{Equation (2.2)}$$

In this final relationship *h, k and l* are obtainable from an indexed diffraction profile. Determination of other structural features, such as atomic positions and therefore bond lengths and angles, requires analysis of the intensities of the reflections. The intensity of a given (*hkl*) reflection depends two key factors, and is defined in Equation (2.3).

$$I(hkl) = \left(\sum_{1}^{N} f_n \cos\varphi_n\right)^2 + \left(\sum_{1}^{N} f_n \sin\varphi_n\right)^2 \qquad \text{Equation (2.3)}$$

where f_n is the scattering factor and φ_n is the phase angle of each atom, n, in the unit cell.

The first key component in Equation (2.3) is the scattering factor, *f*, which is unique to each type of atom. X-rays are scattered by electron density and *f* is defined as the ratio between the scattering from an atom, and the scattering from a free electron. If all the electrons in an atom occupied a single point in space, *f* would therefore be equal to the

atomic number, *Z*. This is clearly not possible and when electrons that occupy different space in an atom scatter X-rays, they do so at slightly differing angles. This causes a small path difference which results in destructive interference, reducing *f*. This is more pronounced where the incident radiation approaches from a larger angle and so, at high angles reflection intensities become increasingly poor.

The second contributor to scattering intensity is the phase angle (φ) between X-rays scattered by different atoms at different positions in the unit cell. For a given set of lattice planes (*hkl*), atoms which sit on the plane that passes through the origin of the unit cell have φ = 0. According to Bragg's Law (Equation (2.1)) the (*hkl*) planes are one wavelength in distance from one another. This relates to a phase angle of 2π, so atoms which sit on the nth parallel plane (from the plane that passes through the origin) have a phase angle of 2πn. For atoms which do not sit on an (*hkl*) plane (and this is usually the case), $\varphi = 2\pi(D_{hkl}/d_{hkl})$, where D_{hkl} is the perpendicular distance between the plane which passes through the origin and the atom.

In practice, Equation (2.3) is only easily applied to the simplest structures. For more complex structures, it may be expressed more generally as Equation (2.4).

$$I(hkl) = \left\{\sum_{1}^{N} f_n \cos 2\pi\,(hx_n + ky_n + lz_n)\right\}^2 + \left\{\sum_{1}^{N} f_n \sin 2\pi\,(hx_n + ky_n + lz_n)\right\}^2$$

Equation (2.4)

where f_n is the scattering factor for atom n at position x_n,y_n,z_n. This quantity is equal to the magnitude of the structure factor (F(*hkl*)) squared, as defined in Equation (2.5). The structure factor is the ratio of the scattering power of the unit cell to the scattering power of a single free electron and is more neatly expressed as Equation (2.6).

$$I(hkl) = |F(hkl)|^2 \qquad \text{Equation (2.5)}$$

$$F(hkl) = \sum_{1}^{N} f_n \exp 2\pi i(hx_n + ky_n + lz_n) \qquad \text{Equation (2.6)}$$

One further complication that must be considered is the thermal motion of atoms. Atoms are not stationary in the lattice positions and vibrate. Where the spacing between

the diffraction planes is small, the thermal motion can be larger than the interplanar distances. This significantly reduces the coherent diffraction, resulting in reduced intensities. Assuming the vibration of an atom is isotropic, a temperature factor that should be included in Equation (2.6) may be determined for each atom, as described in Equation (2.7).

$$T = exp\left(-8\pi^2 U sin^2 \frac{\theta}{\lambda}\right) \qquad \text{Equation (2.7)}$$

where U is the mean squared atomic displacement from the average position of the atom.[119, 120]

2.3.1.2 Powder Diffraction

When first developed, X-ray diffraction was applicable only to large single crystals. It is often not practical or even possible to prepare such a crystal so powder diffraction techniques were soon developed.

An ideal powder for this technique must be well-ground so that it contains a huge number of crystallites that are randomly orientated. The powder may therefore be considered to include all possible orientations of the crystal, and those that adhere to Bragg's law will reflect the incident X-rays. The powder is placed on a sample holder and the diffracted X-rays are collected by a movable detector, as shown in Figure 2.2.

As the crystallites can lie in all directions, the reflections they produce for a given crystallographic plane will all fall on the surface of a cone, as is illustrated in Figure 2.3. These are called Debye-Scherer cones.

Taking a 'slice' from this pattern gives a 1-dimensional pattern of peak intensity with respect to the scattering angle 2θ. Some data is generally lost compared to single crystal experiments, where a 3D pattern of diffraction spots is produced, each with a given intensity. The reduction from a 3- to a 1-dimensional pattern often results in the overlapping of reflections and this can lead to difficulties in determining exact peak position and relative intensity contributions. Nonetheless, this is also a powerful technique for structural characterisation.

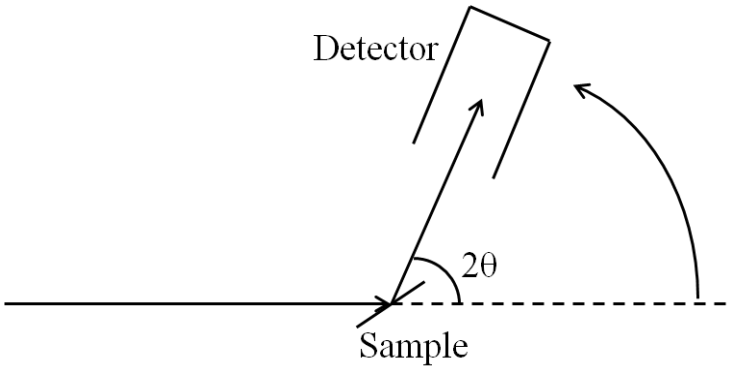

Figure 2.2: Powder diffraction experimental set-up.

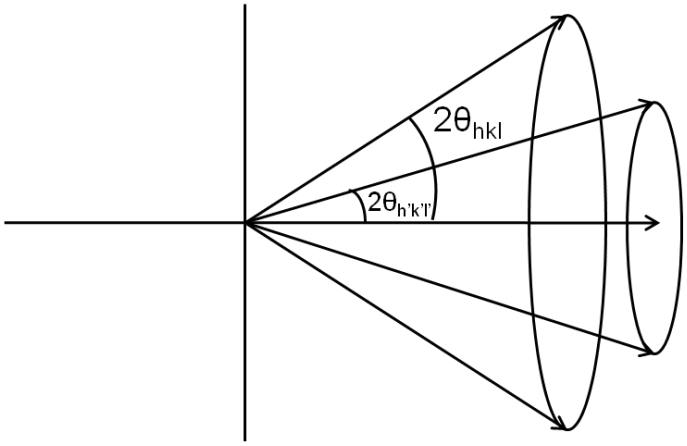

Figure 2.3: Diffraction cones produced by diffraction from a powder sample.

Powder patterns are often used as a 'fingerprint' technique, where collected patterns are compared to those in a database, for rapid phase identification. Careful analysis of the peak positions and intensities can yield unit cell dimensions and atom positions as discussed in section 2.4.1.1 and evaluation of the peak shape can provide information on particle size and strain within a crystal lattice.

2.3.1.3 D8 Advance

Laboratory X-ray powder diffraction patterns were collected using a Bruker D8 Advance diffractometer in reflectance mode. This diffractometer is fitted with a Lynxeye detector and uses a monochromated Cu $K_{\alpha 1}$ radiation source, with a

characteristic wavelength of 1.541 Å. 30 minute scans over the range $20° \leq 2\theta \leq 70°$ (stepsize = 0.014481°/counting time = 0.5 s/step) were collected for all samples to check for phase formation and purity. These were checked against patterns in the ICDD-PDF database, using the software package EVA, for phase identification. Longer scans of 9 hours, collected over the range $10° \leq 2\theta \leq 120°$ (stepsize = 0.009215°/counting time = 2.8 s/step), were subsequently collected for all samples of sufficient quality and these patterns were analysed by Rietveld and Le Bail refinement as discussed in section 2.4.3. A small amount (10 – 20 mg) of finely ground sample was used in each case and the powder was adhered to the sample holder using propanol.

2.3.2 Neutron Powder Diffraction

Neutron powder diffraction is directly analogous to X-ray powder diffraction. Neutron powder diffraction patterns are also composed of reflection peaks of varying intensity, from which unit cell dimensions and atomic positions may be determined. The key difference is the nature of the interaction of neutrons with the structure, which can be advantageous in certain scenarios.

2.3.2.1 Background/Theory

The production of neutrons for scientific experiments can be done in two ways, using either a reactor or spallation source. A nuclear reactor source, such as ILL in Grenoble, produces neutrons through nuclear fission of ^{235}U nuclei. The neutrons are slowed to the appropriate wavelength range by moderators and filters must be used to monochromate the incident beam. This is therefore a constant wavelength source, and d-spacings are obtained by scanning through the angle θ, defined in Bragg's law (Equation (2.1)). This technique was not used for the experiments detailed in this thesis and so will not be discussed further.

An alternative to the reactor is an accelerator based source such as ISIS in the UK. ISIS generates 'bunches' of H^- ions and initially accelerates these in a linear accelerator. The ions are then passed into a synchrotron, where their electrons are stripped away. The resulting protons are then further accelerated and subsequently smashed into a heavy metal target, in this case tungsten. The impact of the high energy protons causes neutrons to be ejected from the nuclei of the tungsten in a process called spallation.

Similar to the reactor source, the resulting neutrons must then be cooled to the required wavelength range by moderators before being directed to the appropriate instrument. To be useful in diffraction experiments, thermal neutrons must be selected as these have wavelengths comparable to the inter-atomic spacing in crystal structures. Different wavelengths can be used for a large number of different types of experiment, but only powder diffraction was performed on the samples in this thesis.

The ability to group the protons into bunches allows pulses of neutrons to be delivered. This means that time-of-flight diffraction experiments can be performed, where the whole neutron beam, with a range of wavelengths is used. In time-of-flight experiments, the detectors are stationary so that the Bragg angle, θ, is kept constant. The time taken by a neutron to travel from the moderator to the detector is then measured. The so-called time-of-flight is related to the wavelength by Equation (2.8).

$$t = \frac{m_n L \lambda}{h}$$

Equation (2.8)

where m_n is the mass of a neutron, L is the path length, λ is the wavelength and h is Planck's constant. In time-of-flight experiments then, θ is constant and λ is measured in order to calculate the d-spacings using Bragg's law.

The diffraction of neutrons by lattice planes may be described in a completely analogous way to the diffraction of X-rays. Neutrons possess scattering factors and structure factors for each element, exactly like X-rays, and lattice parameters and site occupancies may be extracted from the peak positions and intensities, respectively. However, there is one major difference and that is, that while X-rays are scattered by electron density in a structure, neutrons interact directly with the nuclei. There are several advantages to this. Firstly, direct measurement of the atomic positions, rather than the electron density, is possible. Secondly, there is no decrease in scattering power for neutrons at high angles as the interaction between neutron and nucleus is on a length-scale much shorter than that of the wavelength of the neutron. Thirdly, the scattering power, termed the scattering length, is dependent on the properties of the nucleus and this varies somewhat randomly between different atoms, rather than increasing with atomic number. This means that light elements and even different

isotopes of an element may be distinguished using neutrons, while they are often masked and difficult to locate in X-ray diffraction due to their low electron density.

A final distinction between neutrons and X-rays is that neutrons possess spin. This allows the neutron to interact with the electron spins in the atoms of the structure under investigation. This may be exploited and analysis of the magnetic structure of a material is possible. The structure factor for magnetic scattering is similar to that for nuclear scattering, as given in Equation (2.9).

$$F\ (hkl) = -\frac{e^2\gamma}{mc^2}\sum f_i S_{perp} exp\big(2\pi i(hx + ky + lz)\big) \qquad \text{Equation (2.9)}$$

where e is the electron charge, m is neutron mass, γ is the neutron magnetic dipole and c is the speed of light. Together these make up a constant that scales the magnetic intensities to the nuclear peaks. S_{perp} is the projection of the moment onto a given (hkl) plane.

The intensity of the magnetic reflections simply adds to the intensity of the nuclear peaks and may appear as either entirely new peaks, or additional intensity on the nuclear peaks. The intensity of the magnetic peaks does decrease with angle, as the interaction is once again with the electrons in the atoms.[119-121]

2.3.2.2 POLARIS

Analysis of the half-Heusler and TiNiX (X = Si, Ge) samples prepared for this thesis was done using the recently upgraded POLARIS diffractometer at the ISIS facility in Oxfordshire, UK. POLARIS has a path length of 12 m from the moderator and 5 banks of detectors, illustrated in different colours in Figure 2.4. It receives a high neutron flux which, when coupled with the large detector banks, allows for very fast acquisition times or analysis of small sample volumes.

2 g samples were finely ground and loaded into small cylindrical vanadium cans. Vanadium is used as it scatters neutrons only very weakly. This makes it almost 'invisible' to neutrons and any small peaks that are collected are subtracted from the sample datasets at the time of collection. Data reduction and background/instrumental subtractions were performed using the provided Mantid software. For ambient conditions measurements, samples were loaded into a sample changer. Variable

temperature measurements were also performed using a furnace, purpose built for the POLARIS instrument. Collection currents were typically 300 μA, which can be achieved in 2 hours.

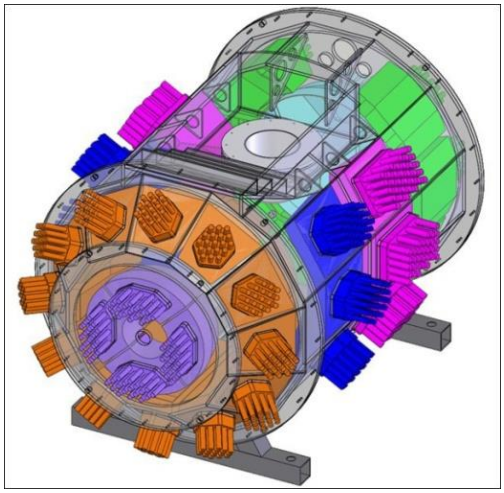

Figure 2.4: Schematic of the POLARIS instrument at ISIS.[122]

2.3.2.3 WISH

The WISH instrument (Figure 2.5) was used to analyse the RMnSbO samples discussed in Chapter 7. WISH is a high resolution diffractometer, with a longer path length that utilises cold neutrons. The longer wavelengths of the neutrons used, allows higher d-spacings to be investigated, which is ideal for investigating magnetic structures. In addition, magnetic peaks can significantly overlap with the nuclear peaks and so high resolution data is required to distinguish between them.

Samples (2 g) for experiments performed on WISH were prepared in a similar manner to the POLARIS experiments. Samples were loaded into vanadium cans and placed in an Oxford Instruments Variox Cryostat. Variable low temperature measurements were performed between 1.5 K and room temperature. The total current collected was between 7 and 20 μA. This is lower than that collected on POLARIS due to the much reduced neutron flux that WISH receives, in comparison.

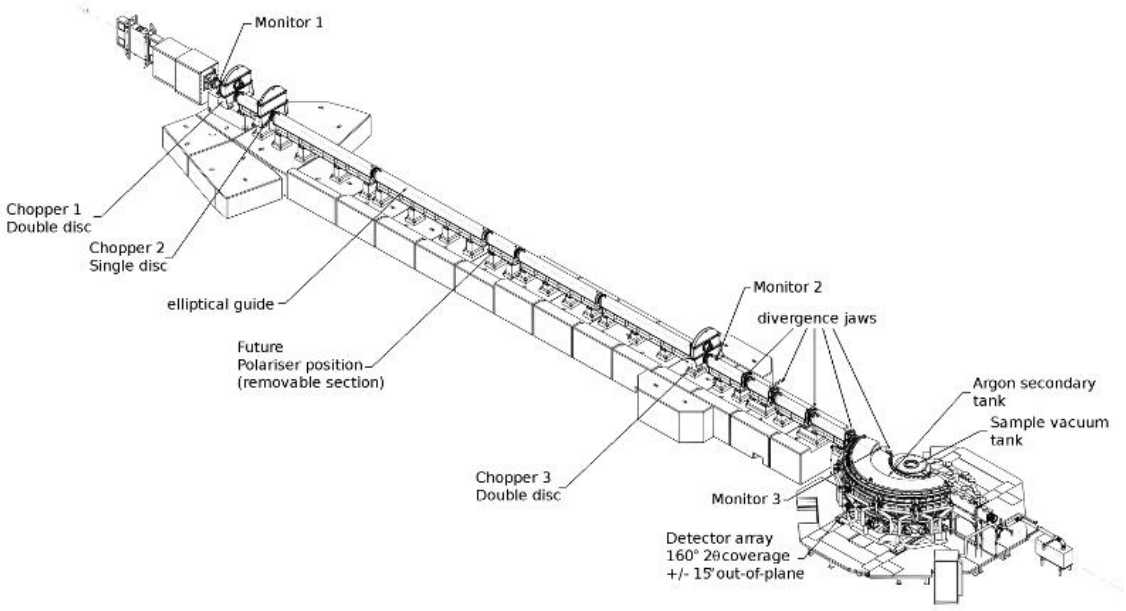

Figure 2.5: Schematic of the WISH diffractometer.[123]

2.3.3 Analysis of Diffraction Data

As discussed in Sections 2.4.1-2, the analysis of diffraction data can provide some extremely useful information. Single crystal diffraction experiments often yield enough information to allow the structure of a previously unknown compound to be completely solved. This is not the case with powder diffraction. Here, the structure can only be refined. This means fitting a model to the observed data, which requires some previous knowledge, or at the very least a good idea, of what the structure might look like. Without a starting model it is very difficult to obtain structural information from a powder pattern. If the pattern can be indexed (which is often not trivial), then lattice parameters may be extracted, but it is difficult to gain information on atomic positions.

2.3.3.1 Rietveld Refinement

Rietveld refinement is the most common method of refining a powder diffraction pattern.[124-127] It is a method of least squares refinement whereby a calculated model is fitted to an observed diffraction profile. The aim of this process is to minimise the residual, S_y, as defined in Equation (2.10).

$$S_y = \sum_i w_i (y_i - y_{ci})^2 \qquad \text{Equation (2.10)}$$

where $w_i = 1/y_i$ is a weighting factor, and y_i and y_{ci} are the observed and calculated intensities, respectively, at step i in the pattern.

This refinement method is built around the idea that the intensity, y, at every step, i, in the pattern, holds information. This may be that there is no reflection at a given position, or that there are multiple reflections in the vicinity that contribute to the observed intensity. From Equation (2.10), it can be seen that the main aim, when carrying out this type of refinement, is to minimise the difference between the observed and calculated intensity.

2.3.3.1.1 Observed Intensities

At a given point in the pattern, i, the observed intensity is made up from the background plus contributions from any reflections at, or near, that point. Each reflection profile has a height, width and shape that give it its intensity, I_K, where K represents the miller indices *h*, *k* and *l*. As previously discussed, the intensity value is directly related to the square of the absolute value of the structure factor, $|F_K|^2$. The structure factor contains information pertaining to the atom positions (x, y and z), thermal parameters (u_s), site occupancies (N_j) and scattering factor (f_j).

2.3.3.1.2 Calculated Intensities

Intensities are calculated taking into account contributions from the background and neighbouring reflections. They are determined using Equation (2.11).

$$y_{ci} = s\sum_K L_K|F_K|^2\phi(2\theta_i - 2\theta_K)P_K A + y_{bi} \qquad \text{Equation (2.11)}$$

where s is a scale factor, L_K contains Lorentz and polarisation factors, F_K is the structure factor, $\varphi(2\theta_i - 2\theta_K)$ is the reflection profile function, P_K is a preferred orientation function, A is an absorption correction function and y_{bi} is the background function.

Each of the factors in Equation (2.11) may be adjusted and refined to minimise S_y, defined in Equation (2.10). The relationships between these factors are however, not linear. It is therefore imperative that a good starting model is used. A poor starting

model is unlikely to allow convergence at all, but if it does, it is likely to find a false minimum.

2.3.3.1.3 The Reflection-Profile Function, ϕ

This function is used to model and refine the peak shapes in the pattern. This is a complex task as many factors directly affect the width and symmetry of the peak. Low resolution constant wavelength peak shapes can often be described by a Gaussian. Equation (2.12) shows how the peak width varies with Bragg angle in this case.

$$FWHM^2 = Utan^2\theta + Vtan\theta + W \qquad \text{Equation (2.12)}$$

where FWHM is the full width at half maximum of the peak, θ is the Bragg angle and U, V and W are refinable parameters.

The Gaussian is often not suitable however, for higher resolution measurements and a pseudo-Voigt function may be used instead. This function is a linear combination of a Gaussian and a Lorentzian function and is parameterised in terms of the relative amounts of Gaussian and Lorentzian used (U, V, W and X, Y, respectively).

The variation of the Lorentzian width with Bragg angle is given in Equation (2.13).

$$FWHM = \frac{X}{\cos\theta} + Y\ tan\theta \qquad \text{Equation (2.13)}$$

In this equation, X relates to the particle size broadening and Y to strain broadening.

2.3.3.1.4 Preferred Orientation Function, P_K

Preferred orientation occurs when the crystallites preferentially align along a certain axis, or set of axes. For example, in layered structures, the crystallites may lie with their layers parallel to the sample holder. This causes systematic problems with intensity, such as increased intensities for all *0k0* reflections. The systematic nature of this problem means that it may be modelled using the preferred orientation function, P_K.

2.3.3.1.5 Absorption Factor, A

Absorption problems arise when the sample absorbs a portion of the incident radiation instead of scattering it all. This can be affected by the elements present and even the size and shape of the sample crystallites but is also heavily dependent on instrument geometry and the type of radiation used. This can be effectively modelled using the effective absorption factor, A, which is often a constant for a given geometry.

2.3.3.1.6 Background Intensity, y_{bi}

The background intensity may be modelled in one of three different ways. The first of these is for the operator to input a table of intensity values. The second is to apply a linear interpolation function between operator-specified points in the pattern. The final method is to apply a specific background function.

2.3.3.1.7 Feedback

Any results obtained through this method of refinement are dependent upon how well the calculated model has been fitted to the observed data. As evidenced in the preceding sections, fitting a model to an observed pattern is far from trivial. Visual inspection of the pattern and fit is often the most instructive method for determining the accuracy of a fit. In addition to this, at each step of a refinement various goodness-of-fit residuals are provided. These are defined in Equation (2.14).

$$R_p = \frac{\Sigma|y_i - y_{ci}|}{\Sigma y_i} \qquad \text{Equation (2.14)}$$

$$wR_p = \left[\frac{\Sigma w_i(y_i - y_{ci})^2}{\Sigma w_i(y_i)^2}\right]^{1/2} \qquad \text{Equation (2.15)}$$

$$\chi^2 = \frac{\sum_i w_i(y_i - y_{ci})^2}{N - p + C} \qquad \text{Equation (2.16)}$$

$$R_F = \frac{\Sigma\left|I_{K,obs}^{1/2} - I_{K,calc}^{1/2}\right|}{\Sigma I_{K,obs}^{1/2}} \qquad \text{Equation (2.17)}$$

In each of these equations, I_K is the intensity of the kth Bragg reflection, y_i is a measure of intensity, w_i is statistical weight, and $(N - p + C)$ represents the number of degrees of freedom where N is the total number of observations, p is the number of refined parameters and C is the number of constraints used in the refining process.

R_P and wR_P are the profile and weighted profile R-factor, respectively and are a measure of the extent to which the Bragg peaks are fitted by the refinement. wR_P takes into account the size of these peaks. R_f^2 is a structure factor analogous to that provided in single crystal refinements. It gives an indication of how reliable the calculated structure is. χ^2 is a direct measure of goodness of fit between the calculated and observed patterns.

2.3.3.2 Le Bail Fitting

Rietveld refinement requires a good starting model in order achieve a good, reliable fit to the data. Sometimes, this is not possible, or it may be inadvisable to make such an assumption at the start of the refinement process. In the process of Rietveld refinement, the structure factors are calculated directly from the model, and so the peak intensities are calculated on the assumption that this model is correct. In certain instances, for example the generation of Fourier maps, this is of little use as a true picture of the observed F_{hkl} values is required.

Le Bail fitting makes no such supposition and does not require a structural model. It begins by assuming all F_{hkl}(calc) = 1 and uses Rietveld algorithms to generate observed values via an iterative process. Where peaks fully overlap the relative contributions are split equally amongst the constituent reflections. Where reflections partially overlap, F_{hkl}(obs) values are moved away from equal only as much as necessary. This method therefore provides the best possible fit of the peak intensities and indeed, the best possible overall fit. From such a fit, it is possible to obtain lattice parameters, a background function and profile parameters, thus it is possible to extract very useful information without having a good starting model. If desired, this can then be used as a starting point from which to test structural models by Rietveld refinement.

2.3.3.3 GSAS

All Rietveld and Le Bail refinements to data collected for this thesis were performed using GSAS, in conjunction with its user interface, EXPGUI.[128, 129] This is the General Structure Analysis System developed by A. C. Larson and R. B. von Dreele which was designed to process X-ray and neutron diffraction data, and is capable of analysing multiple datasets collected for a single sample simultaneously. The program may be used to analyse either single crystal or powder diffraction data, though for this thesis, only powder data was analysed.

2.3.4 Electron Microscopy

Electron microscopy encompasses several techniques that are capable of imaging samples over a wide range of magnitudes on the sub-micrometre scale. In general, these techniques involve bombarding a sample with high energy electrons. In a similar manner to X-rays and neutrons, each element has a different scattering factor f_e for electrons. Like X-rays, the scattering factor is roughly proportional to the atomic number, so that it is very difficult to 'see' light elements in a structure. It is also dependent on the angle, and falls off rapidly with the incident angle of the electron beam. The scattering of electrons is much stronger than for X-rays and neutrons and the interaction of electrons with matter can be much more complex, thus it is impossible to analyze scattering intensities in an analogous manner to that described in section 2.4.1. For this reason, it is very difficult to solve a crystal structure using electron microscopy alone, but it is a versatile technique which can uncover more subtle features that are impossible to detect using other techniques. Used in conjunction with other types of diffraction, it can be an extremely useful tool in explaining the properties displayed by materials.

The strong interaction of electrons with the sample causes several different effects upon impact. The results include un-scattered electrons, diffraction of electrons, inelastic scattering of electrons, generation of secondary electrons and generation of X-rays, all of which may be analysed to probe different features in the structure. It is therefore possible to gain information on the texture, topology, sample surface, local variations in the atomic structure, defects, phase boundaries and vacancies, amongst others. The electron beam is produced from a metal (usually tungsten) filament and accelerated by

an applied voltage. The voltage is directly related to the wavelength of the electrons by Equation (2.18).

$$\lambda = \frac{h}{\sqrt{2meV}} \qquad \text{Equation (2.18)}$$

where h is Planck's constant, m is the mass of the electron, e is its charge and V is the applied voltage.

The electron beam is subsequently focussed and directed by applied magnetic fields onto the sample and the following step depends on the geometry of the measurement and the specific technique in use. Three techniques, which were used for this thesis, will be discussed below.[11, 130-132]

2.3.4.1 Transmission Electron Microscopy

Transmission electron microscopy, as the name suggests, involves passing an electron beam through the sample and analysing the transmitted electrons. It probes features smaller than 0.1 μm in diameter. The first point to consider in the technique is sample preparation. Samples must be very thin in order to avoid all the incident electrons being absorbed. Using higher energy electrons can circumvent this problem somewhat but in general samples must be thinned to < 2000 Å. This is usually done by ion bombardment.

The electrons of interest in TEM experiments are those which are diffracted or remain un-scattered. The wavelength of the electrons is much smaller than those of X-rays and neutrons and so, by Bragg's equation (Equation (2.1)), any diffracted beams occur only at small angles. They do, however, create a diffraction pattern akin to a single crystal diffraction pattern produced by X-rays or neutrons. As discussed though, this is much harder to interpret and requires a good starting model in order to gain any useful information.

It is possible to acquire images by re-focussing the diffracted beams using a series of magnetic lenses. These can be on the atomic scale if the diffracted beams are re-focussed selectively. From this it is possible to gain information about defects and phase boundaries, amongst other things.

2.3.4.2 Scanning Electron Microscopy

This technique is generally used to probe features on the 0.1-1 μm length-scale, although it can be used over a wider range than this. It is a reflectance technique, where the intensity of the reflected and secondary electrons is measured above the sample surface. It usually involves very little sample preparation, although polishing may be desirable where surfaces are very rough and a thin metallic coating may be applied to insulating samples, to prevent charge build-up. An electron beam with a diameter between 50 and 100 Å is initially focussed on one point in the sample and then systematically scanned over an area to produce an image that is a map of the reflected electron intensities. This creates and almost 3-dimensional image that is extremely useful for determining particle shape and size, textures, topography etc.

2.3.4.3 Analytical Electron Microscopy

The X-rays generated by the impact of the electron beam can provide a lot of information about the elements that make up a sample. When an electron hits an atom, an X-ray of a characteristic wavelength is produced. By monitoring the wavelength or energy of the X-rays produced by a sample, it is possible to determine which elements are present. These techniques are called wavelength dispersive and energy dispersive X-ray analysis (EDX), respectively. If the instrument is calibrated, quantitative analysis may be carried out. For example, for a thin sample, the relative quantities of the constituent elements are proportional to their intensities, as described in Equation (2.19).

$$\frac{C_x}{C_y} \propto \frac{I_x}{I_y} \qquad \text{Equation (2.19)}$$

where C_x is the concentration and I_x is the peak intensity for element x.

This technique can be combined with TEM and SEM to produce maps of elemental distribution in a sample.

2.3.4.4 Experimental set-up

Several half-Heusler samples were analysed by transmission electron microscopy (TEM), energy dispersive X-ray (EDX) analysis, and scanning electron microscopy (SEM). EDX analysis and TEM were undertaken at the University of Glasgow by Dr. Donald MacLaren, on a JEOL ARM 200cF instrument operated at 200kV and equipped with a Bruker XFlash detector. Data were acquired under the Spectrum Imaging protocols of Gatan's Digital Micrograph software package. A thin lamella was cut from a sintered pellet using the focused Ga^+ beam of an FEI Nova Dual Beam instrument, employing standard lift-out and polishing techniques. Damage to the surface region was minimised by in-situ deposition of a thin Pt capping layer. The approximately 2.5 × 4.5 μm^2 lamella was thinned to around 100 nm thickness, slightly too thick for high resolution transmission electron microscopy but sufficient to avoid fragmentation of the sintered grains. SEM measurements were performed on polished bars of sample using a Philips XL30 Environmental Scanning Electron Microscope (ESEM), using Oxford instruments INCA energy (EDX) dispersive X-ray analysis system. An operating voltage of 20 kV was used. Measurements were carried out by Dr. James Buckmann (Heriot-Watt University).

2.4 Physical Properties

Measurement of the physical properties is of vital importance in determining effects of making structural changes to materials under investigation. The key properties in thermoelectric research are the resistivity, Seebeck coefficient and thermal conductivity, which were all measured where possible for the samples presented in this thesis.

2.4.1 Resistivity

The resistivity may be calculated from the resistance using Equation (2.20).

$$\rho = \frac{RA}{l} \qquad \text{Equation (2.20)}$$

where ρ is resistivity (Ω m), R is resistance (Ω), A is the cross section area (W x H in Figure 2.6) and l is the length between the inner contacts.

High and low temperature measurements of the resistance were carried out using the 4 probe method, represented schematically in Figure 2.6. In this set-up, a current is driven through the outer contacts and the voltage is measured across the inner contacts. This prevents the measurement from being affected by contact resistance and resistances in the leads etc, which can have a significant impact on measurements, especially for metallic samples with low resistance values.

Low temperature measurements were carried out on a Quantum Design PPMS, between 1.5 K and room temperature. Measurements with variable field, between 0 and 9 T were also performed at various temperature steps. Bars were cut from the annealed pellets using a low-speed diamond saw and copper wires were attached in the arrangement shown in Figure 2.6. These were then soldered to the sample holder and inserted into the sample changer. Measurements were performed under vacuum.

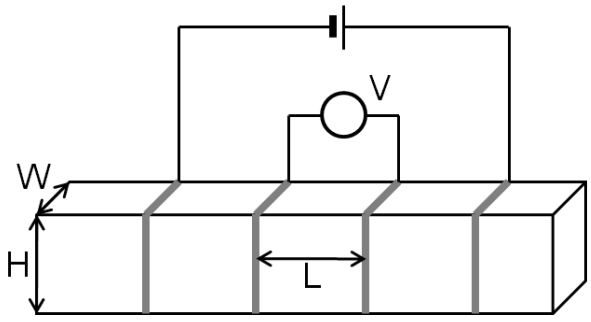

Figure 2.6: Schematic representation of the 4-probe method for measuring resistance.

High temperature measurements, between room temperature and 723 K, were performed using a Linseis LSR-3 Seebeck probe instrument. The sample set-up is represented schematically in Figure 2.7. In this case, the contacts are not adhered to the sample. The sample is clamped between 2 platinum electrodes and the voltage and temperature are measured by two spring loaded platinum thermocouples. These measurements were performed in a helium atmosphere.

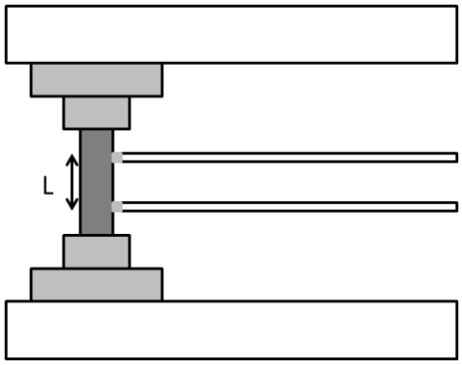

Figure 2.7: Schematic representation of sample set-up in the Linseis LSR-3 Seebeck probe.

2.4.2 Seebeck Coefficient

High temperature Seebeck coefficient measurements were performed simultaneously with the resistivity measurements using the Linseis LSR-3 Seebeck probe instrument. The set-up is therefore exactly the same as described above and represented schematically in Figure 2.7. For the Seebeck measurement, a temperature gradient of 30 K was applied at the electrodes. For the samples investigated for this thesis, this resulted in a gradient of 7 - 8 K over the sample.

2.4.3 Thermal Conductivity

Thermal conductivity measurements were carried out using an Anter FL3000 device. This instrument employs the flash method to calculate the specific heat capacity and thermal diffusivity of a sample and from these values, deduces the thermal conductivity.[133] These measurements require a cylindrical pellet with a diameter of 13 mm. The pellets were coated in graphite so that as much of the incident energy was absorbed as possible.

In the flash method, one side of the sample pellet is subjected to an extremely short but intense pulse of energy. The exposed face of the pellet absorbs this energy and the rise in temperature stimulated on the rear of the pellet is measured. The maximum temperature rise experienced by the rear of the pellet and low long, t_x, it takes for that surface to reach x% of that temperature difference is then determined and the diffusivity can then be calculated using Equation (2.21).

$$\alpha = \frac{k_x L^2}{t_x}$$ Equation (2.21)

where α is the thermal diffusivity ($m^2\ s^{-1}$), L is the thickness of the pellet (m), t_x is the time taken for the rear of the pellet to reach x% of its maximum ΔT and k_x is a constant, the value of which depends on the percentage rise in temperature. In theory, the thermal diffusivity should be constant for all x.

The specific heat capacity, C_P, may also be determined as it is a function of the heat transferred to the sample, Q, and some pre-entered data, including the density (ρ) and the volume (V) of the pellet, as illustrated by Equation (2.22).

$$C_P = \frac{Q}{\rho V \Delta T}$$ Equation (2.22)

In this equation ΔT represents the maximum temperature difference experienced at the rear of the pellet. The specific heat capacity and thermal diffusivity values, along with the density are then combined to give a value of thermal conductivity using the relationship in Equation (2.23).

$$\kappa = \alpha \rho C_P$$ Equation (2.23)

where κ is the thermal conductivity, measured in $W\ m^{-1}\ K^{-1}$.

Chapter 3 – Structural and Thermoelectric Properties of Arc-Melted $Ti_{1-x}Zr_xNiSn$

3.1 Introduction

The most common method employed to reduce κ_{lat} in XNiSn half-Heusler samples is substitution on the X site, as discussed in Chapter 1. The majority of the reported work on half-Heuslers has focussed on the $Zr_{1-x}Hf_xNiSn$ series, which exploits mass fluctuation effects to minimise the thermal conductivity. These samples generally have κ = 4-6 W m^{-1} K^{-1},[77, 79] but the introduction of Ti into this system has been reported to reduce the thermal conductivity values to 2-4 W m^{-1} K^{-1}.[79, 109, 134, 135] These reduced κ values underpin all cases where $ZT \geq 1$ has been reported. The root cause of this reduction in κ is unclear, and very little diffraction/microscopy data is available for these compounds. However, there does appear to be a link between addition of Ti to the system and a reduction in κ, and a key difference between Hf/Zr and Ti is size. The aim of this investigation was therefore to determine whether the large size difference between Ti and Zr could be used to cause additional reductions to the thermal conductivity, perhaps by introducing strain to the system. The focus of this Chapter is the $Ti_{1-x}Zr_xNiSn_{0.95}$ series, where x = 0, 0.05 and 0.5. These samples were analysed by X-ray and neutron powder diffraction and the thermoelectric properties were also characterised.

3.2 Synthesis

The samples in this series were synthesised by arc-melting, as described in section 2.2.2. The resulting 5 g ingots were then vacuum sealed in quartz tubes and annealed at 900 °C for 2 weeks. Nominal $Ti_{1-x}Zr_xNiSn_{0.95}$ samples were prepared by mixing stoichiometric quantities of the elemental starting materials. A 5% Sn deficiency was used to prevent the formation of a Sn impurity phase found predominantly in the Zr-doped samples. A 5 g TiNiSn sample was also prepared using stoichiometric quantities of starting material. The resulting ingots were found to be fully dense and were cut into discs and bars using a low speed diamond saw for thermoelectric property measurements.

3.3 X-ray Powder Diffraction Analysis

Initial inspection of powder X-ray powder diffraction patterns confirmed the formation of the target phases, along with full-Heusler and Ti_5Sn_3 binary impurities, as illustrated by Figure 3.1. These are commonly reported impurities for arc-melted TiNiSn.[82, 108] Directly after arc-melting, the samples contained much more significant amounts of full-Heusler, Sn and Ti-Sn binary impurity phases. Annealing reduced the intensities of these peaks but the impurity phases could not be entirely eradicated. This shows that the half-Heusler phase forms via a full-Heusler phase that is gradually converted to the half-Heusler during the annealing process. Further minor impurity peaks are observable in some samples and it is likely that these belong to another Ti-Sn binary phase. However, this could not be identified by searching against the ICDD-PDF database.

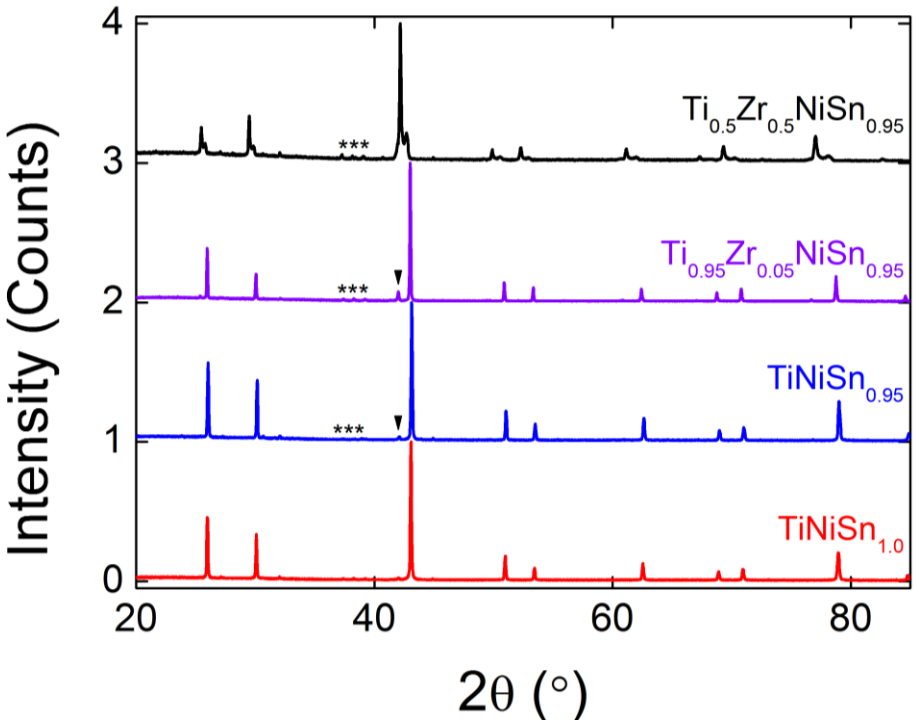

Figure 3.1: Powder X-ray diffraction patterns for the nominal $Ti_{1-x}Zr_xNiSn_{0.95}$ and TiNiSn arc-melted samples. * indicate peaks belonging to the Ti_5Sn_3 impurity phase and peaks marked ▼ belong to a full-Heusler 'TiNi$_2$Sn' phase.

Immediately apparent from the diffraction patterns was significant broadening and splitting of the reflections for $Ti_{0.5}Zr_{0.5}NiSn_{0.95}$. Similar, but less pronounced, broadening is observable in $Ti_{0.95}Zr_{0.05}NiSn_{0.95}$, upon closer inspection. The nature and

origins of this broadening and peak splitting in the Zr-doped samples will first be addressed, followed by in depth structural analysis of the $TiNiSn_{1.0}$ and $TiNiSn_{0.95}$ samples, in the following sections.

3.3.1 $Ti_{0.5}Zr_{0.5}NiSn_{0.95}$

A close-up of the 422 reflection for $Ti_{0.5}Zr_{0.5}NiSn_{0.95}$ is presented in Figure 3.2(a). This clearly demonstrates that a perfect solid solution between TiNiSn and ZrNiSn has not been achieved. The significant splitting of the peak indicates that instead, several different $Ti_{1-x}Zr_xNiSn_{0.95}$ phases are present, each with a different value of x. Rietveld refinement of this pattern was performed, and required a minimum of 4 independent half-Heusler phases to satisfactorily model the complex peak shape. These 4 phases are indicated by the tickmarks and labelled A-D in Figure 3.2(a). The fitted lattice parameters and weight fractions are presented in Table 3.1.

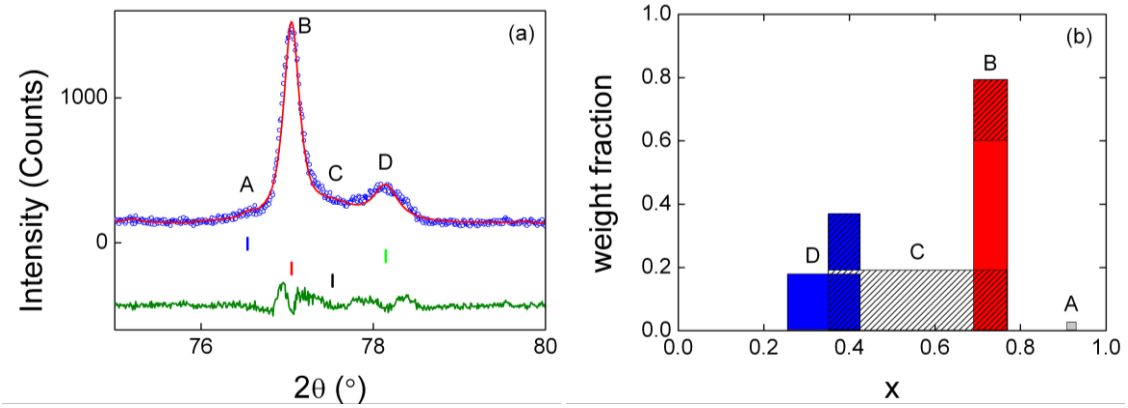

Figure 3.2: (a) 422 reflection for $Ti_{0.5}Zr_{0.5}NiSn_{0.95}$. Blue circles represent the collected data, the red line is the calculated fit and the green line is the difference. Tickmarks represent the 4 half-Heusler phases that were used to fit the data. (b) Schematic representation of the phase distribution within the $Ti_{0.5}Zr_{0.5}NiSn_{0.95}$ sample. Each box (blue, striped, red and grey) represents the Δx range spanned by each of the 4 modelled phases.

Vegard's law was used to determine the Ti:Zr ratio within each sample. The refined lattice parameter of the '$TiNiSn_{0.95}$' sample prepared in this series was found to be 5.929 Å. $ZrNiSn_{0.95}$, prepared in a similar manner, gives a = 6.109 Å. Assuming that a

solid solution between these phases can be formed, and that the lattice parameters follow Vegard's law, an estimation of the value of x in $Ti_{1-x}Zr_xNiSn_{0.95}$ may be made using Equation (3.1).

$$x = \frac{a_{(Ti,Zr)} - a_{Ti}}{a_{Zr} - a_{Ti}} \qquad \text{Equation (3.1)}$$

where $a_{(Ti,Zr)}$ is the refined lattice parameter of a given phase in $Ti_{1-x}Zr_xNiSn_{0.95}$, a_{Ti} is the lattice parameter of TiNiSn and a_{Zr} is the lattice parameter of ZrNiSn.

The calculated x_{Vegard} values for each phase are presented in Table 3.1. These have been combined with the phase fractions for each of these phases to produce an average composition for the sample. This was found to be $Ti_{0.37}Zr_{0.63}NiSn_{0.95}$. The Ti-deficiency is consistent with the observation of Ti_5Sn_3 binary impurities.

Table 3.1: Lattice parameters (a) and molar percentage (mol%) for the $Ti_{1-x}Zr_xNiSn_{0.95}$ series and $TiNiSn_{1.0}$; x calculated from Vegard's law (x_{Vegard}), phase distribution (Δx) and average x for $Ti_{1-x}Zr_xNiSn_{0.95}$ ($x > 0$); y calculated from Vegard's law (y_{Vegard}) and average y for $TiNi_{1+y}Sn_{0.95/1.0}$ and goodness of fit (χ^2) for each sample.

	a (Å)	mol%	x_{Vegard}	Δx	$x_{average}$	y_{Vegard}	$y_{average}$	χ^2
$TiNiSn_{0.95}$	5.9293(1)	35.7(2)	-	-	-	0	0.02	2.8
	5.9352(1)	64.3(1)	-	-	-	0.03		
$Ti_{0.95}Zr_{0.05}NiSn_{0.95}$	5.9452(1)	13.2(5)	0.09	-	0.12	-	-	2.7
	5.9508(1)	74.8(6)	0.12	-		-	-	
$Ti_{0.5}Zr_{0.5}NiSn_{0.95}$	5.9899(2)	17.0	0.34	0.17	0.63	-	-	2.4
	6.0307(4)	18.3	0.56	0.42		-	-	
	6.0614(1)	57.8	0.73	0.08		-	-	
	6.0953(5)	2.7(2)	0.92	0.02		-	-	
$TiNiSn_{1.0}$	5.9341(1)	88.4(1)	-	-	-	0.03	0.03	1.9
	5.9393(1)	11.6(1)	-	-	-	0.06		

In addition to the presence of multiple phases within this sample, there is a large amount of peak broadening for each of the half-Heusler phases. This indicates further compositional variation within this sample, i.e. a further spread of x-values, centred round x_{Vegard}. An attempt at quantifying this effect may be made by analysing the profile functions used to model the peak shape of each phase. GSAS profile function 3, for

constant wavelength diffraction data, was used. Within this, the parameter 'LY' is related to strain broadening, as described in Equation (3.2).

$$S = \frac{\pi}{18000}(LY - LY_i)100\% \qquad \text{Equation (3.2)}$$

where S is strain and LY_i describes any instrumental peak broadening.

Peak broadening due to strain occurs because perturbations to the structure cause some, but not all, Bragg planes to shift slightly, in a non-uniform manner. There is therefore a small spread in d-spacings, centred round a d-spacing value for the ideal, unstrained structure. The strain broadening value, defined in Equation (3.3) may therefore be expressed as:

$$S = \frac{\Delta d}{d}\left(= \frac{\Delta a}{a}\right) \qquad \text{Equation (3.3)}$$

where d represents d-spacings and a is the lattice parameter of a cubic structure.

The spread in d-spacing may be directly equated with a spread in lattice parameters. As indicated (in brackets) by Equation (3.3), this relationship is very simple for cubic structures as the strain must be isotropic. This is an extremely useful relationship as it allows the strain terms obtained from the refinement to be directly converted to a spread in x-values, Δx, as illustrated by Equation (3.4).

$$S = \frac{\Delta a}{a} = \frac{(a_{Zr} - a_{Ti})\Delta x}{a_{Ti} + (a_{Zr} - a_{Ti})x} \approx \frac{(a_{Zr} - a_{Ti})\Delta x}{a_{Ti}} \qquad \text{Equation (3.4)}$$

For all samples in this series, the peak shapes could be sufficiently modelled by refining only the GW and LY terms. GW, which accounts for Gaussian broadening, was found to be 0.1575° for TiNiSn. For the x = 0.05 and 0.5 samples, GW was fixed to this value, as it should be similar for all samples. LY was then allowed to refine freely for each modelled phase. LY_i was taken to be the fitted LY value for the TiNiSn sample (0.08°) which encompasses all instrumental broadening, as well as strain effects that cannot be attributed to Zr-substitution. Δx values, calculated for each refined phase are tabulated in Table 3.1. A schematic representation of the spread in x-values, observed in the nominal $Ti_{0.5}Zr_{0.5}NiSn_{0.95}$ sample, is provided in Figure 3.2(b), and shows that a

continuous spread of $Ti_{1-x}Zr_xNiSn_{0.95}$ phases, between x = 0.255 and 0.77 is present in this sample.

3.3.2 $TiNiSn_{0.95}$ and $TiNiSn_{1.0}$

Subtle peak broadening was also observed in the samples containing no Zr. This is illustrated in Figure 3.3. Two half-Heusler phases were required to fit the peak shape adequately for both $TiNiSn_{0.95}$ and $TiNiSn_{1.0}$. This cannot be attributed to variations in Ti:Zr ratio and indicates another source of compositional variation within these samples. The refined lattice parameters for each phase are very close to one another. For example, Δa = 0.0059 Å for $TiNiSn_{0.95}$ and 0.0052 Å for $TiNiSn_{1.0}$, indicating a more subtle feature.

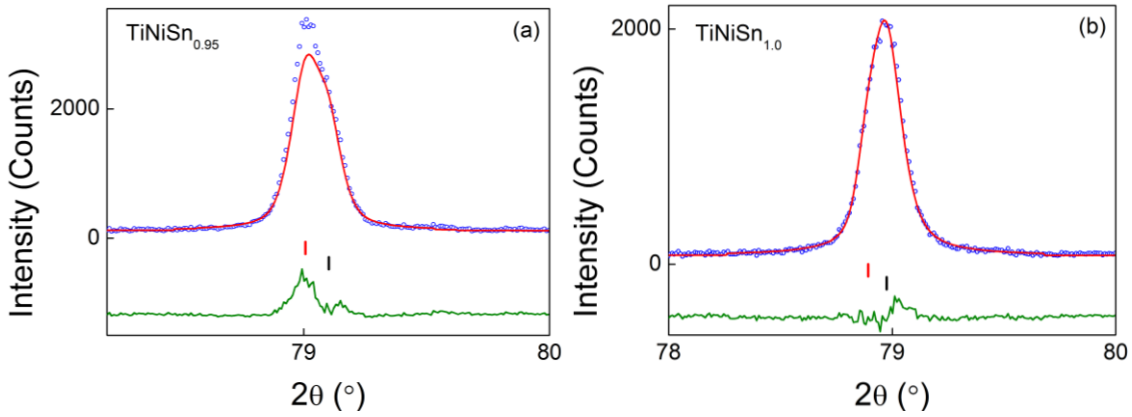

Figure 3.3: (422) reflection for (a) $TiNiSn_{0.95}$ and (b) $TiNiSn_{1.0}$. In both cases, blue circles represent the collected data, the red line is the calculated fit and the green line is the difference. Tickmarks represent the 2 half-Heusler phases that were required to fit the data in each case.

3.3.3 $Ti_{0.95}Zr_{0.05}NiSn_{0.95}$

Inspection of the half-Heusler reflections for this sample, containing minor amounts of Zr, reveals minor splitting of the peaks and some broadening. The peaks are more similar in appearance to the TiNiSn samples than $Ti_{0.5}Zr_{0.5}NiSn_{0.95}$, as illustrated by Figure 3.4. Rietveld refinement of this pattern was performed and two half-Heusler phases were required to fit the peak shape in a satisfactory manner. Refinement of the profile parameters was performed as described in Section 3.3.1. The GW and LY values

obtained were similar to those found for $TiNiSn_{0.95}$ and $TiNiSn_{1.0}$, indicating no additional compositional variation. The lattice parameters obtained for each phase are very similar, differing by only 0.0056 Å. If this difference is attributed to variations in the Ti:Zr ratio, the estimated compositions are $Ti_{0.91}Zr_{0.09}NiSn_{0.95}$ and $Ti_{0.88}Zr_{0.12}NiSn_{0.95}$, with an average composition of $Ti_{0.90}Zr_{0.10}NiSn_{0.95}$. These results are collated in Table 3.1. The difference in lattice parameters is, however, very similar to those found in the TiNiSn samples. It is possible therefore, that this is not a result of varying Ti:Zr content, and the root cause may be the same as for TiNiSn.

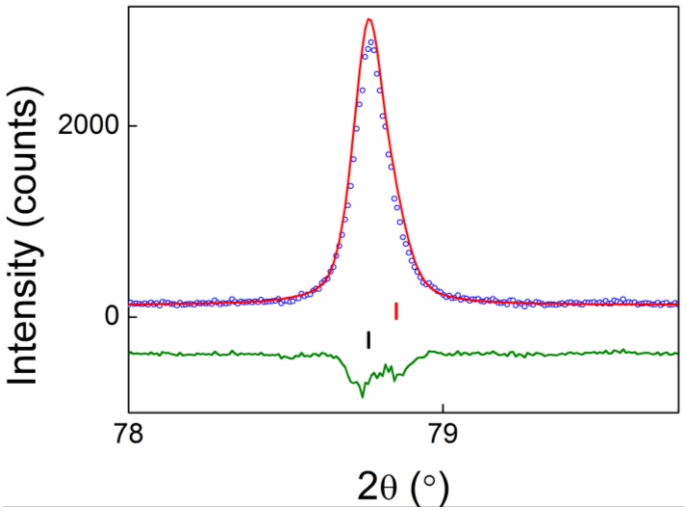

Figure 3.4: 422 reflection for $Ti_{0.95}Zr_{0.05}NiSn_{0.95}$. Blue circles represent the collected data, the red line is the calculated pattern and the green line is the difference. Tickmarks represent the two half-Heusler phases that were required to fit the data.

3.4 Neutron Powder Diffraction of TiNiSn

Neutron powder diffraction experiments were carried out on $TiNiSn_{0.95}$ and $TiNiSn_{1.0}$. Data were collected to a total monitor count of 300 μA on approximately 2 g of each sample, using the POLARIS instrument at the ISIS neutron facility, Oxfordshire. Refinement of the collected data allowed determination of the site occupancies within the structure.

3.4.1 $TiNiSn_{0.95}$

The nominal model, $TiNiSn_{0.95}$, yields χ^2 = 11.2, with large thermal parameters observed for Ti and Sn. A free refinement of the site occupancies indicated an unrealistic composition of $Ti_{0.770(3)}NiSn_{0.842(2)}$ but achieved a much improved, minimum χ^2 = 7.0. Several different models were then investigated in order to replicate this minimum χ^2 value, with a more realistic composition.

Table 3.2: Lattice parameters (a), fractional site occupancies (occ), thermal parameters (U_{iso} / Å^2) and fit statistics for Rietveld refinement of neutron powder diffraction data collected for $TiNiSn_{0.95}$ and $TiNiSn_{1.0}$.

			$TiNiSn_{0.95}$	$TiNiSn_{1.0}$
a (Å)			5.9363(1)	5.9327(1)
Ti	*4a*	Occ	1.000	1.000
		U_{iso}	0.00478(7)	0.00478(7)
Ni(1)	*4c*	Occ	1.000(3)	1.000(3)
		U_{iso}	0.00541(4)	0.00525(5)
Ni(2)	*4d*	Occ	0.058(3)	0.036(3)
		U_{iso}	0.00541(4)	0.00426(5)
Sn	*4b*	Occ	0.991(2)	1.000(2)
		U_{iso}	0.00434(4)	0.00426(5)
χ^2			7.0	6.5
wR_P (%)		*Bank 1*	2.4	2.5
		Bank 2	1.9	1.9
		Bank 3	2.4	2.5
R_p (%)		*Bank 1*	3.1	3.8
		Bank 2	4.1	3.6
		Bank 3	3.2	3.1

$TiNiSn_{0.95}$ contains 9.7(1) wt% $Ti_{1.17(1)}Ni_{1.83(1)}Sn$ and 6.7(3) wt% Ti_5Sn_3 and $TiNiSn_{1.0}$ contains 4.7(2) wt% $TiNi_{1.76(2)}Sn$ and 2.3(1) wt% Ti_5Sn_3, suggesting further TiSn impurities in both samples.

The possibility of Ti-Sn inversion was first explored. Keeping the Ni occupancy of the *4c* site = 1, and allowing some atoms to swap atomic positions produced χ^2 = 7.0, in line with the best fit model. However, 10% inversion was required to reach this value. This is a very large degree of inversion, and is unrealistic given the large degree of covalent bonding in the structure.[56] This conclusion is supported by computational studies,

which predict inversion on the NaCl-type sublattice to be unfavourable.[57] Inversion effects involving the Ni site were also investigated, but there was no evidence to support either Ti-Ni or Ni-Sn inversion.

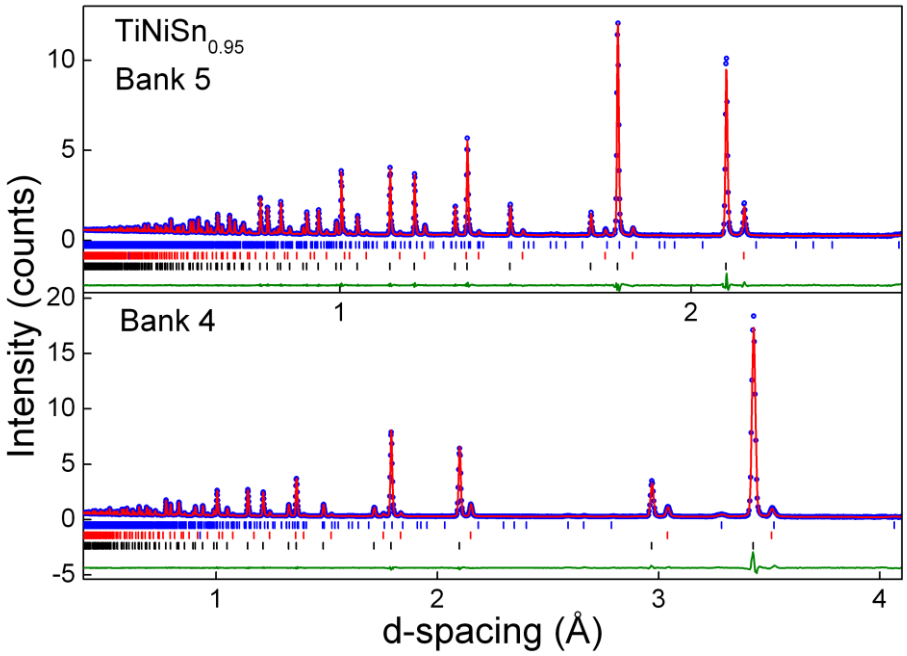

Figure 3.5: Rietveld refinement of a neutron powder diffraction pattern collected for $TiNiSn_{0.95}$. Blue circles represent the collected data, the red line is the calculated pattern and the green line is the difference. Black (lower) tickmarks are reflection markers for TiNiSn, red (middle) markers are for a full-Heusler impurity phase and the blue markers (upper) represent Ti_5Sn_3.

Refinement of the Ni occupancy, fixing Ti and Sn to their nominal values, indicates a composition of $TiNi_{1.118(3)}Sn_{0.95}$, with $\chi^2 = 9.6$. This is clearly not realistic, as the Ni site is over-occupied. The obvious place that can accommodate excess Ni is the nominally vacant tetrahedral *4d* site (M2). Fixing all other site occupancies to their nominal values and allowing the Ni occupancy to refine freely on this *4d* site yields $TiNiSn_{0.95}Ni_{0.049(1)}$, $\chi^2 = 7.6$. Refinement of the Sn occupancy reduces χ^2 further, to 7.0 and yields a composition of $TiNiSn_{0.991(2)}Ni_{0.055(1)}$, indicating that the nominal Sn deficiency does not persist. This data is presented in Table 3.2 and the fit is displayed in Figure 3.5. This model is more likely than Ti-Sn inversion, given that only a 5.5% Ni excess is required, compared with over 10% inversion. Furthermore, the computational work indicates that

Ni on the *4d* site is the lowest energy defect.[106] Excess Ni in the structure is also supported by the observation of TiSn binary impurities within the sample and is in-keeping with the synthesis, which proceeds via a full-Heusler phase (see section 3.3). This may also explain the observation of two peaks for each reflection in the X-ray diffraction profile, as additional Ni within the structure would cause expansion of the lattice. This will be discussed more fully in Section 3.6.1.

3.4.2 $TiNiSn_{1.0}$

Investigation of the site occupancies in this sample was done in an analogous manner to $TiNiSn_{0.95}$. The nominal composition yields $\chi^2 = 8.2$, while Ti-Sn inversion produces $\chi^2 = 6.6$ for 5% inversion. The excess Ni model achieves $\chi^2 = 6.4$ for a composition of $Ti_{1.002(2)}NiSn_{1.000(2)}Ni_{0.036(3)}$. The fit is presented in Figure 3.6.

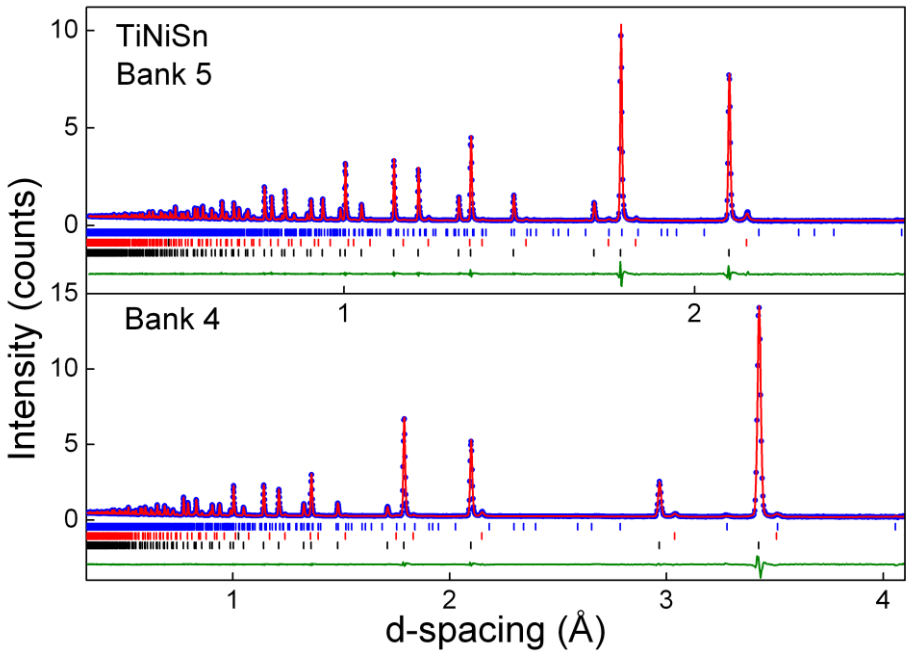

Figure 3.6: Rietveld refinement to neutron powder diffraction pattern collected for $TiNiSn_{0.95}$. Blue circles represent the collected data, the red line is the calculated pattern and the green line is the difference. Black (lower) tickmarks are reflection markers for TiNiSn, red (middle) are for the full-Heusler impurity phase and blue tickmarks (upper) represent Ti_5Sn_3.

The improvement in χ^2 is small, but in conjunction with the observation of TiSn binaries, the smaller perturbation to the structure (3.5% excess Ni vs. 5% inversion) and energy calculations that predict occupation of the interstitial site to be more energetically favourable than inversion on the TiSn sublattice,[57] excess Ni occupying the vacant tetrahedral site in the half-Heusler structure is the most likely model.

3.5 Thermoelectric Properties

3.5.1 $Ti_{1-x}Zr_xNiSn_{0.95}$

All thermoelectric property measurements undertaken for these samples are presented in Figure 3.7. The Seebeck coefficients (S) of the $Ti_{1-x}Zr_xNiSn_{0.95}$ samples were found to be negative, indicating n-type conduction, as expected. The temperature dependence of each sample is similar and all samples reach a maximum S = -175 $\mu V\ K^{-1}$ above 500 K. Resistivity (ρ) measurements indicate semiconducting behaviour in all samples. The magnitudes of ρ are again similar for all samples, with a minimum of 1 mΩ cm achieved at high temperatures in each case. Analysis of the power factor (S^2/ρ) shows a maximum value of 3.5 mW $m^{-1}\ K^{-2}$ for $TiNiSn_{0.95}$ at 650 K. S^2/ρ_{max} shifts to higher temperatures as x increases. $Ti_{0.95}Zr_{0.05}NiSn_{0.95}$ reaches 3 mW $m^{-1}\ K^{-2}$ at 700 K and $Ti_{0.5}Zr_{0.5}NiSn_{0.95}$ reaches the same value at 740 K.

Thermal conductivity measurements of the fully dense samples indicate $\kappa \approx 4$ W $m^{-1}\ K^{-1}$ for all samples, including $TiNiSn_{0.95}$. This appears to be independent of temperature, within the error of the measurement. Using the Wiedemann-Franz Law (Equation (1.14)), it was possible to calculate κ_{el}. This was subsequently subtracted from the total thermal conductivity to produce κ_{lat}, which is plotted in Figure 3.7(d). As may be expected, given the similar behaviour and magnitudes of the resistivity for these samples, κ_{lat} values are also very similar for the whole series.

A κ value of 4 W $m^{-1}\ K^{-1}$ is typical for samples containing mixtures of Ti, Zr and Hf on the X-site, where mass fluctuation effects hinder phonon flow and reduce κ.[82] $Ti_{0.5}Zr_{0.5}NiSn_{0.95}$ therefore behaves as expected but $\kappa = 4$ W $m^{-1}\ K^{-1}$ is exceptionally low for $TiNiSn_{0.95}$. Reported values for TiNiSn samples are generally between 7 and 10 W $m^{-1}\ K^{-1}$ at room temperature,[67, 70, 82, 112] indicating a different mechanism for

reducing κ is present in this case. This may be linked to the additional Ni found in this sample.

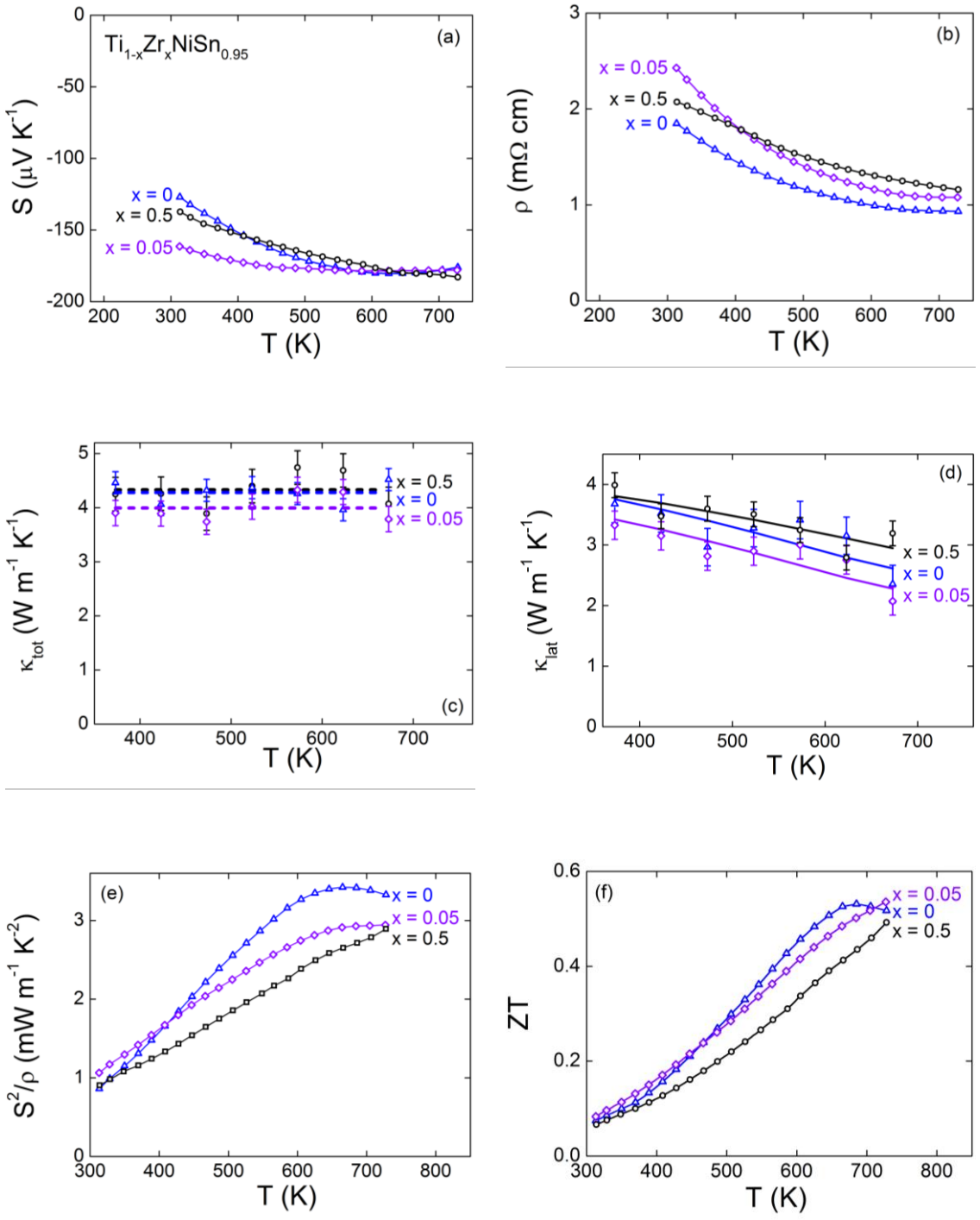

Figure 3.7: Temperature dependence of (a) Seebeck coefficients (S), (b) resistivity (ρ), (c) thermal conductivity (κ_{tot}), (d) lattice thermal conductivity (κ_{lat}), (e) power factor (S^2/ρ) and (f) ZT for the arc-melted $Ti_{1-x}Zr_xNiSn_{0.95}$ samples ($0 \leq x \leq 0.5$).

The thermoelectric properties measured for this series produce a maximum ZT of 0.5 at 700 K for the $Ti_{1-x}Zr_xNiSn_{0.95}$ samples, where x = 0, 0.05 and 0.5. This exceeds the values reported for many samples which utilise substitutions on the X site to optimise thermoelectric properties.[82, 109] The occurrence of ZT = 0.5 for $TiNiSn_{0.95}$ is exceptional, for a nominally non-doped material. Maximum values previously reported for this composition are approximately 0.3-0.4, so the value obtained here offers a significant improvement.[70, 80, 82]

3.5.2 $TiNiSn_{1.0}$

The results of the thermoelectric property measurements carried out for this sample are presented in Figure 3.8. Results for $TiNiSn_{0.95}$ are also presented in this plot for comparison. The Seebeck coefficient for $TiNiSn_{1.0}$ is negative but is larger in magnitude than $TiNiSn_{0.95}$, with a maximum value of -300 $\mu V\ K^{-1}$ between 300 and 400 K, compared to -195 $\mu V\ K^{-1}$ at 600 K. The temperature dependences of each sample also differ from one another. S(T) for $TiNiSn_{0.95}$ increases in magnitude as the temperature is increased and plateaus at approximately 600 K, while $TiNiSn_{1.0}$ has a S(T) that remains almost independent of temperature up to 500 K before decreasing in magnitude very slightly. This suggests that $TiNiSn_{0.95}$ is electron doped in comparison with $TiNiSn_{1.0}$. A thermoelectric material enters a 'compensated' region above a given temperature, where minority carriers begin to significantly contribute to the overall conduction, and this results in a decrease in S. $TiNiSn_{0.95}$ appears to enter the compensated region around 700 K while in $TiNiSn_{1.0}$, this occurs earlier, around room temperature. This, in conjunction with the absolute values of S, indicates that $TiNiSn_{0.95}$ contains a larger number of charge carriers than $TiNiSn_{1.0}$, thus this sample appears to be electron doped in comparison. Inspection of the resistivity values for $TiNiSn_{1.0}$ indicates semi-conducting behaviour and the ρ-values double those for $TiNiSn_{0.95}$, providing further evidence for increased carrier doping in $TiNiSn_{0.95}$, with respect to $TiNiSn_{1.0}$.

Mainly due to its large S-values, $TiNiSn_{1.0}$ exhibits a maximum $S^2/\rho = 4\ mW\ m^{-1}\ K^{-2}$, just below 700 K. In comparison, $TiNiSn_{0.95}$ reaches a maximum of 3.5 $mW\ m^{-1}\ K^{-2}$ at 600 K and decreases thereafter. Thermal conductivity values for $TiNiSn_{1.0}$ are very similar to those for $TiNiSn_{0.95}$, with κ = 4.5 $W\ m^{-1}\ K^{-1}$ and 4.2 $W\ m^{-1}\ K^{-1}$, respectively. The difference is within the error of the measurement. Calculation of ZT from these measurements yields a maximum value of 0.6 at 700 K for $TiNiSn_{1.0}$, indicating that the

results found in the $TiNiSn_{0.95}$ sample were not simply an aberration. The similar magnitude of ZT in these samples suggests that a common feature between them is responsible for the exceptional behaviour.

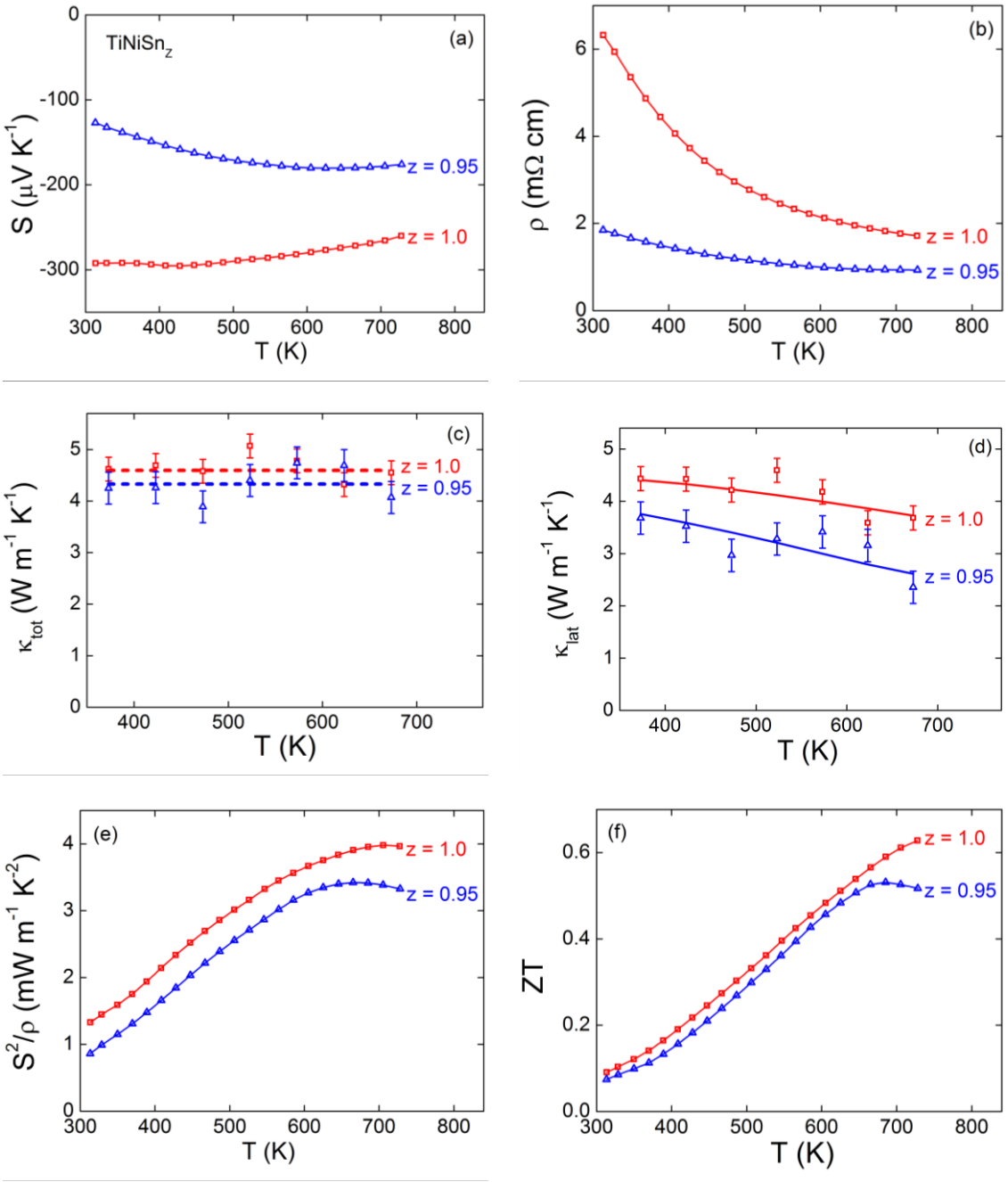

Figure 3.8: Temperature dependence of (a) Seebeck coefficients (S), (b) resistivity (ρ), (c) thermal conductivity (κ_{tot}), (d) lattice thermal conductivity (κ_{lat}), (e) power factor (S^2/ρ) and (f) ZT for $TiNiSn_{0.95}$ and $TiNiSn_{1.0}$.

3.6 Discussion

3.6.1 $TiNiSn_{0.95/1.0}$

$TiNiSn_{0.95}$ and $TiNiSn_{1.0}$ show exceptional thermoelectric properties, culminating in maximum ZT values of 0.5 and 0.6, respectively. The power factor values are large, but the high ZT is mainly due to very low values of thermal conductivity. The high ZT-value in each of these two samples coincides with the observation of excess Ni within their structures. In both cases, using neutron powder diffraction, an additional amount of Ni was located on the normally vacant M2 site in the half-Heusler structure to produce a $TiNi_{1+y}Sn$ composition, where y = 0.055 for the nominal $TiNiSn_{0.95}$ sample and y = 0.035 in $TiNiSn_{1.0}$. The X-ray powder diffraction data support this conclusion. As previously described, two phases with differing lattice parameters were required to adequately fit the peak shapes for each sample. Assuming a solid solution exists between TiNiSn and $TiNi_2Sn$ (the full-Heusler, where all the tetrahedral holes are filled), and that Vegard's law is obeyed, the refined lattice parameters for the nominal $TiNiSn_{0.95}$ sample give compositions of TiNiSn and $TiNi_{1.1}Sn$, with weight fractions of 0.357 and 0.643, respectively (Table 3.1). This results in an average composition of $TiNi_{1.05}Sn$. Similar treatment of the $TiNiSn_{1.0}$ sample yields an average composition of $TiNi_{1.03}Sn$.

Analysis of the thermoelectric properties for these samples shows that the rise in the level of excess Ni coincides with a reduction in lattice thermal conductivity, as illustrated in Figure 3.9. The y = 0 point has been taken from the literature and it can be seen that there is a systematic reduction in κ_{lat} as y increases.[70] A 40% reduction is achieved for a 5.5% excess.

It is not yet clear if these samples also contain full-Heusler nano-inclusions and it is therefore not possible to determine the exact cause of the reduction in thermal conductivity. Electron microscopy analysis of the $TiNiSn_{0.95}$ and $TiNiSn_{1.0}$ samples is required to search for these inclusions. Until then, it is not possible to unambiguously attribute the reduction in the lattice thermal conductivity in these samples to a particular structural feature.

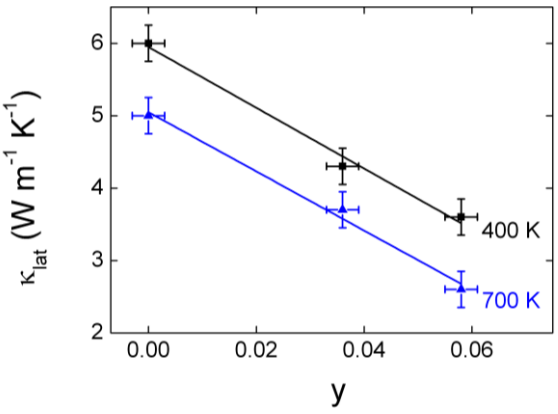

Figure 3.9: Lattice thermal conductivity (κ_{lat}) as a function of excess Ni (y) in $TiNi_{1+y}Sn$, at 400 K and 700 K.

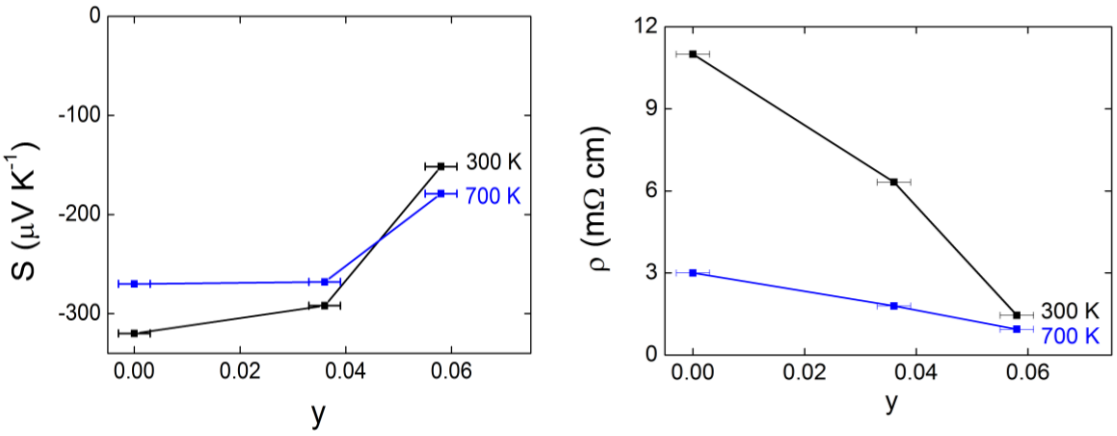

Figure 3.10: (a) Seebeck coefficient (S) and (b) resistivity (ρ) as a function of excess Ni (y) in $TiNi_{1+y}Sn$, at 300 K and 700 K.

As mentioned in Section 3.5.2, there is an apparent carrier doping effect in $TiNiSn_{0.95}$, with respect to $TiNiSn_{1.0}$. If this effect is linked to the additional Ni in the structure, it follows that the $TiNiSn_{1.0}$ sample is electron doped compared to a sample containing no excess Ni. This is confirmed in Figure 3.10, where a clear reduction in the magnitudes of both the S and ρ values occurs as y is increased. The excess Ni in the structure therefore appears to subtly electron dope TiNiSn. However, caution must be exercised here, as the presence of metallic impurities (Ti_5Sn_3 and $TiNi_2Sn$) could also be responsible for these effects. The amount of impurity phase present in the samples also rises as y increases and so it is difficult to discount the possibility that this is causing the apparent doping effect.

3.6.2 $Ti_{1-x}Zr_xNiSn_{0.95}$ (x > 0)

$Ti_{0.5}Zr_{0.5}NiSn_{0.95}$ shows significant peak broadening and splitting of the reflections in the powder X-ray diffraction pattern. Analysis of the diffraction data revealed the existence of an almost continuous distribution of $Ti_{1-x}Zr_xNiSn_{0.95}$ phases, with differing values of x. It is impossible to say, based on the collected X-ray data, whether excess Ni is present in this sample, as any broadening of the peaks that this may cause is masked by the larger effect that the variable phase distribution has on the Bragg reflections. Neutron diffraction experiments are required to explore this as a possibility. $Ti_{0.95}Zr_{0.05}NiSn_{0.95}$ exhibits only a small peak splitting and it is unclear whether this is due to excess Ni or multiphase behaviour. Comparison of these samples is therefore difficult.

It is very difficult to unambiguously attribute the relatively low lattice thermal conductivity to one feature in these materials. As already discussed, excess Ni in TiNiSn appears to cause a reduction in κ and it is not possible to discount the possibility that this may also play a role in the Zr-doped samples. The multiphase behaviour (e.g. $0.255 \leq x \leq 0.77$ and $0.91 \leq x \leq 0.93$ in '$Ti_{0.5}Zr_{0.5}NiSn_{0.95}$') may also play a role, depending on the arrangement of these phases within the sample. If it is on an appropriate length scale, significant scattering of the phonons could occur at the interfaces between areas with differing compositions. Finally, both mass difference and micro-strain may reduce κ. It is impossible to de-convolute these at present. The only indication of what may be the dominant effect in reduction of the thermal conductivity may come from comparison of the two Zr-doped samples. If mass fluctuation and strain effects due to Zr substitutions were solely responsible for lowering κ, it might be expected that the larger effect would be observed in $Ti_{0.5}Zr_{0.5}NiSn_{0.95}$, given that it has a much larger degree of substitution. This argument may also be applied to the multiphase behaviour. This is clearly more prevalent in $Ti_{0.5}Zr_{0.5}NiSn_{0.95}$, with a larger range of different compositions identified. The spread in $Ti_{0.95}Zr_{0.05}NiSn_{0.95}$ is much smaller, with only two identifiable phases present. It may therefore be expected that phonons should be more effectively scattered in $Ti_{0.5}Zr_{0.5}NiSn_{0.95}$. Again, this is clearly not the case as $\kappa \approx 4$ W m^{-1} K^{-1} for each sample. This suggests that excess Ni is perhaps the real cause of lowered thermal conductivity in these samples. If it is the dominant effect and similar quantities of excess Ni are present in these samples, the almost identical values

observed for thermal conductivity make sense. Unfortunately, based on the collected data it is not possible to identify excess Ni within the Zr-doped samples and no unambiguous conclusion can be drawn at present.

3.7 Conclusions

This initial foray into the improvement of half-Heusler materials for thermoelectric applications has uncovered a multitude of interesting features. Excess Ni has been identified in $TiNiSn_{0.95}$ and $TiNiSn_{1.0}$. This was found to occupy the vacant tetrahedral sites in the half-Heusler structure. Significant multiphase behaviour was also discovered in $Ti_{0.5}Zr_{0.5}NiSn_{0.95}$, with compositions ranging between x = 0.255 and 0.93 existing within the sample. These structural features do not appear to diminish the naturally excellent electronic properties of the XNiSn-based thermoelectrics, and thermal conductivity values were found to be 4 W m^{-1} K^{-1} for all samples. This leads to ZT values of around 0.5 at 600 K for the nominal $Ti_{1-x}Zr_xNiSn_{0.95}$ samples and 0.6 at 700 K for $TiNiSn_{1.0}$. These are good values for the Zr-doped samples and are exceptional for the otherwise non-doped $TiNiSn_{0.95/1.0}$ samples. The excellent properties of the TiNiSn samples appear to be linked to the amount of excess Ni present in the samples, though it is not yet clear by which mechanism phonon flow is disrupted. Electron microscopy analysis is vital in order to determine the distribution of Ni within the sample. It is not clear what effect the multiphase behaviour has on the thermoelectric properties and further, systematic investigation of this effect is required. Also worthy of further investigation is the presence of excess Ni in Zr-doped samples. Elemental mapping and neutron powder diffraction experiments are required to fully analyse these structures, to more fully understand the cause and effect of the structural features uncovered. The discoveries made in the analysis of the samples presented in this chapter therefore form the basis of the work in the following two Chapters. Chapter 4 further explores multiphase behaviour in $Ti_{1-x}Zr_xNiSn$ samples, while Chapter 5 offers a systematic study of the effect of excess metals in TiNiSn-based half-Heuslers.

Chapter 4 – Multiphase Behaviour and Interstitial Ni in $X_{1-x}X'_xNiSn$ (X = Ti, Zr, Hf)

4.1 Introduction

The thorough investigation of $Ti_{1-x}Zr_xNiSn$ reported herein was motivated by the significant promise that Ti-containing half-Heusler thermoelectric materials show, in conjunction with the limited information available on their structure.[66, 67, 77-79] The work, presented in Chapter 3, revealed complex multiphase behaviour in arc-melted $Ti_{0.5}Zr_{0.5}NiSn_{0.95}$. This effect has been systematically investigated for the $Ti_{1-x}Zr_xNiSn$ series ($0 \leq x \leq 1$), and the possibility of the presence of excess Ni within this series has also been explored, as a result of the discovery of interstitial Ni in TiNiSn samples, reported in Chapter 3. This investigation has also been extended to HfNiSn, $Ti_{0.5}Hf_{0.5}NiSn$ and $Zr_{0.5}Hf_{0.5}NiSn$ due to the significant impact these structural features may have on the thermoelectric properties.

4.2 Synthesis

Two preliminary $Ti_{1-x}Zr_xNiSn_{0.95}$ series were prepared to establish an optimum synthesis protocol. A 5% Sn deficiency was used in order to prevent formation of Sn impurities found in samples where $x > 0.5$. 3 g samples for these series were prepared by standard solid state reactions. Stoichiometric quantities of the elemental starting materials were ground together and pressed into pellets, then vacuum sealed in quartz tubes. Samples were annealed at 900 °C for an initial 24 hour period. Samples were then reground and pressed. One series was then annealed for a further 3 days, and the other for 6 weeks. Several $Ti_{0.5}Zr_{0.5}NiSn_{0.95}$ samples were also prepared on a 3 g scale, as described above, but with secondary annealing periods ranging from 1 - 4 weeks. A $Ti_{1-x}Zr_xNiSn$ ($0 \leq x \leq 1$) series was subsequently prepared, where formation of Sn impurities was circumvented by wrapping the pellets in Ta foil, prior to vacuum sealing them in quartz tubes. Samples were otherwise prepared as described above, and annealed at 900 °C for 24 hours, then two weeks. HfNiSn, $Ti_{0.5}Hf_{0.5}NiSn$ and $Zr_{0.5}Hf_{0.5}NiSn$ samples were prepared in the same manner. All samples were cooled by removal from the furnace at 900 °C.

Bars were cut from all sample pellets using a low speed diamond saw, for electronic property measurements. 13 mm disks were prepared for some samples so that thermal conductivity measurements could be undertaken. The remainder of the samples were ground into fine powders for diffraction experiments.

In addition to this, densification techniques have been explored and optimisation of the thermoelectric properties has been attempted by varying the Ti:Zr ratio and introducing Sb onto the Sn site. For this purpose a $Ti_{0.5}Zr_{0.5}NiSn_{1.0-y}Sb_y$ ($0 < y \leq 0.05$) was also prepared, as described above.

4.3 $Ti_{1-x}Zr_xNiSn$ ($0 \leq x \leq 1$)

4.3.1 X-ray Powder Diffraction

X-ray powder diffraction patterns collected for the series are presented in Figure 4.1. Patterns for TiNiSn and ZrNiSn exhibit very sharp peaks, while those for the intermediate samples display multiple broad peaks for each Bragg position.

Le Bail fits for each of the diffraction patterns were performed and confirmed the end members to be single phase. Lattice parameters and fit statistics are presented in Table 4.1. The peak shapes of the intermediate samples could be adequately modelled by using 3-4 half-Heusler phases, with differing lattice parameters. This suggests the presence of multiple $Ti_{1-x}Zr_xNiSn$ phases, with varying values of x, within each sample. A representative fit to the pattern collected for $Ti_{0.5}Zr_{0.5}NiSn$ is presented in Figure 4.2, and a close-up of the (422) peak is provided in the inset. The close-up clearly depicts the 4 different half-Heusler phases used, the lattice parameters and molar fractions of which can be found in Table 4.1. Similar fits were used for the x = 0.25 and 0.75 samples.

Rietveld refinements of these patterns were attempted in order to refine the site occupancies and determine the value of x of each refined phase. However, this proved to be impossible so only estimates of x could be determined by evaluating the lattice parameters, using Vegard's law, as previously described in Chapter 3. The calculated x-values were then combined with the weight fractions of each phase to produce an average composition for each sample. These values are presented in Table 4.1, and it

may be observed that they closely match those of the nominal compositions, demonstrating that no change to the composition occurs during the synthesis.

Table 4.1: Nominal composition, lattice parameter (a), Vegard composition (x_i), compositional spread (Δx_i), molar percentage (mol%), average composition (x_{avg}) and goodness-of-fit (χ^2) for $Ti_{1-x}Zr_xNiSn$, as determined by Le Bail analysis of X-ray diffraction data.

x,y	a (Å)	x_i	Δx	mol%	x_{avg}	χ^2
0	5.9300(1)	0	0	100	0	1.9
0.25	5.9340(1)	0.02(1)	0	1.4(7)		
	5.9724(1)	0.24(1)	0.17(1)	71.4(7)	0.27(1)	1.9
	5.9923(2)	0.35(1)	0.16(1)	27.2(7)		
0.5	5.9883(2)	0.33(1)	0.18(1)	17.3(2)		
	6.0189(2)	0.50(1)	0.18(1)	26.7(6)	0.52(1)	2.3
	6.0385(1)	0.61(1)	0.17(1)	55.4(2)		
	6.1024(3)	0.97(1)	0	6.6(6)		
0.75	5.9646(2)	0.20(1)	0.24(1)	7.9(2)		
	6.0662(1)	0.77(1)	0.18(1)	60.4(2)	0.78(1)	2.1
	6.1022(1)	0.97(1)	0.06(1)	31.7(2)		
1.0	6.1079(1)	1	0	100	1	2.1

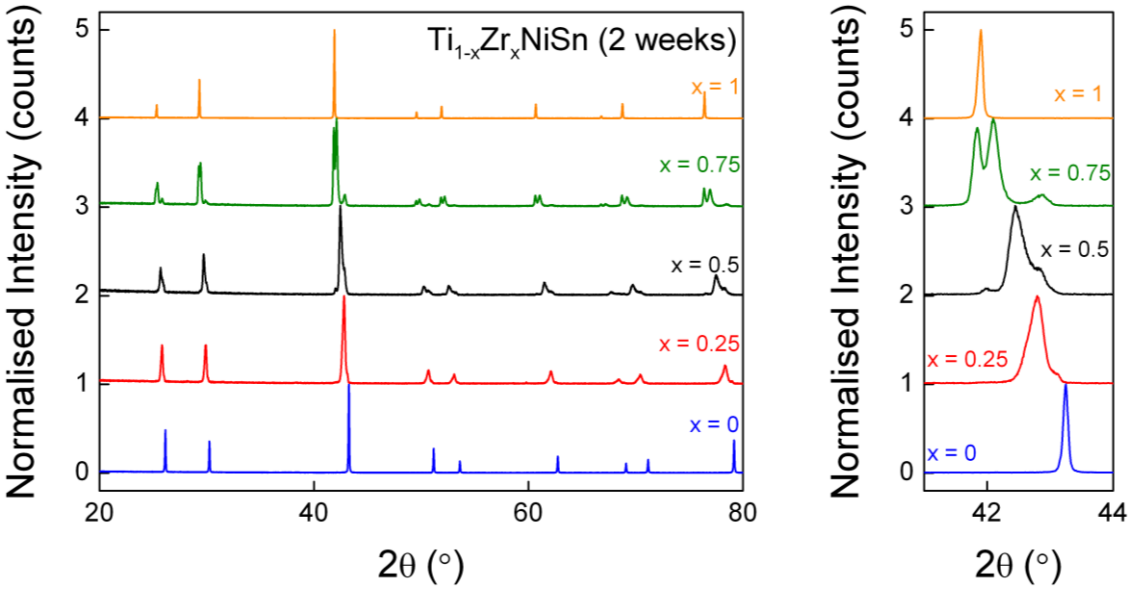

Figure 4.1: X-ray diffraction pattern for the $Ti_{1-x}Zr_xNiSn$ series ($0 \leq x \leq 1$), and close up of the (220) peak for each sample.

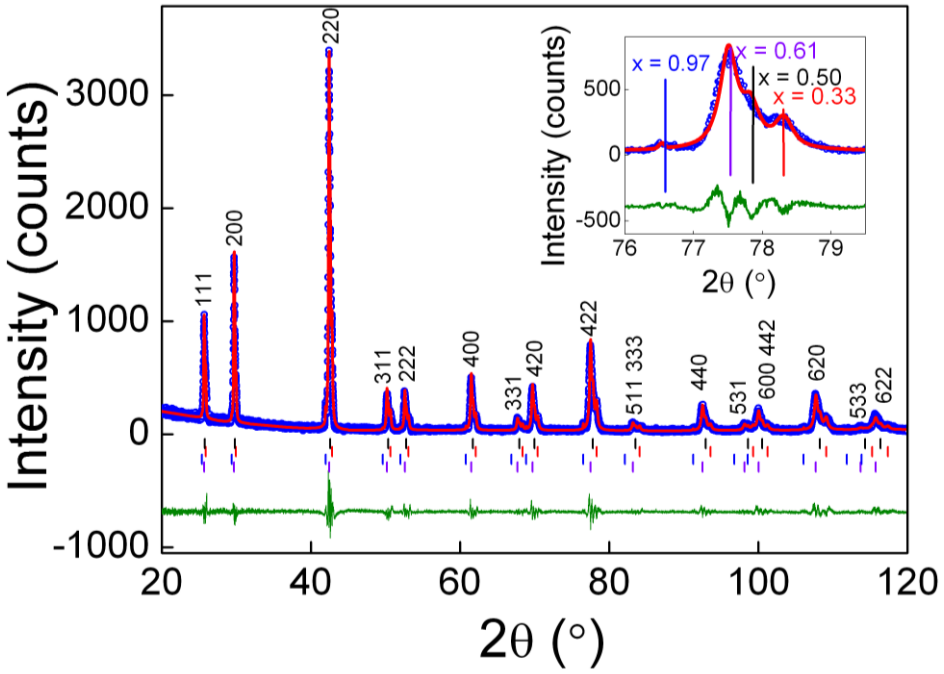

Figure 4.2: Le Bail fit to X-ray powder diffraction data for $Ti_{0.5}Zr_{0.5}NiSn$. Blue circles are the collected data, the red line is the calculated fit and the green line is the difference curve. Tickmarks correspond to the different half-Heusler phases used to fit the pattern. Inset: close up of the (422) peak with tickmarks indicating each of the $Ti_{1-x}Zr_xNiSn$ phases used to fit the pattern.

In addition to the peak splitting found in these samples, there is also a significant degree of peak broadening, indicating further compositional variation. This is exactly analogous to the peak broadening observed in the arc-melted $Ti_{0.5}Zr_{0.5}NiSn$ sample and has therefore been treated in the same manner. It was sufficient to fit the peak shapes using only one Gaussian and one Lorentzian profile parameter. In this case, the end members were found to have GW = 0.12° and LY = 0.05°. This was taken to represent both the instrumental broadening and broadening in the sample that is not due to the mixing of Ti^{4+} and Zr^{4+}. LY was then allowed to refine freely, while GW was kept fixed to 0.12° for the $x \neq 0,1$ samples. The LY value is related to the strain which is, in turn, relatable to $\Delta d/d$ and Δx, as is set out in detail in Chapter 3. The calculated Δx values for each phase in each sample are summarised in Table 4.1.

Each modelled phase therefore has a calculated x value (x_i) and an associated compositional spread (Δx_i). $Ti_{0.5}Zr_{0.5}NiSn$, for example, was modelled by four separate

half-Heusler phases, each of which has a large associated further spread in x-values. A wide range of x-values of almost 0.5 covering $0.24 \leq x \leq 0.7$ are therefore contained within this sample in an almost continuous manner, as represented schematically in Figure 4.3. $Ti_{0.75}Zr_{0.25}NiSn$ contains $0.16 \leq x \leq 0.43$ ($\Delta x \approx 0.3$, Table 4.1). The x = 0.75 sample does not have a semi-continuous distribution but contains phases spanning $0.08 \leq x \leq 0.32$, $0.68 \leq x \leq 0.86$ and $0.94 \leq x \leq 1.0$.

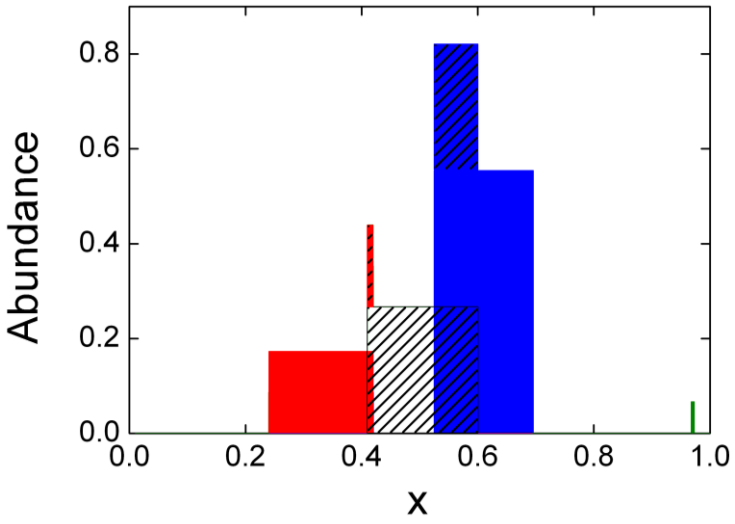

Figure 4.3: Schematic representation of the phase distribution in $Ti_{0.5}Zr_{0.5}NiSn$.

The two $Ti_{1-x}Zr_xNiSn_{0.95}$ series, which were prepared by annealing for 3 days and 6 weeks, show very similar multiphase behaviour to the nominally stoichiometric samples. Data for these series can be found in Appendix 1. Samples where $x \neq 0,1$ were each fitted using 3-4 phases which were found to exhibit signs of further compositional variation. The only discrepancy was that the overall spread in x values is somewhat smaller than observed in the $Ti_{1-x}Zr_xNiSn$ series, e.g. $\Delta x = 0.3$ for $Ti_{0.5}Zr_{0.5}NiSn_{0.95}$ compared with 0.5 for $Ti_{0.5}Zr_{0.5}NiSn_{1.0}$.

One major discrepancy between the two series was discovered, however, in analysis of the $TiNiSn_{0.95}$ sample. $TiNiSn_{1.0}$ was determined to be single phase due to the sharp, symmetric nature of the Bragg reflections in the diffraction pattern. However, all the peaks for the Sn-deficient $TiNiSn_{0.95}$ contain a subtle shoulder, as illustrated by Figure 4.4. The peak shape could therefore only be adequately modelled by using two half-Heusler phases, with different lattice parameters, as was previously observed in the arc-

melted TiNiSn samples. In the arc-melted samples, the peak broadening was explained by the presence of excess Ni within the half-Heusler structure, which was later confirmed by neutron powder diffraction experiments. Treating the current sample in the same manner, an estimate of the amount of excess Ni present in $TiNiSn_{0.95}$ may be made using the lattice parameters of the two phases and Vegard's law. This yields two phases with the compositions TiNiSn and $TiNi_{1.02}Sn$. Combination with their relative phase fractions yields an average composition of $TiNi_{1.01}Sn$. It is possible that excess Ni is present in all the prepared $Ti_{1-x}Zr_xNiSn$ samples, however any peak splitting or broadening caused by this effect is masked by the larger effect caused by mixing Ti^{4+} and Zr^{4+} on the same site and so cannot be detected using X-ray powder diffraction.

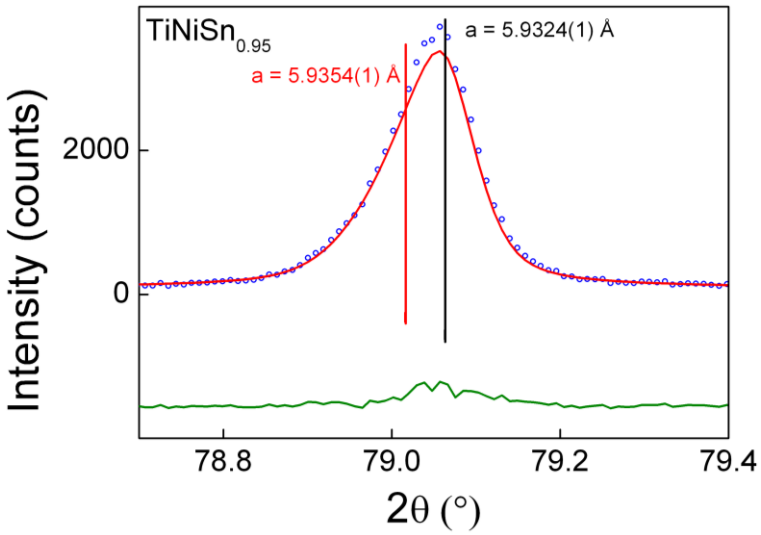

Figure 4.4: Close-up to the Le Bail fit for the (422) peak of $TiNiSn_{0.95}$. Blue circles are the collected data, the red line is the calculated fit and the green line is the difference curve. Tickmarks correspond to the different half-Heusler phases used to fit the pattern.

4.3.2 EDX Analysis

This was carried out only for the $Ti_{0.5}Zr_{0.5}NiSn$ sample. A low magnification image of the prepared FIB (fast-ion-beam) lamella is presented in Figure 4.5. From this, the presence of several particles may be observed. Uneven thinning during ion polishing has caused these particles to separate somewhat from one another. EDX spectroscopic analysis was focussed on four ~ 500 x 500 nm^2 areas, as indicated in Figure 4.5.

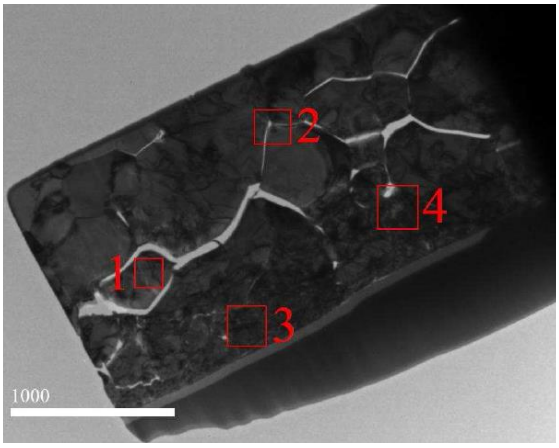

Figure 4.5: FIB lamella cut from a sintered piece of $Ti_{0.5}Zr_{0.5}NiSn$ sample. The scale bar is approximately 2.5 μm.

Figure 4.6 comprises dark field scanning TEM (STEM) images with contrast dominated by thickness, mass and diffraction effects in the left hand column and 'spectrum images' of each region, acquired by collecting EDX spectra from 10 × 10 nm^2 pixels across each area, on the right. Background-subtracted Zr-K, Sn-L, Ti-K and Ni-K EDX peaks were integrated to generate pixel-by-pixel composition maps using (standard-less) Cliff-Lorimer analysis, a protocol that is sufficient to reveal relative composition variations within the lamella but can be less reliable for absolute quantification.[136]

Clear differences were found between the 4 regions under investigation. Grain boundaries are evident in Figure 4.6(a), due to the observation of brighter bands in the STEM image. However, this area appears largely homogeneous, despite the diffraction evidence for the presence of multiple phases of differing Ti:Zr ratios.

Figure 4.6(b) shows no statistically significant compositional fluctuations across the area, even at the grain boundaries, for any of the constituent elements. There is also no indication of nano-inclusions, such as sharp spots or lines, which have been observed in samples containing excess Ni. This observation holds true, even when higher resolution images at shorter length scales were probed.

The area depicted in Figure 4.6(c-d) offers similar findings. A small Ti-impurity was observed but apart from this, the area - which straddles three distinct particles - appears homogeneous. There is no indication that the Ti:Zr ratio varies significantly within or between the particles in this area.

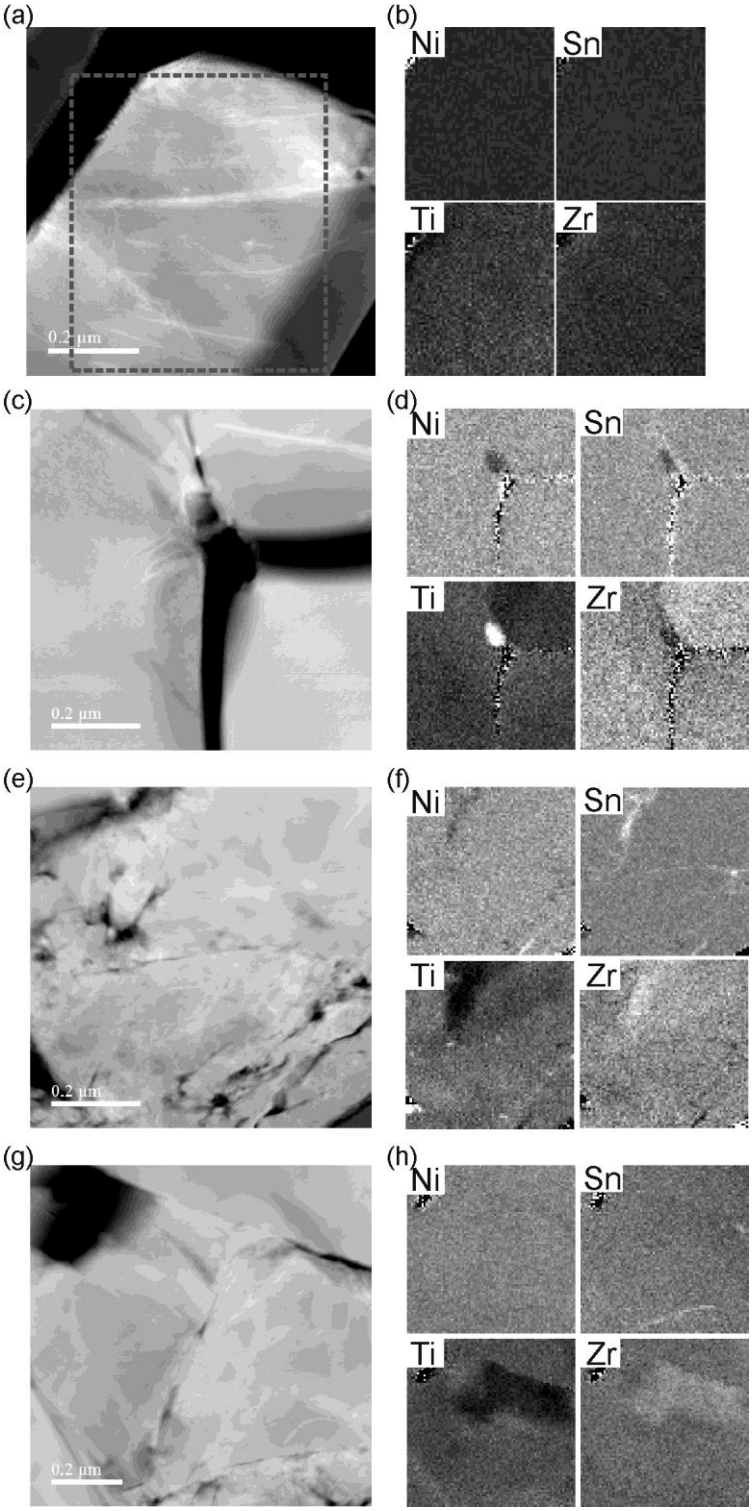

Figure 4.6: Left hand column: dark field STEM images, right hand column: 'spectrum' images for area 1 (a-b), area 2 (c-d), area 3 (e-f) and area 4 (g-h), as identified in Figure 4.5. Brighter areas in the images indicate increased elemental concentration in the given area.

Figure 4.6(e) and (f) are less uniform. Black-white contrast variations in the STEM image indicate that the powdered material has not fully fused and re-crystallised to form uniform particles. There are also regions that contain an obvious Ti-depletion and these are coincident with Zr-rich areas. Narrow bright bands in the Sn map also suggest Sn segregation to grain boundaries, which has been reported for these materials in the past. Figure 4.6(g-h) shows this area to be similar to that portrayed in Figure 4.6(e and f), with a clear Ti-poor/Zr-rich area and some bright Sn bands. The regions with differing Ti:Zr ratios cover relatively large areas and differ from the surrounding areas by less than 10 atomic %.

Despite the different features observed in the four areas, the overall compositions are all very similar. A simple analysis yields typical atomic ratios of 0.13 (Ti), 0.26 (Zr), 0.29 (Ni) and 0.32 (Sn), consistent with the approximate composition $Ti_{0.33}Zr_{0.67}NiSn$. This measured composition is subject to a 10-15% error as the sample could not be thinned enough to allow high-resolution images to be obtained. Nonetheless, it is well within the compositional range indicated by X-ray diffraction and the Ti-deficient nature of this area implies the existence of complementary Ti-rich/Zr-poor particles elsewhere in the sample.

This analysis has therefore revealed two types of particle within this sample. Some appear to be uniform with a composition that may, or may not, match that of the overall pellet. Other particles appear to contain some variation in composition on a 100 nm length scale. These must be further from thermodynamic equilibrium. No evidence for smaller, sub-10 nm inclusions was found. These results are consistent with large-scale multiphase behaviour and continuous compositional spread, as was indicated by diffraction data.

4.3.3 Thermoelectric Properties

Due to the low density of these samples, determination of the absolute value of the thermal conductivity is difficult. It was also only possible to acquire data for two $Ti_{0.5}Zr_{0.5}NiSn_{0.95}$ samples, prepared by annealing for 3 days and 6 weeks, respectively. These results will be discussed fully in Section 5.3.5.

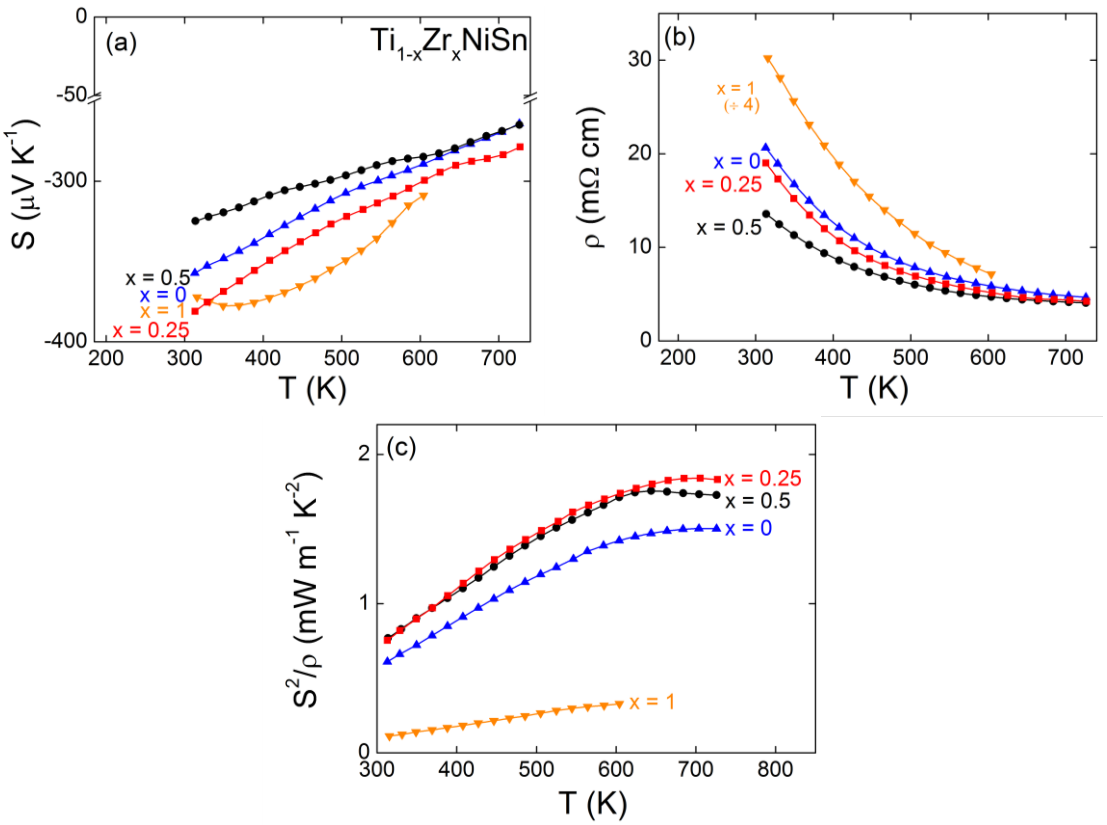

Figure 4.7: Temperature dependence of (a) Seebeck coefficient (S), (b) resistivity (ρ) and (c) power factor (S^2/ρ) for $Ti_{1-x}Zr_xNiSn$.

The temperature dependences of the Seebeck coefficient (S), resistivity (ρ) and power factor (S^2/ρ) are presented in Figure 4.7. TiNiSn, $Ti_{0.75}Zr_{0.25}NiSn$ and $Ti_{0.5}Zr_{0.5}NiSn$ were measured over the temperature range 300 – 730 K. ZrNiSn was found to degrade above 600 K, so values for this sample are reported only up to this value. As previously described in Chapter 4, TiNiSn is a semiconductor with S = -350 μV K^{-1} at room temperature, decreasing in magnitude almost linearly to -275 K at 730 K. $Ti_{0.75}Zr_{0.25}NiSn$ and $Ti_{0.5}Zr_{0.5}NiSn$ show very similar behaviour, with respect to both the temperature dependence and magnitude. The ZrNiSn sample has similar values but different temperature dependence. S increases to a maximum of -375 μV K^{-1}, before decreasing to -300 μV K^{-1} at 600 K.

The ρ(T) values are consistent with semiconducting behaviour. At room temperature, ρ decreases as x is increased ($0 \leq x \leq 0.5$). For example ρ = 20 mΩ cm for TiNiSn is reduced to ρ = 12.5 mΩ cm for $Ti_{0.5}Zr_{0.5}NiSn$. All samples asymptotically approach a value of 5 mΩ cm at 730 K. ZrNiSn produces values over 4 times higher than those of

the rest of the series. This may be due to the much poorer density of this sample (68% vs. 77% for TiNiSn).

The resultant power factors are therefore highest for the x = 0.25 and 0.5 samples. $Ti_{0.5}Zr_{0.5}NiSn$ reaches a maximum of 1.75 mW m^{-1} K^{-2} at 625 K, before levelling off. $Ti_{0.75}Zr_{0.25}NiSn$ reaches a maximum of 1.8 mW m^{-1} K^{-2} at 700 K. These values are an improvement over TiNiSn, which attains a maximum of 1.5 mW m^{-1} K^{-2}. However, the overall improvement is small, indicating that no real doping effect or changes to the electronic structure have been caused by the alterations made to the TiNiSn structure. Analysis of the data collected for the $Ti_{1-x}Zr_xNiSn_{0.95}$ sample, presented in Appendix 1, yields the same conclusion.

4.3.4 Time-Dependent Studies

As described in Section 4.2, several $Ti_{0.5}Zr_{0.5}NiSn_{0.95}$ samples were prepared with different annealing times to determine phase stability. Presented in Figure 4.8(a) are the (422) peaks from each sample. Visual inspection of these peaks indicates that after two weeks, no further change to the phase distribution occurs. Le Bail refinement confirms this as analysis of x_{Vegard} and Δx values reveals no significant change after two weeks. These values are collated in Appendix 1 and are represented schematically in Figure 4.8(b).

To determine the effect of the multiphase behaviour on the thermoelectric properties of these materials, the measurements obtained for the samples annealed for 3 days and 6 weeks are compared in Figure 4.9. Both the Seebeck coefficient and resistivity values were found to be almost identical. The Seebeck coefficient of the 6 week annealed sample was found to reach a maximum of -230 μV K^{-1} at 550 K, after which minority carriers reduce S. The 3 day annealed sample matches the performance of the 6 week sample almost exactly up to 500 K, above which it decreases in magnitude. It therefore achieves a maximum S = -220 μV K^{-1} at 500 K. The resistivity values show a semi-conducting temperature dependence and fall from 5.5 mΩ cm at room temperature to 2 mΩ cm at 700 K. There is a small anomaly at 500 K, consistent with the melting point of Sn, which exists as a small impurity phase in these samples.

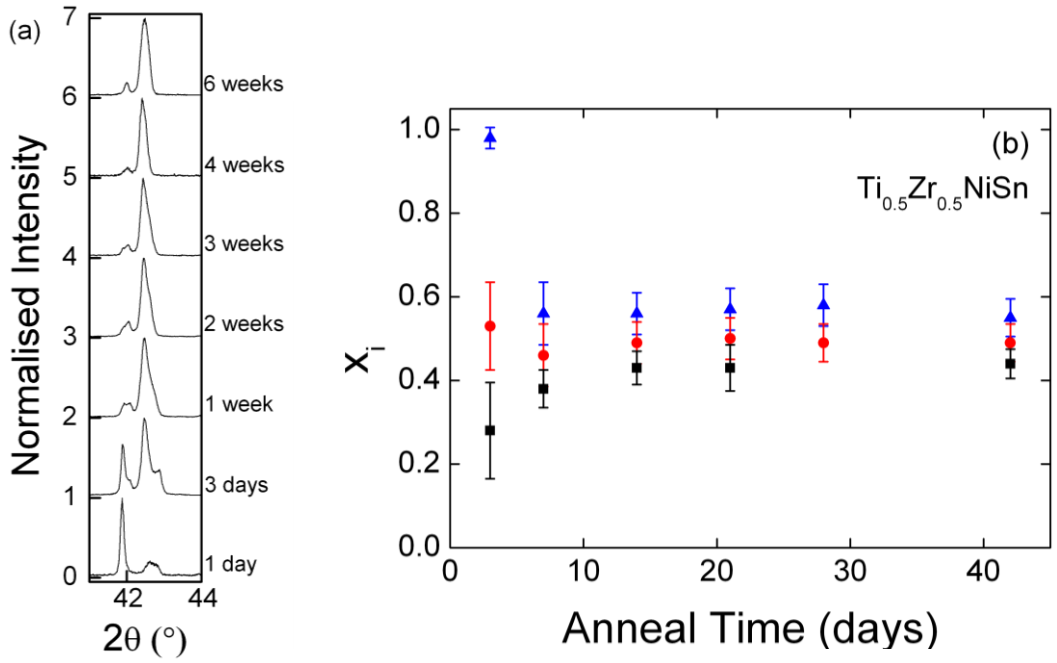

Figure 4.8: (422) diffraction peak for the $Ti_{0.5}Zr_{0.5}NiSn_{0.95}$ samples, annealed for different periods of time. (b) x_i values for each phase used to fit each $Ti_{0.5}Zr_{0.5}NiSn_{0.95}$ sample annealed for a given period of time. Error bars represent the associated compositional spread (Δx) for each phase.

A maximum $S^2/\rho = 1.5$ mW m^{-1} K^{-2} was found for the 3-day annealed sample at 650 K and $S^2/\rho_{max} = 2$ mW m^{-1} K^{-2} was found for the 6-week annealed sample at 650 K. The discrepancy is a result of the differing behaviour of the samples above 500 K, which is likely due to the melting of Sn impurities. The behaviour of the electronic properties of these samples is therefore almost identical, which indicates that the multiphase behaviour does not have a significant effect on the electronic properties of these alloys.

Interpretation of $\kappa(T)$ is not straightforward as the raw data are affected by porosity effects due to the ~80% sample densities. Voids have a low κ and this can dominate the thermal response making it difficult to detect changes intrinsic to the material. The measured $\kappa(T)$ is identical for the 3 d and 6 wk samples and independent of temperature with an average $\kappa = 2.5$ W m^{-1} K^{-1}. This is a rather low value compared to the literature,[59, 66] suggesting porosity effects need to be taken into account. For this reason, the $\kappa(T) = \kappa_{lat}(T) + \kappa_{el}(T)$ data were normalized to the $\kappa(T)$ data for a >95% dense arc-melted $Ti_{0.5}Zr_{0.5}NiSn_{0.95}$ sample. The phase-distributions for these samples are given in Appendix 1.

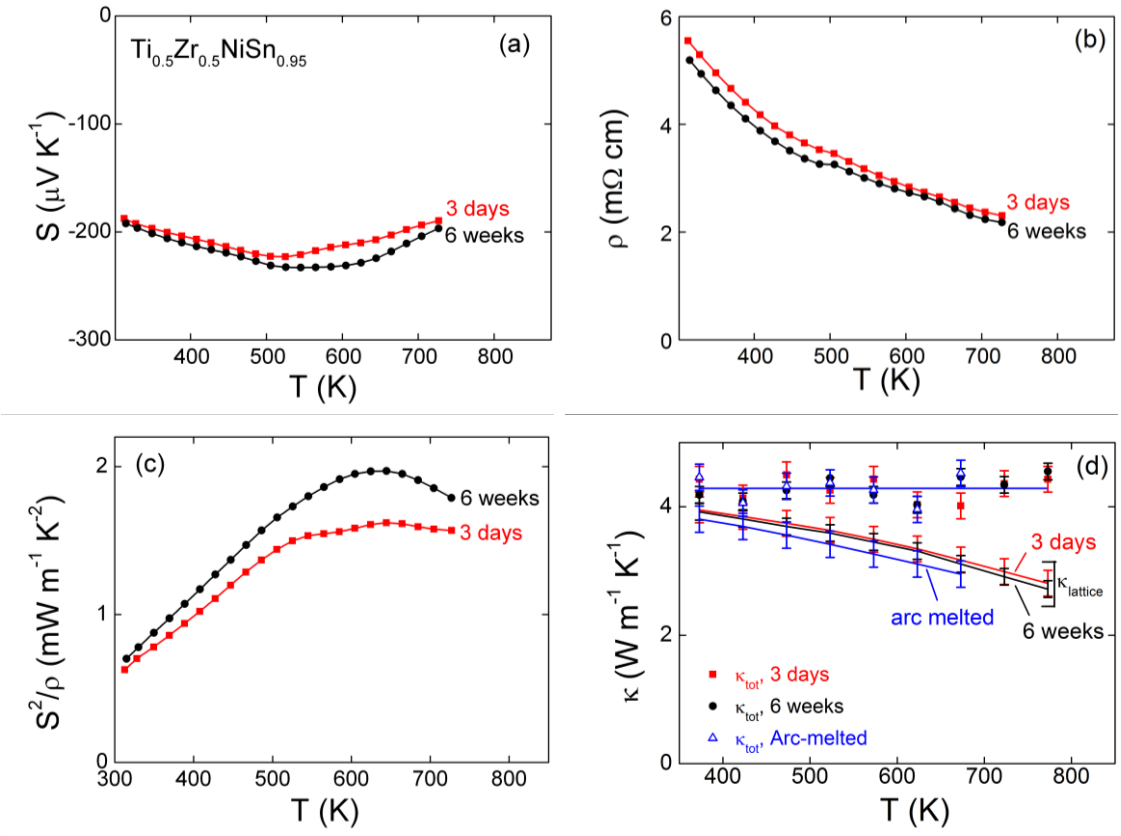

Figure 4.9: (a) Seebeck coefficient (S), (b) resistivity (ρ), (c) power factor (S^2/ρ) and (d) thermal conductivity (κ) for $Ti_{0.5}Zr_{0.5}NiSn$, annealed for 3 days and 6 weeks.

The arc-melted sample has a temperature independent κ(T) between 350 and 700 K with an average κ = 4.3 W m^{-1} K^{-1}. This yields a scaling factor (~1.7) that was applied to $\kappa_{lat}(T) = \kappa(T) - \kappa_{el}(T)$ for the 3 day and 6 week samples, where $\kappa_{el}(T)$ was calculated from the resistivity data using the Wiedemann-Franz Law (Equation (1.15)). The normalised κ(T) and $\kappa_{lat}(T)$ values for the 3 day, 6 week and arc-melted samples are given in Figure 4.9(d). It is clear that the three samples have an identical $\kappa_{lat}(T)$, despite differences in annealing and preparation method. This porosity correction can be justified by similar treatment of the resistivity values. Scaling the resistivity of the annealed samples to the arc-melted sample produces almost identical values.

Due to the requirement for this correction, no real comment on the magnitude of the thermal conductivity can be made and an accurate calculation of ZT is not possible until densification of these samples can be achieved. However, the identical nature of κ_{lat} for both the 3 day and 6 week annealed samples and the arc-melted sample can be commented upon. This suggests that the multiphase behaviour, which differs for each

sample, is not the dominant factor in reducing the thermal conductivity and that phonon scattering caused by the Ti/Zr mass difference is responsible for reducing the thermal conductivity of these samples.

4.3.5 Discussion

$Ti_{1-x}Zr_xNiSn$ samples ($x \neq 0$ or 1) were found to contain multiple half-Heusler phases with varying values of x. For example, X-ray powder diffraction indicates the presence of a continuous distribution of phases, spanning a Δx range of almost 0.5, between x = 0.24 and 0.7 for $Ti_{0.5}Zr_{0.5}NiSn$ and similar ranges were uncovered for the x = 0.25 and 0.75 samples. The Sn-deficient samples (data available in Appendix 1) showed similar behaviour but with a slightly reduced overall spread in x-values, e.g. $\Delta x = 0.3$ for $Ti_{0.5}Zr_{0.5}NiSn_{0.95}$. This implies that the Sn-deficiency may allow better mixing of Ti and Zr within the half-Heusler lattice. TEM images and elemental mapping of the $Ti_{0.5}Zr_{0.5}NiSn$ sample confirmed the multiphase model, with compositional fluctuations observed on a 100 nm length scale, as well as indications of particle by particle or larger-scale, fluctuations.

The presence of a range of compositions within a single sample precludes this system from being under thermodynamic control. If that were the case, either a perfect solid solution, where Ti and Zr are randomly distributed, or two limiting compositions would be observed, and this is clearly not the case. This must be a result of mixing Ti and Zr on the X site rather than an intrinsic difficulty in forming the half-Heusler phase, as the end members TiNiSn and ZrNiSn form single phase samples after 24 hours.

The time dependent study offers further insight into this system. Inspection of the peak shapes in Figure 4.8(a) shows that after the initial 24 hour annealing step, a sharp peak corresponding to a ZrNiSn phase is formed with a very broad hump representing a large distribution of $Ti_{1-x}Zr_xNiSn$ phases. Regrinding and further annealing causes these phases to react and these peaks become narrower in distribution and more intense. Increasing the length of time of the second annealing step causes alterations in the overall phase distribution up to two weeks. However, heating beyond two weeks has little effect. The samples appear to stop reacting and the phase distribution does not change further. This shows that simply heating the sample for longer periods will not allow a solid solution to be formed. The samples prepared for this study could not be

further homogenised after the second annealing step, as adequate pellets could not be pressed. However repeated homogenisation and annealing may be the key to attaining a true solid solution.

With respect to the thermoelectric properties of this series, values for S and ρ are in-keeping with the best reported values in the literature.[79] Mixing of Ti and Zr on the X-site causes a slight reduction in resistivity as x is increased to 0.5. Seebeck coefficients are not affected by this and so power factors are slightly improved for the x = 0.25 and 0.5 samples. This suggests that the multiphase behaviour exhibited by these samples has a very modest impact on their electronic properties. The electron microscopy data presented herein suggests that the major compositional variations occur on a length scale larger than the FIB lamella that was investigated. This is much larger than the average mean free path of an electron and thus it makes sense that the impact of the multiphase behaviour on the electronic properties of these samples is minimal.

As discussed in Section 4.3.4, the thermal conductivity does not differ for samples annealed for 3 days and 6 weeks, despite the large difference in the phase distribution of these samples. The effect that the multiphase behaviour should have on the flow of phonons through the lattice is hard to predict, given the various different length scales involved.[137] The role that sample density plays is also complex and difficult to quantify. However, the almost identical values produced by the two samples indicates that something else may be the dominant force in reduction of the thermal conductivity from 8-10 W m^{-1} K^{-1} to ~ 3-4 W m^{-1} K^{-1}. This then indicates that size and mass fluctuation effects, caused by mixing of Ti and Zr on the X-site are the main contributors to the low thermal conductivity values exhibited by these samples. However, other studies have suggested that multiphase behaviour may have been a contributing factor to κ = 2-3 W m^{-1} K^{-1} being achieved in some (Ti,Zr,Hf)NiSn samples.[134, 135] Given that this effect is kinetically controlled, alternative processing may produce multiphase behaviour on shorter length-scales that do cause phonon scattering. It is possible, however, that other, unidentified features within the reported samples are responsible for the low thermal conductivity values.

4.4 Neutron Powder Diffraction Studies of XNiSn and $X_{0.5}X'_{0.5}NiSn$ (X, X' = Ti, Zr, Hf)

Neutron powder diffraction offers good contrast in scattering lengths between the elements that make up these half-Heusler samples, particularly between X, Ni and Sn. This affords the opportunity to refine the site occupancies within each structure and therefore offers a real chance to gain additional insight into these materials. Detailed analysis of the X-ray data has already been presented in Section 4.3.1 for TiNiSn, ZrNiSn and $Ti_{0.5}Zr_{0.5}NiSn$. A similar treatment of the X-ray data for the remaining samples has also been carried out and is presented below, prior to analysis of the neutron powder diffraction data.

4.4.1 X-ray Diffraction of HfNiSn, $Ti_{0.5}Hf_{0.5}NiSn$ and $Zr_{0.5}Hf_{0.5}NiSn$

X-ray diffraction patterns for the three samples are presented in Figure 4.10, along with $Ti_{0.5}Zr_{0.5}NiSn$, for comparison.

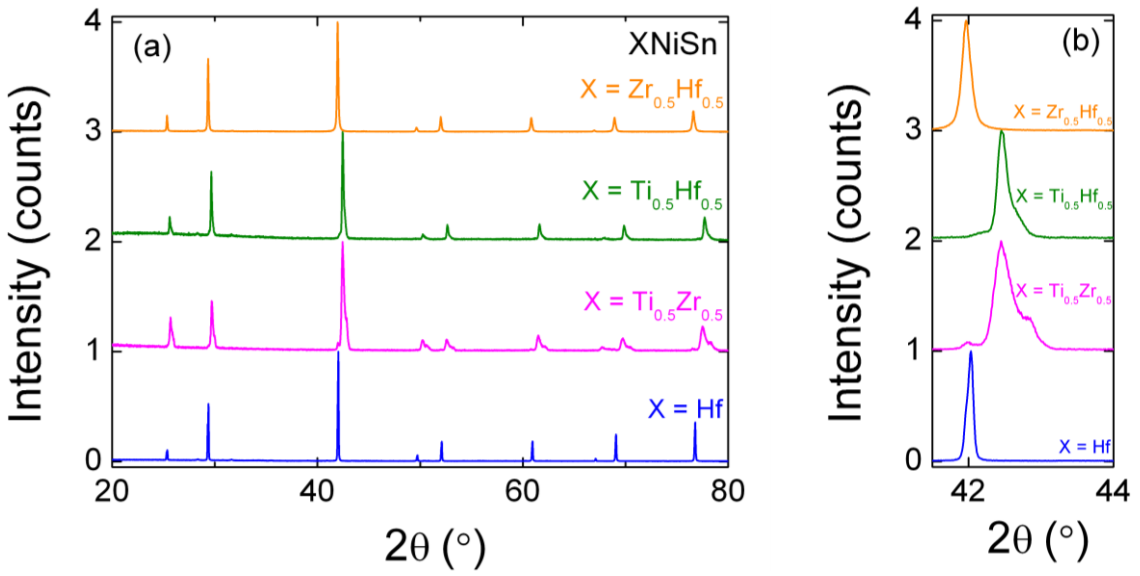

Figure 4.10: (a) X-ray diffraction patterns produced by HfNiSn and $X_{0.5}X'_{0.5}NiSn$ (X, X' = Ti, Zr, Hf) samples, and (b) close up of the (220) peaks for each sample.

From this it may be observed that the HfNiSn pattern is dominated by sharp, symmetric peaks, indicative of a crystalline, single phase sample. This pattern was therefore fitted with a single, half-Heusler phase. Lattice parameters are presented in Table 4.2.

In contrast, the $Ti_{0.5}Hf_{0.5}NiSn$ clearly contains peaks that exhibit substantial broadening and splitting, similar to the peaks produced by $Ti_{0.5}Zr_{0.5}NiSn$. 4 phases were required to adequately fit the peak shape, as demonstrated in Figure 4.11. Calculated x_{Vegard} values, deduced from the lattice parameters of each phase are presented in Table 4.2, along with phase fractions and fit statistics. Combination of the x_{Vegard} values and phase fractions results in an overall composition close to the nominal value. The profile parameters of the HfNiSn sample were found to be almost identical to those of TiNiSn and ZrNiSn (GW = 0.12° and LY = 0.05°). It was therefore possible to estimate the amount of strain, and therefore Δx values for these phases. These values are collated in Table 4.2. For $Ti_{0.5}Hf_{0.5}NiSn$, the compositional range is again semi-continuous and spans $0.32 \leq x \leq 0.61$ ($\Delta x \approx 0.3$, Figure 4.11(b)). This is about 40% smaller than for $Ti_{0.5}Zr_{0.5}NiSn$ due to both a narrower spread in x_i and smaller Δx_i values.

Peaks in the X-ray diffraction pattern for the $Zr_{0.5}Hf_{0.5}NiSn$ pattern (Figure 4.12) appear sharp at a first glance but there is evidence of peak broadening upon closer inspection. Three half-Heusler phases were required to fit the peak shapes in the $Zr_{0.5}Hf_{0.5}NiSn$ pattern and each of these was found to exhibit signs of further broadening, analogous to the peaks produced by $Ti_{0.5}Zr_{0.5}NiSn$ and $Ti_{0.5}Hf_{0.5}NiSn$ samples.

Table 4.2: Nominal composition, lattice parameter (a), Vegard composition (x_i), composition spread (Δx_i), molar percentage (mol%), average composition (x_{avg}) and goodness-of-fit (χ^2) for HfNiSn, $Zr_{0.5}Hf_{0.5}NiSn$ and $Ti_{0.5}Hf_{0.5}NiSn$ as determined by Le Bail analysis of X-ray powder diffraction data.

x,y	a (Å)	x_i	Δx	mol%	x_{avg}	χ^2
HfNiSn	6.0764(1)	0	0	100	0	2.4
$Ti_{0.5}Hf_{0.5}NiSn$	5.9891(2)	0.40(1)	0.16(1)	24.6(6)	0.52(1)	1.4
	6.0058(1)	0.52(1)	0.04(1)	18.1(2)		
	6.0149(1)	0.58(1)	0.05(1)	56.4(6)		
	6.0559(5)	0.86(1)	0.04(1)	0.9(1)		
$Zr_{0.5}Hf_{0.5}NiSn$	6.0849(1)	0.73(2)	0.15(1)	15.4(6)	0.45(1)	2.5
	6.0931(1)	0.47(1)	0.05(1)	56.9(6)		
	6.0992(1)	0.28(2)	0.05(1)	27.8(6)		

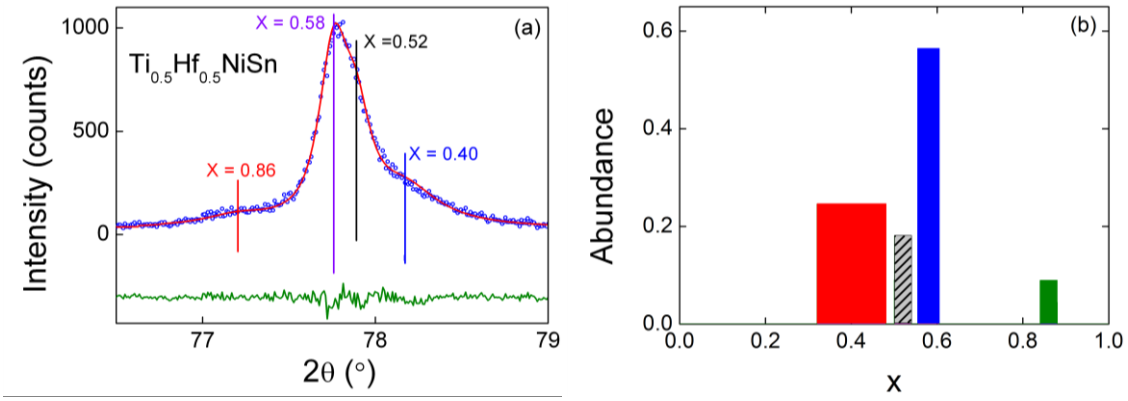

Figure 4.11: (a) close up of the (422) peak in the Le Bail fit to X-ray data collected for $Ti_{0.5}Hf_{0.5}NiSn$. Blue circles are the collected data, the red line is the calculated fit and the green line is the difference curve. Tickmarks correspond to the different half-Heusler phases used to fit the pattern. (b) Schematic of the phase distribution for $Ti_{0.5}Hf_{0.5}NiSn$

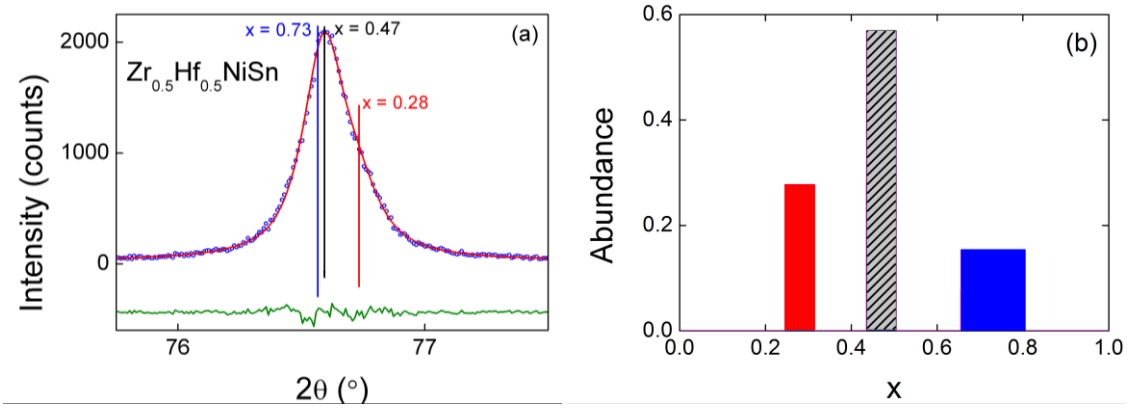

Figure 4.12: (a) close up of the (422) peak in the Le Bail fit to X-ray data collected for $Zr_{0.5}Hf_{0.5}NiSn$. Blue circles are the collected data, the red line is the calculated fit and the green line is the difference curve. Tickmarks correspond to the different half-Heusler phases used to fit the pattern. (b) Schematic of the phase distribution for $Zr_{0.5}Hf_{0.5}NiSn$.

Values of x_{Vegard} and Δx were therefore calculated, and the resultant values are presented in Table 4.2. In this case the phase distribution is not continuous and the approximate compositional boundaries are $0.25 \leq x \leq 0.31$, $0.44 \leq x \leq 0.50$ and $0.64 \leq x \leq 0.80$. The overall composition was calculated to be $Zr_{0.55}Hf_{0.45}NiSn$, in good agreement with the nominal composition.

4.4.2 Neutron Powder Diffraction of XNiSn

The Rietveld fits to the POLARIS data are presented in Figure 4.14. A single half-Heusler phase was used in the fits and the resulting lattice and atomic parameters are reported in Table 4.3. These agree well with values deduced from the X-ray data in all cases. A Rietveld fit to the TiNiSn data that maintains a stoichiometric model, with Ti, Ni and Sn on their expected sites (X, M1, Z), results in χ^2 = 8.8. Two models were subsequently identified that resulted in an improvement in the goodness-of-fit. The first of these involves a 2% excess of Ni, accommodated on the nominally vacant M2 site.

Table 4.3: Lattice parameter (a), site occupancies, thermal parameters (U_{iso} / Å^2) and fit statistics for XNiSn (X = Ti, Zr, Hf), as determined from neutron diffraction data.

X		Ti	Zr	Hf
a (Å)		5.9298(1)	6.1089(1)	6.0795(1)
X	Occ	1.011(3)	1.08(3)	1.00(3)
	U_{iso}	0.00494(7)	0.0057(2)	0.0047(5)
Ni(1)	Occ	1.000(1)	1.06(2)	1.00(1)
	U_{iso}	0.00498(5)	0.00461(6)	0.0046(5)
Ni(2)	Occ	0.024(1)	0.006(1)	0.009(2)
	U_{iso}	0.00498(5)	0.00461(6)	0.0046(5)
Sn	Occ	1	1	1
	U_{iso}	0.00407(5)	0.0021(2)	0.0036(5)
wt%		100	95.00(8)	99.17(3)
χ^2		8.2	9.9	7.4
wR_p / %	Bank 5	3.4	3.0	2.8
	Bank 4	2.0	2.4	2.2
	Bank 3	2.1	2.5	2.2
R_p / %	Bank 5	4.2	4.2	5.1
	Bank 4	3.2	5.0	4.2
	Bank 3	3.6	3.0	3.0
R_f^2 / %	Bank 5	5.7	7.1	8.5
	Bank 4	6.2	6.0	7.3
	Bank 3	7.5	7.2	5.3

ZrNiSn contains 0.93(7) wt% Zr_5Sn_4, 3.36(3) wt% $Ni_{2.67}Sn_2$ and 0.44(1) wt% $ZrNi_2Sn$. HfNiSn contains 0.83(3) wt% HfO_2. The total counting current was 300 μA for each sample.

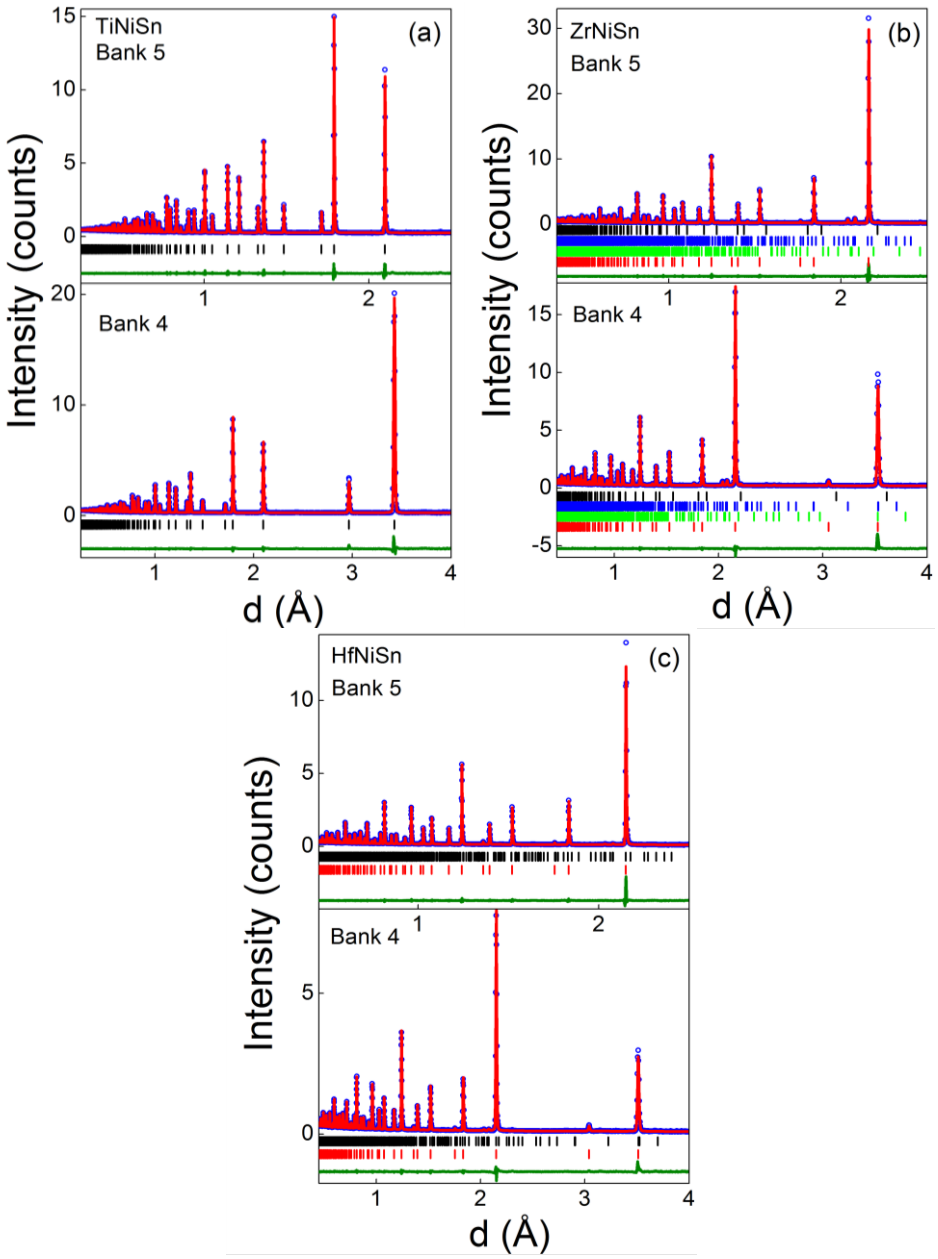

Figure 4.13: Rietveld fit to neutron diffraction data collected for (a) TiNiSn, (b) ZrNiSn, (c) HfNiSn. Blue circles are the collected pattern, the red line is the model fit, the green line is the difference. Tickmarks correspond to the different half-Heusler phases used to model the pattern.

The second model contains 3% inversion of Ti and Sn. Both these models are a-priori possible and produce χ^2 = 8.2. The small degree of inversion may seem plausible but larger degrees of inversion are needed for the previously reported $TiNi_{1.03}Sn$ (6%) and $TiNi_{1.06}Sn$ (10%) samples. The nominal $TiNiSn_{0.95}$ sample that was also prepared by

standard solid state reactions was similarly analysed and best-fit models were found for a $TiNi_{1.056(2)}Sn$ composition or a structure containing 7.5% TiSn inversion. Furthermore, the HfNiSn sample (discussed below) requires 30% inversion, or 1% excess Ni. The amount of excess Ni and degree of inversion is therefore correlated and the increasingly large degrees of inversion required is incompatible with the covalent bonding in these structures.[56] It can therefore be concluded that the presence of interstitial Ni is the most plausible interpretation of the data. This is also supported by computational studies that show excess Ni is much less energetically costly than X/Sn inversion.[106] In addition, recently published experimental work reveals gradual changes in lattice parameter up to y = 0.1 in $TiNi_{1+y}Sn$. This again supports the presence of interstitial Ni.[86]

Examination of the refined site occupancies in ZrNiSn indicates a 6% Sn deficiency within the half-Heusler phase. This is unexpected, and not in keeping with the extensive data on TiNiSn reported in Chapters 3 and 4, where nominally Sn deficient samples always recover to give a Sn-stoichiometric experimental composition. Detailed electron microscopy analysis is required to investigate this further and analysis of the occupancy on the M2 site was not attempted. However, Xie et. al. used synchrotron X-ray diffraction to probe a ZrNiSn sample, prepared by spin-levitation methods and identified a 4.6% Ni excess on the interstitial M2 site.[138] This suggests that interstitial Ni also occurs in ZrNiSn.

HfNiSn was found to contain a small amount of Ni on the M2 site, with a refined value of 0.9(2)%.

4.4.3 Neutron Powder Diffraction of $X_{0.5}X'_{0.5}NiSn$ (X, X' = Ti, Zr, Hf)

4.4.3.1 $Ti_{0.5}Zr_{0.5}NiSn$

The X-ray powder diffraction pattern collected for this sample contained multiple broadened peaks for each reflection, suggesting the presence of multiple $Ti_{1-x}Zr_xNiSn$ half-Heusler phases, with different values of x, within the sample. This was also observed in the neutron pattern which was fitted using 4 half-Heusler phases, as shown in Figure 4.14(a). This was the minimum number of phases required to obtain a reasonable fit to the data.

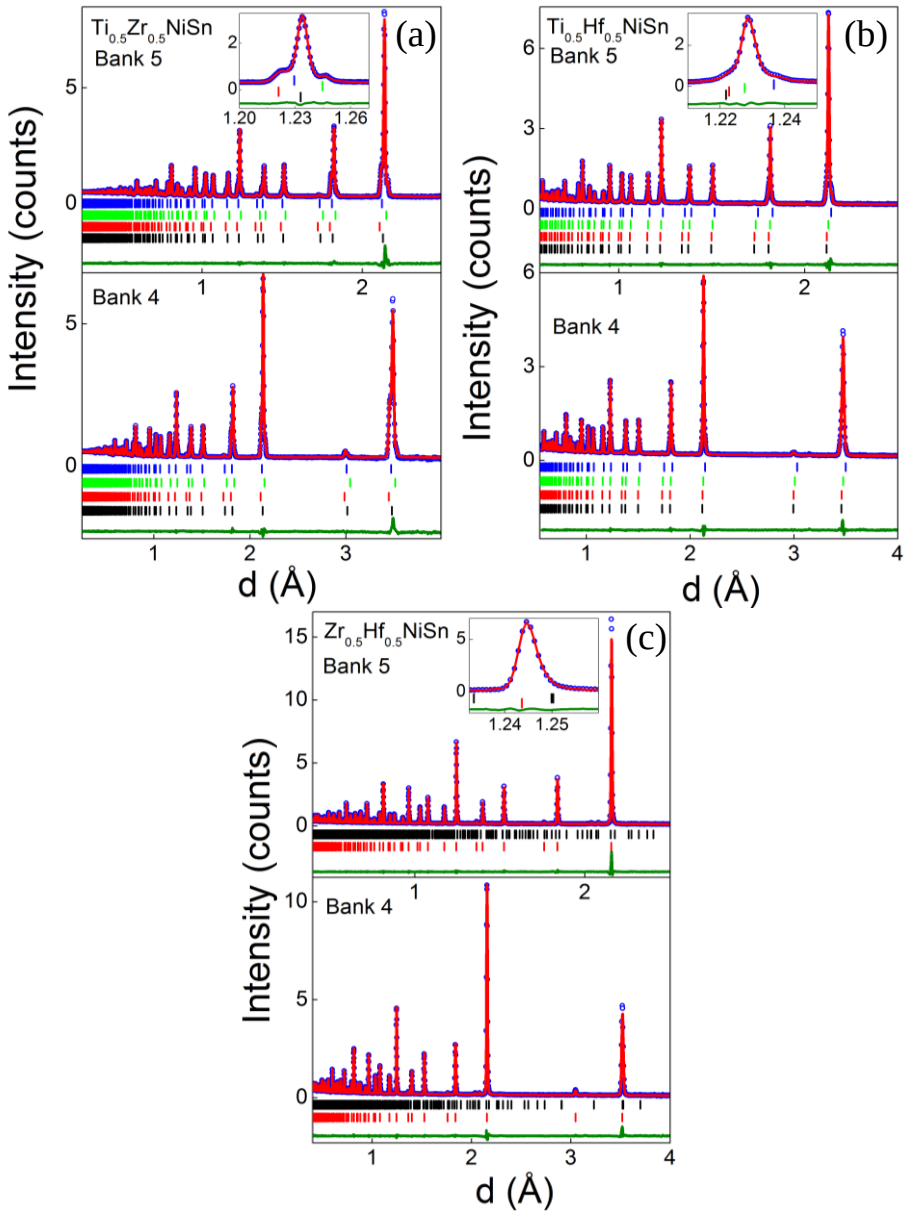

Figure 4.14: Rietveld fit to neutron diffraction data collected for (a) $Ti_{0.5}Zr_{0.5}NiSn$, (b) $Ti_{0.5}Hf_{0.5}NiSn$ and (c) $Zr_{0.5}Hf_{0.5}NiSn$. Blue circles are the collected pattern, the red line is the model fit, the green line is the difference. Tickmarks correspond to the different half-Heusler phases used to model the pattern.

Table 4.4: Lattice parameter (a), site occupancies, thermal parameters (U_{iso}/Å^2), x calculated by Vegard's law (x_V), average x_V and x_R (refined x), and fit statistics for X'$_{0.5}$X'$_{0.5}$NiSn (X, X' = Ti, Zr, Hf).

	a (Å)	mol%		X	X'	Ni(1)	Ni(2)	Sn	x_V	x_{avg}	Ni_{avg}	Δx	χ^2	*Bank*	wR_p	R_p	R_f^2
X=Ti X'=Zr	5.9815(2)	18.3(2)	*Occ*	0.847(3)	0.153(3)	1	0.052(2)	1	0.29			0.12					
			U_{iso}	0.0052(1)	0.0052(1)	0.0052(1)	0.0052(1)	0.0052(1)									
	6.0240(2)	19.7(7)	*Occ*	0.53(1)	0.47(1)	1	-0.003(8)	1	0.53	x_R = 0.49	1.03	0.10	5.5	*1*	2.8	4.6	5.9
			U_{iso}	0.00213(4)	0.00213(4)	0.00213(4)	0.00213(4)	0.00213(4)						*2*	1.6	2.9	3.6
	6.0406(1)	59.2(7)	*Occ*	0.412(6)	0.588(6)	1	0.032(4)	1	0.62	x_V = 0.55		0.07		*3*	1.7	2.9	5.4
			U_{iso}	0.00653(4)	0.00653(4)	0.00653(4)	0.00653(4)	0.00653(4)									
	6.1020(2)	2.7(1)	*Occ*	0.04	0.96	1	0	1	0.96			0.06					
			U_{iso}	0.0010(2)	0.0010(2)	0.0010(2)	0.0010(2)	0.0010(2)									
X=Ti X'=Hf	5.9834(3)	14(1)	*Occ*	0.805(5)	0.195(5)	1	0.030(4)	1	0.36			0.12					
			U_{iso}	0.0050(2)	0.0050(2)	0.0050(2)	0.0050(2)	0.0054(2)									
	6.0046(3)	23(1)	*Occ*	0.46(2)	0.54(2)	1	0.00(2)	1	0.50	x_R = 0.52	1.02	0.04	6.0	*1*	2.0	2.7	1.8
			U_{iso}	0.00524(5)	0.00524(5)	0.00524(5)	0.00524(5)	0.00524(5)						*2*	1.5	2.6	4.8
	6.0157(1)	60.1(9)	*Occ*	0.419(9)	0.581(9)	1	0.014(6)	1	0.57	x_V = 0.52		0.03		*3*	2.0	2.5	2.8
			U_{iso}	0.00524(5)	0.00524(5)	0.00524(5)	0.00524(5)	0.00524(5)									
	6.0604(3)	3.0(8)	*Occ*	0.13	0.87	1	0	1	0.87			0.08					
			U_{iso}	0.00007(7)	0.00007(7)	0.00007(7)	0.00007(7)	0.00007(7)									
X=Zr X'=Hf	6.0926(1)	98.9(1)	*Occ*	0.59(4)	0.41(4)	1	-	1	0.49	x_R = 0.41	1	0.14	10.9	*1*	2.1	4.4	6.0
			U_{iso}	0.0066(2)	0.0066(2)	0.00495(6)	-	0.0017(2)		x_V = 0.55				*2*	2.0	3.1	5.1
														3	2.9	3.7	3.2

$Zr_{0.5}Hf_{0.5}NiSn$ contains 1.1(1) wt% $Ni_{2.67}Sn_2$. Space group: *F-43m*, X/X' occupy site *4a*, Ni(1) occupies site *4c*, Ni(2) occupies site *4d* and Sn occupies site *4b*. The total counting current was 300 μA for each sample

The lattice parameters and site occupancies for the 4 phases are presented in Table 4.4. The Zr content of each phase was calculated from the lattice parameters using Vegard's law (x_V) and by refining the X-site occupancy (x_R). It was not possible to determine x_R for the most minor phase, present at 3%, and the occupancies were kept fixed at the x_V values. The x_R values are plotted against x_V in Figure 4.15. From this figure, it may be seen that, for $x_V \geq 0.5$, there is good agreement between x_R and x_V. At lower values of x_V however, x_V are somewhat larger than x_R. This indicates a departure from Vegard's law for the $Ti_{1-x}Zr_xNiSn$ solid solution at low values of x, with the x_R indicating a lower Zr-fraction than derived from the lattice parameter.

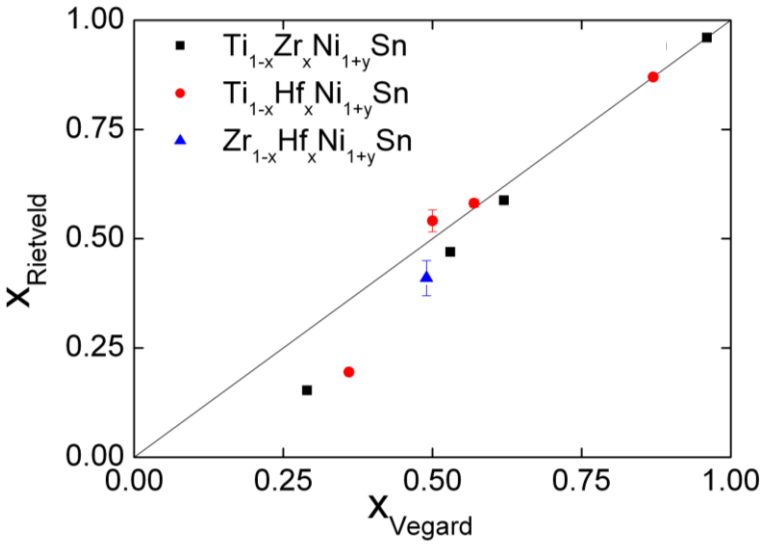

Figure 4.15: Fitted fraction of X-metals (x_R) against those calculated from Vegard's law (x_V) for $X_{1-x}X'_xNiSn$ phases present in the nominal $X_{0.5}X'_{0.5}NiSn$ samples.

Further compositional variation is also indicated by the neutron data as the 'individual' half-Heusler reflections are broadened compared to TiNiSn and ZrNiSn, as was observed in the X-ray data. This broadening has again been quantified in terms of a spread in x values (Δx), centred round the refined x_R value for each phase, by analysing the profile function within each refinement. Bank 5 was used as this is the backscattering bank and has the highest resolution. Profile function 3 for time-of-flight data in GSAS was used to fit the peak shape. Analysis of the refined values for XNiSn (X = Ti, Zr and Hf) revealed all refined parameters to be very similar. An average of the 3 values was therefore taken and these were applied to the $X_{0.5}X'_{0.5}NiSn$ phases. All

profile parameters were then kept fixed, with the exception of γ_1 which models microstrain within the sample. The refined values are related to strain by Equation (4.1).

$$S = \frac{1}{C}\gamma_1 100\% \qquad \text{Equation (4.1)}$$

where C is diffractometer constant C, which relates time-of-flight to d-spacing.

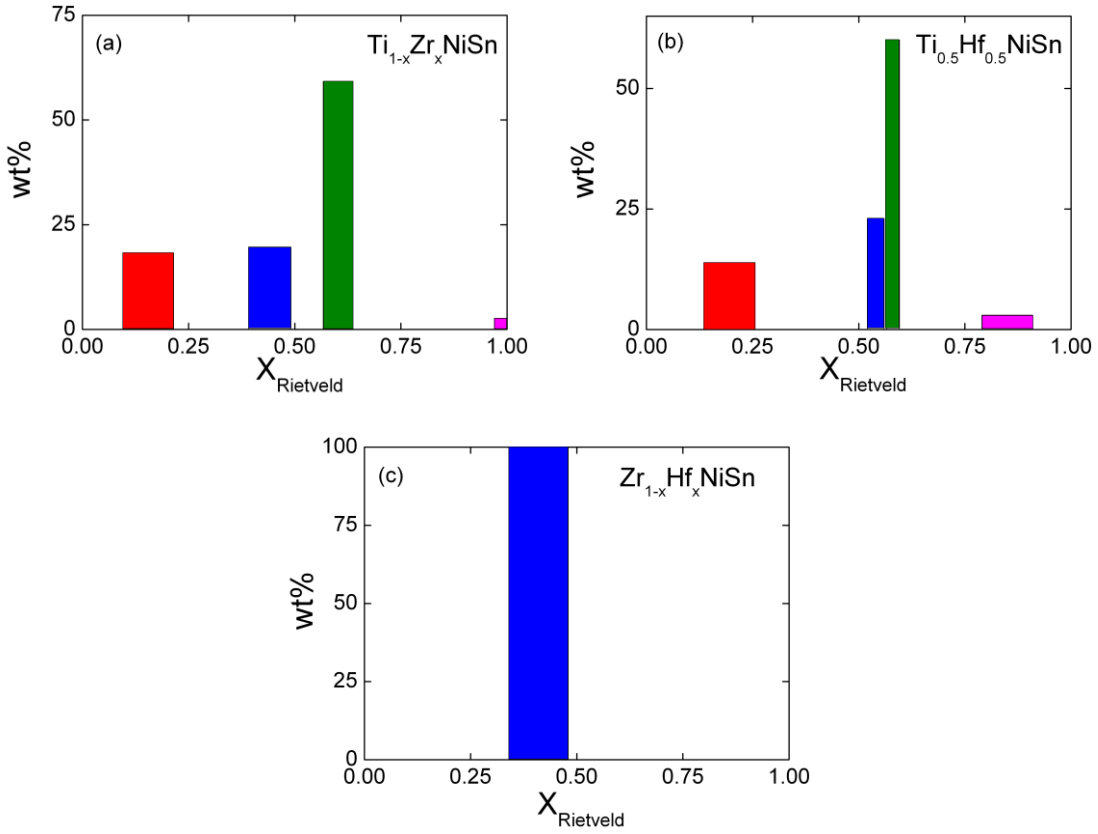

Figure 4.16: Compositional spread (Δx) and phase distribution for each refined phase in the $X_{0.5}X'_{0.5}NiSn$ samples (X = Ti, Zr, Hf) determined from Rietveld refinement of neutron powder diffraction data.

The calculated values for Δx are tabulated for each phase in Table 4.4. A schematic representing the compositional spread is presented in Figure 4.16(a). The neutron data also enabled the refinement of M1 and M2 site occupancies. Refinement of the M2 site occupancy revealed that Ni occupies the M2 site in 2 of the 4 phases. The largest excess of Ni (y = 0.052(2)) was found in the phase with x_R = 0.153(3). The refined M2 site occupancy of each phase is plotted in Figure 4.17. Taking into account the refined x_R,

M and Sn occupancies and the phase fractions of the 4 phases, the average composition of the sample was found to be $Ti_{0.51(1)}Zr_{0.49(1)}Ni_{1.03(1)}Sn$, which is in excellent agreement with the nominal x-value. 3% excess Ni is in-keeping with the data for the end members.

4.4.3.2 $Ti_{0.5}Hf_{0.5}NiSn$

This sample shows similar multiphase behaviour to $Ti_{0.5}Zr_{0.5}NiSn$ and was analysed analogously. The refined Hf occupancies were found to be x_R = 0.195(5), 0.54(2), 0.581(9) and 0.87, where the last value was fixed to x_V due to the low abundance of this phase. The x_R values are in good agreement with x_V for x > 0.5, with a small discrepancy for lower x, as seen in $Ti_{0.5}Zr_{0.5}NiSn$ and illustrated in Figure 4.15. The compositional spreads (Δx) are comparable to those found in $Ti_{0.5}Zr_{0.5}NiSn$ and are shown in Figure 4.16(b). Two of the phases were found to contain Ni on the M2 site. The refined values are presented in Table 4.4 and the Ni content is plotted in Figure 4.17. The average composition was found to be $Ti_{0.48(1)}Hf_{0.52(1)}Ni_{1.02(1)}Sn$, in keeping with the $Ti_{0.5}Zr_{0.5}NiSn$ sample.

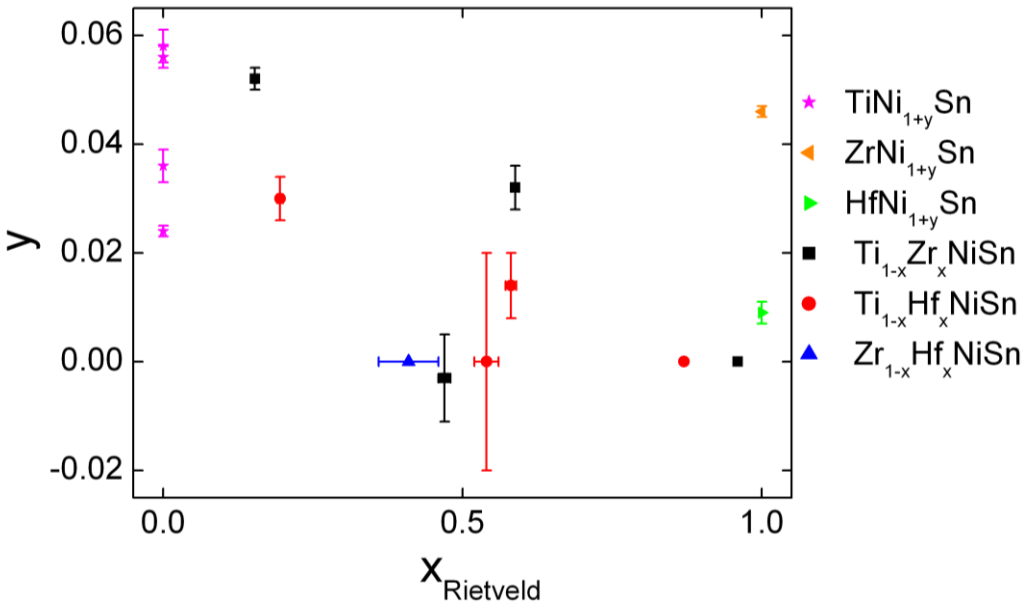

Figure 4.17: Refined M2 site occupancy (y) for each of the $X_{1-x}X'_xNi_{1+y}Sn$ phases present in the nominal $X_{0.5}X'_{0.5}NiSn$ samples (X, X' = Ti, Zr, Hf). *ZrNiSn data from ref. [138], additional TiNiSn points from ref. [139].

4.4.3.3 $Zr_{0.5}Hf_{0.5}NiSn$

The narrow range in lattice parameters observed for this composition (due to the similar radii of Zr and Hf) means only one phase could be identified, instead of the three that were observable in the X-ray data. The refined composition of this sample was found to be $Zr_{0.59(4)}Hf_{0.41(4)}NiSn$, consistent with the X-ray data, and the nominal composition. The lattice and atomic parameters are presented in Table 4.4, along with x, Δx and average compositions. Refinement of the M2 site occupancy suggested this sample is stoichiometric, and does not contain any interstitial Ni.

4.4.4 Temperature-Dependent Studies

4.4.4.1 TiNiSn

Neutron powder diffraction patterns were collected at room temperature and at 100 K intervals, between 373 and 973 K. The fitted lattice parameters, site occupancies and fit statistics are presented in Table 4.5. The unit cell volume was found to increase linearly with T above 300 K, as illustrated in Figure 4.18(a). The trend in the volume expansion could be fitted by Equation (4.2) where A is a scale factor and θ_D is the Debye temperature. From this fit V_0 = 205.4(1) Å^3, A = 2.6(2) and θ_D = 347(22) K. This is consistent with the literature values which put θ_D in the range 360-420 K.[140]

$$V(T) = V_0 coth\left(\frac{\theta_D}{T}\right) \qquad \text{Equation (4.2)}$$

The temperature dependences of the thermal parameters for each atom are plotted in Figure 4.18(b). The similar gradients of a straight line fit and the similar magnitudes indicate that all three atom types vibrate at around the same frequency. The values for Sn are slightly reduced compared with Ti and Ni due to its larger mass. The Ni occupancies on the M1 and M2 sites were also refined for each temperature step and remained between 1-2% in excess.

Table 4.5: Lattice parameter (a), site occupancies, thermal parameters (U_{iso} / Å^2) and fit statistics for TiNiSn between 293 and 973 K as determined from neutron powder diffraction. The 293 K pattern was collected out-with the furnace.

		293 K	373 K	473 K	573 K	673 K	773 K	873 K	973 K
a (Å)		5.9298(1)	5.9333(1)	5.9392(1)	5.9453(1)	5.9514(1)	5.9576(1)	5.9641(1)	5.9710(1)
Ti	*Occ*	1.011(3)	1.004(3)	10.986(3)	0.981(3)	0.994(3)	0.965(3)	1	0.968(4)
	U_{iso}	0.00494(7)	0.0061(1)	0.0075(1)	0.0092(1)	0.0107(1)	0.0124(2)	0.0140(2)	0.0161(2)
Ni(1)	*Occ*	1.000(1)	1.000(0)	1.000(0)	1.002(0)	1.000(0)	1.000(0)	1	1.000(0)
	U_{iso}	0.00498(5)	0.00609(6)	0.00770(6)	0.00938(7)	0.01096(8)	0.01258(9)	0.0144(2)	0.0163(1)
Ni(2)	*Occ*	0.024(1)	0.020(1)	0.019(1)	0.014(1)	0.018(1)	0.009(1)	0.020(1)	0.010(1)
	U_{iso}	0.00498(5)	0.00609(6)	0.00770(6)	0.00938(7)	0.01096(8)	0.01258(9)	0.0144(2)	0.0163(1)
Sn	*Occ*	1	1	1	1	1	1	1	1
	U_{iso}	0.00407(5)	0.00527(9)	0.00727(9)	0.0090(1)	0.0101(1)	0.0126(1)	0.0135(2)	0.0162(2)
Counting Current / μA		300	300	300	300	300	300	300	300
χ^2		8.2	4.1	4.0	4.0	3.8	4.1	4.1	4.2
wR_p	*Bank 5*	3.4	2.0	2.0	2.1	2.1	2.2	2.2	2.2
	Bank 4	2.0	1.4	1.3	1.3	1.2	1.2	1.2	1.4
	Bank 3	2.1	1.0	1.2	1.1	1.1	1.3	1.2	1.2
R_p	*Bank 5*	4.2	2.3	2.5	2.4	2.5	2.6	2.7	2.6
	Bank 4	3.2	2.8	2.3	2.3	2.3	2.1	2.0	2.1
	Bank 3	3.6	1.1	1.3	1.2	1.1	1.4	1.3	1.3
R_f^2	*Bank 5*	5.7	3.4	3.6	4.1	4.5	5.7	6.4	6.4
	Bank 4	6.2	4.3	4.7	7.8	7.5	8.3	8.9	10.7
	Bank 3	7.5	7.5	7.5	10.9	10.5	11.5	10.8	10.0

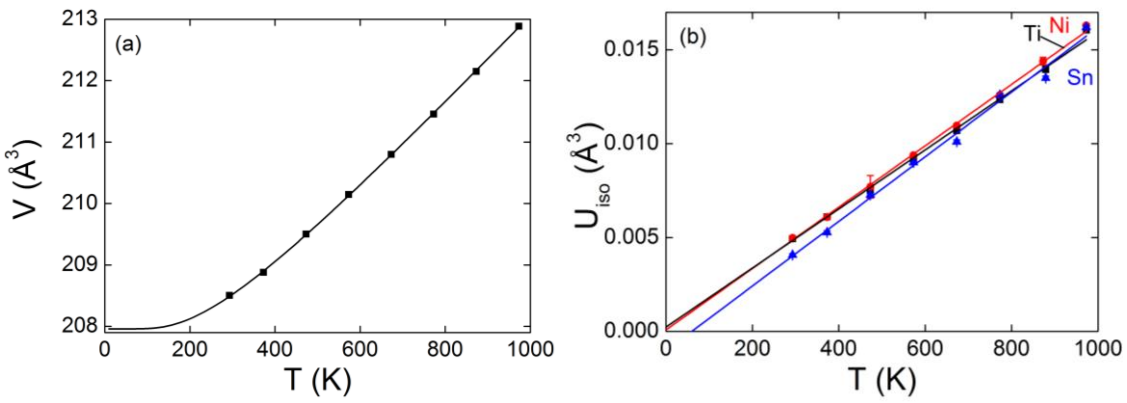

Figure 4.18: (a) Temperature dependence of the unit cell volume of TiNiSn determined from Rietveld refinement of neutron powder diffraction data and fitted by $V(T) = V_0+A\coth(\theta_D/T)$. (b) Temperature dependence of U_{iso}, determined from Rietveld refinement of neutron powder diffraction data, for each atom type in TiNiSn.

4.4.4.2 $Ti_{0.5}Hf_{0.5}NiSn$

Data was collected at 293, 473, 673 and 873 K. Lattice parameters for each phase, weight fractions, site occupancies and fit statistics are presented in Table 4.6. The lattice parameters for each phase were found to increase linearly with temperature. The increase in temperature was found to have very little effect on the distribution of the phases in this sample.

The Ti:Hf ratio remained almost constant for each phase. The Ni(2) content appears to decrease with temperature, however the differences observed are within the margin of error so no definitive claim may be made based on the current data. Only small changes were observed in the less abundant phases, where the occupancies are less easily refined. The weight percentage of each phase also remained almost constant over the entire temperature range. The overall composition therefore does not change significantly with temperature, and nor does the arrangement of the phases within the sample.

Table 4.6: Lattice parameter (a), refined x (x_R), Ni(2) fractional site occupancies, thermal parameters (U_{iso}/Å^2) and fit statistics for the $Ti_{1-x}Hf_xNiSn$ phases in $Ti_{0.5}Hf_{0.5}NiSn$, between 293 and 873 K.

Phase		293 K	473 K	673 K	873 K
1	a (Å)	5.9834(3)	5.9950(3)	6.0074(6)	6.0192(5)
	x	0.195(5)	0.223(5)	0.210(9)	0.206(8)
	Ni(2)	0.030(4)	0.027(4)	0.016(5)	0.011(7)
	mol%	14(1)	16(1)	16(1)	15.5(2)
	U_{iso}	0.0050(2)	0.0060(2)	0.0088(2)	0.0132(4)
2	a (Å)	6.0046(3)	6.0164(2)	6.0285(3)	6.0394(4)
	x	0.54(3)	0.559(9)	0.57(1)	0.59(2)
	Ni(2)	-0.00(2)	0	0	0
	mol%	23(1)	27.6(7)	29.8(9)	25.2(1)
	U_{iso}	0.00524(5)	0.00770(4)	0.01068(5)	0.01378(8)
3	a (Å)	6.0157(1)	6.0262(1)	6.0378(1)	6.0490(1)
	x	0.581(9)	0.588(4)	0.610(5)	0.592(6)
	Ni(2)	0.014(6)	0.012	0	0
	mol%	60.1(9)	54.0(7)	51.8(9)	56.3(1)
	U_{iso}	0.00524(5)	0.00770(4)	0.01068(5)	0.01378(8)
4	a (Å)	6.0604(3)	6.0691(4)	6.0800(4)	6.0919(7)
	x	0.87	0.87	0.87	0.87
	Ni(2)	0.10(1)	0.08(2)	0.09(2)	0.09(2)
	mol%	3.0(8)	2.8(1)	2.9(1)	2.9(2)
	U_{iso}	0.0001(3)	0.0004(5)	0.0021(6)	0.0050(9)
Counting Current/μA		450	200	200	75
χ^2		6.0	2.4	2.4	1.0
wR_p	*Bank 5*	2.0	1.4	1.4	1.7
	Bank 4	1.5	1.0	1.3	1.4
	Bank 3	2.0	2.2	1.9	1.5
R_p	*Bank 5*	2.7	2.5	2.4	2.9
	Bank 4	2.6	1.6	2.8	3.3
	Bank 3	2.5	2.5	2.2	2.0
R_f^2	*Bank 5*	1.8	3.0	3.6	5.2
	Bank 4	4.8	8.8	9.8	7.0
	Bank 3	2.8	3.5	5.3	9.4

4.4.5 Thermoelectric Properties

Electronic properties were measured for the Hf-containing samples are presented in Figure 4.19. The properties of TiNiSn, ZrNiSn and $Ti_{0.5}Zr_{0.5}NiSn$ were discussed in Section 4.3.3.

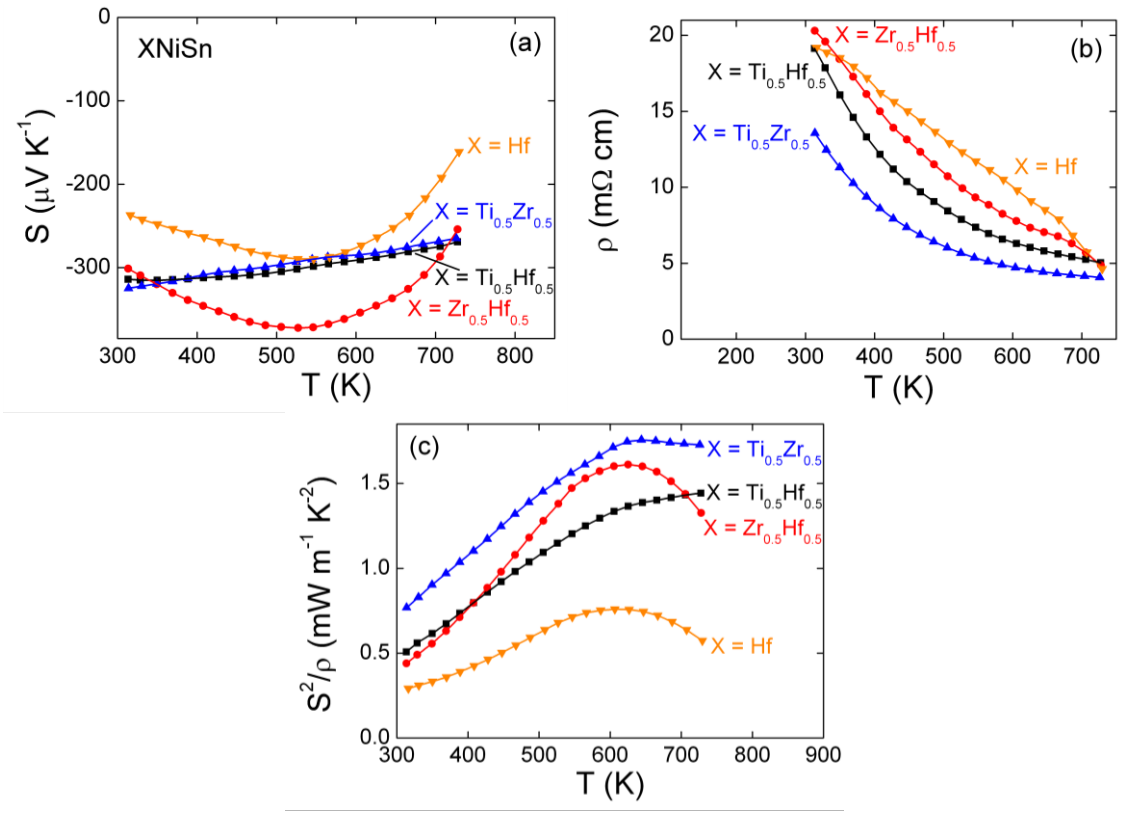

Figure 4.19: Temperature dependence of (a) Seebeck coefficient (S), (b) resistivity (ρ) and (c) power factor (S^2/ρ) for HfNiSn, $Ti_{0.5}Zr_{0.5}NiSn$, $Ti_{0.5}Hf_{0.5}NiSn$ and $Zr_{0.5}Hf_{0.5}NiSn$.

S(T) for HfNiSn is distinctly different to those for TiNiSn and ZrNiSn. A clear maximum of -300 μV K^{-1} is reached at 575 K for HfNiSn, compared with the almost linear decrease observed in the other two samples. ρ(T) does not follow the classical temperature dependence of a semiconductor, but instead shows an almost linear decrease as the temperature is increased, then decreases more dramatically at 675 K and reaches a minimum of 5 mΩ cm 730 K. The resulting power factor reaches a maximum of 0.75 mW m^{-1} K^{-2} at 600 K.

S(T) for $Zr_{0.5}Hf_{0.5}NiSn$ is very similar to that of the HfNiSn sample, and reaches a maximum of -380 μV K^{-1} at 525 K. ρ(T) is also similar, with an almost linear decrease, until 680 K, after which values decrease more rapidly, to 5 mΩ cm at 730 K. The addition of Zr to HfNiSn more than doubles the power factor to 1.6 mW m^{-1} K^{-2} at 600 K.

$Ti_{0.5}Hf_{0.5}NiSn$ shows identical trends to the $Ti_{0.5}Zr_{0.5}NiSn$ sample, with a linear decrease in S over the whole measured temperature range and S_{RT} = -320 μV K^{-1}. Resistivity values are higher than for $Ti_{0.5}Zr_{0.5}NiSn$, but reach a minimum of 5 mΩ cm at 730 K. This results in S^2/ρ_{max} = 1.5 mW m^{-1} K^{-2} at 730 K. Due to the relatively low density of these samples, thermal conductivity measurements were not undertaken.

4.4.6 Discussion

Neutron powder diffraction has provided valuable insight into the stoichiometries of single phase XNiSn and multiphase $X_{0.5}X_{0.5}NiSn$ samples. Rietveld analysis has revealed the presence of excess Ni within the half-Heusler structures. 2% additional Ni was located on the vacant M2 tetrahedral site in the TiNiSn sample investigated here, and 4-6% has been found previously in arc-melted TiNiSn samples (Chapter 3).[139] About 1% is indicated for HfNiSn, while about 4% is reported in the literature for ZrNiSn.[138] Excess Ni was also observed in $Ti_{0.5}Zr_{0.5}NiSn$ and $Ti_{0.5}Hf_{0.5}NiSn$, but not for $Zr_{0.5}Hf_{0.5}NiSn$. Our results indicate the presence of genuine interstitial Ni, distributed throughout the M2 sites in the half-Heusler structure. It appears to be very difficult to prevent this as both arc-melted and solid state samples show similar amounts of excess Ni. It therefore seems likely that most half-Heusler samples will contain some interstitial Ni, in conjunction with the micro- and nano-inclusions of full-Heusler reported by other groups.[26, 90, 92-95, 104] Chai *et* al recently postulated that interstitial Ni is initially formed and that these subsequently cluster to form nano- and eventually micro-inclusions.[93] This is in keeping with our observation of interstitials from neutron diffraction. The observation of interstitials in this work and nano/micro-inclusions elsewhere suggests that these samples are under kinetic control.

Neutron powder diffraction has also allowed further characterisation of the multiphase behaviour, due to the presence of multiple X-metals. Using this technique, we were able to refine the Ti:Zr and Ti:Hf ratios for each of the modelled phases and deduce the compositional spread associated with each phase present. Δx values deduced from the neutron data are narrower than those calculated from the X-ray data. This may be because neutrons are more penetrating than X-rays thus probe more of the bulk sample, while X-rays may provide information on features nearer the surface. This suggests that a large part of the compositional variation occurs close to the surface and that the bulk

shows less variation. This is in-keeping with the TEM analysis which showed very little compositional variation between different areas within and between the investigated particles. The $x_{Rietveld}$ and x_{Vegard} values determined from the neutron powder diffraction are in good agreement, particularly for phases with larger x_V. Discrepancies occur at lower x_V-values but the average x_R and x_V values are identical, suggesting this is an artefact in the refinement, rather than a genuine departure from Vegard's law.

The temperature dependent neutron diffraction study into $Ti_{0.5}Hf_{0.5}NiSn$ showed no change in phase-distribution as the temperature was increased. In addition to the temperature steps reported in Table 4, this sample was held at 600 °C for 10 hours and re-measured at regular intervals. The reflections remained the same shape throughout, indicating no change in the distribution. In terms of application this highlights that these materials show stability to prolonged exposure to high temperatures, which is of vital importance for thermoelectric materials.

4.5 $Ti_{1-x}Zr_xNiSn_{1-y}Sb_y$

Sb-doping on the Sn site of XNiSn-based half-Heuslers is a well-established route to improving the electronic properties of these materials for thermoelectric applications. This substitution introduces additional electrons to the (NiSn) sub-lattice that is largely believed to be responsible for the electronic conduction in these structures. Careful substitution therefore allows optimisation of the carrier concentration resulting in enhancements in the figure-of-merit.

For this reason, Sb-doped samples of $Ti_{0.5}Zr_{0.5}NiSn_{1-y}Sb_y$, y = 0.005, 0.01 and 0.02, were prepared. Careful analysis of the structure was then carried out as this type of doping is often performed as a final step, with little regard to the effect this may have. Electronic properties have also been determined. No thermal conductivity measurements were performed due to the relatively low density of the samples.

4.5.1 X-ray Diffraction

X-ray diffraction patterns of the 3 samples are presented in Figure 4.20.

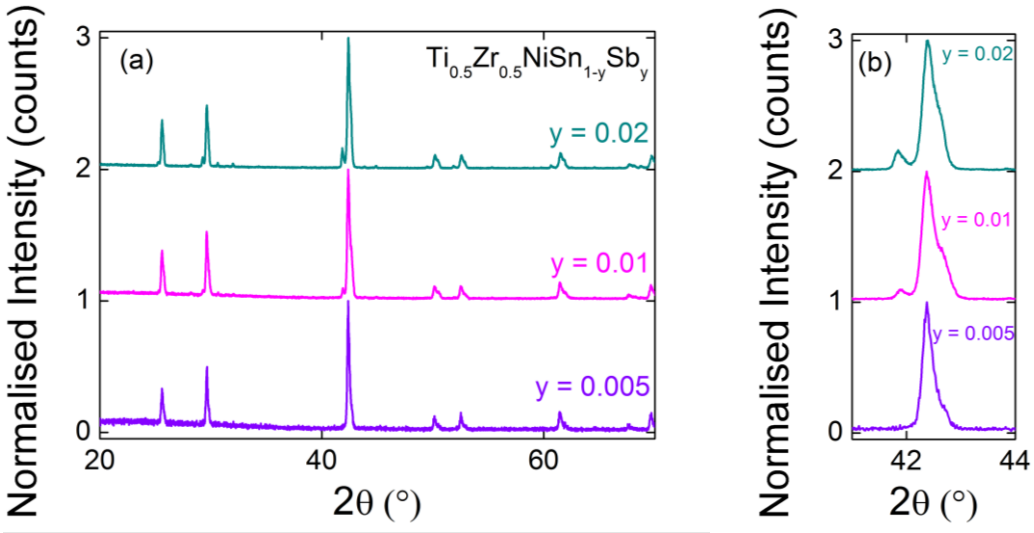

Figure 4.20: (a) X-ray diffraction patterns for the $Ti_{0.5}Zr_{0.5}NiSn_{1-y}Sb_y$ series. (b) close-up for the (220) peak.

From this it may be observed, unsurprisingly, that these samples do not form single phase samples and produce peak shapes consistent with the multiphase behaviour seen in the non-doped samples. These patterns have been treated in exactly the same manner as those presented in Section 4.3.1.

Table 4.7: Nominal composition, lattice parameter (a), Vegard composition (x_i), composition spread (Δx_i), molar percentage (mol%), average composition (x_{avg}) and goodness-of-fit (χ^2) for $Ti_{0.5}Zr_{0.5}NiSn_{1-y}Sb_y$, as determined from X-ray diffraction data.

y	a (Å)	x_i	Δx	mol%	x_{avg}	χ^2
0.005	5.9920(6)	0.35(1)	0.14(1)	12(1)	0.53(1)	1.2
	6.0188(7)	0.50(1)	0.14(1)	37(3)		
	6.0350(5)	0.59(1)	0.10(1)	51(2)		
0.01	5.9977(2)	0.38(1)	0.26(1)	31.7(4)	0.51(1)	2.6
	6.0310(1)	0.57(1)	0.18(1)	67.2(4)		
	6.1005(3)	0.98(1)	0	1.1(1)		
0.02	5.9972(1)	0.38(1)	0.16(1)	26.4(4)	0.51(1)	3.2
	6.0247(1)	0.53(1)	0.18(1)	67.9(4)		
	6.0998(2)	0.95(1)	0.09(1)	5.7(1)		

In each case, three phases were required to adequately fit the peak shape. Each had an associated compositional spread of similar values to those determined for the undoped samples. Lattice parameters and weight fractions are presented in Table 4.7. This

creates a very similar picture to the $Ti_{0.5}Zr_{0.5}NiSn$ sample, with a continuous spread covering a range of $\Delta x \approx 0.4$ for each sample. Combination of the calculated x-values with the associated phase fractions produces values very close to x = 0.5 in all cases.

4.5.2 Electronic Properties

The temperature dependences of the Seebeck coefficient, resistivity and power factor of the three samples are presented in Figure 4.21. Data for $Ti_{0.5}Zr_{0.5}NiSn$ is also replicated here, for comparison. Immediately apparent is a reduction in the Seebeck coefficient, with room temperature values dropping from -320 $\mu V\ K^{-1}$ for y = 0 to -200 $\mu V\ K^{-1}$ for y = 0.05. The values are further reduced as y is increased, reaching S = -100 $\mu V\ K^{-1}$ for y = 0.2. The temperature dependence is also altered, and increases almost linearly with temperature, while the un-doped samples show a decrease. This is consistent with electron-doping.

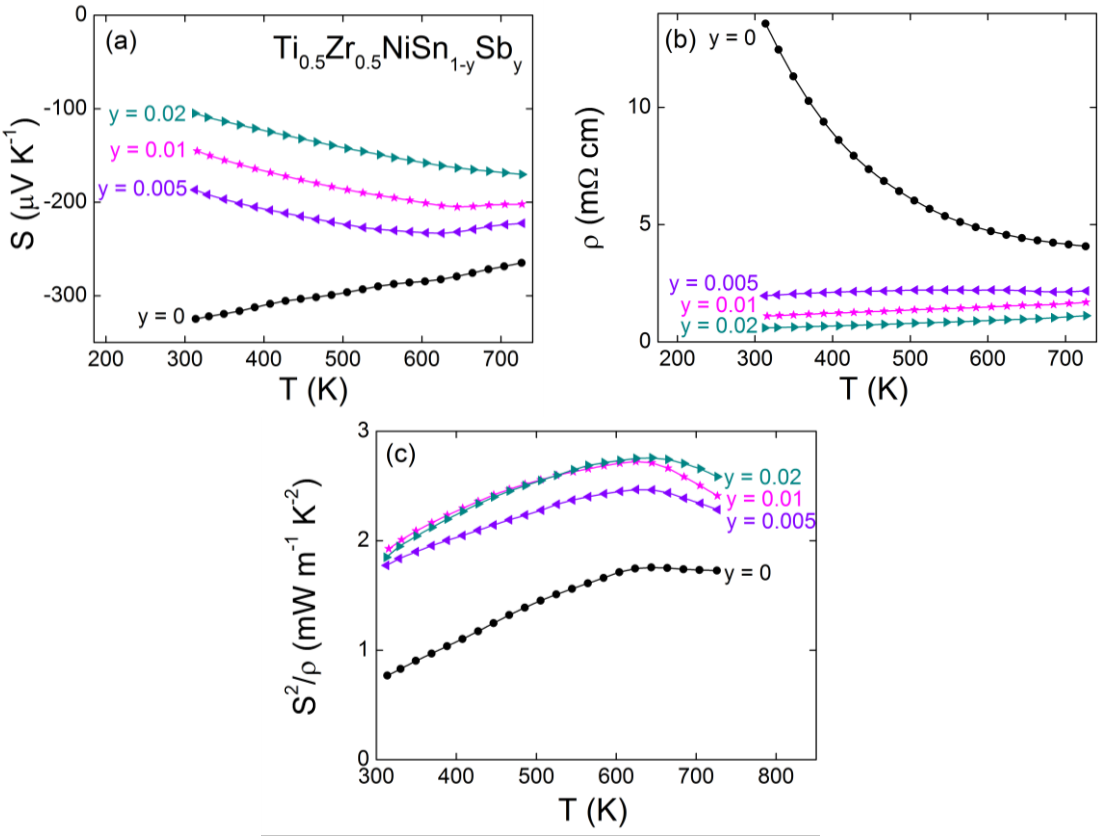

Figure 4.21: Temperature dependences of (a) Seebeck coefficient (S), (b) resistivity (ρ) and (c) power factor (S^2/ρ) for the $Ti_{0.5}Zr_{0.5}NiSn_{1-y}Sb_y$ series.

The temperature dependence of the resistivity immediately becomes metallic at the y = 0.05 level. This is consistent with the Seebeck measurement and the electron doping effect of the Sb substitution. The reduction in the resistivity of these samples more than offsets the reduction in Seebeck coefficient, thus all three out-perform $Ti_{0.5}Zr_{0.5}NiSn$ in terms of power factor. The best performing of the three tested samples is $Ti_{0.5}Zr_{0.5}NiSn_{0.98}Sb_{0.02}$, which achieves a maximum S^2/ρ = 2.75 mW m^{-1} K^{-2} at 675 K. This is very similar to the value achieved by $Ti_{0.5}Zr_{0.5}NiSn_{0.99}Sb_{0.01}$ which suggests that y = 0.02 may be close to the upper limit of useful substitution.

4.5.3 Discussion

Sb-doping is clearly a very effective means of optimising the electronic properties of these materials. The electron doping effect substantially reduces the resistivity and sacrifices the exceptional Seebeck coefficient. A moderately good Seebeck coefficient is maintained for lower doping levels, which allows a substantial increase in the power factor. Densification of these samples is now required so that a full characterisation of the thermoelectric properties may be performed. The multiphase behaviour described in detail for the $Ti_{1-x}Zr_xNiSn$ series is maintained in these samples, and a similar phase distribution was found, in comparison with the undoped samples. This provides further evidence that this behaviour occurs in all XNiSn-based samples with mixed X-metals, regardless of composition and initial synthesis conditions.

4.6 Densification

As evidenced throughout this thesis, densification of samples is important if the thermal conductivity is to be measured with any degree of accuracy. The cold-pressing and annealing-based synthetic procedures used in this chapter and Chapter 5 produce samples between 68 and 83% dense, which is insufficient for these measurements. Arc-melting, as described in Chapter 3, produces fully dense samples but at the cost of losing tight control of the final composition. Alternative, post-anneal techniques have been explored during the course of preparing these samples. These were proved unsuccessful, for the reason set out below.

4.6.1 Hot-Pressing

An in-house hot-press system, summarised in Chapter 2, was used to press a TiNiSn sample after it had been annealed for 2 weeks. Post synthesis, the sample density was calculated to be 75% of the crystallographic density.

The sample was then ground to a fine powder and loaded into the hot-press, as per the description in Chapter 2. A pressure of 60 bar and 650 °C was applied for 30 minutes. The resultant pellet was removed from the press and the graphite that transferred from the mould was removed. The sample was then calculated to be 84% dense. This is still insufficient for reliable thermal conductivity measurements but was pressed at the upper limit of the operating conditions for this particular hot-press.

4.6.2 Spark-Plasma-Sintering

The theory behind spark-plasma-sintering (SPS) is presented in Chapter 2. 5 g test samples were specially prepared as described in Section 4.2. Several temperatures and pressures were used in order to determine optimum conditions. These are summarised in Table 4.8. X-ray diffraction analysis revealed that some samples sintered at 1000 and 1050 °C contained a strong impurity peak associated with carbon. Optimum conditions were therefore determined to be 900 °C and 80 MPa. Peak shapes were not significantly altered by the SPS process, as evidenced in Figure 4.22, indicating that the multiphase behaviour of these samples is maintained. The X-ray patterns, produced before and after SPS have been analysed in the same manner as those for the other samples presented in this Chapter. Results are collated in Table 4.9 and show that while small changes do occur in the precise phase distribution, the overall picture remains the same, with a broad range of x-values present in any given sample.

Table 4.8: SPS conditions for various $Ti_{0.5}Zr_{0.5}NiSn_{1-y}Sb_y$ samples.

Composition	Conditions	Density (%)
$Ti_{0.5}Zr_{0.5}NiSn_{0.95}$	1000 °C / 50 MPa	84
$Ti_{0.5}Zr_{0.5}NiSn_{0.94}Sb_{0.01}$	1050 °C / 80 MPa	96
$Ti_{0.5}Zr_{0.5}NiSn$	1050 °C / 80 MPa	99
$Ti_{0.5}Zr_{0.5}NiSn_{0.99}Sb_{0.01}$	1050 °C / 80 MPa	98
$Ti_{0.5}Zr_{0.5}NiSn_{0.98}Sb_{0.02}$	900 °C / 50 MPa	83
$Ti_{0.5}Zr_{0.5}NiSn$	900 °C / 80 MPa	99

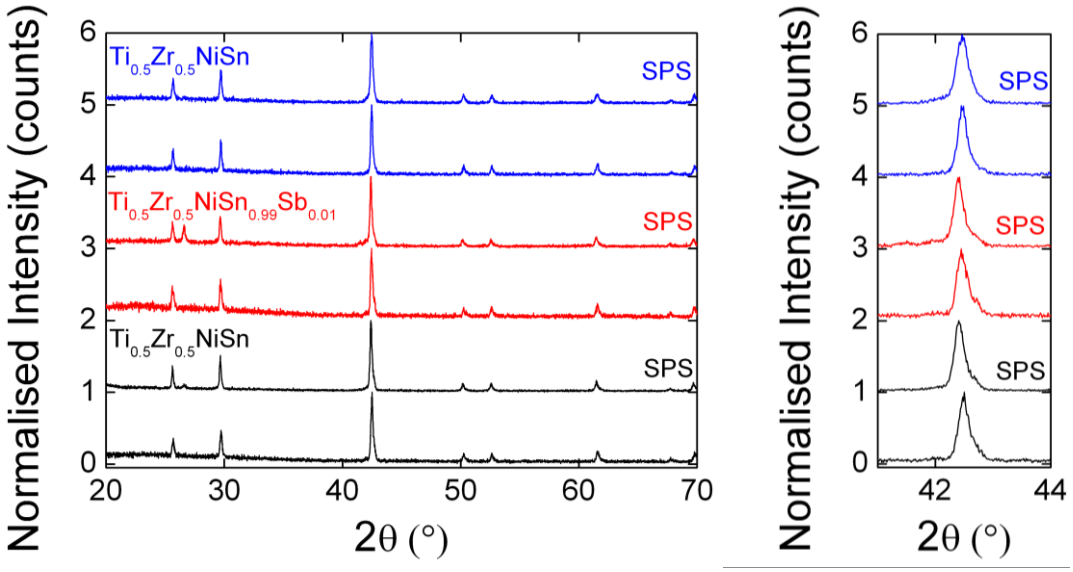

Figure 4.22: X-ray diffraction patterns for 3 $Ti_{0.5}Zr_{0.5}NiSn_{1-y}Sb_y$ samples, pre- and post-SPS.

Table 4.9: Nominal composition, lattice parameter (a), Vegard composition (x_i), composition spread (Δx_i), molar percentage (mol%), average composition (x_{avg}) and goodness-of-fit (χ^2) for samples prepared for SPS, pre- and post-SPS, as determined from X-ray diffraction data.

Composition	**a (Å)**	**x_i**	**Δx**	**mol%**	**x_{avg}**	**χ^2**
$Ti_{0.5}Zr_{0.5}NiSn$ (1) pre-SPS	5.995(1)) 6.014(1) 6.0286(8)	0.37(1) 0.47(1) 0.50(1)	0.12(1) 0.12(1) 0.13(1)	10(1) 29(5) 61(5)	0.48(1)	1.2
$Ti_{0.5}Zr_{0.5}NiSn$ (1) SPS	5.9970(9) 6.021(1) 6.0336(5)	0.37(1) 0.57(1) 0.58(1)	0.13(1) 0.13(1) 0.15(1)	8(1) 28(1) 64(1)	0.56(1)	1.2
$Ti_{0.5}Zr_{0.5}NiSn$ (2) pre-SPS	5.995(2) 6.022(4) 6.0270(7)	0.37(1) 0.52(1) 0.55(1)	0.23(1) 0.23(1) 0.12(1)	9(1) 24(2) 67(1)	0.53(1)	1.2
$Ti_{0.5}Zr_{0.5}NiSn$ (2) SPS	6.003(1) 6.021(1) 6.0330(9)	0.41(1) 0.51(1) 0.58(1)	0.12(1) 0.12(1) 0.21(1)	8(2) 27(7) 64(7)	0.55(1)	1.1
$Ti_{0.5}Zr_{0.5}NiSn_{0.99}Sb_{0.01}$ pre-SPS	5.988(1) 6.011(1) 6.0270(9) 6.096(4)	0.33(1) 0.46(1) 0.55(1) 0.93(1)	0.11(1) 0.11(1) 0.11(1) 0.03(1)	10(1) 33(5) 56(5) 0.7(5)	0.50(1)	1.1
$Ti_{0.5}Zr_{0.5}NiSn_{0.99}Sb_{0.01}$ SPS	6.000(1) 6.024(2) 6.0366(9) 6.097(5)	0.39(1) 0.53(1) 0.60(1) 0.94(1)	0.15(1) 0.15(1) 0.14(1) -	8(1) 27(8) 54(8) 10(2)	0.59(1)	1.4

Bars were cut from the fully-dense SPS pellets for Seebeck coefficient and resistivity measurements, and disks were cut for thermal conductivity measurements. These are summarised in Figure 4.23, below.

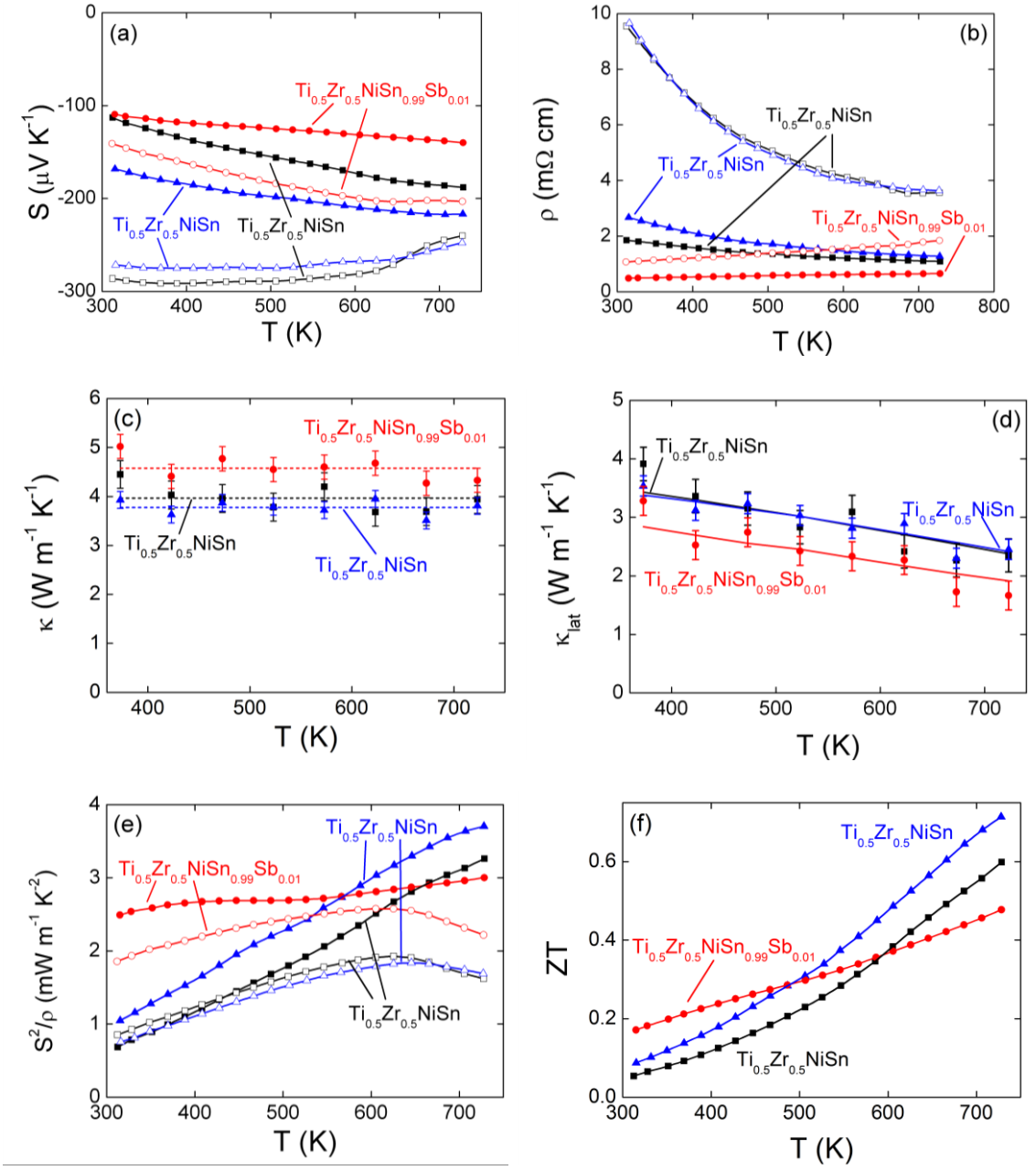

Figure 4.23: Temperature dependence of (a) Seebeck coefficient (S), (b) resistivity (ρ), (c) thermal conductivity (κ), (d) lattice thermal conductivity (κ_{lat}), (e) power factor (S^2/ρ) and (f) ZT for $Ti_{0.5}Zr_{0.5}NiSn_{1-y}Sb_y$ samples, post-SPS. Open symbols indicate measurements prior to SPS. Closed symbols are measurements for samples after SPS.

Immediately apparent from the thermoelectric property measurements is a dramatic reduction in resistivity, for all three samples. The $Ti_{0.5}Zr_{0.5}NiSn$ samples are reduced by a factor of 5 at room temperature, and a factor of 4 at 730 K. $Ti_{0.5}Zr_{0.5}NiSn_{0.99}Sb_{0.01}$ is reduced by over a half across the whole temperature range. Reduction of the resistivity values was expected, as this property is affected strongly by the density of the samples, however, such a large reduction is surprising. As a bulk property, the Seebeck coefficient should not be altered by density changes. All three samples show a decrease in S. Both $Ti_{0.5}Zr_{0.5}NiSn$ samples show a reduction by a factor of three at room temperature and are reduced by a fifth of the original value at 730 K. This is accompanied by a change in temperature dependence.

Prior to SPS the samples show a decrease in S with temperature. This is reversed after the SPS treatment. This is indicative of a significant electron doping effect and demonstrates that the intrinsic properties of these materials are altered by the SPS process used. This is therefore not a viable technique for densification of these samples, where knowledge of the structure is of utmost importance.

The power factor, thermal conductivity and ZT values for the samples post-SPS have been measured and are presented in Figure 4.23. Power factor values reach 3.75 mW m^{-1} K^{-2} for one of the $Ti_{0.5}Zr_{0.5}NiSn$ samples. Thermal conductivity values are consistent with those measured for the arc-melted samples in Chapter 3, as the $Ti_{0.5}Zr_{0.5}NiSn$ samples maintain a value of approximately 4 W m^{-1} K^{-1} over the whole temperature range. $Ti_{0.5}Zr_{0.5}NiSn_{0.99}Sb_{0.01}$ has higher values (≈ 4.5-5 W m^{-1} K^{-1}). The nominal $Ti_{0.5}Zr_{0.5}NiSn$ samples achieve ZT = 0.6 and 0.7, while nominal $Ti_{0.5}Zr_{0.5}NiSn_{0.99}Sb_{0.01}$ reaches ZT = 0.5.

While these are promising values, these samples have been electron-doped in an unknown manner by the SPS process. There are no indications of impurities in the X-ray patterns and based on the current data available on these samples, it is not possible to determine the changes that have occurred within the structure.

4.6.3 Discussion

The techniques outlined above have proved to be unsuitable for densification of the samples presented throughout this thesis. The hot-press described simply cannot attain the conditions required to fully densify these samples. SPS is certainly capable of

achieving full density for these samples, but the current conditions altered the intrinsic properties of the samples. Until this change can be eliminated, this is not a suitable technique for post-synthesis densification. These samples, which were subjected to an additional processing step compared with the other samples presented in Chapters 3 and 4, also exhibit multiphase behaviour. The SPS process did not significantly alter the phase distribution of these samples thus the multiphase arrangement appears to be rather stable and extremely difficult to prevent or eradicate.

4.7 Conclusions

The main focus of this chapter was an investigation of the $Ti_{1-x}Zr_xNiSn$ series, focussing in particular on the multiphase behaviour that was first observed in the arc-melted $Ti_{0.5}Zr_{0.5}NiSn$ sample in Chapter 3. Analysis of the X-ray diffraction data confirmed the presence of multiple half-Heusler phases with differing Zr content, x_i, each with an additional compositional spread, Δx, for x = 0.25, 0.5 and 0.75. This results in an almost continuous distribution of phases, covering a large x-range (e.g. $\Delta x = 0.5$ for $Ti_{0.5}Zr_{0.5}NiSn$). Neutron diffraction confirmed this analysis but smaller Δx values were produced, indicating that the majority of the multiphase behaviour occurs near the sample surface. This is in keeping with microscopy images for $Ti_{0.5}Zr_{0.5}NiSn$ which show little compositional variation within and between some of the grains investigated. In addition, thermoelectric property measurements revealed that multiphase behaviour does not have any significant impact on these samples. Multiphase behaviour is not confined to the $Ti_{1-x}Zr_xNiSn$ series and similar behaviour was identified in $Ti_{0.5}Hf_{0.5}NiSn$ and $Zr_{0.5}Hf_{0.5}NiSn$ and Sb-doped samples. It was not significantly altered by SPS processing. The occurrence of this behaviour in every XNiSn sample with mixed X-metals, regardless of synthesis and composition suggests that these half-Heusler materials are very difficult to produce as perfect solid solutions.

Rietveld analysis of neutron powder data has also demonstrated that genuine interstitial Ni is commonly present in all XNiSn half-Heusler compositions. Electron microscopy data, collected for $Ti_{0.5}Zr_{0.5}NiSn$, did not indicate the formation of full-Heusler inclusions in this sample. This has often been reported for samples that contain intentional excess Ni but does not appear to be the case for these nominally stoichiometric samples. These samples therefore appear to be predisposed to forming

with interstitial Ni which is almost impossible to detect without neutron diffraction. They may therefore be present in many of the reported samples throughout the literature. The effect these interstitials have on the thermoelectric properties is therefore a key concern, thus a systematic investigation has been carried out and is presented in Chapter 5.

In summary, these are clearly complex samples which contain multiple interesting structural features, both within the unit cell and microstructure. Evaluation of the thermoelectric properties reported in the literature, for nominally identical compositions, indicates that combinations of some of these features, and possibly others, are likely present within each of these samples. This highlights the importance of careful structural analysis as part of the study of half-Heusler thermoelectrics, so that a good understanding of the correlation between certain features and the resulting properties may be determined.

Chapter 5 – Interstitial Doping in TiNiSn

5.1 Introduction

A relatively novel approach to reducing the thermal conductivity of XNiSn-based half-Heusler alloys is the introduction of excess Ni. The $TiNiSn_{0.95/1.0}$ samples presented in Chapter 3 were found to contain between 3.5 and 5.5% interstitial Ni and achieved $\kappa = 4$ W m^{-1} K^{-1}, leading to a maximum ZT value of 0.6 at 700 K.[139] In Chapter 4, interstitial Ni was also identified in other XNiSn and $X_{0.5}X'_{0.5}NiSn$ samples (X,X' = Ti, Zr, Hf).

While reduction in κ is of vital importance to improving ZT, advances in power factor must also be achieved. The samples presented in this chapter were prepared with a view to altering the electronic properties of TiNiSn through the introduction of excess metal to the structure. It has been reported that addition of extra Ni to the half-Heusler structure causes simultaneous enhancement of the Seebeck coefficient and electrical conductivity due to the formation of full-Heusler nano-inclusions within the half-Heusler matrix.[90] Other reports show enhanced Seebeck coefficients with a smaller than expected reduction in the electrical conductivity, also coinciding with the presence of full-Heusler nano-inclusions.[89] However, the exact nature of the effect of adding excess Ni to this system is not yet clear. While some work does show these remarkable improvements to the electronic behaviour of these systems, others do not. Differing results have also been found regarding the incorporation of Ni into the structure. While several reports cite the formation of nano-inclusions,[90, 92-95, 104, 105] others do not.[87, 141]

The recently published work cited above reports the formation of either nano- or micro-inclusions of a full-Heusler phase upon introduction of excess Ni to the half-Heusler structure. The effects of interstitial Ni are, however, not well explored. The aim of this chapter was therefore to investigate how the excess metals are incorporated into the TiNiSn structure. Three series were prepared, using Ni, Co and Cu as the additional metal. The $TiNi_{1+y}Sn$ series was prepared with y ranging from 0 to 1 to investigate the structural changes over the whole possible range. Two $TiNiM_ySn$ series, where M = Co and Cu and y = 0.025, 0.05 and 0.075 were prepared to further explore the possibility of using excess metal as a means to controlling the electronic properties of these materials.

5.2 Synthesis

All three series, $TiNiM_ySn$ (M = Ni, Co, Cu and $0 \leq y \leq 1$), were prepared on a 3 g scale by standard solid state reactions. Stoichiometric quantities of the powdered starting materials were mixed for all samples. The mixtures were then pressed into pellets, wrapped in Tantalum foil and vacuum sealed in quartz tubes. Samples were initially annealed at 900 °C for 24 hours, then homogenised and annealed at 900 °C for a further 2 weeks. The annealed pellets were 70-80% dense. Bars were cut from these pellets using a low-speed diamond saw for thermoelectric property measurements and electron microscopy analysis. The remainder of the sample was finely ground for X-ray and neutron powder diffraction experiments.

5.3 X-ray Powder Diffraction

All samples were initially analysed by X-ray powder diffraction to determine phase formation and purity. In all cases, sharp peaks that could be indexed by the half-Heusler *F-43m* space group were identified. In addition the $TiNi_{1+y}Sn$ samples, where $y > 0.1$, were found to contain a minor full-Heusler ($TiNi_2Sn$) impurity phase. As illustrated by Figure 5.1, there is an increase in intensity of the full-Heusler phase as y is increased. No other impurity peaks are observable in the patterns until $y = 1$, where a Ni_3Sn_2 phase is identifiable. The $TiNiCu_ySn$ and $TiNiCo_ySn$ samples produced X-ray diffraction patterns containing sharp peaks which could all be indexed to the half-Heusler structure, as can be seen in Figure 5.2. No evidence for a full-Heusler phase or any impurity phases exists for these samples.

Rietveld refinement of each of the diffraction patterns displayed in Figure 5.1 and Figure 5.2 was performed, and representative fits for the $y = 0.05$ samples are displayed in Figure 5.3. Lattice parameters and weight fractions, where appropriate, for the three series are presented in Table 5.1 and Table 5.2.

Table 5.1: lattice parameters (a), weight fraction (wt%), calculated y (y_{Vegard}), average composition and goodness-of-fit (χ^2) obtained from Rietveld refinement of X-ray diffraction data for $TiNi_{1+y}Sn$

y	Half-Heusler Phase			Full-Heusler Phase			Average Composition	χ^2
	a (Å)	mol%	y_{Vegard}	a (Å)	mol%	y_{Vegard}		
0	5.9300(1)	100	0	-	-	-	TiNiSn	2.0
0.025	5.9309(1)	100	0.005	-	-	-	$TiNi_{1.005}Sn$	1.4
0.05	5.9356(1)	100	0.033	-	-	-	$TiNi_{1.033}Sn$	1.4
0.075	5.9352(1)	100	0.032	-	-	-	$TiNi_{1.032}Sn$	1.3
0.1	5.9378(1)	96.9(3)	0.047	6.0752(5)	3.1(3)	0.884	$TiNi_{1.066}Sn$	1.2
0.25	5.9407(1)	62.4(3)	0.065	6.0756(1)	37.6(3)	0.884	$TiNi_{1.318}Sn$	1.2
0.5	5.9401(1)	22.8(3)	0.061	6.0744(1)	77.2(3)	0.876	$TiNi_{1.643}Sn$	1.3
1	-	-	-	6.0948(1)	90.7(5)	1	$TiNi_2Sn$	1.2

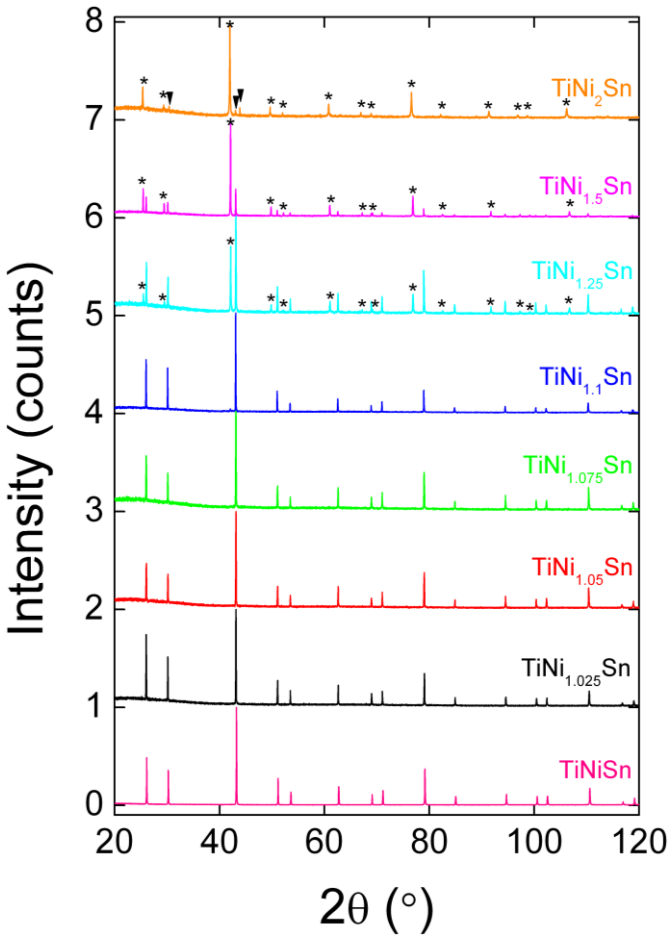

Figure 5.1: X-ray diffraction patterns collected for the $TiNi_{1+y}Sn$ series. * indicate peaks belonging to the full-Heusler 'TiNi$_2$Sn' phase and peaks marked ▼ belong to the Ni_3Sn_2 impurity phase.

Table 5.2: Lattice parameters (a), and goodness-of-fit (χ^2) obtained from Rietveld refinement of X-ray diffraction data for $TiNiCo_ySn$ and $TiNiCu_ySn$.

y	a (Å)	χ^2
$TiNiCo_ySn$		
0.025	5.9295(1)	1.7
0.05	5.9363(1)	1.3
0.075	5.9453(1)	1.2
$TiNiCu_ySn$		
0.025	5.9334(1)	1.3
0.05	5.9404(1)	1.3
0.075	5.9464(1)	1.2

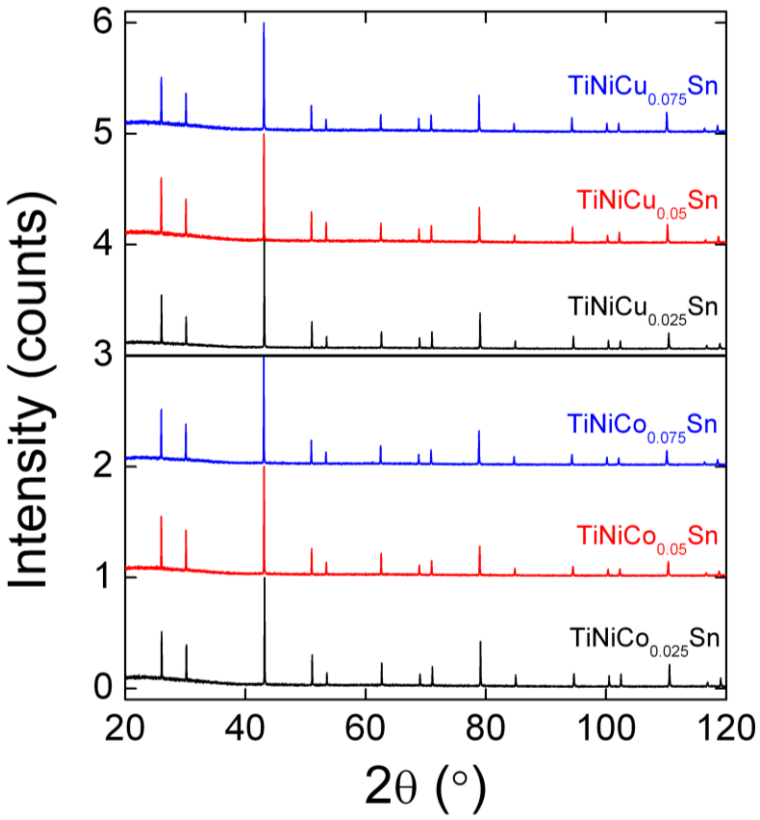

Figure 5.2: X-ray powder diffraction patterns collected for the $TiNiCo_ySn$ and $TiNiCu_ySn$ series.

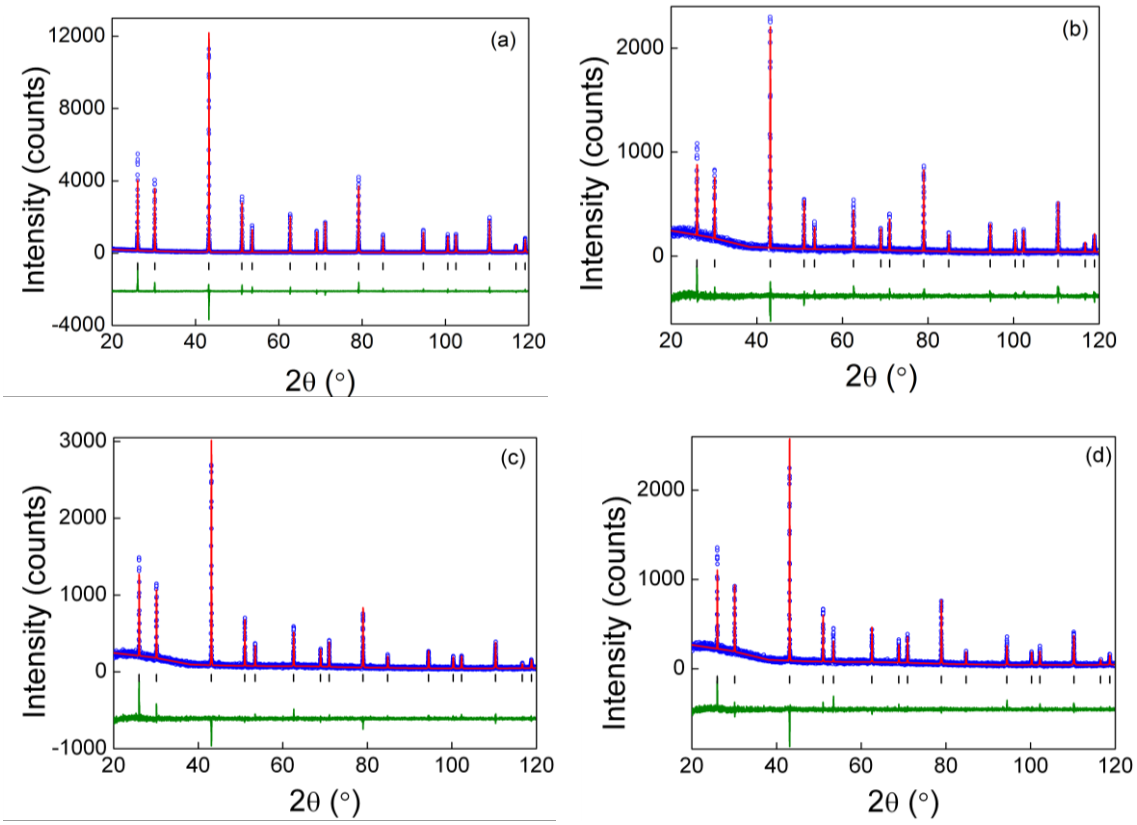

Figure 5.3: Rietveld refinement fits to X-ray powder diffraction data collected for (a) TiNiSn, (b) $TiNi_{1.05}Sn$, (c) $TiNiCo_{0.05}Sn$ and (d) $TiNiCu_{0.05}Sn$. Blue circles are the collected data, the red line is the calculated fit and the green line is the difference. Tickmarks correspond to the half-Heusler Bragg positions.

Analysis of the lattice parameters of the half-Heusler phases of the $TiNi_{1+y}Sn$ samples reveals an increase in a, as y is increased to just above the nominal y = 0.1 level. Thereafter, the lattice parameter values show no real change, as illustrated in Figure 5.4. This indicates that excess Ni has been introduced into the half-Heusler phase. The expansion of the unit cell up to y = 0.1, suggests that increasing amounts of excess Ni are being introduced to the phase, with an upper limit of 10% excess Ni allowed.

An estimation of the amount of excess Ni in the half-Heusler phase in the $TiNi_{1+y}Sn$ samples may be made using Vegard's law, as per Equation (5.1) below. The results of these calculations are presented in Table 5.1 and suggest that 6-7% excess Ni can be accommodated in TiNiSn.

$$y = \frac{a_{int} - a_{HH}}{a_{FH} - a_{HH}} \qquad \text{Equation (5.1)}$$

where a_{HH} is the lattice parameter of TiNiSn, a_{FH} is the lattice parameter of $TiNi_2Sn$ and a_{int} is the lattice parameter of the intermediate composition.

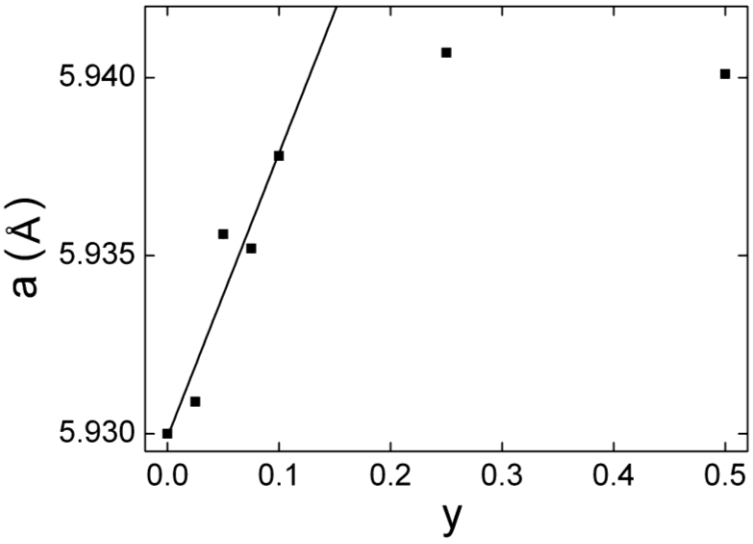

Figure 5.4: Change in lattice parameter (a) with nominal doping level (y) in $TiNi_{1+y}Sn$.

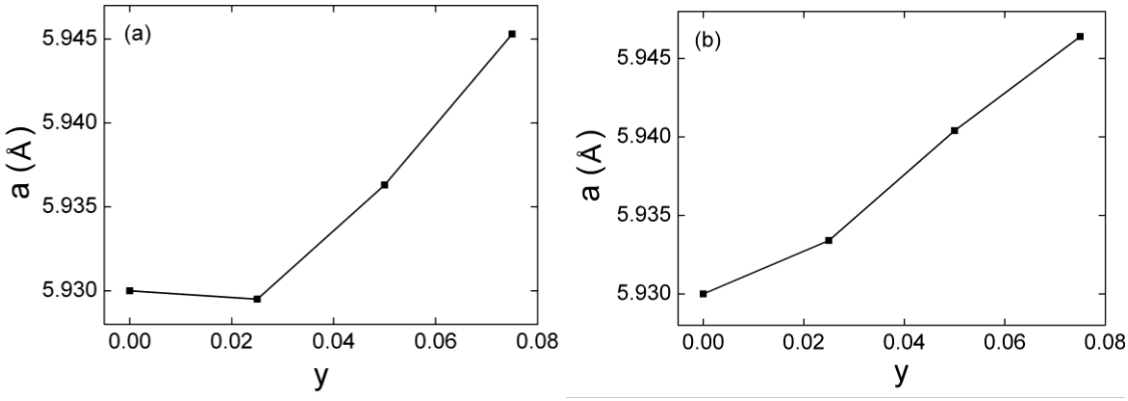

Figure 5.5: Change in lattice parameter (a) with nominal doping level (y) for (a) $TiNiCo_ySn$ and (b) $TiNiCu_ySn$.

The Co- and Cu-doped series also show an increase in lattice parameter as y is increased, as displayed in Figure 5.5. This indicates that the excess metal has been introduced to the half-Heusler structure. The lattice parameters, along with fit statistics for the refinements are presented in Table 5.2. As there is no data available regarding the lattice parameters of TiNiCoSn or TiNiCuSn, no estimate of the amount of excess

metal present in these structures can be made from the lattice parameter using Vegard's law.

5.4 Neutron Powder Diffraction

5.4.1 $TiNi_{1+y}Sn$

Rietveld refinement was carried out on neutron powder diffraction data collected for each sample in this series, with a view to refining site occupancies and determining the amount of excess Ni that was successfully introduced to the half-Heusler phase. Data for the TiNiSn sample was presented and analysed in detail in Chapter 4 and is repeated here only for comparison. The results obtained from the neutron data for each of the $TiNi_{1+y}Sn$ samples match well with those obtained from the X-ray data. Lattice parameters for both the half- and full-Heusler phases, along with their molar percentages are presented in Table 5.3. A best fit model was achieved by placing the excess Ni on the normally vacant M2 site. The refined site occupancies are also presented in Table 5.3. The level of excess Ni in the half-Heusler phase increases with the nominal y-value as expected, although the nominal and experimental compositions do not match due to the presence of the full-Heusler phase. From the refined values, a maximum of 8% interstitial Ni was successfully added to the half-Heusler.

Refinement of the site occupancies for the full-Heusler phase revealed a composition of $Ti_{1.2}Ni_{1.8}Sn$ in all cases, where some excess Ti occupies the Ni sites. Combination of the site occupancies over the two phases, taking into account the related phase fractions, yields the average compositions summarised in Table 5.3. These compositions closely match the nominal values, with the exception of a 2% Ni excess, over and above the nominal value. This is observed in every sample and suggests that the TiNiSn-based half-Heuslers naturally form with a small amount of excess Ni, when prepared by the methods set out in Section 4.2. This is in-keeping with results found in the XNiSn and $X_{0.5}X'_{0.5}NiSn$ samples presented in Chapter 4.

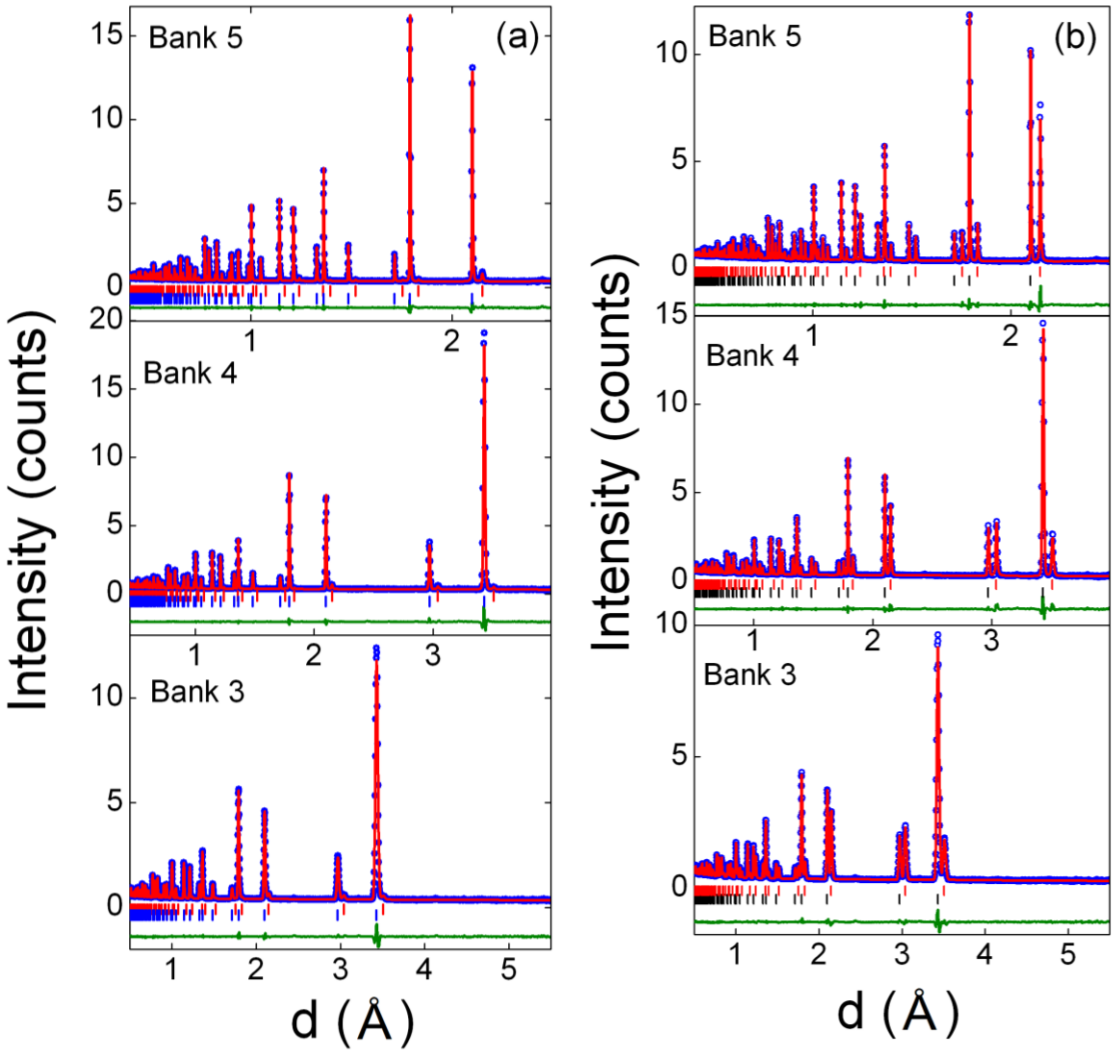

Figure 5.6: Rietveld refinement fits to neutron diffraction data collected for (a) $TiNi_{1.05}Sn$, and (b) $TiNi_{1.25}Sn$. Blue circles are the collected data, the red line is the calculated fit and the green line is the difference. Upper (red) tickmarks correspond to the full-Heusler Bragg positions. Lower tickmarks correspond to the half-Heusler phase.

Table 5.3: Lattice parameters (a), molar percentages, fractional occupancies, temperature displacement factors (U_{iso} / Å^2), and refined compositions for the $TiNi_{1+y}Sn$ series from fits against Polaris neutron powder diffraction data.

	y		0	0.025	0.05	0.075	0.1	0.25	0.5	1
Half-Heusler	**a (Å)**		5.9297(1)	5.9305(1)	5.9355(1)	5.9349(1)	5.9371(1)	5.9386(1)	5.9394(1)	-
	Weight %		100	98.94(6)	95.5(2)	94.8(2)	92.5(1)	69.1(1)	35.4(1)	-
	Ti *(4a)*	Occ	1	1	1	1	1	1	1	-
		U_{iso}	0.00494(7)	0.00447(7)	0.00436(7)	0.00439(7)	0.00435(7)	0.00438(9)	0.0041(2)	-
	Ni *(4c)*	Occ	1	1	1	1	1	1	1	-
		U_{iso}	0.00499(5)	0.00495(5)	0.00514(5)	0.00511(5)	0.00539(5)	0.00569(6)	0.0059(1)	-
	Ni *(4d)*	Occ	0.021(1)	0.041(1)	0.056(1)	0.060(1)	0.071(1)	0.078(1)	0.080(2)	-
		U_{iso}	0.00499(5)	0.00495(5)	0.00514(5)	0.00511(5)	0.00539(5)	0.00569(6)	0.0059(1)	-
	Sn *(4b)*	Occ	1	1	1	1	1	1	1	-
		U_{iso}	0.00405(6)	0.00399(6)	0.0408(5)	0.00406(5)	0.00418(5)	0.00432(7)	0.0045(1)	-
	Fitted Composition		$TiNi_{1.021(1)}Sn$	$TiNi_{1.041(1)}Sn$	$TiNi_{1.056(1)}Sn$	$TiNi_{1.060(1)}Sn$	$TiNi_{1.071(1)}Sn$	$TiNi_{1.078(1)}Sn$	$TiNi_{1.080(2)}Sn$	-
Full-Heusler	**a (Å)**		-	6.0691(4)	6.0756(3)	6.0764(2)	6.0767(1)	6.0750(1)	6.0744(1)	6.0955(1)
	Weight %		-	1.06(6)	4.5(2)	5.2(2)	7.5(1)	30.9(1)	64.6(1)	94.40(6)*
	Ti *(4a)*	Occ	-	1	1	1	1	1	1	1
		U_{iso}	-	0.001	0.011(1)	0.008(1)	0.0084(3)	0.0070(2)	0.0072(1)	0.0054(1)
	Ni *(8c)*	Occ	-	0.86(4)	0.88(1)	0.95(1)	0.94(1)	0.925(2)	0.925(1)	0.991(2)
		U_{iso}	-	0.001	0.0105(7)	0.0131(6)	0.0123(3)	0.0118(1)	0.01192(7)	0.01195(7)
	Ti *(8c)*	Occ	-	0.14(2)	0.12(1)	0.05(1)	0.06(1)	0.075(2)	0.075(1)	
		U_{iso}	-	0.001	0.0105(7)	0.0131(6)	0.0123(3)	0.0118(1)	0.01192(7)	
	Sn *(4b)*	Occ	-	1	1	1	1	1	1	1
		U_{iso}	-	0.001	0.009(1)	0.009(1)	0.0085(3)	0.0085(2)	0.0084(1)	0.00705(9)
	Fitted Composition		-	$Ti_{1.28(2)}Ni_{1.72(2)}Sn$	$Ti_{1.24(1)}Ni_{1.76(1)}Sn$	$Ti_{1.10(1)}Ni_{1.90(1)}Sn$	$Ti_{1.122(5)}Ni_{1.878(5)}Sn$	$Ti_{1.150(2)}Ni_{1.850(2)}Sn$	$Ti_{1.150(1)}Ni_{1.850(1)}Sn$	$TiNi_{1.982(4)}Sn$
Overall Composition			$TiNi_{1.021(1)}Sn$	$Ti_{1.00(2)}Ni_{1.05(2)}Sn$	$Ti_{1.01(1)}Ni_{1.08(1)}Sn$	$Ti_{1.00(1)}Ni_{1.10(1)}Sn$	$Ti_{1.007(5)}Ni_{1.119(5)}Sn$	$Ti_{1.039(2)}Ni_{1.278(2)}Sn$	$Ti_{1.088(1)}Ni_{1.533(1)}Sn$	$TiNi_{1.982(4)}Sn$
$\chi^2_{(Rietveld)}$ / $\chi^2_{(Le\ Bail)}$			1.04	1.39	1.15	1.13	1.12	1.16	1.21	2.14
wR_p (%)		Bank 1	3.13	2.32	2.23	2.14	2.08	2.46	3.66	2.50
		Bank 2	1.95	1.88	2.04	1.88	1.88	2.62	2.07	2.51
		Bank 3	2.11	2.84	3.07	2.51	2.58	2.69	2.47	2.99
R_p (%)		Bank 1	3.55	2.88	2.53	2.55	2.35	3.59	5.74	3.22
		Bank 2	3.22	3.57	3.81	3.49	3.48	4.09	3.32	3.67
		Bank 3	3.59	3.57	3.64	3.22	3.18	3.24	2.94	3.33

*Sample contains 6.60(6)% Ni_3Sn_2.

5.4.2 TiNiCo$_y$Sn

Assuming that Co occupies the interstitial M2 site yields unrealistic compositions for all three samples. For example, refinement of the data collected for the nominal $TiNiCo_{0.025}Sn$ sample indicates a composition of $TiNiCo_{0.090(2)}Sn$ with $\chi^2 = 7.3$, while the nominal $TiNiCo_{0.075}Sn$ sample produces $TiNiCo_{0.345(2)}Sn$ with $\chi^2 = 6.9$. These are the minimum possible values for χ^2, and match values from Le Bail fits, performed for each sample.

Due to the high symmetry of these structures, independent refinement of the site occupancies is not possible and only relative contributions can be determined. The scattering lengths for each of the constituent atoms in these samples are collated in Table 5.4. The large over-estimation of Co occupancy on the *4d* site indicates that a much more strongly scattering element may sit on this site. The logical conclusion is therefore that some Ni atoms occupy the vacant tetrahedral site in the structure. Fixing the Co occupancy to its nominal value and allowing Ni to freely refine on the *4d* site also produces a best fit model. For the y = 0.025 sample, a very reasonable composition with only 1.6(1)% excess Ni is observed. However, analysis of the y = 0.05 and 0.075 samples yields excess Ni levels of 4.2(1)% and 6.5(1)%, respectively. These values are larger than is realistic, given the apparent purity of the samples and this suggests that this is not the correct model.

Table 5.4: Neutron scattering lengths of atoms used in this chapter.

Element	**Scattering Length (fm)**
Ti	-3.44
Co	2.49
Ni	10.3
Cu	7.72
Sn	6.23

Models were subsequently explored which allowed Ni and Co to be distributed across the two tetrahedral sites (M1 and M2) and a best-fit model was produced where the nominal amount of Co was placed on the half-Heusler M1 site. This causes displacement of some Ni onto the M2 site. Free refinement of the Ni content on the M2

site results in a small Ni excess in all 3 cases: 0.4% for y = 0.025, rising to 2.4% for y = 0.075. A representative fit is presented in Figure 5.7(a), and the results of the fit are collated in Table 5.5.

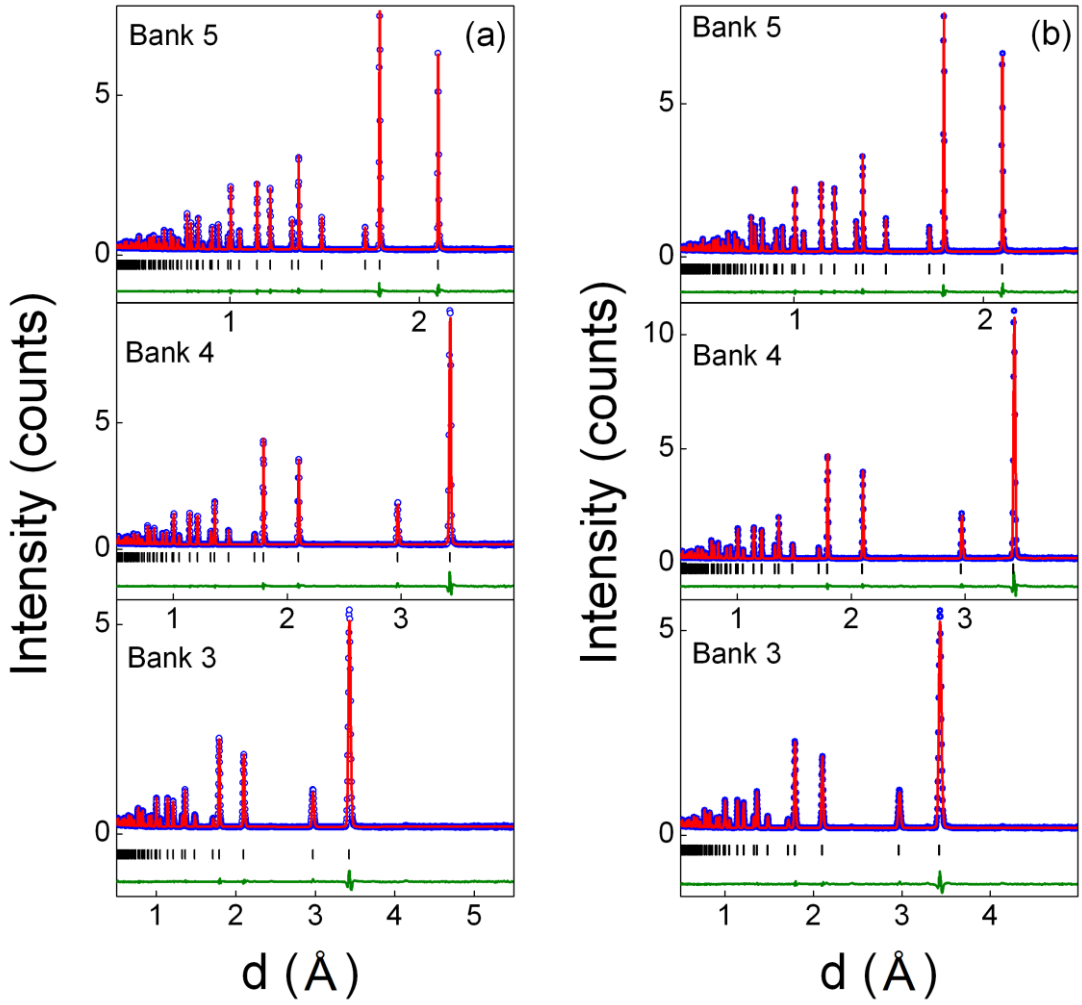

Figure 5.7: Rietveld refinement fits to neutron diffraction data collected for (a) $TiNiCo_{0.05}Sn$, and (b) $TiNiCu_{0.25}Sn$. Blue circles are the collected data, the red line is the calculated fit and the green line is the difference. Tickmarks correspond to the half-Heusler Bragg positions.

Table 5.5: Lattice parameters (a), weight fractions, fractional occupancies, temperature displacement factors (U_{iso} / Å^2), and refined compositions for the $TiNiCo_ySn$ series from fits against Polaris neutron powder diffraction data.

y		0.025	0.05	0.075
a (Å)		5.9309(1)	5.9368(1)	5.9462(1)
Ti *(4a)*	Occ	1	1	1
	U_{iso}	0.00473(8)	0.00453(7)	0.00484(7)
Ni *(4c)*	Occ	0.975	0.95	0.925
	U_{iso}	0.00478(5)	0.00507(5)	0.00571(5)
Co *(4c)*	Occ	0.025	0.05	0.075
	U_{iso}	0.00478(5)	0.00507(5)	0.00571(5)
Ni *(4d)*	Occ	0.029(1)	0.065(1)	0.099(1)
	U_{iso}	0.00481(5)	0.00507(5)	0.00571(5)
Co *(4d)*	Occ	0	0	0
	U_{iso}	-	-	-
Sn *(4b)*	Occ	1	1	1
	U_{iso}	0.00404(6)	0.00412(5)	0.00473(5)
Refined Composition		$TiNi_{1.004(1)}Co_{0.025}Sn$	$TiNi_{1.015(1)}Co_{0.05}Sn$	$TiNi_{1.024(1)}Co_{0.075}Sn$
$\chi^2_{(Rietveld)}/\chi^2_{(Le\ Bail)}$		1.02	1.01	1.00
wR_p (%)	Bank 1	2.69	2.43	2.45
	Bank 2	2.10	1.94	2.10
	Bank 3	3.26	2.93	3.43
R_p (%)	Bank 1	3.09	2.81	2.92
	Bank 2	3.51	3.61	3.68
	Bank 3	3.75	3.75	3.91

5.4.3 TiNiCu$_y$Sn

A starting model with Ti, Ni and Sn site occupancies fixed to unity on the *4a*, *4c* and *4b* sites, respectively, was used. The Cu occupancy of the *4d* site was allowed to refine freely and this lead to goodness-of-fit values that matched those obtained from Le Bail refinements, and thus a best-fit model was achieved. Cu occupancies were found to be higher than expected, with the y = 0.025 sample refining to a composition of $TiNiCu_{0.052(2)}Sn$, y = 0.05 producing $TiNiCu_{0.080(2)}Sn$ and y = 0.075 refining to $TiNiCu_{0.102(2)}Sn$. As argued in Section 5.4.2, this suggests that a more strongly scattering element may also sit on the *4d* site. Further investigation revealed that addition of 2% Ni to this site allowed the Cu occupancy to refine to its nominal value. The fit to $TiNiCu_{0.05}Sn$ is presented in Figure 5.7(b), and lattice parameters and site occupancies are presented in Table 5.6, along with other data acquired from the fit. This

solution is in-keeping with the observation of 2% excess Ni over and above the nominal value in every $TiNi_{1+y}Sn$ sample, and the occurrence of excess Ni in $TiNiCo_ySn$, XNiSn and $X_{0.5}X'_{0.5}NiSn$ samples.

Table 5.6: Lattice parameters (a), weight fractions, fractional occupancies, temperature displacement factors (U_{iso} / Å^2), and refined compositions for the $TiNiCu_ySn$ series from fits against Polaris neutron powder diffraction data.

y		0.025	0.05	0.075
a (Å)		5.9343(1)	5.9395(1)	5.9471(1)
Ti *(4a)*	Occ	1	1	1
	U_{iso}	0.00468(8)	0.00465(8)	0.00500(8)
Ni *(4c)*	Occ	1	1	1
	U_{iso}	0.00493(5)	0.00492(5)	0.00548(5)
Ni *(4d)*	Occ	0.020(1)	0.020(1)	0.020(1)
	U_{iso}	0.00493(5)	0.00492(5)	0.00548(5)
Cu *(4d)*	Occ	0.026(1)	0.054(0)	0.076(1)
	U_{iso}	0.00493(5)	0.00492(5)	0.00548(5)
Sn *(4b)*	Occ	1	1	1
	U_{iso}	0.00409(6)	0.00406(6)	0.00453(6)
Refined Composition		$TiNi_{1.020(1)}Cu_{0.026(1)}Sn$	$TiNi_{1.020(1)}Cu_{0.054(0)}Sn$	$TiNi_{1.020(1)}Cu_{0.076(1)}Sn$
$\chi^2_{(Rietveld)}$ / $\chi^2_{(Le\ Bail)}$		0.99	0.99	0.99
wR_p (%)	Bank 1	2.40	2.32	2.43
	Bank 2	2.03	1.92	1.95
	Bank 3	3.23	2.66	3.21
R_p (%)	Bank 1	2.86	2.76	2.93
	Bank 2	3.72	3.55	3.58
	Bank 3	3.79	3.61	3.64

5.5 Electron Microscopy

Preliminary low magnification SEM and EDX analysis of TiNiSn and $TiNiM_{0.05}Sn$ (M = Ni, Co, Cu) was performed. Images and compositions are presented in Appendix 2. This indicated that all samples are homogeneous and there was no evidence to suggest micron-sized full-Heusler inclusions. No Ni, Cu or Co – containing impurities were observed in the areas probed, indicating incorporation of the deliberate excess metals into the structures. The $TiNi_{1.5}Sn$ sample was also analysed and phase separation into a half-Heusler and Ni-deficient full-Heusler phase was observed, as expected.

The $TiNi_{1.05}Sn$ sample was investigated in more detail and TEM was performed in conjunction with EDX. This showed the sample to be homogeneous over the investigated area and no nano-inclusions of the full-Heusler within the half-Heusler phase were observed. Instead, it was determined that an off-stoichiometric half-Heusler phase of the approximate composition '$TiNi_{1.15}Sn$' is formed. This phase is homogeneous throughout the sample, with very little compositional variation observed, as demonstrated in Figure 5.8. Genuine interstitial Ni is therefore present in this sample, contrary to the predictions of the phase diagram.[99]

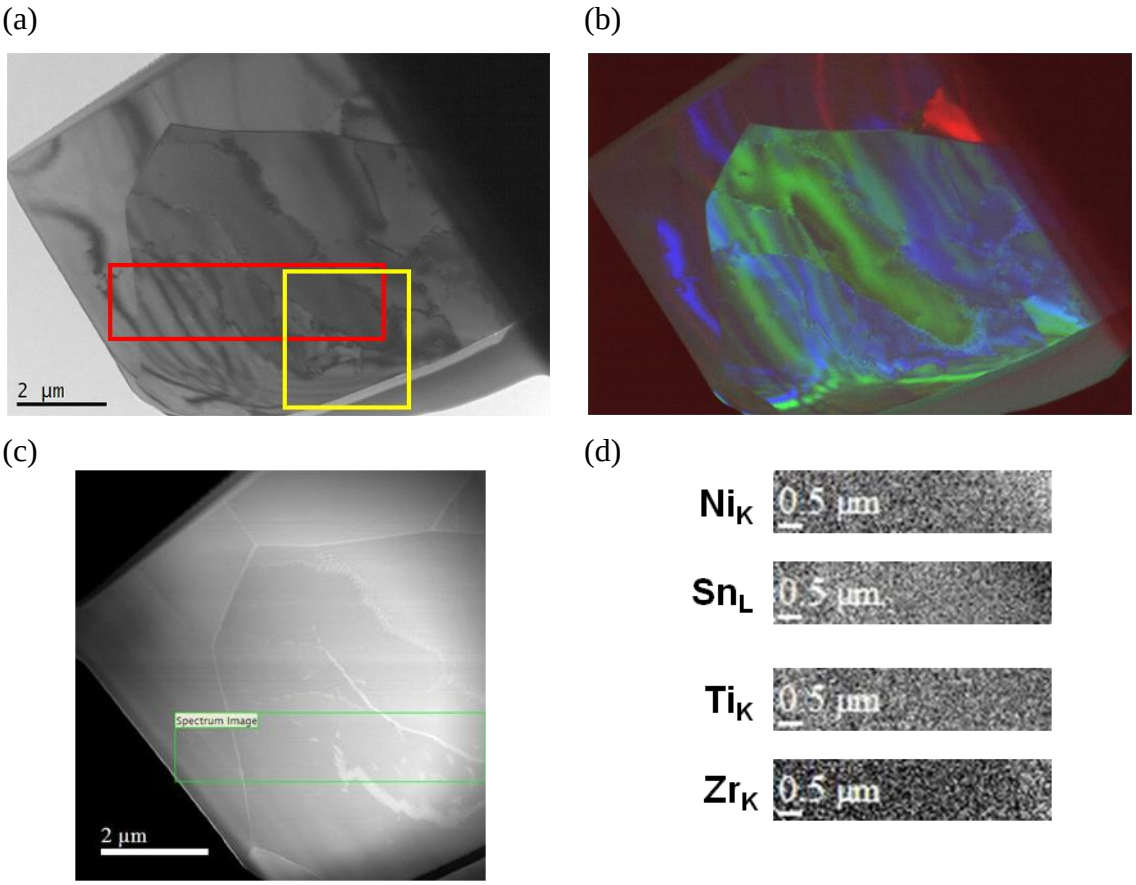

Figure 5.8: (a-c) Low magnification TEM images collected for $TiNi_{1.05}Sn$. (d) Elemental maps for the area outlined in red in image (a): EDX composition = $TiNi_{1.15}Sn$.

An interesting feature that could be identified was hexagonal patterning at some of the grain boundaries, as illustrated in Figure 5.9. The origin of this effect is, as yet, unclear. The composition of this phase was determined to be $Ti_{1.2}Ni_{1.8}Sn$ which is in excellent

agreement with the composition of the phase-separated full-Heusler, identified by neutron powder diffraction. Further investigation of this feature is required.

(a) (b)

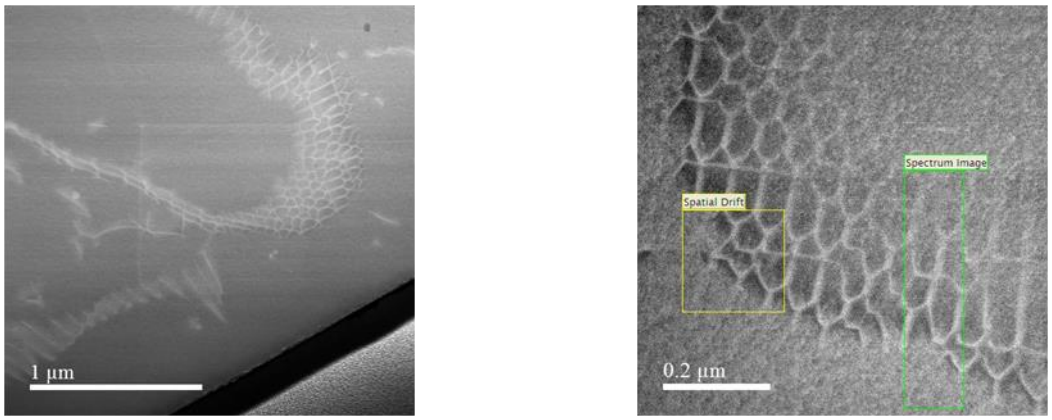

(c)

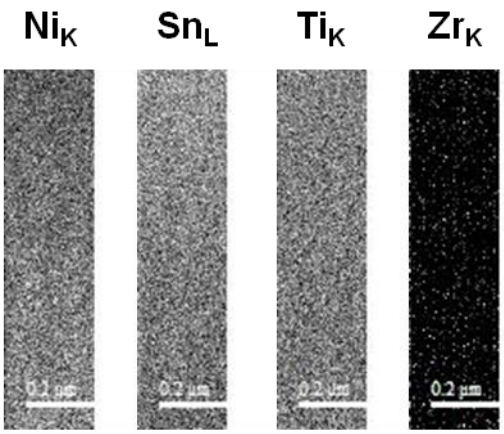

Figure 5.9: Low magnification TEM images for $TiNi_{1.05}Sn$. (a-b) close up of the area outlined in yellow in Figure 5.8(a), highlighting the hexagonal pattern. (c) elemental maps of the area outlined in green in image (b).

5.6 Thermoelectric Properties

5.6.1 $TiNi_{1+y}Sn$

The temperature dependence of the Seebeck coefficient (S), resistivity (ρ) and power factor (S^2/ρ) for each sample in this series are presented in Figure 5.10(a-c). As expected, TiNiSn is an n-type thermoelectric, with a large S_{RT} = -357 µV K^{-1}. This decreases steadily in magnitude to -264 µV K^{-1} at 700 K. ρ(T) values reveal

semiconducting behaviour, and ρ_{min} = 4.7 mΩ cm is achieved at 700 K. Combination of these properties results in S^2/ρ_{RT} = 0.6 mW m^{-1} K^{-2} and S^2/ρ_{max} = 1.5 mW m^{-1} K^{-2} at 700 K.

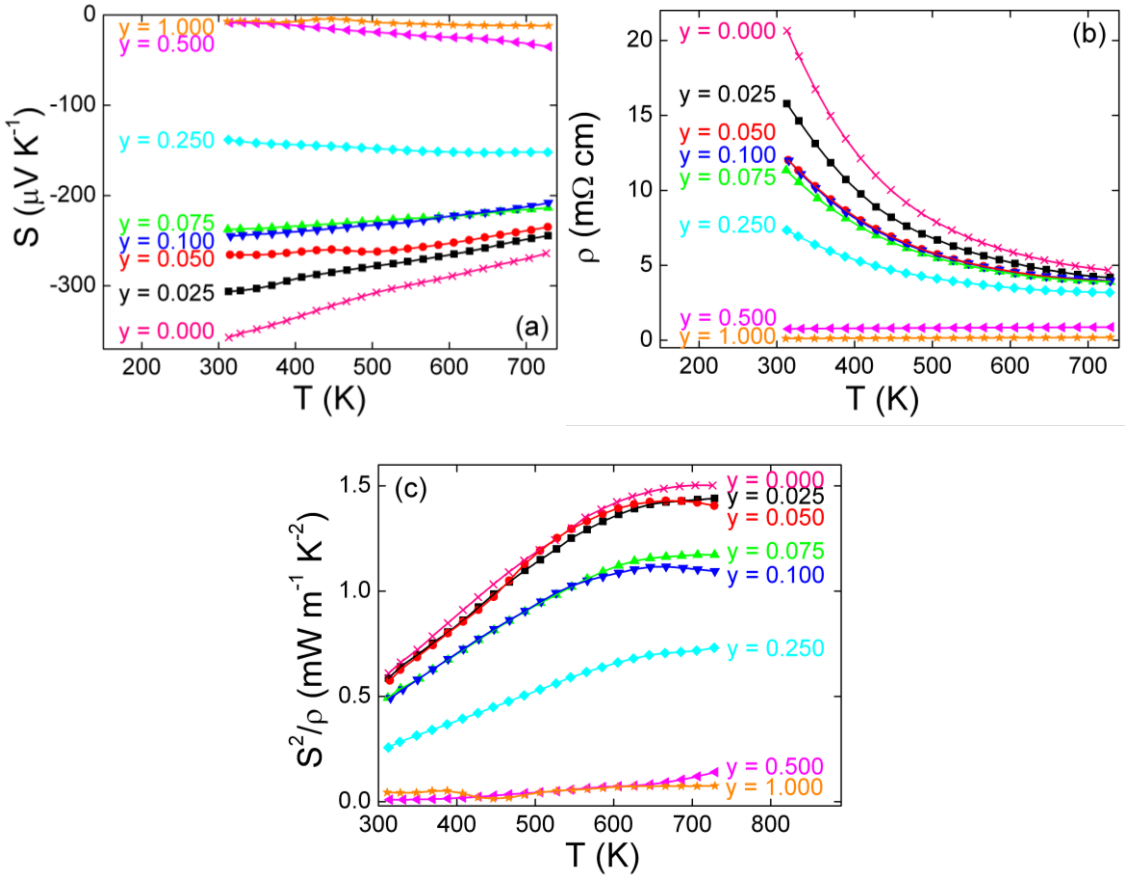

Figure 5.10: Temperature dependences of (a) Seebeck (S), (b) resistivity (ρ) and (c) power factor (S^2/ρ) for the $TiNi_{1+y}Sn$ series.

Addition of excess Ni to these samples causes a systematic reduction in the Seebeck coefficient. At low y-values there is a clear decrease in |S| with temperature, but as y is increased S becomes increasingly independent of temperature, indicating more metallic-type behaviour. S = -150 μV K^{-1} is found over the entire temperature range for $TiNi_{1.25}Sn$. This value is still relatively large, suggesting the sample is not truly metallic. On the other hand S_{RT} ~ -8 μV K^{-1}, for $TiNi_{1.5}Sn$ and $TiNi_2Sn$. This low value is typical of metals.

The resistivity results, shown in Figure 5.10(b), confirm these observations, with a semiconducting temperature dependence observed for the $TiNi_{1+y}Sn$ samples up to y =

0.25. The absolute value of the resistivity decreases as y is increased. For example, ρ_{RT} = 20.6 mΩ cm for TiNiSn is reduced to ρ_{RT} = 7.3 mΩ cm for $TiNi_{1.25}Sn$. This reduction is very systematic, suggesting carrier doping as y is increased. For $TiNi_{1.5}Sn$ and $TiNi_2Sn$, the values for the resistivity are very low, with ρ_{RT} = 0.76 mΩ cm and ρ_{RT} = 0.12 mΩ cm, respectively. These values increase slightly as the temperature is increased, consistent with metallic behaviour.

Figure 5.10(c) shows the temperature dependence of the power factor values for the $TiNi_{1+y}Sn$ series. The combined result of lowering the Seebeck effect and resistivity simultaneously, as y is increased, is an overall reduction in the power factor. The maximum S^2/ρ = 1.5 mW m^{-1} K^{-2} achieved by TiNiSn is systematically reduced to 0.7 mW m^{-1} K^{-2} for $TiNi_{1.25}Sn$. $TiNi_{1.5}Sn$ and $TiNi_2Sn$ show a linear increase over the temperature range but have much reduced maximum power factors values (in the measured range) of 0.14 and 0.08 mW m^{-1} K^{-2}, respectively.

5.6.2 $TiNiCo_ySn$

Addition of Co to TiNiSn causes a large change in the electronic properties of this series, as may be observed in Figure 5.11. The Seebeck values are small and positive at room temperature, with values of S ≈ 44 μV K^{-1} at 300 K. A transition to n-type conduction occurs rapidly as the temperature is increased. This occurs earliest for $TiNiCo_{0.025}Sn$, at 345 K, and occurs at higher temperatures as y is increased. $TiNiCo_{0.025}Sn$ achieves a maximum S = -192 μV K^{-1} at 586 K. S_{max} decreases, and occurs at higher temperatures, as y is increased.

$TiNiCo_{0.025}Sn$ values observe the temperature dependence of a classical semiconductor (Figure 5.11(b)), however $TiNiCo_{0.05}Sn$ and $TiNiCo_{0.075}Sn$ show more complex behaviour. These two samples also show an anomaly between 500 and 600 K. This is consistent with the melting point of Sn which, while not seen in the diffraction patterns, was observed in SEM images for $TiNiCo_{0.05}Sn$. The values of resistivity produced by $TiNiCo_{0.025}Sn$ are large, with ρ = 330 mΩ cm at 300 K, in-keeping with depletion of n-type carriers and the n-p transition. However, as y is increased further, these values are reduced and become more in-line with values observed for TiNiSn. This is indicative of hole-doping behaviour in these samples. The resulting power factor values for these

samples are decreased. They rise steadily with temperature, achieving a maximum of 0.19 mW m^{-1} K^{-2} at 730 K for $TiNiCo_{0.025}Sn$.

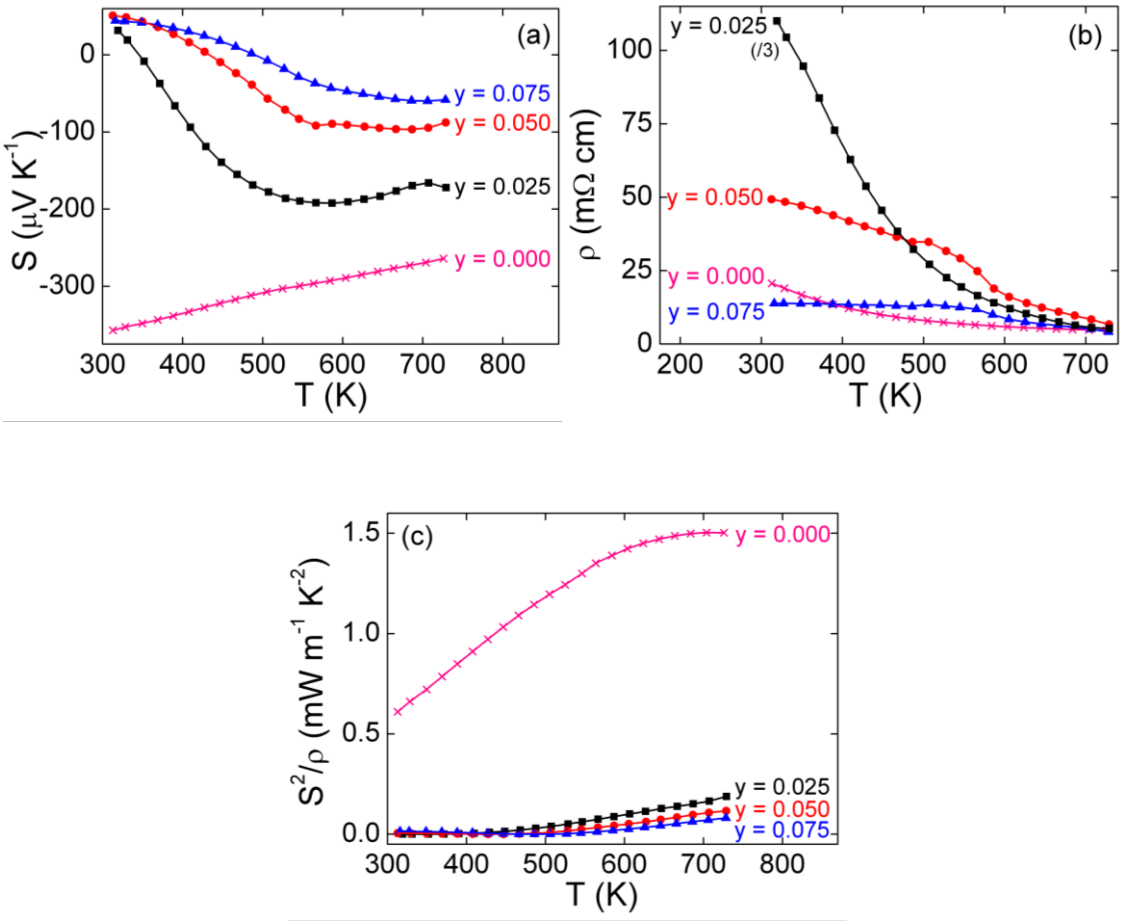

Figure 5.11: Temperature dependences of (a) Seebeck (S), (b) resistivity (ρ) and (c) power factor (S^2/ρ) for the $TiNiCo_ySn$ series.

5.6.3 $TiNiCu_ySn$

Addition of Cu to TiNiSn causes a large reduction in the values of the Seebeck coefficient, as may be observed in Figure 5.12. For example, room temperature values for $TiNiCu_{0.025}Sn$ and $TiNiCu_{0.075}Sn$ are S = -116 and -66 μV K^{-1}, respectively. A complete reversal in temperature dependence is also observed with Cu-doped samples displaying an increase in the magnitude of S as the temperature is increased, e.g. S = -189 μV K^{-1} at 730 K.

Resistivity measurements revealed the onset of metallic behaviour, even for y = 0.025. Very small values are observed (compared to those displayed by TiNiSn) and are found

to decrease as y is increased, e.g. ρ = 1.8 mΩ cm for $TiNiCu_{0.025}Sn$ and ρ = 1.0 mΩ cm for $TiNiCu_{0.075}Sn$ at 730 K. These results indicate that these samples are electron doped, compared to TiNiSn.

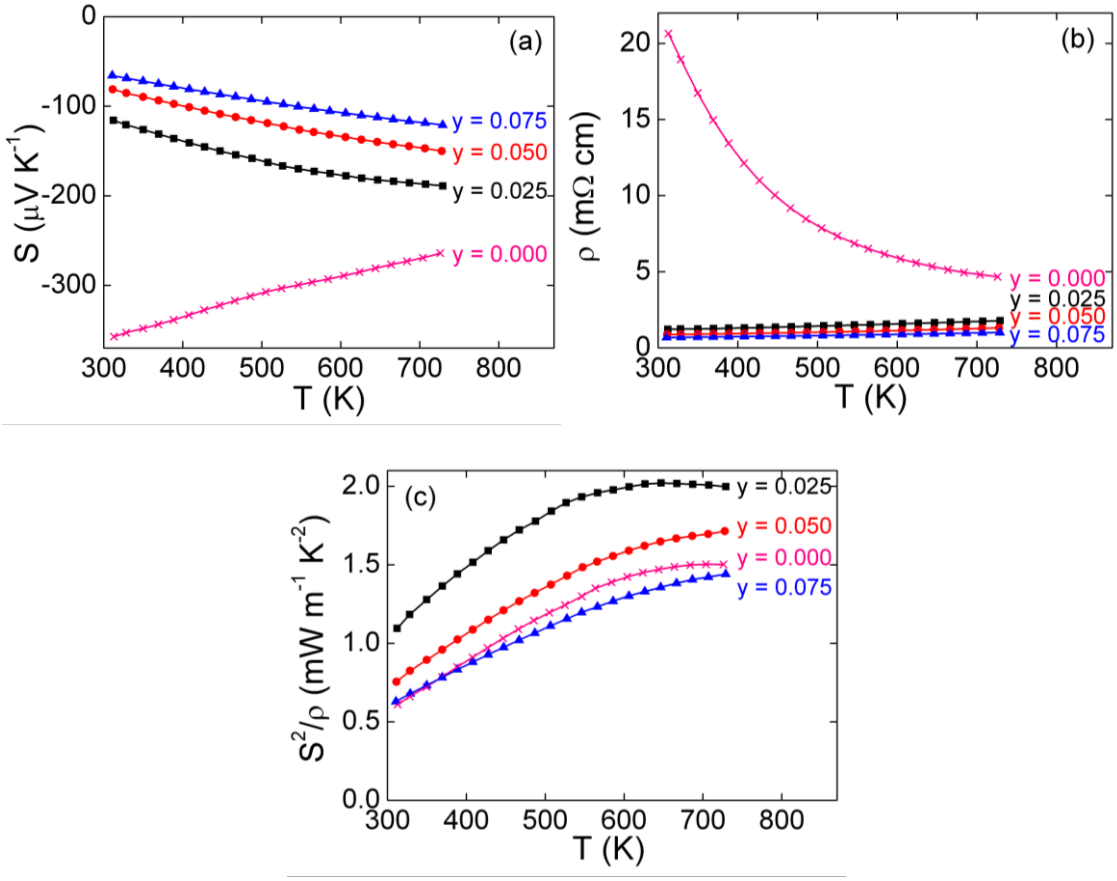

Figure 5.12: Temperature dependences of (a) Seebeck (S), (b) resistivity (ρ) and (c) power factor (S^2/ρ) for the $TiNiCu_ySn$ series.

The drastic reduction in resistivity values somewhat offsets the reduction in S in these samples and an overall improvement in power factor is observed for $TiNiCu_{0.025}Sn$ over TiNiSn, as it reaches a maximum S^2/ρ = 2 mW m^{-1} K^{-2} just below 700 K. $TiNiCu_{0.05}Sn$ shows a slightly reduced value in comparison, but still outperforms TiNiSn, reaching a value of 1.7 mW m^{-1} K^{-2} at 730 K. The temperature dependence of this sample also suggests that a further increase will occur at higher temperatures. The reduction in S observed in $TiNiCu_{0.075}Sn$ is too large to be offset by the lowered resistivity, thus the power factor suffers and a maximum S^2/ρ = 1.4 mW m^{-1} K^{-2} is observed at 730 K.

5.7 Discussion

Powder diffraction and electron microscopy experiments carried out on $TiNiM_ySn$ samples indicate that the excess metals were successfully introduced to the TiNiSn structure as genuine interstitials. This may be a kinetically stabilised arrangement and it is possible that with further heating, the Ni atoms may coalesce to form full-Heusler inclusions as observed in the literature where further processing techniques have been performed.[90, 93, 105]

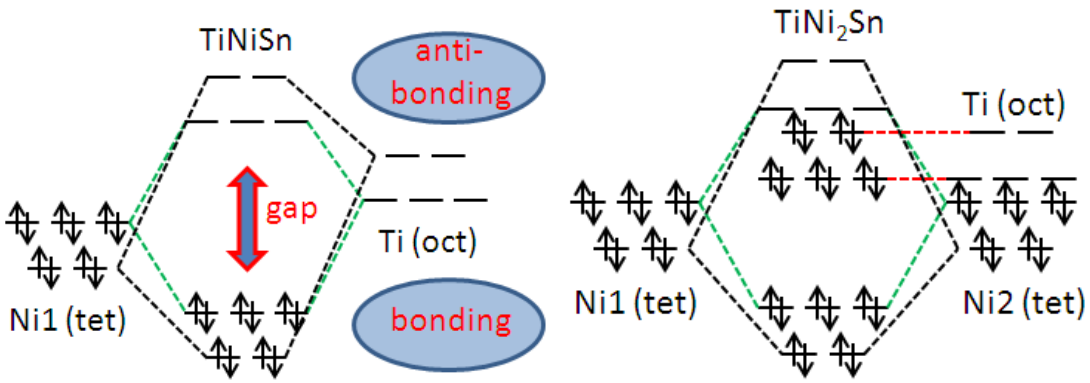

Figure 5.13: Molecular orbital diagrams for TiNiSn and $TiNi_2Sn$.[56]

No simultaneous enhancement of S and σ was observed in these samples. Instead, the gradual changes in S and ρ are consistent with a regular carrier doping effect. This is consistent with the presence of genuine interstitials as may be deduced through examination of the electronic structure of these materials.

First approximations of the molecular orbital diagrams for TiNiSn and $TiNi_2Sn$ are presented in Figure 5.13. For the half-Heusler structure, the valence and conduction bands are made up from the titanium and nickel d-orbitals. The anti-bonding conduction band has predominantly Ti character, while Ni is the main contributor to the bonding valence band. The bonding/anti-bonding pair for the full-Heusler phase is composed from the d-orbitals of the two Ni atoms in the structure, and the Ti d-orbitals contribute non-bonding orbitals within the band gap, close in energy to the conduction band. By placing interstitial Ni in the half-Heusler structure, a hybrid between the two arrangements must be achieved. Given the subtlety of the doping effect, and

preservation of the temperature dependence (for $y < 0.25$), the valence electrons of the interstitial Ni must remain largely localised. Cu was also located on the interstitial M2 site and possesses an additional electron. Transfer of this electron to the half-Heusler conduction band explains the dramatic transition to metallic behaviour upon addition of any Cu. Co was found to occupy the M1 site in the half-Heusler structure, and displaces Ni onto the M2 site. As Co has one less electron than Ni, the valence band is incomplete and contains holes that may move through the band. This accounts for the observation of p-type conductivity at room temperature.

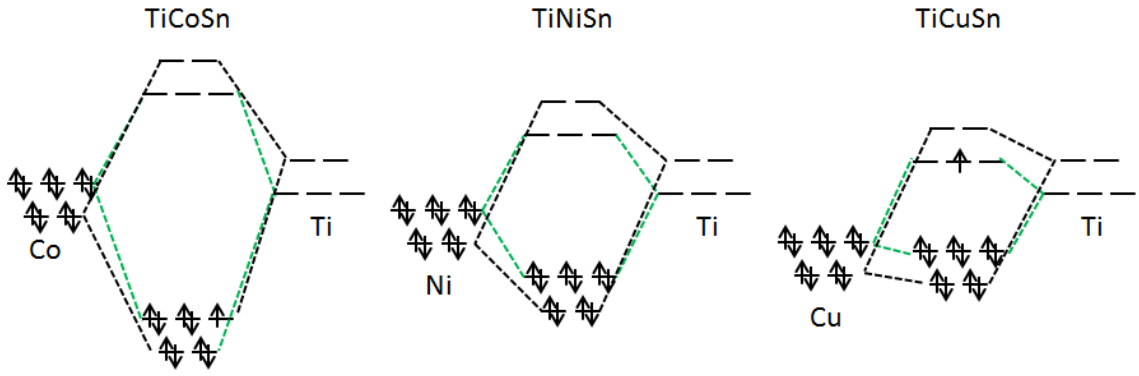

Figure 5.14: Schematic of the molecular orbital diagrams for TiCoSn, TiNiSn and TiCuSn.

The preferred site occupation of Cu and Co may also be rationalised through consideration of the molecular orbital diagram. Co and Ti orbitals are closer in energy than Ni and Ti. Better orbital overlap should therefore result in a stronger bonding interaction that stabilises the valence band as illustrated in Figure 5.14. The opposite is true of the Cu and Ti orbitals. As these are less well energetically matched, the orbital overlap is poorer and the conduction band is destabilised, as illustrated in Figure 5.14. These arguments are supported by the observation that TiCoSn (an itinerant ferromagnet) has the HH structure,[142] whereas TiCuSn has a different hexagonal LiGaGe structure.[143]

5.8 Conclusions

The collected diffraction and microscopy data and the electronic property measurements correlate well, and provide a clear picture of the effect of interstitial doping in these $TiNiM_ySn$ series. These results demonstrate that genuine interstitials can be introduced to the half-Heusler structure. A limit of 8% interstitial doping is possible for Ni, and both Co and Cu can be added up to, at least, the 7.5% level. The results obtained for these samples indicate that, in all cases, an unintentional 2% excess Ni naturally occurs in these TiNiSn-based samples. These interstitials are difficult to spot without neutron diffraction. It is therefore possible that small amounts of interstitial Ni occur, undetected, in most TiNiSn-based samples. Measurement of the electronic properties of the samples prepared for this chapter demonstrate that the presence of interstitials within the half-Heusler structure causes a doping effect. Intentional addition of interstitial metal to the half-Heusler structure therefore represents a new route to optimisation of the electronic properties of these materials.

Chapter 6 – Structure and Properties of TiNiX (X = Si, Ge)

6.1 Introduction

TiNiX compositions (where X = Si or Ge) show a number of similarities to the TiNiSn-based half-Heuslers. The bonding within the two structures is broadly similar and both may be described in terms of a Zintl-type model. To a first approximation, the TiNiX structure comprises a covalently bound $(NiX)^{n-}$ lattice that forms ionic bonds to Ti^{n+} cations. In the strict Zintl-counting scheme, the oxidation states should be Ti^{4+}, Ni^{0} and X^{4-}. In reality, however, it has been calculated that Ti does not fully transfer its valence electrons to the (NiX) sublattice.[144] The bonding is therefore, once again, somewhat intermediate between ionic and covalent in both cases.

The main difference between these TiNiX compositions and the half-Heuslers is the structure. TiNiX compositions crystallise in a TiNiSi-type structure that is orthorhombic with the *Pnma* space group. Ni and X bond to form layers of 6-membered rings in a graphitic-type arrangement, as demonstrated in Figure 6.1.

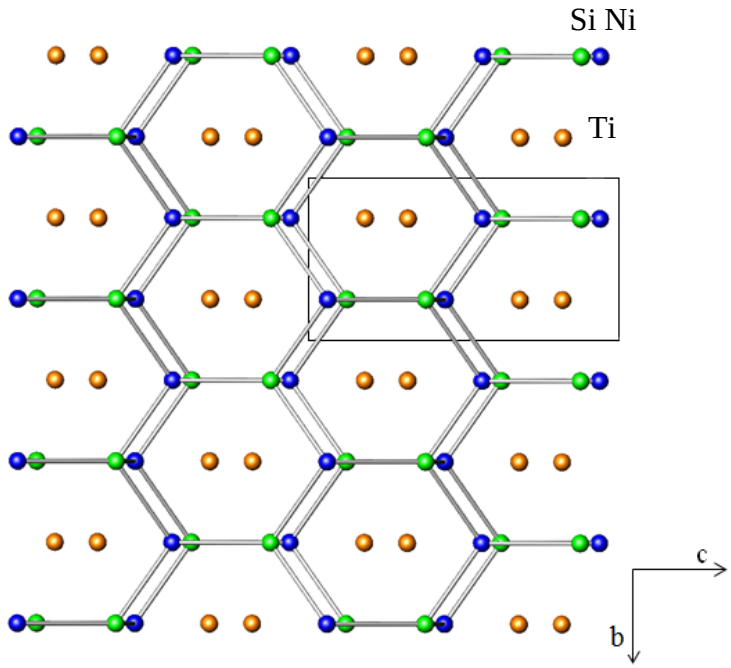

Figure 6.1: TiNiSi-type structure, looking down the a-axis.

These layers are actually puckered, as illustrated by the side-on view in Figure 6.2. They stack along the a-axis and are interlinked, with Ni-X bonds forming 4-membered

rings between the layers. The Ti cations occupy the space between the layers in the channels that run the length of the a-axis Figure 6.1.

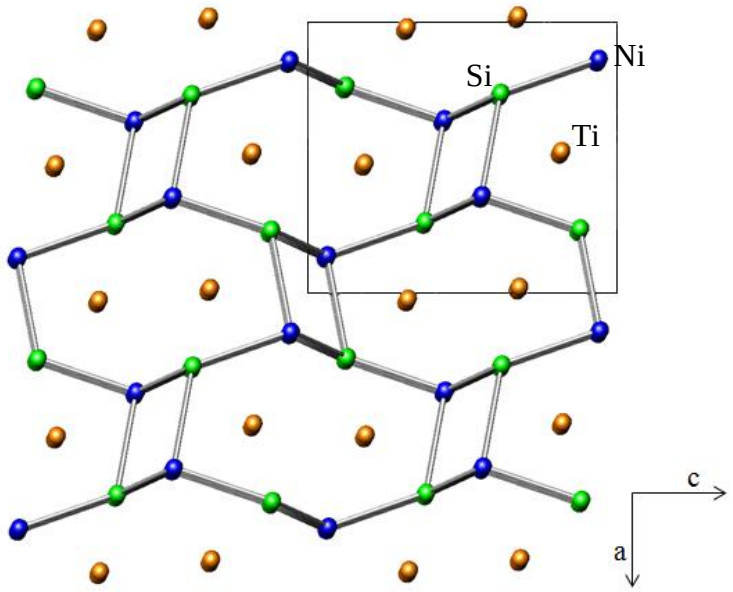

Figure 6.2: TiNiSi-type structure, viewed down the b-axis.

On comparison with the half-Heusler structure, the tetrahedral bonding between Ni and X is maintained, although in this case edge-sharing tetrahedra are present, which are not found in the half-Heusler structure. The bonding environment for Ti is drastically altered, in comparison. This has a large impact on the bonding and band structure of these materials. The most significant result is that the strong Ti-Ni interactions are no longer observed. This interaction is responsible for the formation of the band gap in the half-Heusler phases. The absence of a strong Ti-Ni interaction in the TiNiX compositions means that no band gap is formed and metallic behaviour is observed in these materials.[145]

This structure-type represents the most commonly adopted structure for equiatomic ABC compounds.[145] Examples exist where A can be any of the first row transition metals and B can also be varied greatly. This results in a large number of different compositions and properties. In ANiSi compositions, for example, Pauli paramagnetism has been observed where A = Sc-V, while ferromagnetism has been reported for compositions where A = Cr-Fe.[144] In some compositions where B is a second or third

row transition metal, superconductivity has been observed: T_c – 2.3 K was reported for HfRhSi;[146] and T_c = 3.5 K was found in TaPtSi.[147] Some investigation of the thermoelectric properties of this structure-type has also been undertaken. A study of CePtSn, CeNiSn, CeRhSb and CeRhAs, which all adopt the TiNiSi-type structure revealed high Seebeck coefficients along with relatively low resistivity values, below room temperature.[148] This combination is highly desirable in potential thermoelectric materials and shows the promise that these structures do have. The most successful related thermoelectric material to date is $Ca_{0.84}Ce_{0.16}Ag_{0.87}Sb$, which achieved ZT = 0.7 at 1079 K. This adopts a hexagonal structure, in which the bonds between the graphitic-type layers are longer than those in the *Pnma* orthorhombic structure adopted by TiNiSi and TiNiGe. The parent material is CaAgSb and does adopt the orthorhombic cell. ZT approaching 0.1 at 700 K are reported for this composition, based on ρ = 0.25 mΩ cm, S = 50 μV K^{-1} and κ = 4.5 mW m^{-1} K^{-1}. Ce substitution causes the transition to the hexagonal structure and results in ρ = 1 mΩ cm, S = 100 μV K^{-1} and κ = 1.5 mW m^{-1} K^{-1} at 1079 K.[149] Identification of respectable ZT values in TiNiSi-type structures could therefore result in very high-efficiency thermoelectrics with the appropriate substitutions. The aim of the work presented in this chapter was therefore to investigate the structure and properties of TiNiSi and TiNiGe and to determine their potential as new thermoelectric materials.

6.2 Experimental Methods

TiNiSi was prepared on a 5 g scale by arc-melting stoichiometric quantities of the elemental starting materials. No further annealing was undertaken as this resulted in degradation of the sample. TiNiGe was also prepared by arc-melting, and in this case, the ingot was then vacuum sealed in a quartz tube and annealed at 900 °C for 3 days.

The resulting ingots were cut into bars and discs for electronic property and thermal conductivity measurements, respectively. The remaining sample was ground for X-ray and neutron powder diffraction, in the case of TiNiSi. Powders ground from samples, prepared in the same manner but on a smaller scale were used for SQUID measurements.

6.3 Structural Properties

6.3.1 TiNiSi

Laboratory X-ray diffraction confirmed formation of the TiNiSi phase, with no observable impurities. Neutron diffraction was subsequently carried out and the Rietveld fits to the collected data for banks 4 and 5 are presented in Figure 6.3. Lattice parameters, atomic positions, site occupancies, thermal parameters and selected bond angles and distances are collated in Table 6.1, along with the fit statistics for the refinement.

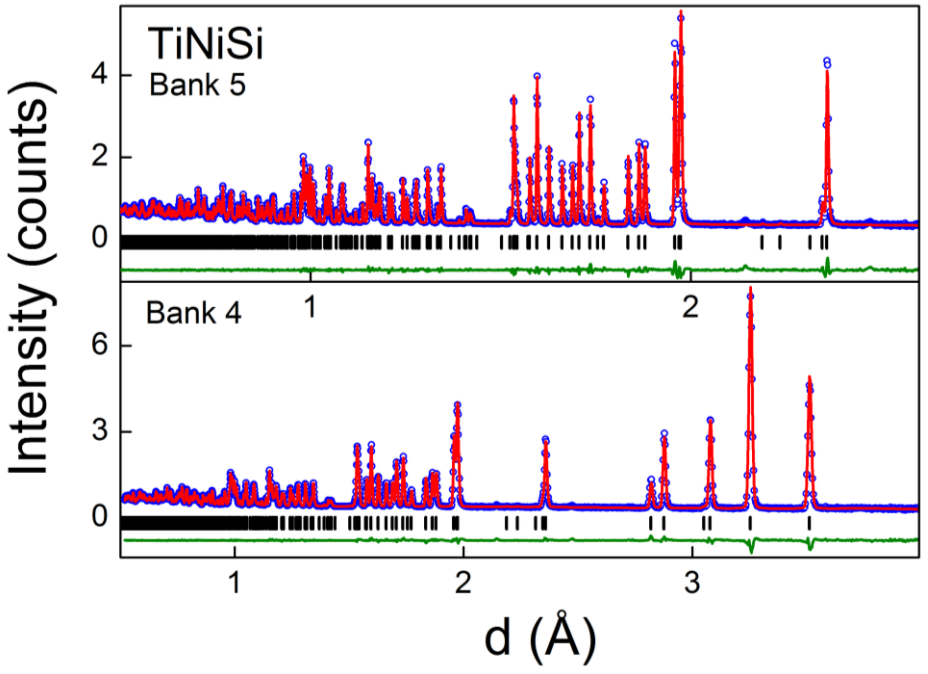

Figure 6.3: Rietveld fit to neutron powder diffraction data collected on POLARIS for TiNiSi. Blues circles represent the collected data, the red line is the calculated model and the green line is the difference between the two. Black tickmarks are markers for the Bragg positions of the TiNiSi phase.

The reported TiNiSi structure was found to fit the data well. Inspection of the Ni-Si-Ni and Si-Ni-Si bond angles reveals that none of these angles measures 109.5°, which is the bond angle for ideal tetrahedra. They also deviate substantially from the 120° angle found in a perfect honeycomb lattice, highlighting the puckered nature of the graphitic-type layers. The bond angles in this layer are illustrated in Figure 6.4(a).

Table 6.1: Lattice parameters, atomic positions (X and Z), site occupancies (occ), thermal parameters (U_{iso}), selected bond angles and distances and fit statistics for the Rietveld fits to neutron diffraction data collected for TiNiSi and X-ray diffraction data collected for TiNiGe. Ti, Ni and X each occupy a unique (x, ¼, z) site. * indicates the angles within the graphitic-type layers. **indicates angles that make up the 4-membered rings that link the graphitic layers.

		TiNiSi	TiNiGe
a (Å)		6.15380(6)	6.2446(1)
b (Å)		3.66984(4)	3.7487(1)
c (Å)		7.02172(7)	7.1471(1)
Ti	***Occ***	0.989(3)	1
	U_{iso} (Å^2)	0.0038(1)	0.0072(6)
	x	0.02236(9)	0.0253(3)
	z	0.68085(8)	0.6826(2)
Ni	***Occ***	0.986(2)	1
	U_{iso} (Å^2)	0.00453(6)	0.0148(6)
	x	0.14153(3)	0.1361(3)
	z	0.06003(3)	0.0591(3)
Si/Ge	***Occ***	1	1
	U_{iso} (Å^2)	0.0042(1)	0.0114(4)
	x	0.26596(8)	0.2563(3)
	z	0.37750(6)	0.3778(2)
Ni - X (Å)		2.3577(5) 2.3091(3) 2.3523(5)	2.399(2) 2.375(1) 2.414(2)
Ni - X - Ni (°)		127.21(1)* 119.68(2) 105.24(2)* 69.79(1)**	127.33(5)* 118.99(8) 104.20(9)* 67.69(6)**
X – Ni - X (°)		116.398(9)* 98.22(1) 105.243(2)* 110.22(1)**	115.44(5)* 97.47(7) 104.20(9)* 112.31(6)**
χ^2		5.8	4.0
Bank 5	wR_p	1.9	13.9
	R_p	2.6	10.2
	R_f^2	1.6	13.0
Bank 4	wR_p	1.6	-
	R_p	2.9	-
	R_f^2	3.0	-
Bank 3	wR_p	2.4	-
	R_p	3.5	-
	R_f^2	9.1	-

The 4-membered rings that link the layers do not form a perfect square, and are distorted, with the Ni-Si-Ni angle measuring 69.79(1)° and the Si-Ni-Si angle measuring 110.22(1)°. This distortion maximises the distance between the Si atoms which are more electronegative than Ni, as illustrated in Figure 6.4(b).[144]

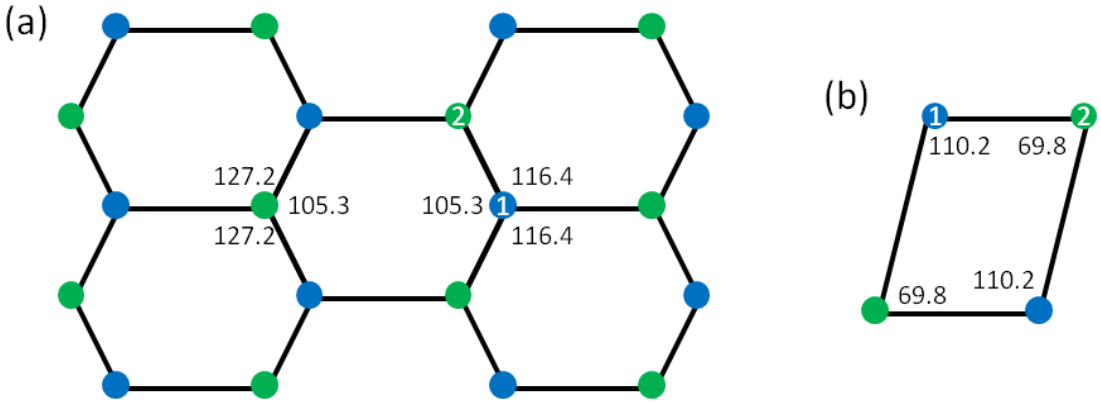

Figure 6.4: Bond angles in (a) the graphitic layers and (b) the 4-membered rings that link the layers in TiNiSi. Blue circles are Ni and green are Si.

6.3.2 TiNiGe

Inspection of the X-ray powder diffraction pattern collected for this sample confirmed formation of the TiNiGe phase. Minor impurity peaks were also observable. Searches against the ICDD-PDF database did not yield any elemental, binary or ternary matches that adequately fitted these peaks. The Rietveld fit to the X-ray data is shown in Figure 6.5 and the impurity peaks are marked with *. Refined lattice parameters, site positions, thermal parameters and bond lengths and angles are summarised in Table 6.1.

The lattice parameters are slightly larger than those reported for TiNiSi, as may be expected due to the larger size of Ge, compared with Si. The Ni-Ge bond distances are correspondingly longer. Five out of six of the bond angles within the 6-membered rings are decreased upon comparison with the NiSi lattice, indicating increased puckering of the layers. This is likely driven by the lengthening of the Ge-Ge distance in the 4-membered ring.

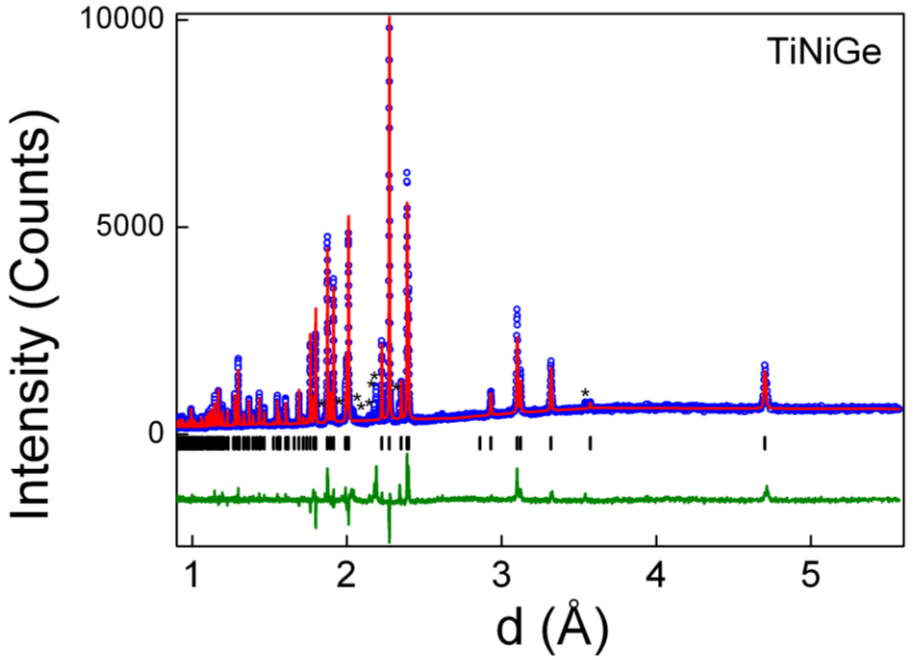

Figure 6.5: Rietveld fit to XRD data collected for TiNiGe. Blues circles represent the collected data, the red line is the calculated model and the green line is the difference between the two. Black tickmarks are markers for the Bragg positions of the TiNige phase. * mark the unidentified impurity peaks.

6.4 Physical Properties

6.4.1 Thermoelectric Properties

The high temperature thermoelectric properties of the two compositions are presented in Figure 6.6. The Seebeck values for both samples are negative, indicating n-type conduction. The magnitudes of the values are low, with S_{RT} = -45 μV K^{-1} for TiNiSi and S_{RT} = -20 μV K^{-1} observed in TiNiGe. The temperature dependence of the resistivity indicates metallic-type behaviour although the S values are rather large for a good metal. The ρ-values are low, with ρ_{RT} = 1 mΩ cm for TiNiSi and ρ_{RT} = 0.6 mΩ cm for TiNiGe. The resulting power factor values are 0.18 mW m^{-1} K^{-2} and 0.06 mW m^{-1} K^{-2} at room temperature for TiNiSi and TiNiGe, respectively.

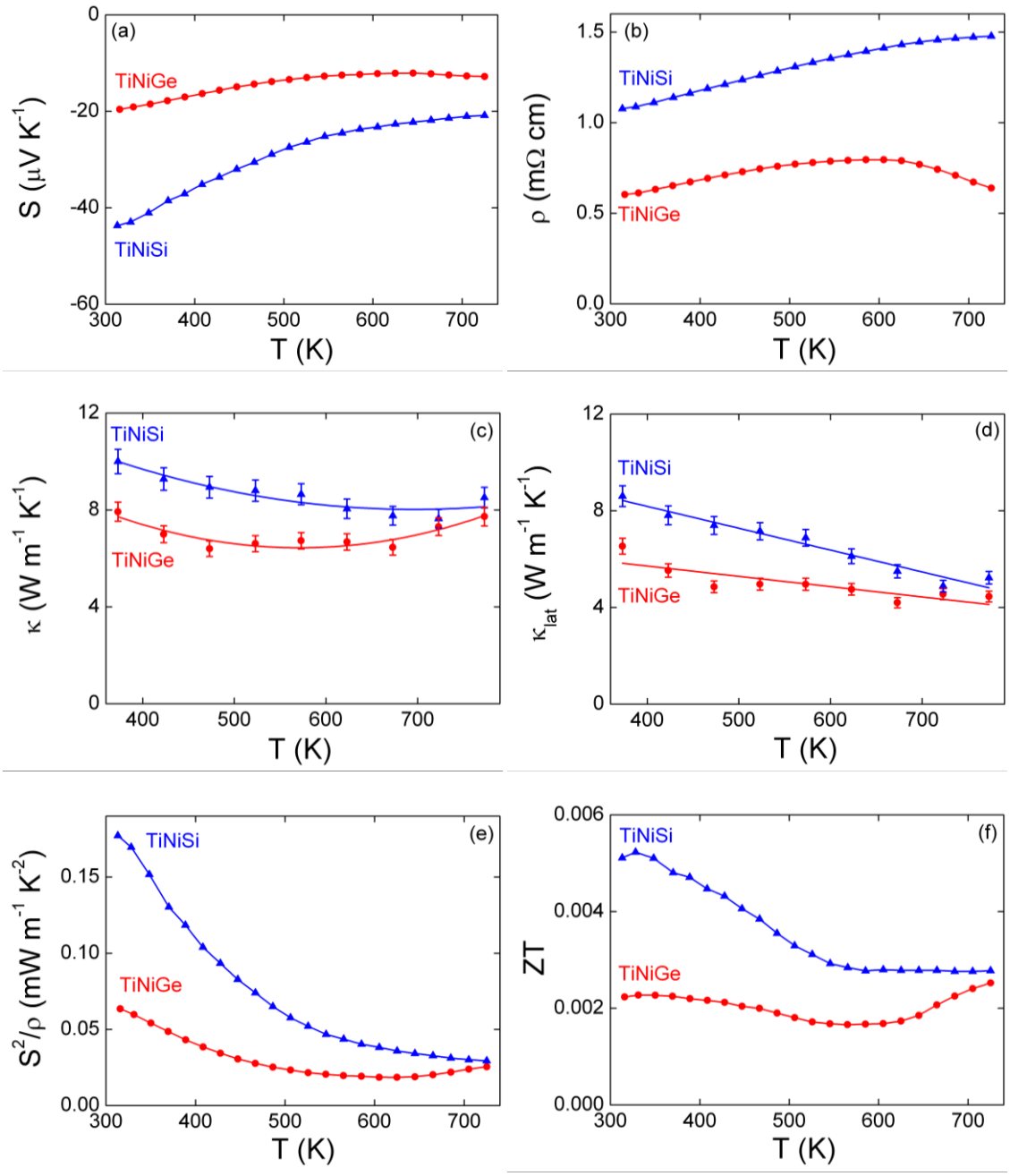

Figure 6.6: Temperature dependences of (a) the Seebeck coefficient (S), (b) resistivity (ρ), (c) total thermal conductivity (κ), (d) lattice thermal conductivity (κ_{lat}), (e) power factor (S^2/ρ) and (f) ZT for TiNiSi and TiNiGe.

Low temperature resistivity measurements were also obtained for these samples and are presented in Figure 6.7. The measured values are consistent with the high temperature values. The temperature dependence is consistent with a bad metal or degenerate semiconductor. In addition there is a deviation at 175-250 K in the TiNiSi measurement.

The origin of this behaviour is unknown and it may just be an artefact in the measurement. Calculation of the residual resistivity ratio (RRR), as per Equation (6.1), yields RRR = 1.5 for TiNiSi and 2.9 for TiNiGe which is more in line with a degenerate semiconductor or very poor metal, where disorder and/or impurities cause scattering.

$$RRR = \frac{R_{300\,K}}{R_{4\,K}} \qquad \text{Equation (6.1)}$$

where $R_{n\,K}$ is the resistance at n K.

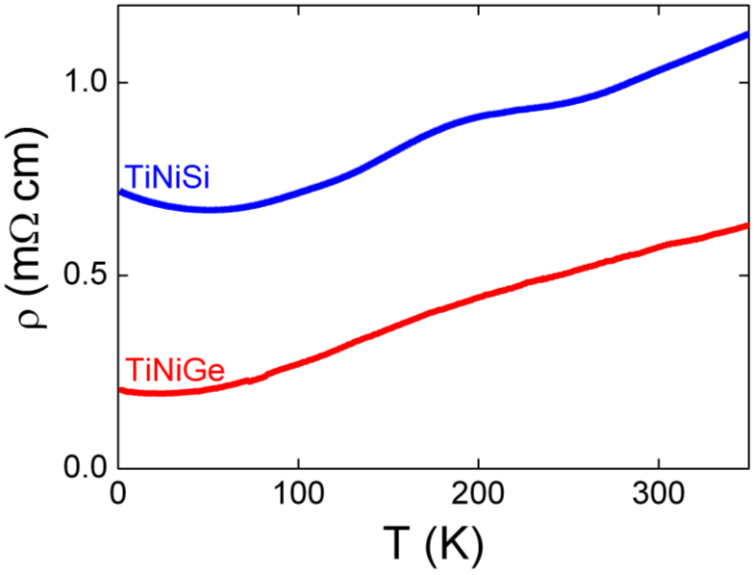

Figure 6.7: Temperature evolution of resistivity (ρ) for TiNiSi and TiNiGe between 2 K and room temperature.

The thermal conductivity for these two compositions is high, for thermoelectric applications. In these samples κ is dominated by κ_{lat}. TiNiSi produces κ_{RT} = 10 W m^{-1} K^{-1} which decreases to 8 W m^{-1} K^{-1} at 775 K. In TiNiGe, κ_{RT} = 8 W m^{-1} K^{-1} decreases to ~6.5 W m^{-1} K^{-1} at 600 K, before increasing again to 8 W m^{-1} K^{-1} at 775 K. These values are low for metallic samples and are consistent with literature values for TiNiSn.[66, 72] The κ_{lat} values show a general decrease with temperature over the whole measured range, indicating that the upturn in κ_{tot} values is due to ambipolar effects.

Based on these properties, TiNiSi reaches ZT_{max} = 5x10^{-3} at room temperature. ZT then decreases with temperature up to 550 K, after which a value of 3.1x10^{-3} is maintained.

ZT = $2x10^{-3}$ for TiNiGe is maintained and is almost independent of temperature in the range 300 – 650 K. Above 650 K, ZT begins to increase and reaches $2.5x10^{-3}$ at 725 K.

6.4.2 Magnetic Properties

The response of the resistivity to a magnetic field was probed at 2 K for each sample. Results are presented in Figure 6.8. A large magnetoresistance was observed for TiNiGe, where a 44% increase in resistivity occurred in a 9 T field. A 10 % increase was observed in TiNiSi.

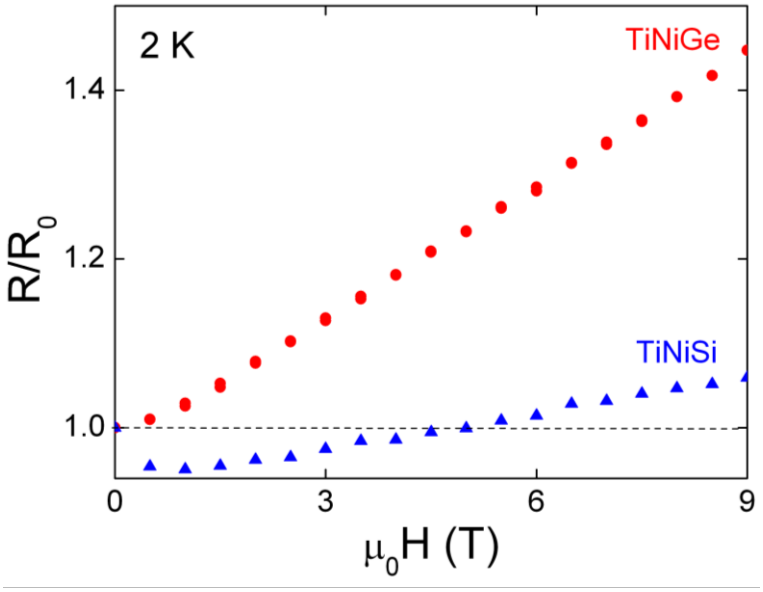

Figure 6.8: Field dependence of resistivity at 2 K for TiNiSi and TiNiGe.

Magnetic susceptibility measurements are presented in Figure 6.9. Both samples show very low χ values that are independent of temperature over most of the measured temperature range, indicating Pauli paramagnetism. Each sample also exhibits a paramagnetic tail at low temperatures. A plot of 1/χ vs. T for the paramagnetic tail, fitted by a straight line between 1.8 and 4 K in each case, allowed an estimation of the Curie (C) and Weiss (θ) constants, as per Equation (6.2).

$$\chi = \frac{C}{T - \theta} \qquad \text{Equation (6.2)}$$

C ≈ 1.3(2)x10^{-3} emu Oe^{-1} mol^{-1} K and θ ≈ -9.7(2) K was determined for TiNiSi and C ≈ 1.5(1)x10^{-3} emu Oe^{-1} mol^{-1} K and θ ≈ -8.4(1) K was found for TiNiGe.

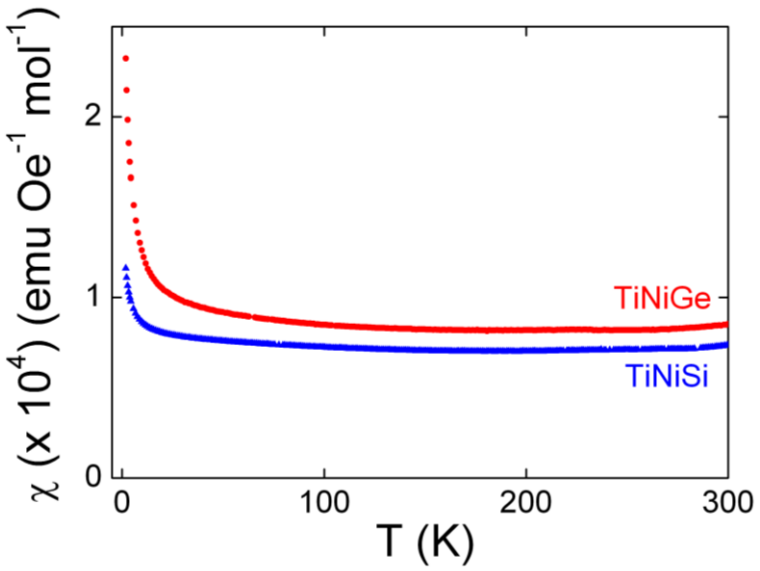

Figure 6.9: Temperature dependence of magnetic susceptibility for TiNiSi and TiNiGe.

6.5 Conclusions

TiNiSi and TiNiGe were prepared and their structures determined. Both were found to adopt the orthorhombic TiNiSi-type structure, discussed in section 6.1. TiNiSi was found to be phase pure, within the limits of diffraction and fully stoichiometric, within the error of the site occupancy refinement. The TiNiGe sample was found to contain an impurity phase, which has not been successfully identified as yet. Searches against the ICDD-PDF database and attempts at indexing the unit cell for the impurity phase have, so far, failed.

Maximum ZT values were found to be 5x10^{-3} at room temperature for TiNiSi and 2.5x10^{-3} at 725 K for TiNiGe. These values are low for thermoelectric applications but do not discount any potential that samples based on these compositions might have. The resistivity values for both compositions are low, thus alterations to the structure should focus on improvement of S and reduction of κ. Both can be improved by reduced dimensionality. S is improved by sharper bands in the density of states, as previously described, while phonon transport can be significantly disrupted in a layered structure. Elongation of the 'interlayer' bonds between the graphitic layers in the TiNiSi-type

structure exacerbates the layered nature of this material. This was very recently achieved in the $Ca_{1-x}Ce_xAg_{1-y}Sb$ series upon addition of Ce, and resulted in a three-fold reduction in κ and doubling of S.[149] Substitution on the X site is therefore of key interest in the improvement of TiNiGe and TiNiSi for thermoelectric applications.

Chapter 7 – Structure and Properties of RMnSbO (R = Nd, La)

7.1 Introduction

Compounds based on AM_2Pn_2 and AMPnO (where A is an alkaline earth or rare earth element, M is a transition metal and Pn is a pnictogen) have undergone intensive investigation since 2008, as a result of the discovery of T_C = 26 K in F-doped LaFeAsO[150]. A huge number of materials where MPn = FeAs have now been synthesised and T_cs up to 55 K have been observed in LnFeAsO (Ln = Sr, Sm) and up to 40 K in AFe_2As_2 (A = Ba,K).[151, 152]

The elements occupying each of the A, M and Pn sites can be varied, resulting in a large number of possible compositions. Many of these have now been investigated and diverse structural and electronic properties have been uncovered.[153, 154] Low temperature superconductivity is found where Fe or As are replaced by Ni and P, respectively.[155, 156] Co and Mn containing compounds also offer a wide range of fascinating properties. For example, itinerant ferromagnetism has been observed in LnCoPnO[157, 158] (where Ln = lanthanide and Pn = As/P) and local moment antiferromagnetism is found in materials such as the insulating $BaMn_2As_2$.[159] Furthermore, large magnetoresistance and antiferromagnetic ordering in F- and H-doped LnMnAsO[160-162] has been observed and there is speculation that LaMnPO could exhibit superconductivity at temperatures higher than the iron-based oxy-arsenides, if antiferromagnetic ordering can be destroyed.[163]

A relatively unexplored subset of these structures are those where Pn = Sb, with relatively few examples reported to exist. A small body of work focussing on LnZnSbO (R = La, Ce, Pr, Nd, and Sm) has now been formed,[164, 165] and RMnSbO (R = La, Ce, Pr, Nd, Sm and Gd) have also been synthesised, but little characterisation has been carried out thus far.[166, 167] One detailed study into the structure and properties of PrMnSbO has been reported, and shows antiferromagnetic ordering of both the Mn and Pr and a structural phase transition to the orthorhombic space group *Pmmm*, similar to its iron-arsenide equivalent.[168] This demonstrates that these compounds may have as much to offer as their As/P-containing analogues. Compounds of the form AMn_2Sb_2 and AMnSbO therefore represent an exciting opportunity to investigate the properties of a relatively unexplored set of compounds.

7.1.1 Structure

The RMnSbO (R = La, Nd) compositions crystallise with the ZrCuSiAs-type structure.[169] This is tetragonal with the *P4/nmm* space group. It is a layered structure with the stacking sequence ABAB… along the c-axis, as illustrated in Figure 7.1.

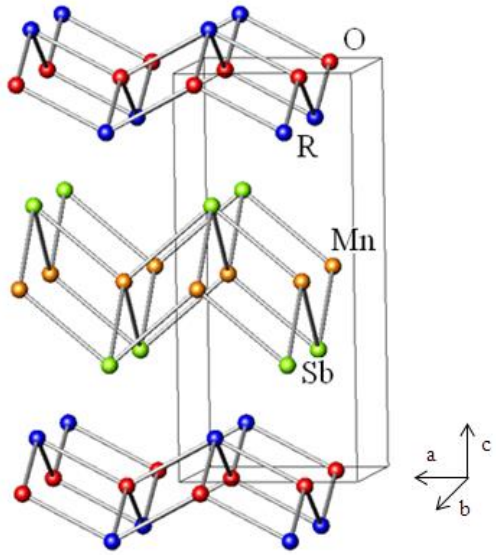

Figure 7.1: Schematic representation of the crystal structure of RMnSbO.

In RMnSbO, (where R = La, Nd) (RO_2R) layers are interspersed with ($SbMn_2Sb$) layers. Within the layers, each O is coordinated to 4 R-atoms and each Mn is coordinated by 4 Sb atoms in a tetrahedral arrangement, as highlighted by the structure in Figure 7.1. This may alternatively be described as a square net of Mn atoms with Sb sitting alternately above and below the holes in the square Mn net. In the RO_2R layer, the square net is composed of the oxygen atoms which the R species sit above and below.

These compounds can be described using an ionic model. For RMnSbO, this results in the presence of R^{3+}, Mn^{2+}, Sb^{3-} and O^{2-}. The layers are therefore $(RO)^{+}(MnSb)^{-}$ which clearly represents the charge transfer between the layers. In these compounds the ($SbMn_2Sb$) layer is considered to be responsible for charge carrier transport. The (RO_2R) layer is insulating and acts as a charge reservoir for the conducting layer.

In the general composition, RTMPnO (where R is a rare earth, TM is a transition metal and Pn is a Pnictogen element) bonding within these layers is covalent in character,

while the bonding between them has ionic character. Combined with the charge transfer between layers, the Zintl-type characteristics of these structures are clear. However, the actual charges are generally found to be smaller than indicated above and the bonding is, in reality, somewhere between ionic and covalent in both cases. In addition, significant metallic bonding can also occur between the TM atoms within a layer if the 3d shell is not full.[154, 170] The precise nature of the bonding within and between layers is dependent on the constituent elements thus varies from composition to composition.[171] The electronic structure and resulting properties can therefore vary greatly, as evidenced by the variety of behaviours summarised in Section 7.1.

7.1.2 Potential Thermoelectric Properties

The structure of RMnSbO offers several features that make it attractive for thermoelectrics research. The effects of reduced dimensionality on the Seebeck coefficient were discussed in Chapter 1, thus the layered nature of the structure could promote high S values. The presence of both ionic and covalent bonding may also promote phonon scattering along the c–axis. These effects have been successfully observed in the related LaCuSeO compounds, where S_{max} = 290 μV K^{-1} at 650 K was observed and κ_{RT} was calculated to be 2.1 W m^{-1} K^{-1}.[172]

The structure is also related to the high-efficiency thermoelectric Zintl-material, XZn_2Sb_2, where covalently bound $(ZnSb)^{n-}$ layers are stacked alternately with X^{n+} cations, as illustrated by Figure 7.2.[32] The Zn_2Sb_2 slabs are the 'electron-crystal' in this PGEC compound,[18] and promote carrier transport, while the carrier concentration can be manipulated from the X site. Alloying on this site also creates point defects to reduce the thermal conductivity. $Ca_xYb_{1-x}Zn_2Sb_2$ compositions have yielded high ZT values based on this idea. The end members themselves have reasonably low thermal conductivity values with κ = 4 W m^{-1} K^{-1} reported for $YbZn_2Sb_2$ at room temperature and κ = 2.75 W m^{-1} K^{-1} reported for $CaZn_2Sb_2$. This is reduced to κ = 1.25 W m^{-1} K^{-1} for the x = 0.5 composition.[34] The Seebeck coefficients in this series are highest for higher values of x, eg. $CaZn_2Sb_2$ (S_{max} = 190 μV K^{-1} at 675 K, compared with 90 μV K^{-1} at 750 K for $YbZn_2Sb_2$). This is because Ca has fewer electrons than Yb to donate to the ZnSb slab thus the carrier concentration is lower. This is, however, offset by lowering of the electrical conductivity and the highest ZT values are therefore found for

$YbZn_2Sb_2$ and the x = 0.25 sample, which both yield ZT_{max} = 0.55 at 750 K. Other impressive ZT values in this class of compounds include ZT = 0.31 at 675 K in $BaZn_2Sb_2$ which has a room temperature κ = 1.6 W m^{-1} K^{-1},[173] and ZT = 0.919 at 713 K in $EuZn_2Sb_2$ which has κ = 1.312 W m^{-1} K^{-1}.[174]

Comparison of the XZn_2Sb_2 and RMnSbO structures reveals several similarities. Although the geometry of the bonding is not identical, the covalently bound $(MnSb)^-$ conducting layers can be equated to the Zn_2Sb_2 slabs that are responsible for the electron-crystal properties in XZn_2Sb_2. The $(RO)^+$ layers then take the place of the X^{n+} cations and can be manipulated to inhibit phonon transport or alter carrier concentration. Investigation of RMnSbO structures could, therefore, uncover promising thermoelectric properties.

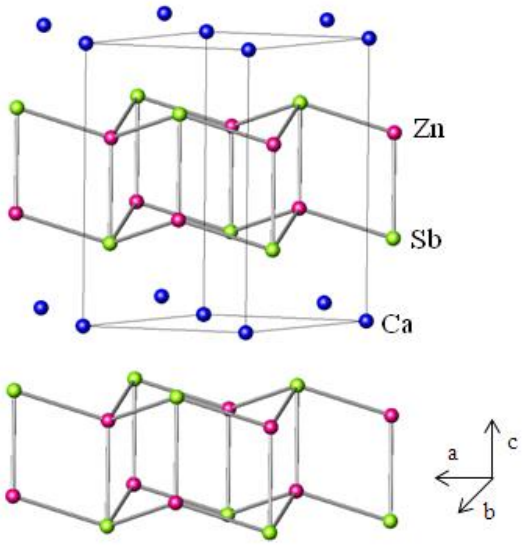

Figure 7.2: Schematic representation of the crystal structure of $CaZn_2Sb_2$.

7.1.3 Aims

NdMnSbO and LaMnSbO form part of an almost unexplored subset of the AMPnO materials. They have therefore been synthesised and variable temperature neutron and synchrotron X-ray powder diffraction experiments have been combined with physical property analysis, in order to characterise these materials for the first time.

7.2 Experimental

Samples were prepared by standard solid state reactions using RSb, Mn_2O_3 and elemental Mn precursors. These powders were mixed using an agate mortar and pestle, pressed into pellets and wrapped in Ta foil, prior to being vacuum sealed in a quartz tube. The samples were then heated at 900 °C for 24 hours. The RSb precursors were prepared by arc-melting the elements in an argon atmosphere. A 15-20% excess of Sb was used to allow for losses during this process.

Laboratory powder X-ray diffraction was performed to check for sample purity and temperature dependent synchrotron X-ray powder diffraction patterns were collected on the I11 instrument at Diamond, Rutherford Appleton Laboratories, UK for NdMnSbO. Variable temperature neutron powder diffraction data were collected on the WISH instrument at ISIS, Rutherford Appleton Laboratories, UK for both LaMnSbO and NdMnSbO.

The temperature dependences of field and zero-field cooled magnetic susceptibilities were measured using a Quantum Design Magnetic Property Measurement System. Electrical resistance, magnetoresistance and heat capacity measurements were carried out using a Quantum Design Physical Property Measurement System. Resistance measurements were performed in the standard 4-probe geometry.

7.3 Results and Discussion

7.3.1 Structure

7.3.1.1 Nuclear Structure

Laboratory X-ray powder diffraction confirmed both LaMnSbO and NdMnSbO formed in the tetragonal *P4/nmm* space group. LaMnSbO was determined to be phase pure within the limits of diffraction, while NdMnSbO was found to contain minor amounts of Nd_2O_3 (2.80(5) wt%) and MnSb (1.87(8) wt%).

Temperature dependent neutron diffraction studies were undertaken for both samples. Rietveld fits for data collected at 1.4 K and 250 K are illustrated in Figure 7.3 and Figure 7.4.

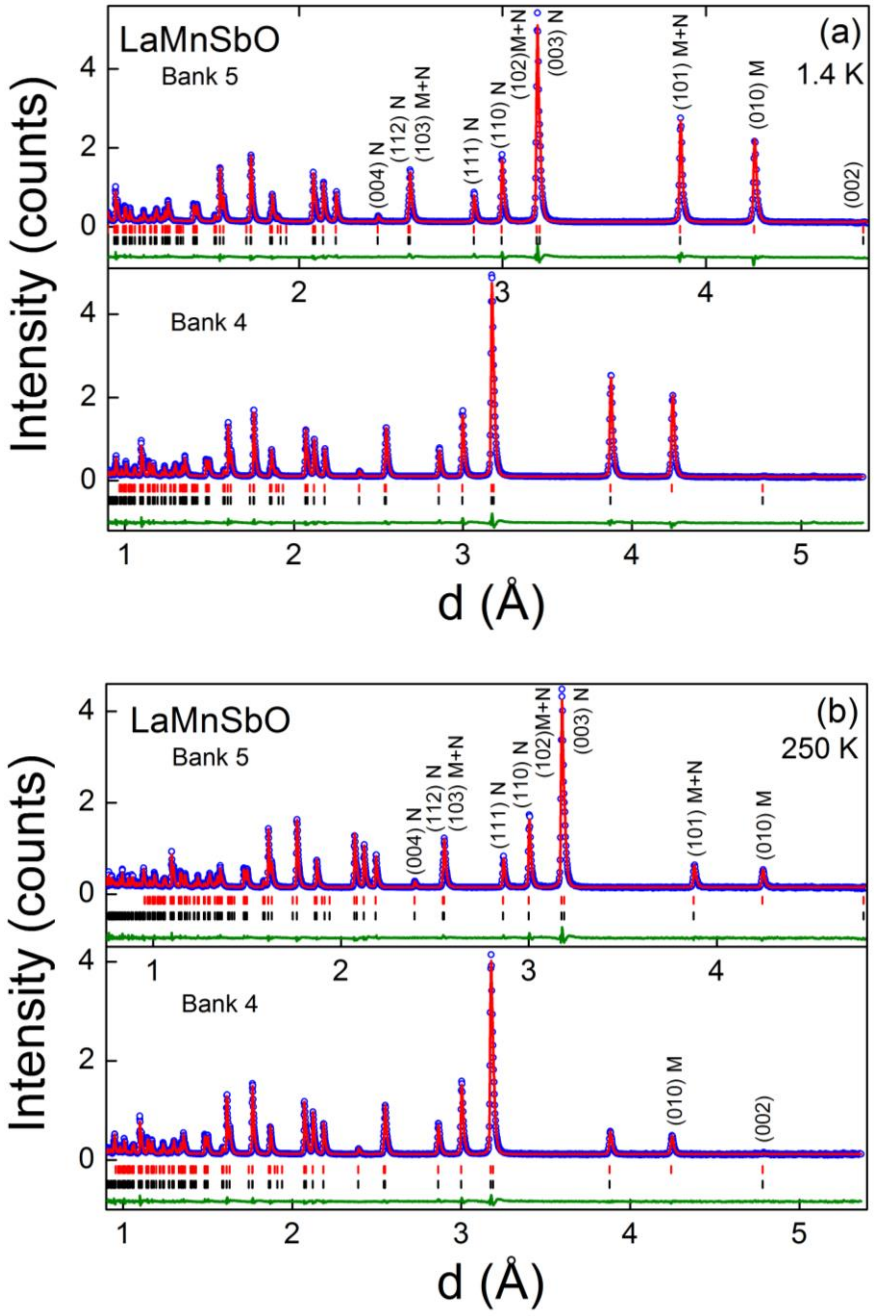

Figure 7.3: Rietveld fits to neutron diffraction data, collected using the WISH instrument at ISIS, for LaMnSbO at 1.4 K (a) and 250 K (b). Blue circles are the collected data, the red line is the calculated fit and the green line is the difference. Upper (red) tickmarks correspond to the magnetic unit cell and lower (black) represent the nuclear structure. Peaks marked M have a magnetic contribution, those marked N have a nuclear contribution and those marked M+N have contributions from both.

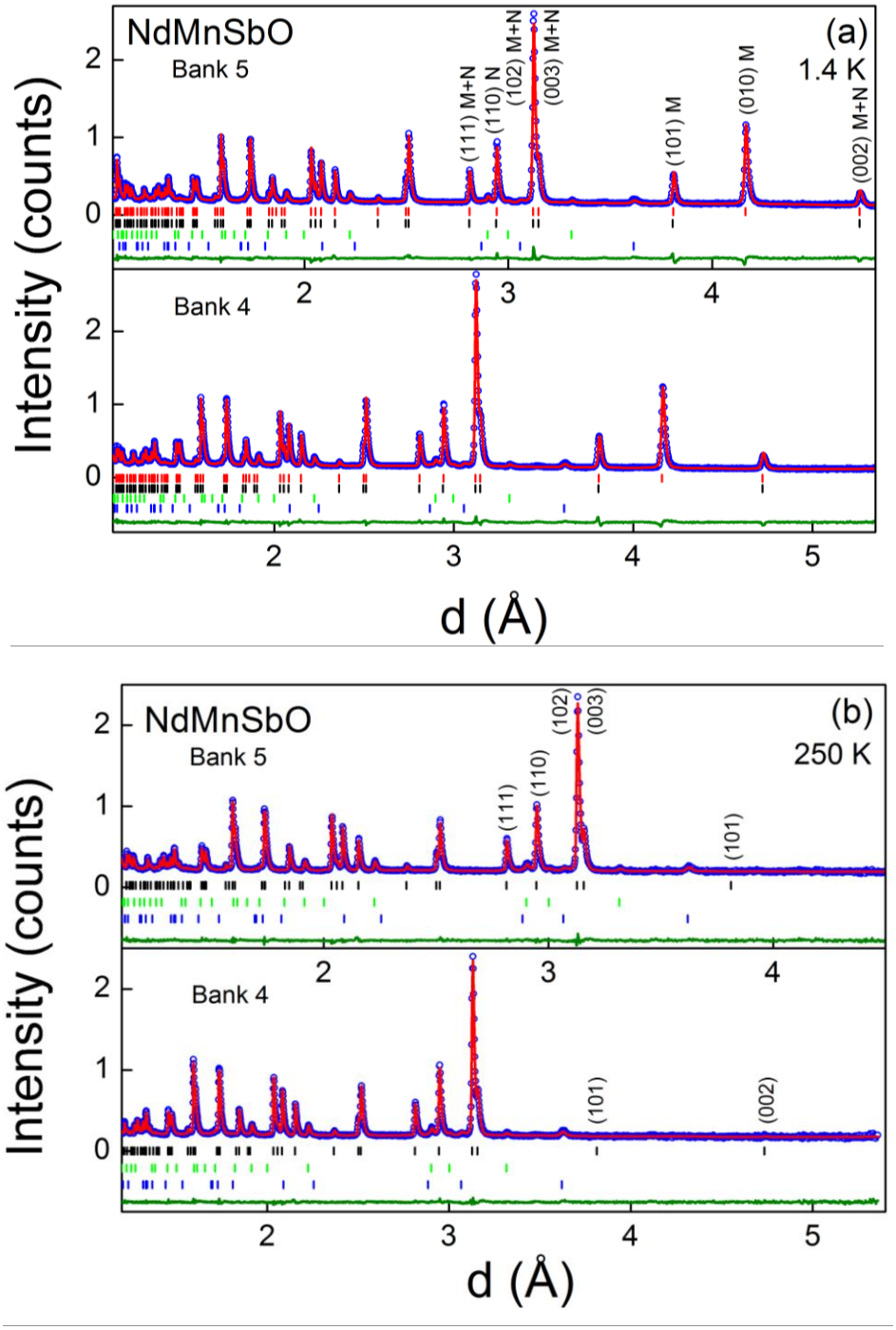

Figure 7.4: Rietveld fits to neutron diffraction data collected using the WISH instrument at ISIS, for NdMnSbO at 1.4 K (a) and 250 K (b). Blue circles are the collected data, the red line is the calculated fit and the green line is the difference. Red (top) tickmarks correspond to the magnetic unit cell, black represent the nuclear structure, green indicate Nd_2O_3 and blue (bottom) correspond to MnSb. Peaks marked M have a magnetic contribution, those marked N have a nuclear contribution and those marked M+N have contributions from both.

Table 7.1: Lattice parameters, atomic positions (Z), fractional site occupancies, thermal parameters (U_{iso}), magnetic moments (M), selected bond lengths and angles and fit statistics for given temperatures as determined from Rietveld refinement of NPD data collected on WISH for RMnSbO, R = La & Nd.

		LaMnSbO		NdMnSbO	
		1.4 K	*250 K*	*1.4 K*	*250 K*
a (Å)	Nuclear	4.2357(1)	4.2426(1)	4.1571(1)	4.1633(1)
	Magnetic	-	-	4.1598(1)	-
c (Å)		9.5441(1)	9.5627(1)	9.4368(2)	9.4635(1)
V(Å^3)	Nuclear	171.236(1)	172.129(1)	163.06(1)	164.26(1)
	Magnetic	-	-	163.27(1)	-
R	Z	0.1193(1)	0.1189(1)	0.1164	0.1165(1)
	Occupancy	0.987(5)	0.980(5)	1	1
	U_{iso}	0.0093(3)	0.0115(3)	0.0079(3)	0.0072(4)
	$\|M_x\|$ (μ_B)	-	-	1.75(1)	-
Mn	Occupancy	0.991(5)	0.986(5)	0.979(3)	0.970(2)
	U_{iso} (Å^2)	0.0099(4)	0.0140(4)	0.0079(3)	0.0072(4)
	$\|M_x\|$ (μ_B)	-	-	3.34(1)	-
	$\|M_z\|$ (μ_B)	3.496(9)	1.55(1)	-	-
Sb	Z	0.6811(1)	0.6812(1)	0.6857	0.6855(1)
	Occupancy	1	1	0.993(2)	0.988(2)
	U_{iso} (Å^2)	0.0084(4)	0.0123(4)	0.0079(3)	0.0072(4)
O	Occupancy	0.990(4)	0.980(4)	0.982(2)	0.978(2)
	U_{iso} (Å^2)	0.0111(4)	0.0124(4)	0.0079(3)	0.0072(4)
R-O (Å)		2.4046(4)	2.4066(4)	2.3611(1)	2.3567(4)
R-O-R (°)		123.45(4)	123.60(4)	124.28(1)	124.09(1)
		102.97(2)	102.90(2)	102.61(1)	102.69(2)
Mn-Sb (Å)		2.7347(5)	2.7377(5)	2.7427(1)	2.7246(6)
Sb-Mn-Sb (°)		113.59(1)	113.55(1)	115.16(1)	114.57(2)
		101.51(3)	101.58(3)	98.61(1)	99.70(3)
R-Sb (Å)		3.5493(7)	3.5586(7)	3.4553(1)	3.4909(7)
Collection current (μA)		20	7	20	7
χ^2		10.6	3.3	5.7	1.7
wR_p	Bank 5	4.6	4.1	3.3	2.8
	Bank 4	4.4	3.9	3.0	2.3
	Bank 3	3.9	3.9	3.0	2.8
R_p	Bank 5	4.3	3.7	3.2	2.5
	Bank 4	3.9	3.4	2.8	2.1
	Bank 3	3.3	3.4	2.7	2.6
R_f^2	Bank 5	5.6	5.1	7.7	3.8
	Bank 4	4.0	6.7	5.8	3.5
	Bank 3	6.2	10.9	5.0	4.4

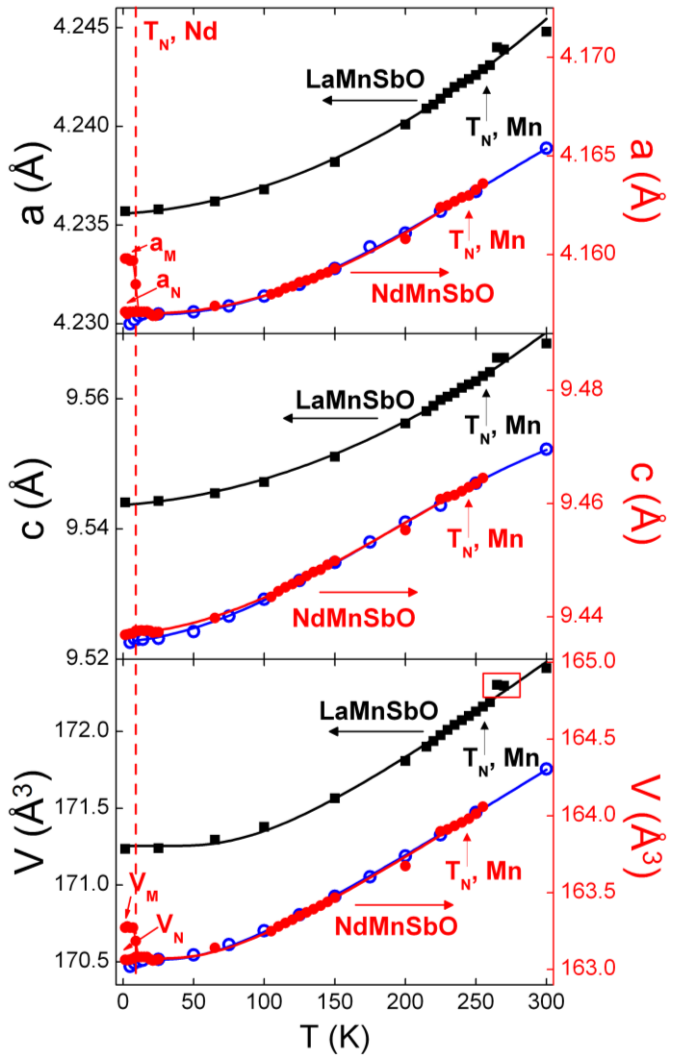

Figure 7.5: Temperature dependence of the lattice parameters for LaMnSbO (left hand axis, black squares) determined from neutron diffraction and NdMnSbO (right-hand axis) determined from neutron (red, closed circles) and X-ray synchrotron (blue, open circles) diffraction.

No structural transitions were observed and the *P4/nmm* structure persists down to 2 K. Lattice parameters, refined site occupancies and positions, thermal parameters and selected bond lengths and angles are summarised in Table 7.1. Bond distances and angles in the LaO and NdO layers do not differ significantly from those in LnFeAsO, LnMnAsO and LnCoAsO.[157, 175, 176] There are, however, significant differences in the MnSb layers. Mn-Sb in LaMnSbO was found to be 2.74 Å, compared with 2.41 Å for Fe-As in LaFeAsO and 2.56 Å for Mn-As in LaMnAsO. The Mn-As bond is longer than the Fe-As bond due to the more covalent nature of the bonding in LaMnAsO,

compared with LaFeAsO. This results in more localised electrons and a bigger cation, hence the longer bond. This may also play a role in determining the length of the Mn-Sb bond in LaMnSbO but the much longer bond length is also consistent with the larger Sb atom. The Mn-Sb bonds in NdMnSbO are also longer than their Mn-As counterparts in NdMnAsO.

The Sb-Mn-Sb bond angles also differ significantly. Sb-Mn-Sb = 113.6º and 101.6º in LaMnSbO, while As-Fe-As angles have been reported at 113.5º and 107.5º in LaFeAsO and As-Mn-As = 110.7º and 107.0º in LaMnAsO.[161, 177] The Sb-Mn-Sb bond angles in NdMnSbO are 98.6º and 115.2º, thus differ significantly from the As-Mn-As angles in NdMnAsO, which are 105.2º and 111.7º. There is therefore a significant departure from the ideal tetrahedral shape in the $MnSb_4$ units in both samples prepared here, which is thought to have a significant impact on magnetic interactions and resulting properties of these samples.[178, 179]

Figure 7.5 illustrates the temperature dependence of the lattice parameters for each sample. In this plot, the WISH data collected for NdMnSbO has been scaled to match the I11 data. Both the a- and c-axis were found to lengthen as the temperature was increased. Fits to the temperature progression of the volume, as per Equation (4.2) are shown in Figure 7.5 and yield θ_D = 147(8) K for LaMnSbO and 113(4) K for NdMnSbO.

7.3.1.2 Magnetic Structure

In LaMnSbO, magnetic ordering of the Mn atoms was observed in patterns collected below 265 K. The magnetic unit cell was fitted, with a starting model based on the ordering observed in PrMnSbO.[168] Mn ordering was found to be fully commensurate with the nuclear unit cell. The Mn moments align antiferromagnetically in a checkerboard pattern, with moments aligned along the c-axis. The temperature dependence of the magnitude of the magnetic moment is plotted in Figure 7.6. A critical fit to the data was performed, between 150 K and 260 K, using the expression set out in Equation (7.1).

$$m(T) = m_0\left(1 - \frac{T}{T_N}\right)^{\beta} \qquad \text{Equation (7.1)}$$

where T_N is the ordering temperature and β is the critical exponent. This yields m_0 = 3.9(1) μ_B, T_N = 256.3(6) K and β = 0.24(1). This β-value is lower than that expected for a 3-dimensional Heisenberg model (β=0.365), possibly due to the layered nature of this material.

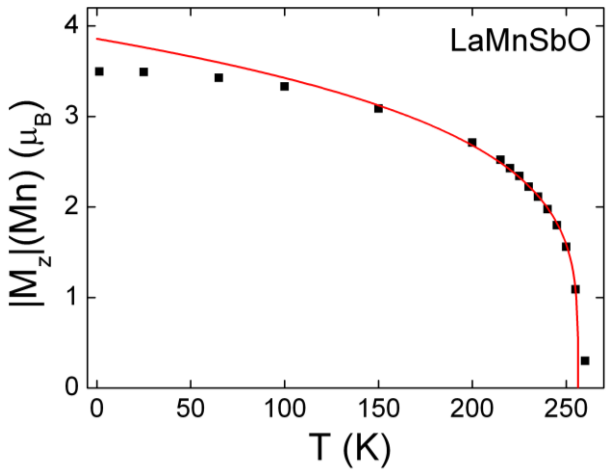

Figure 7.6: Temperature dependence of the Mn magnetic moment in LaMnSbO.

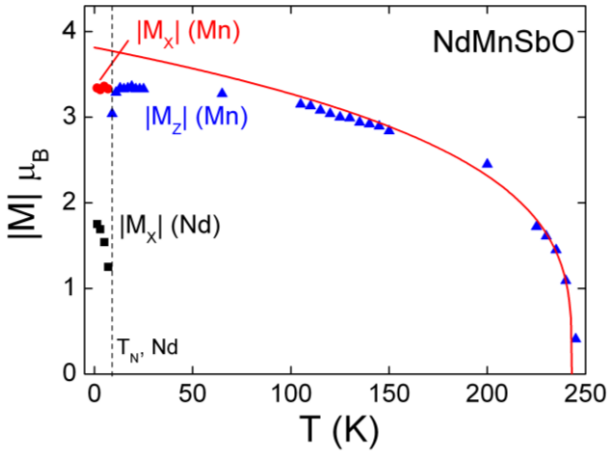

Figure 7.7: Temperature dependence of the magnetic moments in NdMnSbO.

Ordering of the Mn atoms was also observed in NdMnSbO. The magnitudes of the magnetic moments are plotted in Figure 7.7, and the fit between 150 and 250 K gives M_0 = 3.8(1), β = 0.32(1) and T_N = 245.2(2) K. $|M_Z|$ (Mn) can be observed to decrease slightly below 13 K. This precedes the magnetic ordering of Nd below 9 K. At this temperature, Nd and Mn are found to order perpendicular to the c-axis, rather than

parallel to it. The reduction in $|M_Z|$ (Mn) just above this temperature therefore suggests that the Mn moments are reorienting as a result of the alignment of Nd spins, as previously described for NdMnAsO[175] NdFeAsO[180], and PrMnSbO.[168]

Rietveld refinement of the magnetic ordering below 9 K revealed that the magnetic cell is not fully commensurate with the nuclear structure. A model maintaining identical unit cell dimensions for the two phases failed to correctly fit the positions of the magnetic peaks, as can be seen in Figure 7.8(a). Refinement of $a_{M,}$ independently of a_N, (a_M = magnetic and a_N = nuclear) was found to solve this problem (Figure 7.8(b)). c_N was kept equal to c_M and the tetragonal symmetry was maintained in the magnetic phase. This yields a_M = 4.1616(1) Å and a_N = 4.1589(1) Å, a difference of 0.0027 Å = 1/1540 a_N. The good fit to the magnetic intensities obtained in this fit suggests only a small deviation from co-linearity occurs, perhaps due to very slow precession of the moments. If this is the case, a complete revolution of the moment occurs every 1540 unit cells.

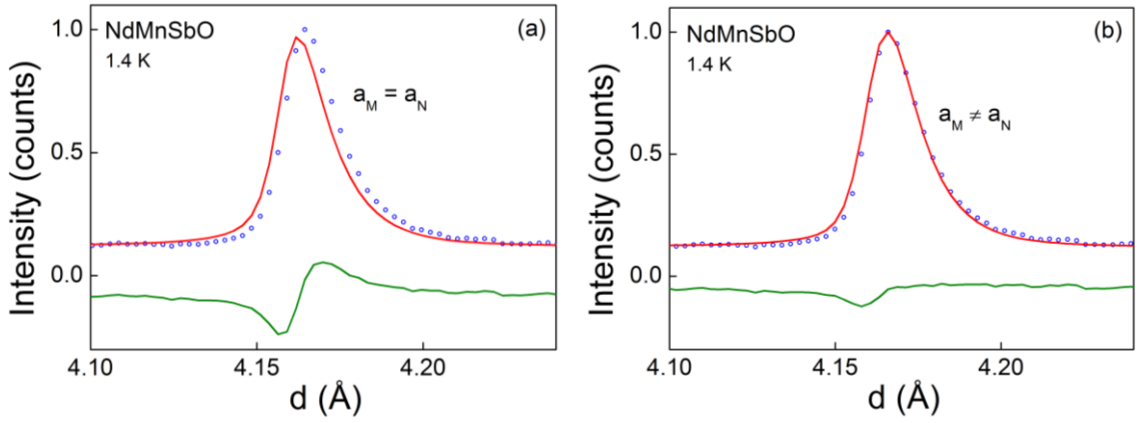

Figure 7.8: Close up of the (010) peak for NdMnSbO at 1.4 K where (a) the magnetic unit cell and nuclear unit cell are fixed to be equal and (b) the magnetic unit cell was allowed to refine independently of the nuclear unit cell. Blue circles are the collected data, the red line is the calculated fit and the green line is the difference.

7.3.2 Physical Properties

7.3.2.1 Thermoelectric Properties

Low temperature resistivity measurements revealed LaMnSbO to be semiconducting from 2 – 350 K (Figure 7.9), with values approaching 0.3 kΩ cm at room temperature.

The magnitude of the resistivity is above the measurable range of the Linseis-LSR Seebeck probe, thus it was not possible to obtain high temperature resistivity or Seebeck data.

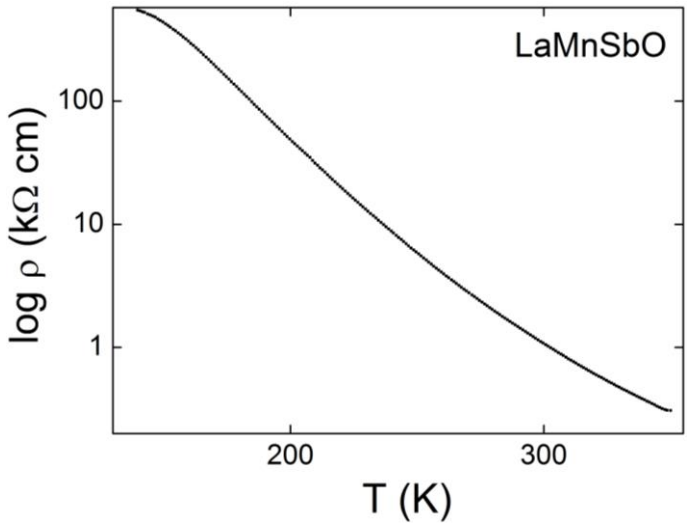

Figure 7.9: Temperature dependence of resistivity (ρ) for LaMnSbO.

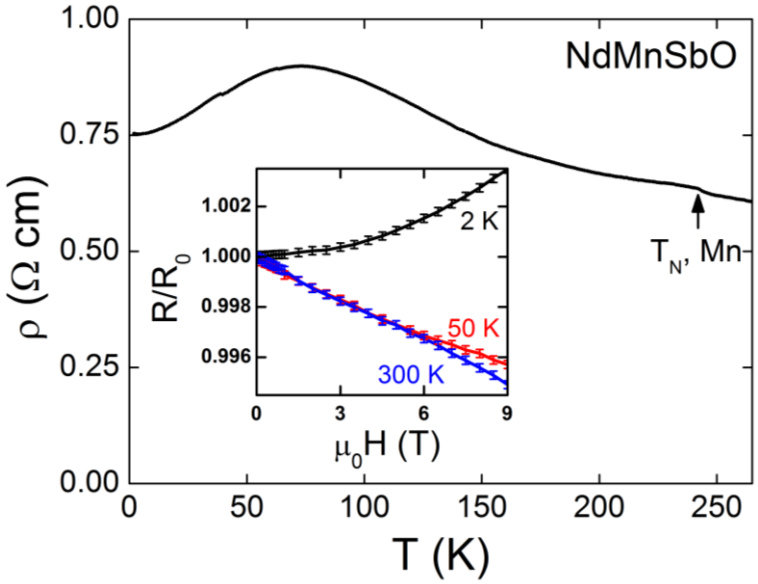

Figure 7.10: Temperature (T) evolution of resistivity (ρ) for NdMnSbO between 2 and 260 K. Inset: Field dependence of ρ at 2 K, 50 K and 300 K.

NdMnSbO exhibits resistivity values over 5 orders of magnitude lower than those measured for LaMnSbO. The data is presented in Figure 7.10 and shows

semiconducting behaviour above 70 K. Between 2 and 70 K, however, an increase in resistivity with temperature is observed, consistent with metallic-type behaviour. A maximum value of $\rho = 0.9\ \Omega$ cm was reached at 73 K and this slowly decreases to 0.6 Ω cm just above 250 K.

The temperature dependence of the resistivity is not consistent with either Arrhenius or variable-range-hopping behaviour, for either sample. A small discontinuity in the NdMnSbO data may be observed just below 250 K. This coincides with the ordering of Mn within the structure. Magnetic field dependent resistivity measurements were also undertaken for NdMnSbO. These revealed a small positive magnetoresistance at 2 K, while a small negative value was observed at 50 and 300 K, as shown in the inset to Figure 7.10.

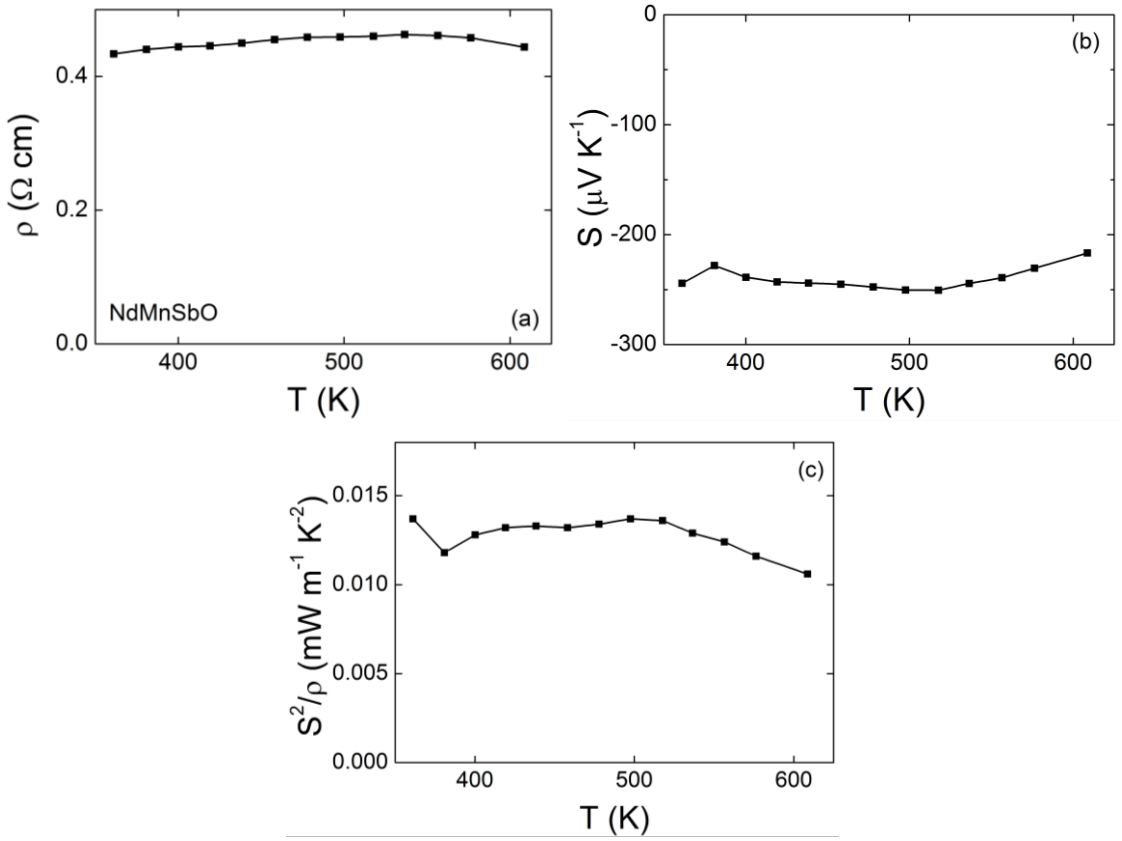

Figure 7.11: Temperature dependence of (a) resistivity (ρ), (b) Seebeck coefficient (S) and (c) power factor (S^2/ρ) for NdMnSbO in the Temperature range 350 – 600 K.

The resistivity of NdMnSbO was sufficiently low to allow high temperature measurements of the Seebeck and resistivity to be made for this sample. The results are displayed in Figure 7.11. The Seebeck coefficient is negative, indicating n-type behaviour. A promising S = -250 μV K^{-1} is found at room temperature and this is maintained until just above 500 K, where a slight decrease in magnitude is observed, possibly due to the onset of hole conduction. The room temperature resistivity value is quite high for a good thermoelectric material, at ρ = 0.425 Ω cm at room temperature. This is consistent with the low temperature data, which indicates ρ = 0.6 Ω cm at 250 K. Above room temperature, there is a slight increase in the resistivity with temperature, consistent with degenerate semiconducting behaviour.

The power factor has a maximum value of S^2/ρ = 0.0014 mW m^{-1} K^{-2} at 510 K. This rather low value is a result of the high resistivity of this sample, which may be a result of the poor density. For comparison, in $La_{1-x}Sr_xCuOSe$ samples, S^2/ρ_{max} = $1x10^{-2}$ mW m^{-1} K^{-2} at 650 K was reported for x = 0 and S^2/ρ_{max} = $1.4x10^{-1}$ mW m^{-1} K^{-2} at 650 K was reported for x = 0.05.[172] There is therefore scope to improve these properties. Densification of these samples is required but doping may also be effective in decreasing ρ. If this can be achieved without having a significant impact on the Seebeck coefficient, these structures could still offer a new option for thermoelectrics research.

7.3.2.2 Magnetic Susceptibility

The magnetic susceptibility data is plotted in Figure 7.12. Negligible difference between the field- and zero field- cooled measurements is observed for both samples. The temperature dependences are characteristic of local moment magnetism but do not obey the Curie-Weiss law. At low temperatures, two transitions are observed for NdMnSbO. The first is at 9 K, consistent with the Nd ordering temperature, and the second is observed at 5 K and is likely due to Nd^{3+} crystal field splitting. No such behaviour is observed in the data for LaMnSbO.

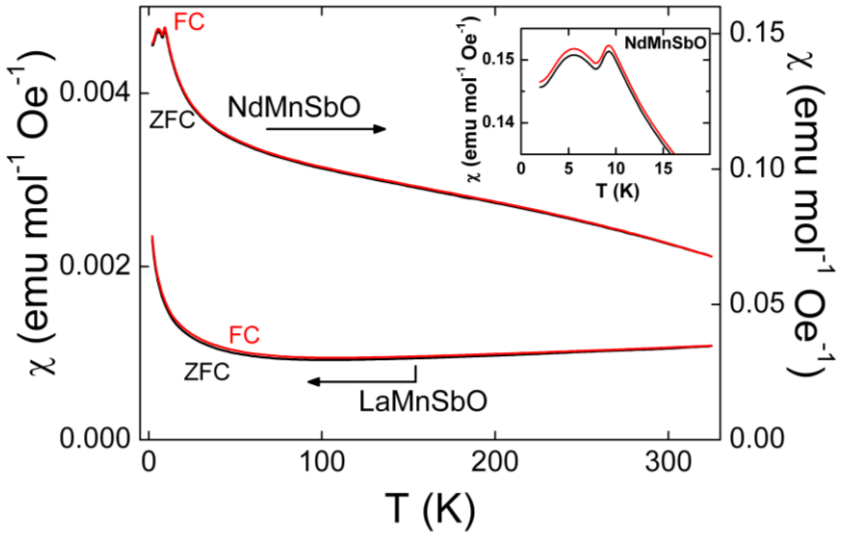

Figure 7.12: Temperature dependence of the magnetic susceptibility χ(T) for LaMnSbO (left-hand axis) and NdMnSbO (right-hand axis) between 2 K and room temperature. Inset: Low temperature (0 – 20 K) χ(T) for NdMnSbO.

7.3.2.3 Heat Capacity

Measurement of the heat capacity shows two peaks in the low temperature data, at 5 and 9 K for NdMnSbO (Figure 7.13(a)). This corresponds to the transitions observed in the magnetic susceptibility data. No such features are observed in the LaMnSbO data, which has a smaller heat capacity than its Nd analogue over most of the temperature range. Based on the estimated θ_D values (θ_D = 147(8) K for LaMnSbO and 113(4) K for NdMnSbO), the heat capacity for NdMnSbO is expected to increase faster, as observed, as per Equation (7.2).

$$C_{Phonons} \propto \left(\frac{T}{\theta_D}\right)^3 \qquad \text{Equation (7.2)}$$

A plot of C/T vs. T^2 may be used to determine the electronic contribution to the heat capacity using the relationship defined in Equation (7.3). Inspection of the plot in Figure 7.9(b) shows γ to be negligible for both samples.

$$\frac{C}{T} = \gamma + AT^2 \qquad \text{Equation (7.3)}$$

where C is the heat capacity, T is temperature, γ is the electronic contribution to C and A is a constant.

The entropy associated with the Neel ordering of Nd and crystal field splitting in NdMnSbO was calculated by integrating C/T with respect to T, as defined in Equation (7.4).

$$S = \int_{0\,K}^{15\,K} \frac{C}{T}\, dT \qquad \text{Equation (7.4)}$$

where S is the entropy, C is the heat capacity and T is the temperature.

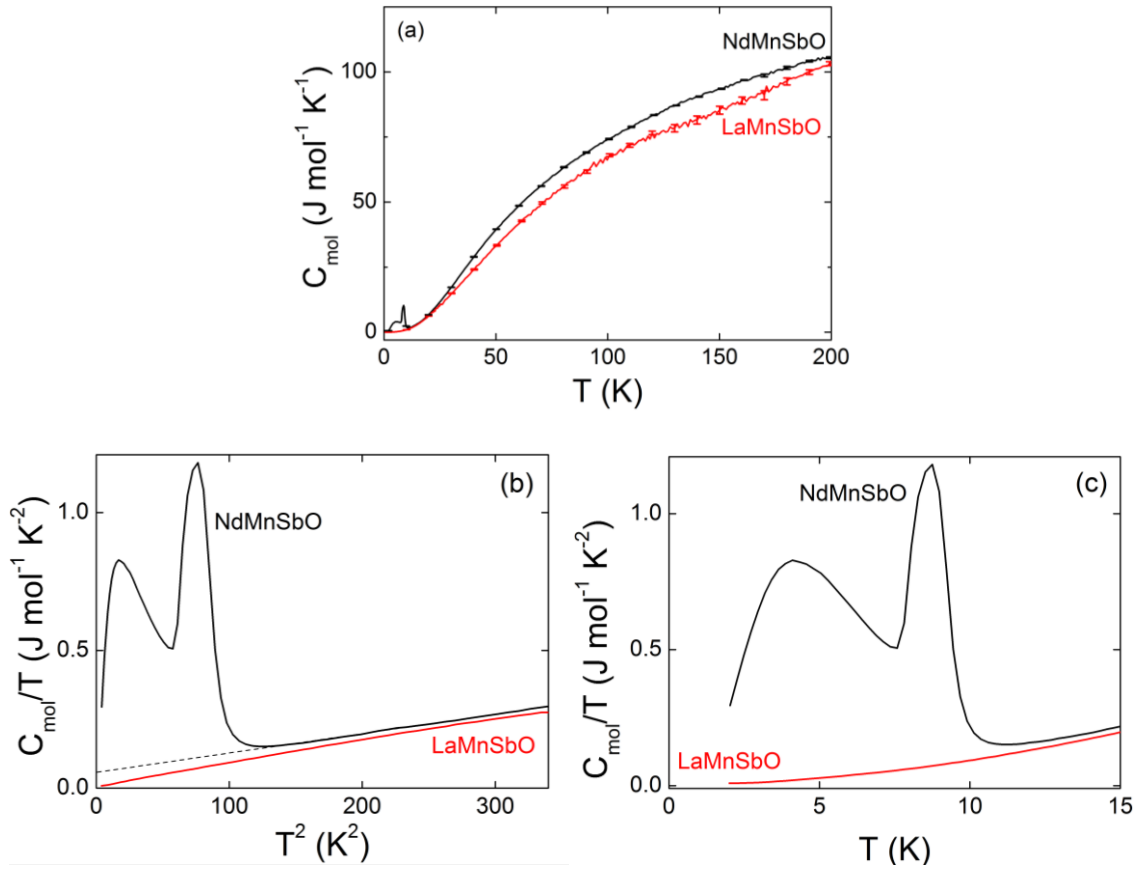

Figure 7.13: Temperature dependence of the heat capacity (C) for LaMnSbO and NdMnSbO. (a) C vs. T, (b) C/T vs. T^2 and (c) C/T vs. T.

The heat capacity of the LaMnSbO sample was first subtracted from the data collected for NdMnSbO, to account for entropy in the system not due to the ordering and crystal field splitting. C/T plotted against T is presented in Figure 7.13(c) and the entropy was

calculated to be 5.38 J mol^{-1} K^{-1}. This can be compared to S = Rln(2J+1) which, for J = ½, yields 5.7 suggesting that the Nd has J = ½.

7.4 Conclusions

LaMnSbO and NdMnSbO have been successfully synthesised and both structural and physical properties have been characterised. Both compositions crystallise in the *P4/nmm* space group which is maintained down to 2 K. The Mn moments order antiferromagnetically at approximately 250 K in both samples and the Nd moments align at 9 K in NdMnSbO. The magnetic ordering does not appear to be commensurate below $T_{N,Nd}$ as a very small difference in the 'a' lattice parameter (i.e. $a_M \neq a_N$) was required to correctly fit the magnetic peak positions. Further work is required to determine the nature of this incommensurability.

Both compositions possess large resistivity values. LaMnSbO, in particular, has a high ρ for thermoelectric applications, with values in the kΩ cm range and the Seebeck coefficient could not be measured for this sample. NdMnSbO produced ρ = 0.425 Ω cm at room temperature, which is also rather large for thermoelectric applications. The Seebeck coefficient is, however, also large with S = -250 μV K^{-1} at room temperature. These values are comparable with a LaZnSbO sample that was also investigated for its thermoelectric properties. ρ = 0.53 Ω cm, S = 160 μV K^{-1} and κ = 1 W m^{-1} K^{-1} lead to ZT_{max} = 0.0325 at 650 K for this sample.[181] These structures are therefore prone to very low thermal conductivity, which preserves interest in them as potential thermoelectric materials.

Clearly large improvements in these compounds must be made to produce competitive materials. First and foremost, densification is required to reduce the resistivity to the intrinsic values of these compositions. Thereafter, there are multiple ways in which these structures can be manipulated and it is possible that, with the correct doping/substitution, power factor values could be significantly improved. As these compositions are n-type, electron doping is likely to result in a decrease in ρ. As the MnSb layer is considered to be the conducting layer in these materials, this could be achieved by Fe doping on the Mn-site. Alternatively, indirect doping can be achieved by altering the NdO layer. For example, F-substitution on the O-site would provide the NdO layer with an extra electron to transfer to the (MnSb) layer thus would increase the

negative charge in the conducting layer. Care must be taken not to destroy the large Seebeck coefficient, but the layered nature of the structure may allow it to maintain a high S, despite the increase in carrier concentration.

Chapter 8 – Conclusions

Zintl materials are of huge interest in the field of thermoelectrics. Their often complex structures include both ionic and covalent bonding thus they epitomise the requirements of a phonon-glass-electron-crystal (PGEC) compound.[32, 33, 35] Materials that adhere to the PGEC concept must contain separate components that are responsible for the electrical and phonon transport so that κ_{lat} is effectively decoupled from $S^2/(\rho\kappa_{el})$. If this is achieved, alterations to the structure that promote charge carrier transport do not also promote phonon transport. Similarly, changes that disrupt phonon flow should not negatively impact on charge transport. This allows independent optimisation of the two terms, making possible the attainment of high ZT-values. Owing to this decoupling, Zintl materials have enjoyed much success in the field of thermoelectrics with skutterudites, clathrates and the recently reported $Yb_{11}MnSb_{14}$ all reaching ZT values in excess of 1.[30, 31, 36]

Many materials exist that display similar features to Zintl materials, although they do not adhere to the strict definition of a Zintl phase. These therefore also offer much potential and are worthy of investigation for their thermoelectric properties. With this in mind, three distinct structure types that can all be described with reference to a Zintl-type model were investigated in the work presented in this thesis. The first of these, namely the half-Heuslers, are well established to be promising thermoelectric materials but significant improvement of their properties has been hindered by a lack of knowledge regarding the interplay between composition, crystal, nano- and micro-structure. The work presented in Chapters 3-5 attempted to address this problem, in addition to exploring new routes to attain high ZT values. In addition to this, four compositions not previously investigated for their thermoelectric properties, were identified and characterised: TiNiX (X = Si, Ge) (Chapter 6) and RMnSbO (Chapter 7).

8.1 XNiSn-based Half-Heuslers

The focus of much of the work reported in Chapters 3-5 is a detailed investigation of the structure of these compounds. X-ray and neutron powder diffraction were used to probe features of the unit cell, but also provided significant insight into the microstructure. Complementary electron microscopy analysis allowed the nano- and micro-structures to

be further investigated. Coupled with measurement of the thermoelectric properties, this has allowed explanation of the observed properties, and has provided a number of insights for the optimisation of ZT for XNiSn-based half-Heuslers. Microscopy is routinely used to probe structural features of these materials but this work was the first, and to our knowledge remains the only, investigation of these compositions using neutron powder diffraction. This provides a description of the bulk sample, as opposed to the snapshots of small areas that microscopy analysis provides. This has provided new detailed information regarding the unit cell and micro-structural features in these compositions. This has allowed identification of two distinct structural phenomena that are common to all prepared samples.

The first of these is the multiphase behaviour, described in Chapters 3 and 4. This was identified in all $X_{1-x}X'_xNiSn$ samples, where $x \neq 0, 1$. This behaviour was found to be common to samples prepared by arc-melting and solid state reactions, nominally stoichiometric and Sn-deficient samples, Sb-doped samples and samples that had undergone SPS densification. In all cases, a semi-continuous distribution of $X_{1-x}X'_xNiSn$ phases was found. The precise range and distribution of x-values found in each sample was found to vary, depending on the synthesis protocol and processing techniques employed, however a relatively large range ($\Delta x = 0.3$-0.5) was covered in each case. The fact that no particular x-values are favoured and the discrepancies in precise distributions suggest that this is a kinetically-driven effect, controlled by the slow mixing of the X-metals. Interestingly, the neutron powder diffraction data collected on the present samples indicated a smaller compositional range than the X-ray data suggested. This suggests that the multiphase behaviour is more pronounced at the surface of the samples, with the bulk exhibiting much less variation. This is in keeping with the TEM analysis of a $Ti_{0.5}Zr_{0.5}NiSn$ sample, which showed little variation in X-metal ratio between separate grains under investigation. This implies that the compositional variations occur over large length-scales in these samples and explains why no significant change is induced in the thermoelectric properties.

Neutron diffraction has also allowed the identification of 0-3% interstitial Ni in all the presented XNiSn-based samples, where excess Ni is randomly distributed across the vacant interstitial sites in the structure. This is not predicted by the phase diagram for TiNiSn and has not previously been investigated in any detail. The $TiNiM_ySn$ (M = Ni,

Co, Cu) samples presented in Chapter 5 provided no evidence for the nano- or micro-inclusions reported by other groups and provide further evidence that genuine interstitial Ni is possible for these structures. The observation of interstitials in this work and inclusions in others suggests that this is also a kinetically-driven effect. Chai *et al* recently posited that interstitials form first, which then begin to coalesce to form nano- then micro-inclusions.[93] Interstitials and inclusions may not then be mutually exclusive and it is likely that interstitials are present in most XNiSn-based compositions.

A predisposition to forming with excess Ni in the structure is significant, as the work presented in Chapters 3 and 5 demonstrates that interstitial metal has a doping effect on the thermoelectric properties of these compositions. Thermoelectric property measurements for the $TiNi_{1+y}Sn$ and arc-melted samples clearly showed that interstitial Ni causes electron doping. The arc-melted samples presented in Chapter 3 also showed a reduction in κ_{lat} upon the introduction of increasing amounts of interstitial Ni. Electron microscopy analysis of the arc-melted samples is required to discount the formation of full-Heusler nano-inclusions in these samples, however the change in electronic properties is consistent with those reported in the $TiNi_{1+y}Sn$ sample reported in Chapter 5, which do not contain such inclusions. This suggests that interstitial Ni atoms may act as scattering centres for phonons, and thus reduce the thermal conductivity.

The Co- and Cu-doped samples presented in Chapter 5 represent the first instance of using alternative transition metals as the excess metal where, for only minor levels of excess, significant doping effects were achieved. A 33% improvement of the maximum power factor value from 1.5 mW m^{-1} K^{-2} to 2 mW m^{-1} K^{-2} at 700 K was observed for $TiNiCu_{0.025}Sn$ and an n- to p-type transition was seen in $TiNiCo_ySn$. Densification of these samples is now required to determine κ and ZT.

8.2 TiNiX (X = Si, Ge)

TiNiX structures, where X = Si or Ge were synthesised and their properties characterised. TiNiGe was found to contain some impurities thus improvement of the synthetic conditions for this sample is required. These samples are characterised by low resistivity values. This is combined with low S and high κ resulting in rather low ZT

values. Outside of the field of thermoelectrics, low temperature transport data indicate that these samples (TiNiGe in particular) may have significant magnetoresistance properties.

8.3 RMnSbO (R = La, Nd)

LaMnSbO and NdMnSbO were prepared and their structure and properties investigated. These structures form part of a relatively unexplored subset of the AMPnO structures. Both samples maintain the tetragonal *P4/nmm* space group down to 2 K. Antiferromagnetic ordering of the Mn moments was observed at 256 K in LaMnSbO and 245 K in NdMnSbO. The Nd moments in NdMnSbO were also found to order antiferromagnetically at 9 K and this ordering is not commensurate with the nuclear cell. Further analysis is required to determine the nature of this incommensurability. These samples are semiconducting with prohibitively large ρ-values for thermoelectric applications. However, S for NdMnSbO is large: S_{RT} = -250 μV K^{-1}. In addition, similar materials (e.g LaZnSbO) have been demonstrated to have low κ.[181] Combined with the high S produced by NdMnSbO, these samples may yet have some potential thus further investigation is warranted.

8.4 Further Work

The work presented in Chapters 3-5 provides a detailed structural characterisation of the XNiSn-based half-Heuslers, utilising neutron and X-ray powder diffraction. Such investigations should be extended to other half-Heusler compositions to determine whether multiphase behaviour and excess transition metals are also prevalent in these systems. XCoSb-based systems are of particular interest, given that they provide a p-type counterpart to XNiSn and also show very promising thermoelectric efficiencies. In addition, the possibility of Ni-deficiency in TiNiSn should be explored.

With regard to the particular samples prepared for this thesis, densification is a key priority, so that assessment of the thermoelectric performance may be completed with thermal conductivity measurements. TEM analysis of the arc-melted samples presented in Chapter 3 may also be useful in providing further insight into the effect that the distribution of interstitial Ni has on the thermoelectric properties of these materials.

Substitutions must be investigated in both TiNiX and RMnSbO. While the samples presented in chapters 6 and 7 do not perform particularly well as thermoelectrics, both show some promising characteristics and warrant further investigation.

In TiNiX, S must be increased and κ decreased to substantially improve the thermoelectric efficiency of these samples. Both these properties may be improved by reduced dimensionality as was exemplified by $Ca_{1-x}Ce_xAg_{1-y}Sb$, where a transition from orthorhombic to hexagonal symmetry was accompanied by a 7-fold increase in ZT.[149] Identification of suitable dopants should be attempted in order to optimise these materials. If this is achieved, higher ZT values may be obtainable.

Densification of the RMnSbO samples is required to gain an accurate indication of the intrinsic resistivity and thermal conductivity of these samples. Thereafter, substitutions in either the insulating or conducting layers may be implemented in an attempt to optimise the thermoelectric properties. As the Seebeck coefficients appear to be relatively large, initial focus should be on reduction of the large resistivity values. This could involve electron doping in the MnSb layer, by Fe-substitution on the Mn site, for example. The NdO layer may also be doped by replacing O with F.

8.5 Final Remarks

Three distinct sets of materials have been investigated and assessed for their potential in the field of thermoelectrics. The work presented throughout this thesis aimed to provide strong structural characterisation of each of these compositions, in order to elucidate structure-property relationships and provide insight into possible routes for further optimisation. This has been achieved primarily using neutron powder diffraction. Each of the series investigated was found to have some promise in this field. TiNiX and RMnSbO are new compositions with respect to thermoelectric investigations. They provide a good starting point and substitutions should be investigated that may significantly improve their performance. The half-Heuslers are well established as thermoelectric materials but only recently has detailed attention been paid to the structural features, on various length-scales, that can have a significant impact on the properties. With increased knowledge of such features, as presented in this thesis, targeted design of half-Heuslers and significant advances in ZT should be possible.

References

[1] V.S. Arunachalam, E.L. Fleischer, MRS Bulletin, 33 (2008) 264-276.

[2] J. Baxter, Z. Bian, G. Chen, D. Danielson, M.S. Dresselhaus, A.G. Fedorov, T.S. Fisher, C.W. Jones, E. Maginn, U. Kortshagen, A. Manthiram, A. Nozik, D.R. Rolison, T. Sands, L. Shi, D. Sholl, Y. Wu, Energy & Environmental Science, 2 (2009) 559-588.

[3] T.M. Tritt, H. Bottner, L. Chen, MRS Bulletin, 33 (2008) 366-368.

[4] M.H. Elsheikh, D.A. Shnawah, M.F.M. Sabri, S.B.M. Said, M.H. Hassan, M.B.A. Bashir, M. Mohamad, Renewable and Sustainable Energy Reviews, 30 (2014) 337-355.

[5] S.B. Riffat, X. Ma, Applied Thermal Engineering, 23 (2003) 913-935.

[6] D.M. Rowe, Renewable Energy, 16 (1999) 1251-1256.

[7] L. Weiling, T. Shantung, Chin.Sci.Bull., 49 (2004) 1212-1219.

[8] L.E. Bell, Science, 321 (2008) 1457-1461.

[9] F.J. DiSalvo, Science, 285 (1999) 703-706.

[10] G. Mahan, B. Sales, J. Sharp, Physics Today, 50 (1997) 42-47.

[11] P. Day, A.K. Cheetham, Solid State Chemistry: Techniques, Oxford University Press, Oxford, 1987.

[12] J.R. Sootsman, D.Y. Chung, M.G. Kanatzidis, Angewandte Chemie International Edition, 48 (2009) 8616-8639.

[13] G.J. Snyder, E.S. Toberer, Nature Materials, 7 (2008) 105-114.

[14] N.F. Mott, H. Jones, The Theory of the Properties of Metals and Alloys, Dover Publications, New York, 1958.

[15] M.S. Dresselhaus, G. Chen, M.Y. Tang, R.G. Yang, H. Lee, D.Z. Wang, Z.F. Ren, J.P. Fleurial, P. Gogna, Advanced Materials, 19 (2007) 1043-1053.

[16] C. Kittel, Introduction to Solid State Physics, 8 ed., Wiley, New York, 2005.

[17] A.R. West, Basic Solid state Chemistry, John Wiley & Sons, Chichester, 1984.

[18] G.A. Slack, CRC Handbook of Thermoelectrics, CRC, Boca Raton, Florida, 1995.

[19] G.S. Nolas, J. Poon, M.G. Kanatzidis, MRS Bulletin, 31 (2006) 199-205.

[20] G.S. Nolas, D.T. Morelli, T.M. Tritt, Annual Review of Materials Science, 29 (1999) 89-116.

[21] D. Vashaee, A. Shakouri, Physical Review Letters, 92 (2004) 106103.

[22] J.R. Sootsman, H. Kong, C. Uher, J.J. D'Angelo, C.-I. Wu, T.P. Hogan, T. Caillat, M.G. Kanatzidis, Angewandte Chemie International Edition, 47 (2008) 8618-8622.

[23] M. Mikami, R. Funahashi, Journal of Solid State Chemistry, 178 (2005) 1670-1674.

[24] G.M. Beensh-Marchwicka, E. Prociów, W. Mielcarek, Crystal Research and Technology, 36 (2001) 1035-1043.

[25] S.V. Faleev, F. Léonard, Physical Review B, 77 (2008) 214304.

[26] M. Zebarjadi, K. Esfarjani, M.S. Dresselhaus, Z.F. Ren, G. Chen, Energy & Environmental Science, 5 (2012) 5147-5162.

[27] G.S. Nolas, J. Sharp, H.J. Goldsmid, Thermoelectrics: Basic Principles and New Materials, Springer, New York, 2001.

[28] E. Skrabeck, D.S. Trimmer, CRC Handbook of Thermoelectrics, CRC, Boca Raton, Florida, 1995.

[29] Z.H. Dughaish, Physica B: Condensed Matter, 322 (2002) 205-223.

[30] X. Tang, Q. Zhang, L. Chen, T. Goto, T. Hirai, Journal of Applied Physics, 97 (2005) 093712.

[31] A. Saramat, G. Svensson, A.E.C. Palmqvist, C. Stiewe, E. Mueller, D. Platzek, S.G.K. Williams, D.M. Rowe, J.D. Bryan, G.D. Stucky, Journal of Applied Physics, 99 (2006) 023708.

[32] S.M. Kauzlarich, S.R. Brown, G. Jeffrey Snyder, Dalton Transactions, (2007) 2099-2107.

[33] E.S. Toberer, A.F. May, G.J. Snyder, Chemistry of Materials, 22 (2009) 624-634.

[34] F. Gascoin, S. Ottensmann, D. Stark, S.M. Haïle, G.J. Snyder, Advanced Functional Materials, 15 (2005) 1860-1864.

[35] G.J. Snyder, M. Christensen, E. Nishibori, T. Caillat, B.B. Iversen, Nature Materials, 3 (2004) 458-463.

[36] S.R. Brown, S.M. Kauzlarich, F. Gascoin, G.J. Snyder, Chemistry of Materials, 18 (2006) 1873-1877.

[37] R. Venkatasubramanian, E. Siivola, T. Colpitts, B. O'Quinn, Nature, 413 (2001) 597-602.

[38] C.J. Vineis, A. Shakouri, A. Majumdar, M.G. Kanatzidis, Advanced Materials, 22 (2010) 3970-3980.

[39] K.F. Hsu, S. Loo, F. Guo, W. Chen, J.S. Dyck, C. Uher, T. Hogan, E.K. Polychroniadis, M.G. Kanatzidis, Science, 303 (2004) 818-821.

[40] H. Lin, E.S. Bozin, S.J.L. Billinge, E. Quarez, M.G. Kanatzidis, Physical Review B, 72 (2005) 174113.

[41] J. Androulakis, C.-H. Lin, H.-J. Kong, C. Uher, C.-I. Wu, T. Hogan, B.A. Cook, T. Caillat, K.M. Paraskevopoulos, M.G. Kanatzidis, Journal of the American Chemical Society, 129 (2007) 9780-9788.

[42] J.R. Sootsman, R.J. Pcionek, H. Kong, C. Uher, M.G. Kanatzidis, Chemistry of Materials, 18 (2006) 4993-4995.

[43] S. Ogut, K. Rabe, Physical Review B, 51 (1995) 10443.

[44] J. Pierre, R.V. Skolozdra, J. Tobola, S. Kaprzyk, C. Hordequin, M.A. Kouacou, L. Karla, R. Currat, E. Lelievre-Berna, Journal of Alloys and Compounds, 262-263 (1997) 101-107.

[45] R.A. de Groot, Journal of Magnetism and Magnetic Materials, 54-57 (1986) 1377-1380.

[46] J. Tobola, J. Pierre, Journal of Alloys and Compounds, 296 (2000) 243-252.

[47] F.G. Aliev, V.V. Kozyrkov, V.V. Moshchalkov, R.V. Scolozdra, K. Durczewski, Zeitschrift für Physik B Condensed Matter, 80 (1990) 353-357.

[48] J. Pierre, R.V. Skolozdra, Y.K. Gorelenko, M.A. Kouacou, Journal of Magnetism and Magnetic Materials, 134 (1994) 95-105.

[49] J. Pierre, L. Karla, K. Kaczmarska, Physica B, 259-261 (1999) 845-846.

[50] D. Jung, H.J. Koo, M.H. Whangbo, Journal of Molecular Structure: THEOCHEM, 527 (2000) 113-119.

[51] R. Nesper, Angewandte Chemie International Edition in English, 30 (1991) 789-817.

[52] H.C. Kandpal, C. Felser, R. Seshadri, Journal of Physics D: Applied Physics, 39 (2006) 776-785.

[53] L. Offernes, P. Ravindran, A. Kjekshus, Journal of Alloys and Compounds, 439 (2007) 37-54.

[54] S.J. Poon, T.M. Tritt, Y. Xi, S. Bhattacharya, V. Ponnambalam, A.L. Pope, R.T. Littleton, V.M. Browning, Bandgap features and thermoelectric properties of Ti-based half-Heusler alloys, in: Thermoelectrics, 1999. Eighteenth International Conference on, 1999, pp. 45-51.

[55] J. Tobola, J. Pierre, S. Kaprzyk, R.V. Skolozdra, M.A. Kouacou, J. Phys.: Condens. Matter, 10 (1998) 1013.

[56] T. Graf, C. Felser, S.S.P. Parkin, Progress in Solid State Chemistry, 39 (2011) 1-50.

[57] P. Larson, S.D. Mahanti, S. Sportouch, M.G. Kanatzidis, Physical Review B, 59 (1999) 15660.

[58] J. Tobola, J. Pierre, S. Kaprzyk, R.V. Skolozdra, M.A. Kouacou, Journal of Magnetism and Magnetic Materials, 159-200 (1996).

[59] H. Muta, T. Kanemitsu, K. Kurosaki, S. Yamanaka, Journal of Alloys and Compounds, 469 (2009) 50-55.

[60] J. Yang, H. Li, T. Wu, W. Zhang, L. Chen, J. Yang, Advanced Functional Materials, 18 (2008) 2880-2888.

[61] Y. Xia, S. Bhattacharya, V. Ponnambalam, A.L. Pope, S.J. Poon, T.M. Tritt, Journal of Applied Physics, 88 (2000) 1952-1955.

[62] Y. Xia, V. Ponnambalam, S. Bhattacharya, A.L. Pope, S.J. Poon, T.M. Tritt, Journal of Physics: Condensed Matter, 13 (2001) 77.

[63] V. Ponnambalam, Y. Xia, S. Bhattacharya, A.L. Pope, S.J. Poon, T.M. Tritt, Half-Heusler phases as prospective p-type thermoelectric materials, in: Thermoelectrics, 2005. ICT 2005. 24th International Conference on, 2005, pp. 391-394.

[64] W. Xie, Q. Jin, X. Tang, Journal of Applied Physics, 103 (2008) 043711-043715.

[65] T.M. Tritt, M.G. Kanatzidis, H.B. Lyon Jr., G. Mahan, Thermoelectric Materials - New Directions and Approaches, in: Materials Research Society Symposium, San Fransisco, California, 1997, pp. 109-114.

[66] C. Uher, J. Yang, S. Hu, D.T. Morelli, G.P. Meisner, Physical Review B, 59 (1999) 8615.

[67] S. Bhattacharya, A.L. Pope, R.T. Littleton Iv, T.M. Tritt, V. Ponnambalam, Y. Xia, S.J. Poon, Applied Physics Letters, 77 (2000) 2476-2478.

[68] H.-H. Xie, C. Yu, B. He, T.-J. Zhu, X.-B. Zhao, Journal of Electronic Materials, 41 (2012) 1826-1830.

[69] L.P. Romaka, Y.V. Stadnyk, A.M. Goryn, Y.K. Gorelenko, R.V. Skolozdra, MgAgAs structure type solid solutions as a new thermoelectric material, in: Thermoelectrics, 1997. Proceedings ICT '97. XVI International Conference on, 1997, pp. 516-519.

[70] H. Muta, T. Kanemitsu, K. Kurosaki, S. Yamanaka, *"Effect of carrier doping on the thermal conductivity of MNiSn based half-Heusler alloy"*, in: 25th International Conference on Thermoelectrics, 2006, pp. 120-123.

[71] V.A. Romaka, E.K. Hlil, Y.V. Skolozdra, P. Rogl, Y.V. Stadnyk, L.P. Romaka, A.M. Goryn, Semiconductors, 43 (2009) 1115-1123.

[72] H. Muta, T. Kanemitsu, K. Kurosaki, S. Yamanaka, Journal of Alloys and Compounds, 469 (2009) 50-55.

[73] J.W. Simonson, D. Wu, W.J. Xie, T.M. Tritt, S.J. Poon, Physical Review B, 83 (2011) 235211.

[74] Y.V. Stadnyk, A.M. Goryn', Y.K. Gorelenko, L.P. Romaka, N.A. Mel'nichenko, Inorg. Mater., 46 (2010) 842-846.

[75] H. Hohl, A.P. Ramirez, C. Goldmann, G. Ernst, B. Wolfing, E. Bucher, Journal of Physics: Condensed Matter, 11 (1999) 1697-1709.

[76] J. Yang, G.P. Meisner, L. Chen, Applied Physics Letters, 85 (2004) 1140-1142.

[77] S.R. Culp, S.J. Poon, N. Hickman, T.M. Tritt, J. Blumm, Applied Physics Letters, 88 (2006) 042106.

[78] Q. Shen, L. Chen, T. Goto, T. Hirai, J. Yang, G.P. Meisner, C. Uher, Applied Physics Letters, 79 (2001) 4165-4167.

[79] S. Sakurada, N. Shutoh, Applied Physics Letters, 86 (2005) 082105.

[80] S.-W. Kim, Y. Kimura, Y. Mishima, Intermetallics, 15 (2007) 349-356.

[81] H. Muta, T. Yamaguchi, K. Kurosaki, S. Yamanaka, Thermoelectric properties of ZrNiSn based half Heusler compounds, in: Thermoelectrics, 2005. ICT 2005. 24th International Conference on, 2005, pp. 351-354.

[82] T. Katayama, S. Kim, Y. Kimura, Y. Mishima, Journal of Electronic Materials, 32 (2003) 1160-1165.

[83] S. Chen, Z.F. Ren, Materials Today, 16 (2013) 387-395.

[84] T. Morimura, M. Hasaka, M. Yoshimoto, Journal of Alloys and Compounds, 416 (2006) 155-159.

[85] J.E. Douglas, C.S. Birkel, M.-S. Miao, C.J. Torbet, G.D. Stucky, T.M. Pollock, R. Seshadri, Applied Physics Letters, 101 (2012) 183902.

[86] J.E. Douglas, C.S. Birkel, N. Verma, V.M. Miller, M.-S. Miao, G.D. Stucky, T.M. Pollock, R. Seshadri, Journal of Applied Physics, 115 (2014) 043720.

[87] C.S. Birkel, J.E. Douglas, B.R. Lettiere, G. Seward, N. Verma, Y. Zhang, T.M. Pollock, R. Seshadri, G.D. Stucky, Physical Chemistry Chemical Physics, 15 (2013) 6990-6997.

[88] K. Biswas, J. He, I.D. Blum, C.I. Wu, T.P. Hogan, D.N. Seidman, V.P. Dravid, M.G. Kanatzidis, Nature, 489 (2012) 414-418.

[89] J.P.A. Makongo, D.K. Misra, J.R. Salvador, N.J. Takas, G. Wang, M.R. Shabetai, A. Pant, P. Paudel, C. Uher, K.L. Stokes, P.F.P. Poudeu, Journal of Solid State Chemistry, 184 (2011) 2948-2960.

[90] J.P.A. Makongo, D.K. Misra, X. Zhou, A. Pant, M.R. Shabetai, X. Su, C. Uher, K.L. Stokes, P.F.P. Poudeu, Journal of the American Chemical Society, 133 (2011) 18843-18852.

[91] J.P.A. Makongo, X. Zhou, D.K. Misra, C. Uher, P.F.P. Poudeu, Journal of Solid State Chemistry, 201 (2013) 280-287.

[92] P. Sahoo, Y. Liu, J.P.A. Makongo, X.-L. Su, S.J. Kim, N. Takas, H. Chi, C. Uher, X. Pan, P.F.P. Poudeu, Nanoscale, 5 (2013) 9419-9427.

[93] Y.W. Chai, Y. Kimura, Acta Materialia, 61 (2013) 6684-6697.

[94] Y.W. Chai, Y. Kimura, Applied Physics Letters, 100 (2012) 033114.

[95] Y. Liu, P. Sahoo, J.P.A. Makongo, X. Zhou, S.-J. Kim, H. Chi, C. Uher, X. Pan, P.F.P. Poudeu, Journal of the American Chemical Society, 135 (2013) 7486-7495.

[96] J.P. Heremans, C.M. Thrush, D.T. Morelli, Journal of Applied Physics, 98 (2005) 063703.

[97] D.T. Do, S.D. Mahanti, J.J. Pulikkotil, ArXiv, 1312.2985 [cond-mat.mes-hall] (2013).

[98] K. Biswas, J. He, Q. Zhang, G. Wang, C. Uher, V.P. Dravid, M.G. Kanatzidis, Nature Chemistry, 3 (2011) 160-166.

[99] Y.V. Stadnyk, R.V. Skolozdra, Inorg. Mater., 27 (1991) 1884-1885.

[100] K. Kirievsky, Y. Gelbstein, D. Fuks, Journal of Solid State Chemistry, 203 (2013).

[101] V.V. Romaka, P. Rogl, L. Romaka, Y.V. Stadnyk, A. Grytsiv, O. Lakh, V. Krayovskii, Intermetallics, 35 (2013) 45-52.

[102] V.V. Romaka, P. Rogl, L. Romaka, Y. Stadnyk, N. Melnychenko, A. Grytsiv, M. Falmbigl, N. Skryabina, Journal of Solid State Chemistry, 197 (2013) 103-112.

[103] H. Muta, T. Kanemitsu, K. Kurosaki, S. Yamanaka, Materials Transactions, 47 (2006) 1453-1457.

[104] H. Hazama, R. Asahi, M. Matsubara, T. Takeuchi, Journal of Electronic Materials, 39 (2010) 1549-1553.

[105] H. Hazama, M. Matsubara, R. Asahi, T. Takeuchi, Journal of Applied Physics, 110 (2011) 063710.

[106] P. Larson, S.D. Mahanti, M.G. Kanatzidis, Physical Review B, 62 (2000) 12754-12762.

[107] K. Miyamoto, A. Kimura, K. Sakamoto, M. Ye, Y. Cui, K. Shimada, H. Namatame, M. Taniguchi, S.I. Fujimori, Y. Saitoh, E. Ikenaga, K. Kobayashi, J. Tadano, T. Kanomata, Applied Physics Express, 1 (2008) 081901.

[108] Y. Gelbstein, N. Tal, A. Yarmek, Y. Rosenberg, M.P. Dariel, S. Ouardi, B. Balke, C. Felser, M. Köhne, Journal of Materials Research, 26 (2011) 1919-1924.

[109] K. Kurosaki, T. Maekawa, H. Muta, S. Yamanaka, Journal of Alloys and Compounds, 397 (2005) 296-299.

[110] M. Zou, J.-F. Li, B. Du, D. Liu, T. Kita, Journal of Solid State Chemistry, 182 (2009) 3138-3142.

[111] S. Bhattacharya, T.M. Tritt, Y. Xia, V. Ponnambalam, S.J. Poon, N. Thadhani, Applied Physics Letters, 81 (2002) 43-45.

[112] S. Bhattacharya, M.J. Skove, M. Russell, T.M. Tritt, Y. Xia, V. Ponnambalam, S.J. Poon, N. Thadhani, Physical Review B, 77 (2008) 184203.

[113] G. Joshi, X. Yan, H. Wang, W. Liu, G. Chen, Z. Ren, Advanced Energy Materials, 1 (2011) 643-647.

[114] G. Joshi, T. Dahal, S. Chen, H. Wang, J. Shiomi, G. Chen, Z. Ren, Nano Energy, 2 (2013) 82-87.

[115] X. Yan, W. Liu, H. Wang, S. Chen, J. Shiomi, K. Esfarjani, H. Wang, D. Wang, G. Chen, Z. Ren, Energy & Environmental Science, 5 (2012) 7543-7548.

[116] X. Yan, G. Joshi, W. Liu, Y. Lan, H. Wang, S. Lee, J.W. Simonson, S.J. Poon, T.M. Tritt, G. Chen, Z.F. Ren, Nano Letters, 11 (2010) 556-560.

[117] L.E. Smart, E.A. Moore, Solid State Chemistry: An Introduction, 3rd ed., CRC Press, Boca Raton, 2005.

[118] A.R. West, Solid State Chemistry and its Applications, John Wiley & Sons, Chichester, 1984.

[119] D. McKie, C. McKie, Essentials of Crystallography, Blackwell Scientific Publications, Oxford, 1986.

[120] C. Hammond, The Basics of Crystallography and Diffraction, 2nd ed., Oxford University Press, Oxford, 2001.

[121] S.M. Bennington, R.I. Smith, A.C. Hannon, ISIS Neutron Training Course Booklet, ISIS, STFC, Harwell, 2012.

[122] http://www.isis.stfc.ac.uk/instruments/polaris/, in, 11/12/13.

[123] http://www.isis.stfc.ac.uk/instruments/wish/science/wish-science6445.html, in, 11/12/13.

[124] L.B. McCusker, R.B. von Dreele, D.E. Cox, D. Louer, P. Scardi, Journal of Applied Crystallography, 32 (1999) 36-50.

[125] H.M. Rietveld, Journal of Applied Crystallography, 2 (1969) 65-71.

[126] H.M. Rietveld, Acta Crystallographica, 22 (1967) 151-152.

[127] R.A. Young, The Rietveld Method, Oxford University Press, Oxford, 1993.

[128] A.C. Larson, R.B. Von Dreele, in General Structure Analysis System (GSAS), (2000).

[129] B.H. Toby, Journal of Applied Crystallography, 34 (2001) 210-213.

[130] J.P. Eberhart, Structural and Chemical Analysis of Materials, John Wiley & Sons, Chichester, 1991.

[131] T.G. Rochow, P.A. Tucker, Introduction to Microscopy by Means of Light, Electrons, X-rays, or Acoustics, 2nd ed., Plenum Press, New York, 1994.

[132] E.M. Slayter, H.S. Slayter, Cambridge University Press, Cambridge, 1992.

[133] P.S. Gaal, M.-A. Thermitus, D.E. Stroe, Journal of Thermal Analysis and Calorimetry, 78 (2004) 185-189.

[134] M. Schwall, B. Balke, Physical Chemistry Chemical Physics, 15 (2013) 1868-1872.

[135] S. Populoh, M.H. Aguirre, O.C. Brunko, K. Galazka, Y. Lu, A. Weidenkaff, Scripta Materialia, 66 (2012) 1073-1076.

[136] D.B. Williams, C.B. Carter, Transmission Electron Microscopy Springer, New York, 1996.

[137] J. Shiomi, K. Esfarjani, G. Chen, Physical Review B, 84 (2011) 104302.

[138] H.-H. Xie, J.-L. Mi, L.-P. Hu, N. Lock, M. Chirstensen, C.-G. Fu, B.B. Iversen, X.-B. Zhao, T.-J. Zhu, CrystEngComm, 14 (2012) 4467-4471.

[139] R.A. Downie, D.A. MacLaren, R.I. Smith, J.W.G. Bos, Chemical Communications, 49 (2013) 4184-4186.

[140] P. Hermet, K. Niedziolka, P. Jund, RSC Advances, 3 (2013) 22176-22184.

[141] J.E. Douglas, C.S. Birkel, M.-S. Miao, C.J. Torbet, G.D. Stucky, T.M. Pollock, R. Seshadri, Applied Physics Letters, 101 (2012) 183902-183904.

[142] M.A. Kouacou, J. Pierre, R.V. Skolozdra, Journal of Physics: Condensed Matter, 7 (1995) 7373.

[143] M.G. Shelyapina, N. Koblynk, L. Romaka, Y.V. Stadnyk, O. Boda, E.K. Hlil, P. Wolfers, D. Fruchart, J. Tobola, Journal of Alloys and Compounds, 347 (2002) 43.

[144] G.A. Landrum, R. Hoffmann, J. Evers, H. Boysen, Inorganic Chemistry, 37 (1998) 5754-5763.

[145] S.V. Ackerbauer, A. Senyshyn, H. Borrmann, U. Burkhardt, A. Ormeci, H. Rosner, W. Schnelle, M. Gamża, R. Gumeniuk, R. Ramlau, E. Bischoff, J.C. Schuster, F. Weitzer, A. Leithe-Jasper, L.H. Tjeng, Y. Grin, Chemistry – A European Journal, 18 (2012) 6272-6283.

[146] I. Shirotani, Y. Konno, Y. Okada, C. Sekine, S. Todo, T. Yagi, Solid State Communications, 108 (1998) 967.

[147] S. Yashiro, A. Kasahi, R. Kasai, H. Samata, Y. Nagata, Journal of Alloys and Compounds, 309 (2000) 51-56.

[148] T. Takabatake, T. Sasakawa, J. Kitgawa, T. Suemitsu, Y. Echizen, K. Umeo, M. Sera, Y. Bando, Physica B, 328 (2003) 53-57.

[149] J. Wang, X.-C. Liu, S.-Q. Xia, X.-T. Tao, Journal of the American Chemical Society, 135 (2013) 11840-11848.

[150] Y. Kamihara, T. Watanabe, M. Hirano, H. Hosono, Journal of the American Chemical Society, 130 (2008) 3296-3297.

[151] G. Wu, Y.L. Xie, H. Chen, M. Zhong, R.H. Liu, B.C. Shi, Q.J. Li, X.F. Wang, T. Wu, Y.J. Yan, J.J. Ying, X.H. Chen, Journal of Physics: Condensed Matter 21 (2009) 142203.

[152] M. Rotter, M. Tegel, D. Johrendt, Physical Review Letters, 101 (2008) 107006.

[153] D.C. Johnston, Advances in Physics, 59 (2010) 803-1031.

[154] R. Pottgen, D. Johrendt, Zeitschrift fur Naurforschung, 63b (2008) 1135-1148.

[155] Y. Kamihara, H. Hiramatsu, M. Hirano, R. Kawamura, H. Yanagi, T. Kamiya, H. Hosono, Journal of the American Chemical Society, 128 (2006) 10012-10013.

[156] T. Watanabe, H. Yanagi, T. Kamiya, Y. Kamihara, H. Hiramatsu, M. Hirano, H. Hosono, Inorganic Chemistry, 46 (2007) 7719-7721.

[157] A. Marcinkova, D.A.M. Grist, I. Margiolaki, T.C. Hansen, S. Margadonna, J.-W.G. Bos, Physical Review B, 81 (2010) 064511.

[158] H. Yanagi, R. Kawamura, T. Kamiya, Y. Kamihara, M. Hirano, T. Nakamura, H. Osawa, H. Hosono, Physical Review B, 77 (2008) 224431.

[159] A. Pandey, R.S. Dhaka, J. Lamsal, Y. Lee, V.K. Anand, A. Kreyssig, T.W. Heitmann, R.J. McQueeney, A.I. Goldman, B.N. Harmon, A. Kaminski, D.C. Johnston, Physical Review Letters, 108 (2012) 087005.

[160] E.J. Wildman, J.M.S. Skakle, N. Emery, A.C. McLaughlin, Journal of the American Chemical Society, 134 (2012) 8766-8769.

[161] N. Emery, E.J. Wildman, J.M.S. Skakle, G. Giriat, R.I. Smith, A.C. McLaughlin, Chemical Communications, 46 (2010) 6777-6779.

[162] T. Hanna, S. Matsuishi, K. Kodama, T. Otomo, S.-i. Shamoto, H. Hosono, Physical Review B, 87 (2013) 020401.

[163] J.W. Simonson, Z.P. Yin, M. Pezzoli, J. Guo, J. Liu, K. Post, A. Efimenko, N. Hollmann, Z. Hu, H.-J. Lin, C.-T. Chen, C. Marques, V. Leyva, G. Smith, J.W. Lynn, L.L. Sun, G. Kotliar, D.N. Basov, L.H. Tjeng, M.C. Aronson, Proceedings of the National Academy of Sciences, 109 (2012) E1815-E1819.

[164] S. Komatsuzaki, Y. Ohki, M. Sasaki, Y. Takahashi, K. Takase, Y. Takano, K. Sekizawa, Magnetic Properties of LnOZnSb (Ln = La, Ce, Pr), in: Low Temperature Physics: 24th International Conference on Low Temperature Physics, 2006, pp. 1255.

[165] Y. Takano, S. Komatsuzaki, H. Komasaki, T. Watanabe, Y. Takahashi, K. Takase, Journal of Alloys and Compounds, 451 (2008) 467-469.

[166] I. Scellenberg, T. Nilges, R. Pottgen, Zeitschrift fur Naturforschung, 63b (2008) 834.

[167] J. Gurgul, M.T. Rinke, I. Schellenberg, R. Pöttgen, Solid State Sciences, 17 (2013) 122-127.

[168] S.A.J. Kimber, A.H. Hill, Y.-Z. Zhang, H.O. Jeschke, R. Valentí, C. Ritter, I. Schellenberg, W. Hermes, R. Pöttgen, D.N. Argyriou, Physical Review B, 82 (2010) 100412.

[169] V. Johnson, W. Jeitschko, Journal of Solid State Chemistry, 11 (1974) 161-166.

[170] I.R. Shein, A.L. Ivanovskii, Journal of Structural Chemistry, 50 (2009) 552-555.

[171] K. Guo, Z.Y. Man, Q. Cao, G., H.H. Chen, X. Guo, J.T. Zhao, Chemical Physics, 380 (2011) 54-60.

[172] M. Yasukawa, K. Ueda, H. Hosono, Journal of Appled Physics, 95 (2004) 3594-3597.

[173] X.-J. Wang, M.-B. Tang, J.-T. Zhao, H.-H. Chen, X.-X. Yang, Applied Physics Letters, 90 (2007) 232107.

[174] H. Zhang, J.-T. Zhao, Y. Grin, X.-J. Wang, M.-B. Tang, Z.-Y. Man, H.-H. Chen, X.-X. Yang, The Journal of Chemical Physics, 129 (2008) 164713.

[175] A. Marcinkova, T.C. Hansen, C. Curfs, S. Margadonna, J.W.G. Bos, Physical Review B, 82 (2010) 174438.

[176] A. Marcinkova, E. Suard, A.N. Fitch, S. Margadonna, J.W.G. Bos, Chemistry of Materials, 21 (2009) 2967-2972.

[177] L. Boeri, O.V. Dolgov, A.A. Golubov, Physica C, 469 (2009) 628-634.

[178] N. Qureshi, Y. Drees, J. Werner, S. Wurmehl, C. Hess, R. Klingeler, B. Buchner, M.T. Fernandez-Diaz, M. Braden, Physical Review B, 82 (2010).

[179] J.W. Lynn, P. Dai, Physica C, 469 (2009) 469-476.

[180] A. Marcinkova, T.C. Hansen, J.W.G. Bos, Journal of Physics: Condensed Matter, 24 (2012) 256007.

[181] K. Guo, Z.-Y. Man, X.-J. Wang, H.-H. Chen, M.-B. Tang, Z.-J. Zhang, Y. Grin, J.-T. Zhao, Dalton Transactions, 40 (2011) 10007-10013.

Appendix 1

Contained in this appendix are the X-ray diffraction and thermoelectric property data collected for the $Ti_{1-x}Zr_xNiSn_{0.95}$ series referred to in Chapter 4. Two series were prepared as described in section 4.2.

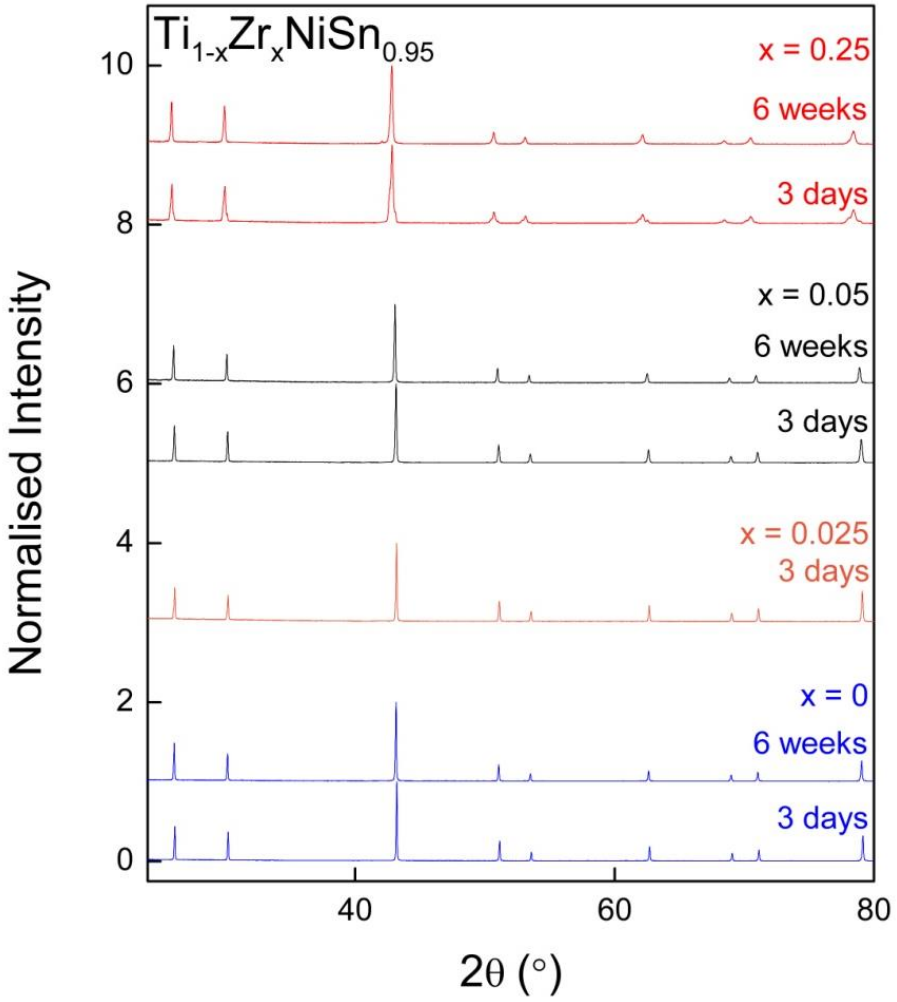

Figure 1: Laboratory X-ray powder diffraction patterns for the $Ti_{1-x}Zr_xNiSn_{0.95}$ series ($0 \leq x \leq 0.25$).

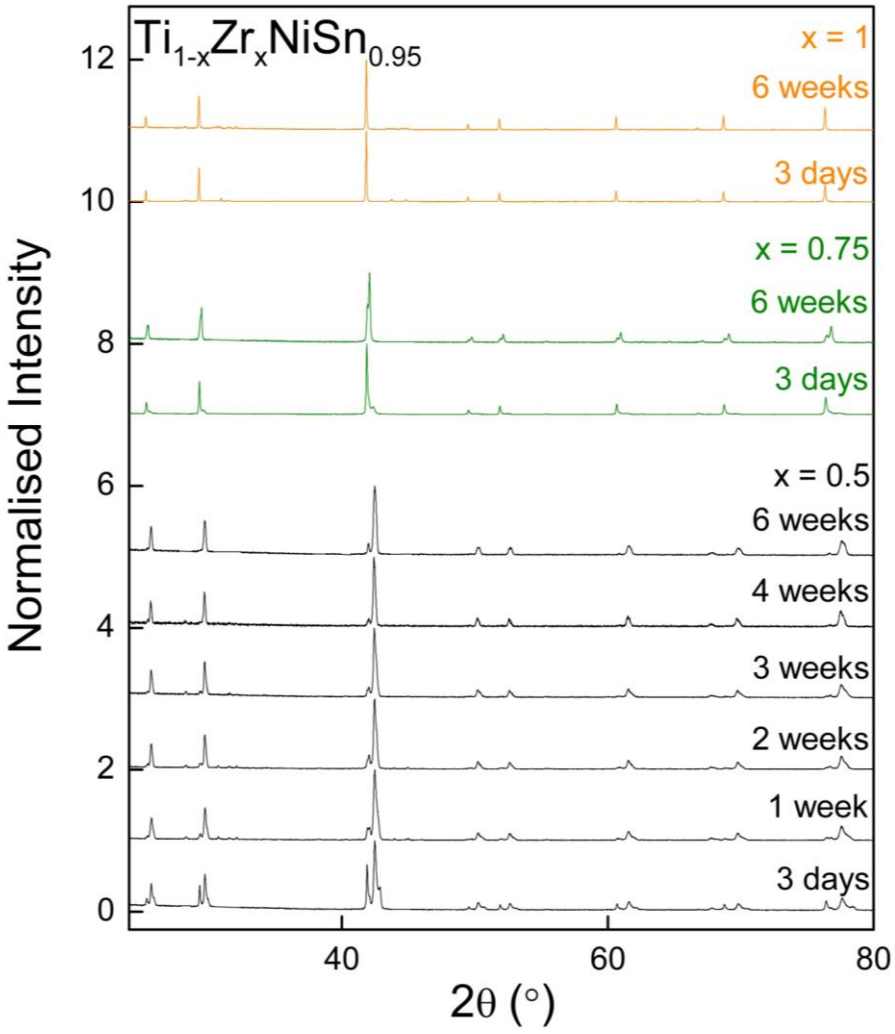

Figure 2: Laboratory X-ray powder diffraction patterns for the $Ti_{1-x}Zr_xNiSn_{0.95}$ series ($0.5 \leq x \leq 1$).

Table 1: Nominal compositions, anneal time, lattice constants (a), experimental compositions (using Vegard's law – x_{Veg}), composition variance (Δx), molar percentages (mol%), average composition (x_{avg}) , and goodness of fit (χ^2) for the $Ti_{1-x}Zr_xNiSn_{0.95}$ compositions.

x	Anneal Time	a (Å)	x_{Vegard}	Δx	mol%	x_{avg}	χ^2
0	3 days	5.9282(1)	N/A	0	79(1)	N/A	2.9
		5.9319(1)		0	21(1)		
	6 weeks	5.9325(1)		0	50		1.8
		5.9355(1)		0.02(1)	50		
0.025	3 days	5.9313(1)	0.02(1)	0.01(1)	73(1)	0.023	2.9
		5.9351(1)	0.04(1)	0.01(1)	27(1)		
0.05	3 days	5.9331(1)	0.03(1)	0.01(1)	38.4(9)	0.05	3.1
		5.9390(1)	0.06(1)	0.03(1)	61.6(9)		
	6 weeks	5.9410(1)	0.05(1)	0.01(1)	45(2)	0.07	1.5
		5.9462(1)	0.08(1)	0.05(1)	55(2)		
0.25	3 days	5.9393(1)	0.06(1)	-0.01(1)	2.5(8)		
		5.9722(1)	0.25(1)	0.16(1)	78.0(6)	0.27	3.3
		5.9974(1)	0.39(1)	0.11(1)	19.6(5)		
	6 weeks	5.9654(1)	0.19(1)	0.04(1)	22.0(6)		
		5.9748(1)	0.24(1)	0.09(1)	56.5(3)	0.25	1.9
		5.9908(1)	0.33(1)	0.15(1)	20.4(5)		
		6.0749(1)	0.81(1)	0.07(4)	1.1(1)		
0.5	3 days	5.9786(1)	0.28(1)	0.23(1)	16.7(2)		
		6.0221(1)	0.53(1)	0.21(1)	62.2(1)	0.57	2.9
		6.0856(1)	0.88(1)	0.11(1)	4.8(2)		
		6.1041(1)	0.98(1)	0.05(1)	16.3(3)		
	1 week	5.9917(1)	0.38(1)	0.09(1)	10.8(3)		
		6.0108(1)	0.46(1)	0.15(1)	56.6		
		6.0289(1)	0.56(1)	0.15(1)	21.6(3)	0.56	2.2
		6.0820(1)	0.86(1)	0.07(1)	3.8(2)		
		6.1016(1)	0.97(1)	0.10(1)	7.1(2)		
	2 weeks	6.0029(1)	0.43(1)	0.08(1)	16.7(5)		
		6.0170(1)	0.49(1)	0.10(1)	24.2(4)		
		6.0292(1)	0.56(1)	0.10(1)	46.7	0.56	1.7
		6.0837(1)	0.87(1)	0.13(1)	8.7(3)		
		6.1020(1)	0.97(1)	0.08(1)	3.7(2)		
	3 weeks	6.0034(1)	0.43(1)	0.11(1)	20.1(6)		
		6.0182(1)	0.50(1)	0.10(1)	26.1(4)		
		6.0306(1)	0.57(1)	0.10(1)	46.2	0.55	1.6
		6.0838(1)	0.87(1)	0.05(1)	3.8(2)		
		6.1006(1)	0.97(1)	0.08(1)	3.7(2)		
	4 weeks	6.0177(1)	0.49(1)	0.09(1)	29.1		
		6.0320(1)	0.58(1)	0.10(1)	63.7(8)	0.57	1.9
		6.0880(1)	0.88(1)	0.19(1)	7.3(2)		
	6 weeks	6.0076(1)	0.44(1)	0.07(1)	24.5(7)		
		6.0194(1)	0.49(1)	0.09(1)	36.7(6)	0.52	1.5
		6.0302(1)	0.55(1)	0.09(1)	32.9(9)		
		6.0867(1)	0.89(1)	0.07(1)	6.0(2)		
0.75	3 days	6.0394(1)	0.62(1)	0.33(1)	21.4(5)		
		6.0871(1)	0.89(1)	0.16(1)	20.6(8)	0.89	4.3
		6.1053(1)	0.99(1)	0.03(1)	58.0(6)		
	6 weeks	6.0798(1)	0.84(1)	0.07(1)	67.1(3)	0.88	1.6
		6.1022(1)	0.97(1)	0.09(1)	32.8(3)		
1.0	3 days	6.1075(1)	N/A	0.01(1)	100	N/A	5.7
	6 weeks	6.1080(1)		0	100		1.9
0.5, 0.025	4 weeks	6.0003(1)	0.39(1)		22	0.505	1.6
		6.0088(1)	0.44(1)		8		
		6.0193(1)	0.49(1)		49		
		6.0278(1)	0.54(1)		12		
		6.0844(3)	0.87(1)		5		
		6.1001(5)	0.96(1)		4		

Appendix 2

The SEM images referred to in Chapter 5 are presented in Figures 1-5, below. Table 1 contains the estimated atomic ratios for each area displayed, as determined by elemental mapping. The areas investigated are largely homogeneous, with no indication of formation of micron sized full-Heusler inclusions. The only features observed are consistent with impurity phases, present at levels below the detection limits of X–ray diffraction. Apparent in Figure 1, is a TiSn binary impurity in TiNiSn. The image for $TiNi_{1.05}Sn$ is dominated by the surface topography (Figure 2). The image for $TiNi_{1.5}Sn$ is presented in Figure 3. Separate areas that are relatively rich and deficient in Ni are observable in these images, indicating full-Heusler and half-Heusler domains within this sample. Ti, Sn and TiSn inclusions are observable in the images for $TiNiCo_{0.05}Sn$ (Figure 4) and $TiNiCu_{0.05}Sn$ (Figure 5).

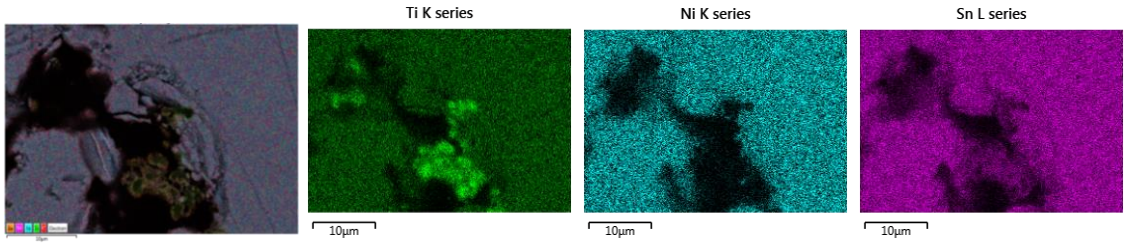

Figure 1: Low magnification SEM images for TiNiSn, highlighting TiSn binary inclusions.

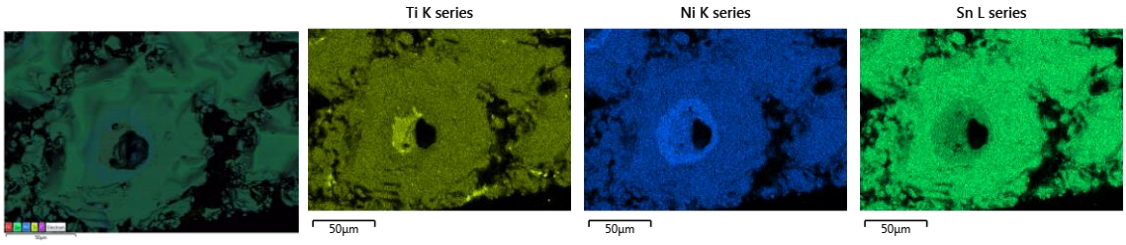

Figure 2: Low magnification SEM images for $TiNi_{1.05}Sn$, highlighting rough surface topography.

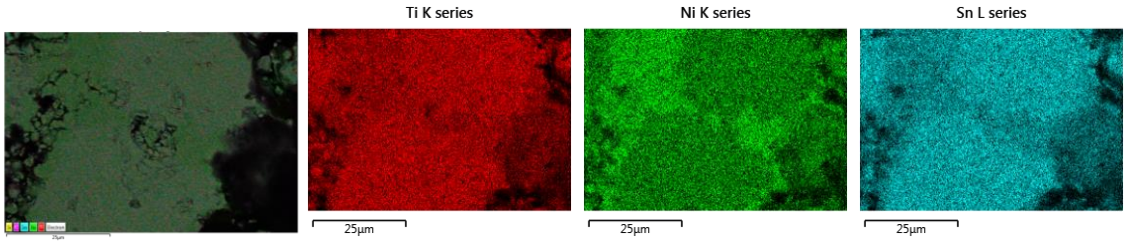

Figure 3: Low magnification SEM images for $TiNi_{1.5}Sn$, highlighting Ni rich and deficient areas, consistent with full- and half-Heusler domains.

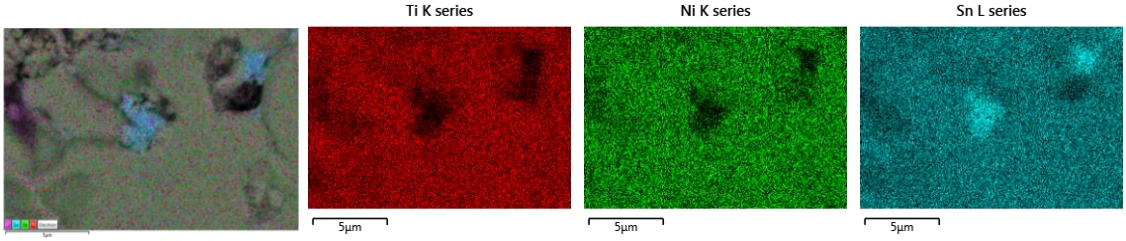

Figure 4: Low magnification SEM images for $TiNiCo_{0.05}Sn$, highlighting Sn inclusions.

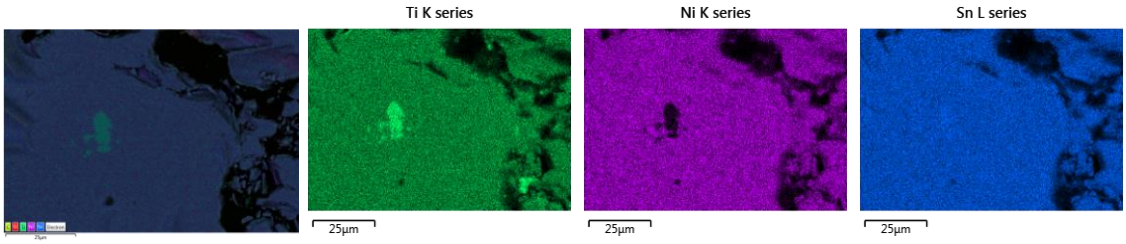

Figure 5: Low magnification SEM images for $TiNiCo_{0.05}Sn$, highlighting TiSn binary inclusion.

Table 1: Approximate atomic ratios of elements in the areas displayed in Figures 1-5, determined by elemental mapping.

	Ti	Ni	Co	Cu	Sn
TiNiSn	0.46	0.39	-	-	0.44
$TiNi_{1.05}Sn$	0.44	0.42	-	-	0.38
$TiNi_{1.5}Sn$	0.44	0.46	-	-	0.44
	0.38	0.46	-	-	0.38
$TiNiCo_{0.05}Sn$	0.42	0.41	0.03	-	0.45
$TiNiCu_{0.05}Sn$	0.44	0.39	-	0.02	0.44